University of Alberta

Study of Weak Interactions in Xenon Atom Containing van der Waals Complexes

by

Qing Wen

A thesis submitted to the Faculty of Graduate Studies and Research

in partial fulfillment of the requirements for the degree of Doctor of Philosophy

Department of Chemistry

Edmonton, Alberta

Fall 2007

Your file Votre référence
ISBN: 978-0-494-33092-0
Our file Notre référence
ISBN: 978-0-494-33092-0

Abstract

Microwave spectra of seven Xe containing van der Waals complexes, namely Xe-N_2, Xe-CH_4, Xe-H_2O, Xe-$(H_2O)_2$, Xe-NH_3, Ne-Xe-NH_3, and Xe-O_2, were recorded using a Fourier transform microwave spectrometer. Nuclear quadrupole hyperfine structures arising from the ^{131}Xe (nuclear spin $I = 3/2$), ^{14}N ($I = 1$), D ($I = 1$), and ^{17}O ($I = 5/2$) nuclei and magnetic hyperfine structures due to the interactions of the electron spin of O_2 ($S = 1$) and the nuclear spins of ^{129}Xe ($I = 1/2$) and ^{131}Xe were detected and analyzed. The spectroscopic results were complemented by *ab initio* potential energy surfaces of Xe-N_2, Xe-CH_4, Xe-H_2O, Xe-NH_3, and Xe-O_2, dipole moment calculations of Xe-CH_4, and a geometry optimization of Xe-$(H_2O)_2$. Both spectroscopic and *ab initio* results were used to derive information about structure and dynamics of the complexes.

Both recorded rotational spectra and *ab inito* potential energy surfaces of Xe-N_2 and Xe-O_2 are in accord with T-shaped structures of the complexes. For the Xe-N_2 complex, the rotational spectra derived from *ab initio* potential energy surfaces were directly compared to the recorded spectra. A scaled potential energy surface with "microwave accuracy" was obtained. For the Xe-CH_4, Xe-H_2O, and Xe-NH_3 dimers, transitions within various tunneling states were observed. The observed spectra indicate large amplitude internal rotation motions of the CH_4, H_2O, and NH_3 subunits and the inversion motion of NH_3 within the corresponding dimers. Both *a*- and *b*- type transitions were measured for the Xe-$(H_2O)_2$ and Ne-Xe-NH_3 van der Waals trimers. Information about structures and vibrational motions of the trimers were compared

with those of corresponding dimers. Non-additive three-body effects were detected for both trimers and interpreted.

This work has furthered the understanding of the Xe-molecule interactions. In particular, the observed ^{131}Xe nuclear quadrupole coupling constants have provided detailed insight into the electronic environment of the Xe atom. The variations of these constants among different binding partners further prove that Xe is a sensitive atomic probe of its environment. This work is a stepping stone towards achieving molecular level interpretations of *in vivo* ^{129}Xe NMR/MRI results.

Preface

This thesis is based upon the research I have conducted at University of Alberta during January 2003 to August 2007. Some of the results presented in this thesis have been published. Here, I provide the reference for these results and they will not be repeatedly cited in the following chapters.

Chapter 3:

Qing Wen and Wolfgang Jäger, "Microwave Spectra of the Xe-N_2 van der Waals Complex: A Comparison of Experiment and Theory." *J. Chem. Phys.* **122**, 214310 (2005).

Chapter 4:

Qing Wen and Wolfgang Jäger, "Microwave and *Ab Initio* Studies of the Xe-CH_4 van der Waals Complex." *J. Chem. Phys.* **124**, 014301 (2006).

Chapter 5:

Qing Wen and Wolfgang Jäger, "Rotational Spectroscopic and *Ab Initio* Studies of the Xe-H_2O van der Waals Dimer." *J. Phys. Chem. A* **110**, 7560 (2006).

Qing Wen and Wolfgang Jäger, "Rotational Spectra of the Xe-$(H_2O)_2$ van der Waals Trimer: Xenon as a Probe of Electronic Structure and Dynamics." *J. Phys. Chem. A* **111**, 2093 (2007).

Acknowledgements

It is my pleasure to acknowledge my Ph. D. supervisor, Dr. Wolfgang Jäger, for his invaluable guidance and support over the past 4.5 years. I am extremely appreciating all the opportunities he gave me to attend conferences, learn and grow as a scientist.

I am grateful to many researchers in the Department of Chemistry who have provided me help regarding my research projects. In particular, I would like to thank Dr. Y. Xu for sharing her expertise on weakly bound complexes, Dr. A. Brown, Dr. P.-N. Roy, Dr. M. Klobukowski, and Dr. C. C. Lovallo for their advice in the computational studies.

I also want to acknowledge all the members of the Jäger and Xu groups, both past and present, for their useful suggestions and stimulating discussions during the course of my research. Special thank to Dr. W. Topic for sharing her experience about Ph. D. studies. Thanks to Z. Su, J. Landry, J. Michaud for their support and friendship.

Finally, I wish to express my appreciation to my parents, Y. Wen and S. Deng. Without their unselfish love, endless support and belief in me, this thesis would have been impossible. I also want to thank all my friends in Edmonton who made my life here colorful. And Y. Zhao, whose encouragement and support become special to me during the last stage of my Ph. D. research.

Table of Contents

List of Tables

List of Figures

List of Symbols

English letters

A	rotational constant $A = \frac{h}{8\pi^2 I_a}$
b	$b_F - c/3$
b_F	Fermi contact coupling constant
B	rotational constant $B = \frac{h}{8\pi^2 I_b}$
$\overline{B}$	$(B+C)/2$
c	dipole-dipole coupling constant
C	rotational constant $C = \frac{h}{8\pi^2 I_c}$
D_0	zero point corrected binding energy
D_e	binding energy
D_J, D_{JK}, D_K, d_1, d_2	quartic centrifugal distortion constants corresponding to Watson's *S*-reduction Hamiltonian
e	charge of electron
E	energy
g	magnetic g factor = magnetic moment (in Bohr magnetons or sometimes in nuclear magnetons) divided by angular momentum (in units $h/2\pi$). This is negative for electron spin or orbital angular momentum
h	Planck's constant
$\boldsymbol{F}$	force constant matrix
$\boldsymbol{F}$	total angular momentum
F	total angular momentum quantum number
H_J, H_{JK}, H_{KJ}, H_K, h_1, h_2, h_3	sextic centrifugal distortion constants corresponding to Watson's *S*-reduction Hamiltonian
H_r	rotational Hamiltonian
$\boldsymbol{I}$	nuclear spin angular momentum
I	nuclear spin angular momentum quantum number

I	moment of inertia tensor of molecule
I_a, I_b, I_c	principal components of moment of inertia tensor
$\boldsymbol{j}$	total angular momentum of monomer subunit
j	total angular momentum quantum number of monomer subunit
$\boldsymbol{J}$	total angular momentum of complex excluding nuclear spin
J	total angular momentum quantum number of complex excluding nuclear spin
k	force constant
k	Boltzmann constant
k	projection of angular momentum $\boldsymbol{j}$ onto principal symmetry axis of monomer
K	projection of angular momentum $\boldsymbol{j}$ onto intermolecular axis of complex
k_a, k_c	quantum numbers representing internal rotor states of monomer subunit which is an asymmetric rotor
K_a, K_c	K values of the limiting prolate and oblate symmetric tops, respectively, in an asymmetric rotor
m	mass of molecule
M	nuclear spin-rotation coupling tensor
M_{aa}, M_{bb}, M_{cc}	principal components of nuclear spin-rotation coupling tensor
q	electric field gradient tensor
Q	nuclear or electric quadrupole moment tensor
R	van der Waals distance
R_e	equilibrium distance
$\boldsymbol{S}$	electron spin angular momentum
S	electron spin angular momentum quantum number
T	absolute temperature

Greek letters

χ	nuclear quadrupole coupling tensor
χ_{aa}, χ_{bb}, χ_{cc}	principal components of nuclear quadrupole coupling tensor
χ_{ab}, χ_{ac}, χ_{bc}	off-diagonal elements of nuclear quadrupole coupling tensor
γ	Sternheimer shielding factor
γ	electron spin-rotation coupling tensor
Δ	deviation of calculated values from experimental values
Δ_J, Δ_{JK}, Δ_K, δ_J, δ_K	quartic centrifugal distortion constants corresponding to Watson's *A*-reduction Hamiltonian
$\Delta\nu$	difference between observed and calculated frequency
ΔZPE	zero-point vibrational energy correction
Φ	electric hexadecapole moment, a fourth rank tensor
Φ_J, Φ_{JK}, Φ_{KJ}, Φ_K, ϕ_J, ϕ_{JK}, ϕ_K	sextic centrifugal distortion constants corresponding to Watson's *A*-reduction Hamiltonian
φ	zenith angle in spherical coordinate system
λ	electron spin-spin coupling tensor
η	asymmetry parameter of nuclear quadrupole coupling tensor, defined as $\lvert\chi_{bb}-\chi_{cc}\rvert/\chi_{aa}$
θ	azimuth angle in spherical coordinate system
μ	electric dipole moment
μ	reduced mass
Π	quantum number $K = 1$
σ	standard deviation of the fit
$\mathbf{\Sigma}$	projection of electron spin angular momentum onto molecular axis
Σ	quantum number $K = 0$
ν	frequency
Ω	electric octopole moment, a third rank tensor

CHAPTER 1 Introduction

Van der Waals interactions occur between all molecules and atoms. These interactions have two essential features: the short-range repulsive force and the long-range attractive force. At some intermediate distances between each pair of atoms or molecules the repulsive and attractive forces become equivalent. Atoms or molecules will bind together and generate a van der Waals complex near these equilibrium structures.

These van der Waals interactions, also called intermolecular interactions, although much weaker than chemical bonds, determine many properties of condensed phase matter, for example, properties of surfaces and structures of molecular crystals.[1] In addition, they play a significant role in many physical, chemical and biological processes, including phase transitions,[2,3,4] solvation processes,[5,6] protein folding,[1,7] and enzyme reaction.[1,8] Therefore, detailed knowledge about intermolecular interactions on a molecular basis is crucial for the fundamental understanding of these macroscopic properties and phenomena.

The particular interest of this thesis is the intermolecular interactions between a xenon (Xe) atom and molecular environments. This research is motivated by the fact that the dispersion interaction, which is the most important attractive contribution to the intermolecular forces, is pronounced in Xe-molecule complex systems. The

dispersion interaction arises from the correlation between electron motions in different atoms or molecules. As electrons constantly move, an atom or molecule can generate an instantaneous electric dipole when the electron distribution is unsymmetrical about the nucleus. This instantaneous dipole distorts the electron distribution of a second atom or molecule, and therefore leads to an electrostatic attraction between the two atoms or molecules. For a large atom, such as Xe, the electron distribution can be easily distorted by any interactions because its valence electrons are relatively far from the nucleus. Such an electronic perturbation can be directly transmitted to the nucleus in the case of ^{129}Xe (nuclear spin quantum number I = 1/2) isotope, and as a consequence, affects the observable quantities in ^{129}Xe nuclear magnetic resonance (NMR) spectroscopy, for example, chemical shifts and relaxation parameters. Due to the high sensitivity of its NMR parameters to the environment, the ^{129}Xe nucleus has become an important atomic probe for structure characterization of condensed phases, especially microporous materials, such as zeolites[9] and clathrates.[10,11]

Since an optical pumping scheme was developed to achieve high spin polarization of ^{129}Xe and significantly enhance the sensitivity of NMR signals,[12] ^{129}Xe NMR and magnetic resonance imaging (MRI) methods have been widely applied in *in vivo* studies to obtain high resolution images of biological tissues, especially human lungs.[13,14] These high resolution images are usually difficult to obtain by conventional X-ray and ^{1}H MRI methods because of low concentrations of signal sources in the gas phase. The ^{129}Xe NMR/MRI method has the potential to be used for the investigation, diagnosis, and treatment of various pulmonary diseases. In addition to lung images, ^{129}Xe NMR/MRI studies have been extended to blood and other tissues of the body.[15]

Such applications have become a very promising method to, for example, characterize the blood flow and to probe brain functions under certain physiological conditions.[16]

The specific information about the structure and molecular distribution at the host site is encoded in the ^{129}Xe NMR/MRI results because the NMR signals highly depend on the intermolecular interactions of the Xe atom with its environments. To extract such information requires a fundamental understanding of Xe-host site interactions, for example, accurate interaction potentials. As a first step, Xe-molecule interaction potential energy surfaces, which describe the interaction potential energies as functions of relative positions and orientations of Xe and molecules, need to be constructed as ingredients for the corresponding magnetic shielding surfaces that are required for an interpretation of the NMR/MRI data. These potentials can be used as test cases for the construction of more complex Xe-host site interaction potentials and perhaps also to build them assuming pairwise additivity. In recent years, C. J. Jameson and coworkers have calculated *ab initio* interaction potentials and magnetic shielding surfaces of binary systems that contain a Xe atom and another binding partner, such as Ne, Ar, Kr, Xe,[17] CO, N_2, CO_2,[18, 19] CH_4, and CF_4 (Ref. 19), and of Xe in cages of up to 48 water molecules.[20] These calculations have been tested against experimental ^{129}Xe NMR data,[10,11,21,22,23,24] and provided necessary information for the calculations of average ^{129}Xe chemical shifts in liquids, such as water and other solvents containing CH_3-, CH_2-, CH-, CF_3-, CF_2-, and CF- moieties, via molecular dynamics methods.[25,26]

To fully interpret the ^{129}Xe NMR/MRI data, it is necessary to gain more detailed insight into the Xe-molecule interaction potentials. High resolution spectra, for example microwave spectra, of van der Waals complexes are a delicate probe of

the corresponding interaction potential energy surfaces and have been used in the past to gauge and improve *ab initio* and semi-empirical potentials.[27,28,29,30] Our approach is to compare the spectra calculated from these potentials with the experimental ones, and then to apply a scaling procedure to adjust the potentials accordingly to achieve satisfactory agreement with the experimental data.[27,28] In the Ne-N_2 (Ref. 29) and Ar-N_2 (Ref. 30) systems, the potential energy surfaces have achieved spectroscopic accuracy by changing one or more parameters, such as well depths and intermolecular separations. They reproduce experimental rotational transition frequencies within 0.1%.

A number of microwave studies of Xe-atom/molecule complexes have been previously reported, including Rg-Xe (Rg = Ne, Ar, and Kr),[31] Ne_2-Xe,[32] Xe-HCl,[33,34] Xe-HF,[35] Xe-CO_2,[36] Xe-NO_2,[37] Xe-CO,[38] Xe-C_6H_6,[39] and Xe-dimethyl ether.[40] From the determined spectroscopic constants, some information about molecular structure, well depth, energy barrier, zero-point motion, and radial and angular anisotropy of the interaction potential was extracted. In particular, the ^{131}Xe nuclear quadrupole coupling constants (χ) provide detailed information about the distortion of the spherically symmetric electric charge distribution of the free Xe atom as a result of weak intermolecular interactions. Such distortion originates in the microscopic environment of the Xe atom and is directly measured in NMR/MRI experiments. The degree of distortion depends uniquely on the type, position, and orientation of the surrounding molecules. Therefore, knowledge about how the electronic structure of the Xe atom is affected by the surrounding molecular distribution will be crucial in bridging the gap between the macroscopic phenomena observed in NMR/MRI experiments and their microscopic, molecular level interpretations. Previous

microwave studies proposed two major mechanisms responsible for the distortion of electric charge cloud around the Xe nucleus. One is the electric field gradient produced by the electric multipole moments of the partner molecules, taking into account large amplitude internal motions and intermolecular vibrations. This mechanism plays a dominant role in the systems of Xe-HCl [χ_{aa} = -4.9(2) MHz],[33,34] Xe-HF [χ_{aa} = -8.54(4) MHz],[35] and Xe-CO_2 [χ_{aa} = -3.05(6) MHz].[36] An extrapolation of ^{131}Xe nuclear quadrupole coupling constants of the Xe-HCl and Xe-HF complexes to the limit of zero electric multipole moments results in a small value of -0.243±1.6 MHz (See Figure 3 of Ref. 41). This value is on the same order of magnitude as the χ_{aa} values in the mixed rare gas complexes, including Ne-Xe [χ_{aa} = 0.3878(9) MHz], Ar-Xe [χ_{aa} = 0.723(4) MHz], Kr-Xe [χ_{aa} = 0.708(9) MHz],[31] and Ne_2-Xe [χ_{aa} = 0.564(2) MHz],[32] where the multipole moments of the partner molecules vanish. These values were interpreted in terms of the second mechanism, electron correlation interaction between electron clouds of the Xe atom and the partner molecules. In some cases like Xe-NO_2 [χ_{aa} = -0.95(1) MHz],[37] Xe-CO (χ_{aa} ~0.03 MHz),[38] and Xe-dimethyl ether [χ_{aa} = 4.57(3) MHz],[40] both these mechanisms have significant contributions, and therefore, the ^{131}Xe nuclear quadrupole coupling constants are a result of a balance between these two effects.

The primary goal of this thesis is to further the understanding of the Xe-molecule interactions, for example, to build accurate Xe-molecule interaction potentials. For this work, I select seven Xe atom containing van der Waals complexes, namely Xe-N_2, Xe-CH_4, Xe-H_2O, Xe-$(H_2O)_2$, Xe-NH_3, Xe-Ne-NH_3, and Xe-O_2, and will present them using a combined theoretical and experimental approach. The study

of each of these complexes will help to interpret ^{129}Xe NMR/MRI data because all these binding partners of Xe are main constituents of air and the human body, or closely related to important functional groups of proteins in living tissues. In this work, rotational spectra of each complex were recorded using a Fourier transform microwave spectrometer. Interaction potentials of five complexes, Xe-N_2, Xe-CH_4, Xe-H_2O, Xe-NH_3, and Xe-O_2, were constructed using *ab initio* methods. These potentials were used to complement spectroscopic results to extract information about molecular structure and dynamics. Spectroscopic results, in turn, validate the application of *ab inito* methods in the construction of accurate interaction potentials. In particular, in the Xe-N_2 system, as shown in Chapter 3, the rotational transition frequencies and spectroscopic constants calculated from *ab initio* potential energy surfaces were directly compared to the experiment results, and a scaled potential energy surface was obtained and can reproduce experimental transition frequencies within 0.01%.

The entire thesis is divided into 8 chapters. The present chapter, Chapter 1, gives a brief introduction and motivation for this work. Chapter 2 describes the experimental and theoretical approaches applied in this thesis, including the experimental setup of the Fourier transform microwave spectrometer used for recording the spectra, and *ab initio* methods for theoretical studies. Both experimental and theoretical results of the seven Xe atom containing complexes are presented in five separate chapters, with Xe-N_2 in Chapter 3, Xe-CH_4 in Chapter 4, Xe-H_2O and Xe-$(H_2O)_2$ in Chapter 5, Xe-NH_3 and Xe-Ne-NH_3 in Chapter 6, and Xe-O_2 in Chapter 7. In Chapter 8, general conclusions from this thesis work are provided.

References

[1] *Structural Chemistry and Molecular Biology*, edited by A. Rich and N. Davidson, (Freeman, San Francisco, 1968).

[2] J. O. Hirschfelder, C. F. Curtiss, and R. B. Bird, *Molecular Theory of Gases and Liquids*, (Wiley, New York, 1954).

[3] R. E. Miller, Science, **24**, 447 (1988).

[4] S. Sugano, *Microcluster Physics*, (Springer, Berlin, 1991).

[5] P. Kebarle, Annu. Rev. Phys. Chem. **28**, 445 (1997).

[6] A. Stace, Science, **294**, 1292 (2001).

[7] A. Kormychev and S. Leikin, Proc. Natl. Acad. Sci. USA **95**, 13579 (1988).

[8] W. Ferdinand, *The Enzyme Molecule*, (Wiley, London, 1976).

[9] N. Kato, T. Ueda, H. Omi, K. Miyakubo, and T. Eguchi, Phys. Chem. Chem. Phys. **6**, 5427 (2004).

[10] J. A. Ripmeester, C. I. Ratcliffe, and J. S. Tse, J. Chem. Soc., Faraday Trans. 1, **84**, 3731 (1988).

[11] J. A. Ripmeester and C. I. Ratcliffe, J. Phys. Chem. **94**, 8773 (1990).

[12] G. Navon, Y.-Q. Song, T. Room, S. Appelt, R. E. Taylor, and A. Pines, Science, **271**, 1848 (1996).

[13] A. Cherubini, and A.Bifone, Prog. Nucl. Magn. Reson. Spectrosc. **42**, 1 (2003).

[14] B. M. Goodson, J. Magn. Reson. **155**, 157 (2002).

[15] M. S. Albert, G. D. Cates, B. Driehuys, W. Happer, B. Saam, C. S. Springer, Jr., and A. Wishnia, Nature, **370**, 199 (1994).

[16] K. Uğurbil, G. Adriany, P. Andersen, W. Chen, R. Gruetter, X. Hu, H. Merkle, D.-S. Kim, S.-G. Kim, J. Strupp, X. H. Zhu, and S. Ogawa, Annu. Rev. Biomed. Eng. **2**, 633 (2000).

[17] C. J. Jameson, D. N. Sears, and A. C. de Dios, J. Chem. Phys. **118**, 2575 (2003).

[18] A. C. de Dios, and C. J. Jameson, J. Chem. Phys. **107**, 4253 (1997).

[19] D. N. Sears, and C. J. Jameson, J. Chem. Phys. **121**, 2151 (2004).

[20] D. Stueber, and C. J. Jameson, J. Chem. Phys. **120**, 1560 (2004).

[21] K. A. Udachin, G. D. Enright, C. I. Ratcliffe, and J. A. Ripmeester, J. Am. Chem. Soc. **119**, 11481 (1997).

[22] C. J. Jameson, A. K. Jameson, and S. M. Cohen, J. Chem. Phys. **65**, 3401 (1976).

[23] C. J. Jameson, A. K. Jameson, and S. M. Cohen, J. Chem. Phys. **66**, 5226 (1977).

[24] C. J. Jameson, A. K. Jameson, and H. Parker, J. Chem. Phys. **68**, 3943 (1978).

[25] C. J. Jameson and S. Murad, Chem. Phys. Lett. **380**, 556 (2003).

[26] C. J. Jameson, D. N. Sears, and S. Murad, J. Chem. Phys. **121**, 9581 (2004).

[27] J. M. M. Howson and J. M. Hutson, J. Chem. Phys. **115**, 5059 (2001).

[28] M. Meuwly and J. M. Hutson, J. Chem. Phys. **110**, 8338 (1999).

[29] W. Jäger, Y. Xu, G. Armstrong, M. C. L. Gerry, F. Y. Naumkin, F. Wang, and F. R. W. McCourt, J. Chem. Phys. **109**, 5420 (1998).

[30] W. Jäger, M. C. L. Gerry, C. Bissonnette, and F. R. W. McCourt, Faraday Discuss. **97**, 105 (1994).

[31] W. Jäger, Y. Xu, and M. C. L. Gerry, J. Chem. Phys. **99**, 919 (1993).

[32] Y. Xu, W. Jäger, and M. C. L. Gerry, J. Chem. Phys. **100**, 4171 (1994).

[33] M. R. Keenan, L. W. Buxton, E. J. Campbell, T. J. Balle, and W. H. Flygare, J. Chem. Phys. **73**, 3523 (1980).

[34] E. J. Campbell, L. W. Buxton, M. R. Keenan, and W. H. Flygare, Phys. Rev. A **24**, 812 (1981).

[35] F. A. Baiocchi, T. A. Dixon, C. H. Joyner, and W. Klemperer, J. Chem. Phys. **75**, 2041 (1981).

[36] M. Iida, Y. Ohshima, and Y. Endo, J. Phys. Chem. **97**, 357 (1993).

[37] C. J. Whitham, R. J. Low, and B. J. Howard, Chem. Phys. Lett. **286**, 408 (1998).

[38] K. A. Walker, T. Ogata, W. Jäger, M. C. L. Gerry, and I. Ozier, J. Chem. Phys. **106**, 7519 (1997).

[39] Th. Brupbacher, J. Makarewicz, and A. Bauder, J. Chem. Phys. **101**, 9736 (1994).

[40] W. Caminati, A. Millemaggi, J. L. Alonso, A. Lesarri, J. C. López, and S. Mata, Chem. Phys. Lett. **392**, 1 (2004).

[41] E. J. Campbell, L. W. Buxton, and A. C. Legon, J. Chem. Phys. **78**, 3483 (1983).

CHAPTER 2 Experimental and Theoretical Approaches

This chapter outlines the experimental and theoretical approaches applied for the study of Xe containing van der Waals complexes. It is divided into two sections. The first section gives an overview of microwave spectroscopy and describes the experimental technique used for recording the rotational spectra. The second section introduces the *ab initio* computational methods used for theoretical studies.

2.1 Microwave spectroscopy

2.1.1 Introduction and Overview of theoretical background

The interaction potentials of weakly bound van der Waals complexes typically have well depths around 100 cm^{-1} and the ground vibrational state is located well above the potential minimum. For example, the interaction potential of the Xe-N_2 complex has a well depth of 122.4 cm^{-1} and the ground vibrational state is about 20 cm^{-1} above the potential minimum. Intermolecular van der Waals vibrational bending and stretching modes typically occur in the energy range between 10 and 50 cm^{-1}. For example, in the Xe-N_2 complex, the van der Waals stretching frequency is estimated to be around 40 cm^{-1}, while the intramolecular N≡N stretching frequency is at about 2300 cm^{-1} (Ref. 1). Energy differences between rotational states are on the order of several GHz (1GHz $\approx$ 0.03 cm^{-1}). Therefore, many pure rotational transitions of van der Waals complexes fall into the microwave frequency region (0.03-0.3 cm^{-1}) and rotational

spectra of complexes with a permanent dipole moment can be detected using microwave spectroscopy. The theory of this spectroscopic method has been discussed in details in, for example, Refs. 2, 3, and 4. Here, only a brief theoretical background is given.

According to quantum mechanics, the rotational energies of molecules are quantized. The energies of rotational levels of a diatomic rigid molecule can be determined by solving the eigenvalues for its rotational Hamiltonian, $H_r = J^2/2I$. Here, the total angular momentum J is a constant of the rotational motion, and thus the corresponding quantum number J is a good quantum number to specify the rotational levels. I is the moment of inertia of the molecule. The resulting energy level expression is $E_J = BJ(J+1)$. The rotational constant B is defined as $B = \frac{h}{8\pi^2 I}$. In general, rotational transitions with selection rules $\Delta J = \pm 1$ are allowed.

For more complex symmetric and asymmetric top molecules, it is convenient to consider the rotation of the molecule about the principal axes of the moment of inertia tensor (a-, b-, and c- axes). Conventionally, these axes, called principal inertial axes, are selected to satisfy $I_c \geq I_b \geq I_a$ with the corresponding rotational constants A, B, and C. These are defined as $A = \frac{h}{8\pi^2 I_a}$, $B = \frac{h}{8\pi^2 I_b}$, and $C = \frac{h}{8\pi^2 I_c}$, and are in the sequence $A \geq B \geq C$. Symmetric top molecules can be divided into two subdivisions, namely prolate and oblate symmetric tops. A prolate symmetric top, such as NH_3, has $A > B = C$, and its a- inertial axis lies along the principal symmetry axis, while $A = B > C$ for an oblate symmetric top, such as BF_3, where the c- axis is the principal symmetry axis. For a symmetric rotor, the quantum number K, which represents the

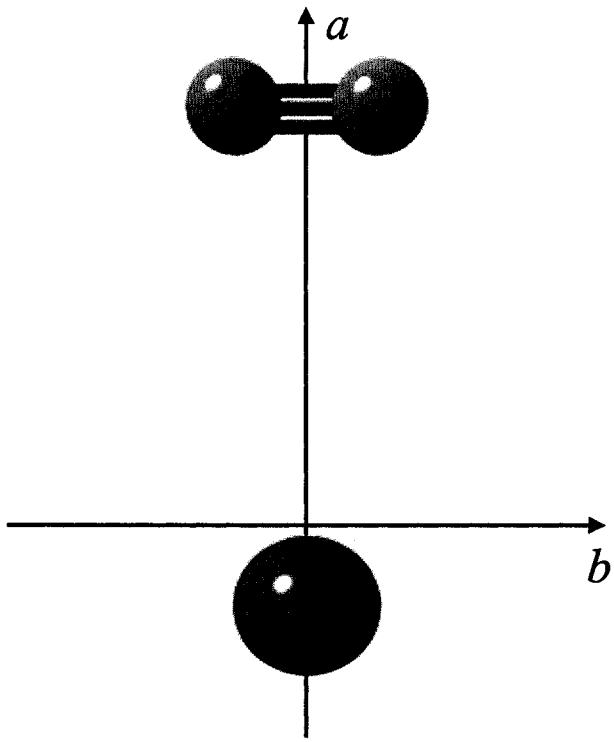

Figure 2-1: Structure of the Xe-N_2 complex. The *a*- and *b*- axes indicate the principal inertial axes of the system, and the *c*- axis is perpendicular to the plane of the complex.

projection of the angular momentum ***J*** onto the principal symmetry axis, is used to specify the rotational states, in addition to the total angular momentum quantum number *J*.

For an asymmetric top molecule, the principal inertial axes are selected to satisfy $I_c > I_b > I_a$ and $A > B > C$. Taking the Xe-N_2 complex as an example, a T-shaped structure as illustrated in Figure 2-1 is assumed based on its equilibrium structure obtained from the *ab initio* calculation (see Chapter 3). The complex has the least moment of inertia about the axis which passes through the Xe atom and the center of mass of the N_2 monomer, and this axis is selected as the *a*- axis (see Figure 2-1). The

moment of inertia about the *c*- axis, which is perpendicular to the plane of the complex, has the maximum value. The *b*- axis, perpendicular to both *a*- and *c*- axes, is parallel to the N_2 molecular axis. Rotational motion about the *a*- axis refers to the rotation of N_2 monomer itself within the complex, while rotations about *b*- and *c*- axes correspond to the end-over-end rotations of the Xe-N_2 complex. Since there is no permanent dipole moment along the N_2 molecular axis, the rotation of the N_2 monomer is not observable in microwave spectroscopy. Only the end-over-end rotation of the complex can be detected.

For asymmetric top molecules, there is no set of convenient quantum numbers which can both well specify the rotational states and have simple physical meanings. Conventionally, the rotational states of an asymmetric rotor are labeled by the quantum number J and two pseudo quantum numbers, K_a and K_c, which represent the K values of the limiting prolate and oblate symmetric tops respectively. K_a and K_c are no longer good quantum numbers. Figure 2-2 gives a correlation diagram of the asymmetric rotor energy levels with those of the limiting prolate and oblate symmetric tops. Rotational transitions with ΔK_a = even and ΔK_c = odd require a non-zero dipole moment along the *a*- axis and designated *a*- type transitions. *b*- type transitions due to a dipole moment along the *b*- axis have ΔK_a = even and ΔK_c = even. For *c*- type transitions, ΔK_a = odd and ΔK_c = even. The Xe-N_2 complex has a dipole moment component only along the *a*- axis, and as a result, only *a*- type transitions can be observed (see Chapter 3). In general, it may be possible to determine all rotational constants A, B, and C from the measured transition frequencies. The rotational constants are directly related to the moments of inertia, and thus the structure of a

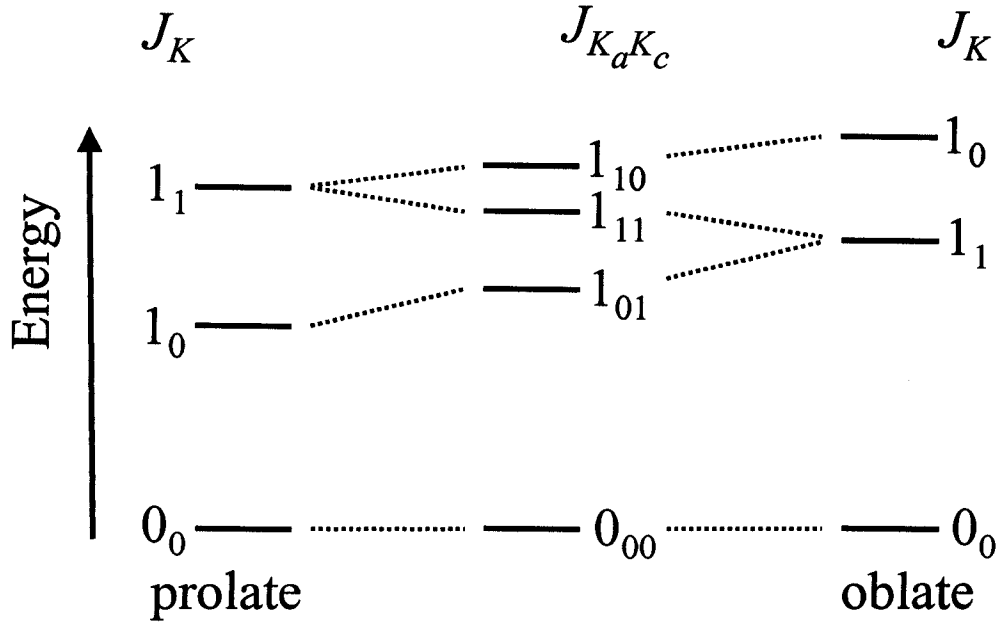

Figure 2-2: A schematic correlation diagram of asymmetric rotor energy levels with those of the limiting prolate and oblate symmetric tops (redrawn from Ref. 3).

molecule. Therefore, the rotational constants can be used to derive structural parameters of a molecule.

Van der Waals complexes undergo large amplitude vibrational motions and, as a result, the rotational constants are insufficient to describe the energies of the rotational states. For example, the moment of inertia of a molecule increases as J increases due to centrifugal forces. Centrifugal distortion constants are used to account for this effect. The quartic distortion constant D_J and sextic constant H_J are usually included in the energy expressions of diatomic or linear molecules, $E_J = BJ(J+1)-D_J J^2(J+1)^2+H_J J^3(J+1)^3$. For an asymmetric rotor, combinations of centrifugal distortion constants, (D_J, D_{JK}, D_K, d_1, d_2, Watson's S-reduction) or (Δ_J, Δ_{JK}, Δ_K, δ_J, δ_K, Watson's A-reduction), are used to describe these effects.[5] The centrifugal distortion constants

contain information about the vibrational motions of molecules, and can be used to determine a harmonic molecular force field.[3]

Some van der Waals complexes also undergo large amplitude internal rotation motions. For example, in the Xe-CH_4, Xe-H_2O and Xe-NH_3 complexes, the CH_4, H_2O and NH_3 subunits undergo nearly free internal rotation motions. These internal rotation motions can lead to splittings of the observed rotational transitions. From these splittings it is sometimes possible to determine the barrier to internal rotation.

The high resolution capability of the spectrometer makes it possible to measure hyperfine structures arising from, for example, non-zero nuclear or electron spins. For example, nuclear quadrupole hyperfine structures were observed for complexes containing quadrupolar nuclei with nuclear-spin quantum number $I > ½$, such as ^{131}Xe ($I = 3/2$) and ^{14}N ($I = 1$). This hyperfine structure results from the interaction between the nuclear quadrupole moment and the electric field gradient at the quadrupolar nucleus. This interaction couples the nuclear spin angular momentum $\boldsymbol{I}$ with the rotational angular momentum $\boldsymbol{J}$ to form a resultant total angular momentum $\boldsymbol{F}$. In covalently bound molecules, the main contribution to the electric field gradient at the quadrupolar nucleus comes from the chemical bonds involved. The nuclear quadrupole coupling constants can therefore often be used to elucidate the nature of chemical bonds and probe the electron densities.[6] The nuclear quadrupole coupling constants in weakly bound van der Waals complexes can be classified into two types. The electric field gradient at the site of a quadrupolar nucleus in a molecular monomer, such as ^{14}N in the Xe-N_2 complex, is determined by the chemical bonds within the subunit. The experimentally determined ^{14}N nuclear quadrupole coupling constants in this complex

can be interpreted as projection of the corresponding constants of the N_2 monomer onto the principal inertial axes of the complex, averaged over the large amplitude bending motions. Rare gas atoms with a nuclear quadrupole moment, such as the ^{131}Xe nucleus in the Xe-N_2 complex, are not involved in any chemical bond. The magnitude of the electric field gradient in these cases is much smaller. The main contributions to the electric field gradient at the nucleus are the electric multipole moments of the molecular subunits, such as the electric quadrupole and octopole moments of N_2, averaged over the large amplitude vibrational motions, and the dispersion interactions. Since the electric field gradient is sensitive to the relative orientation of the subunits for both types of quadrupolar nuclei, the nuclear quadrupole coupling constants can be used to determine the effective orientations. For detailed interpretations of the nuclear quadrupole coupling constants of each investigated Xe containing complex, please refer to Chapters 3 to 7.

2.1.2 Experimental technique

A pulsed nozzle, Balle-Flygare type, Fourier transform microwave (FTMW) spectrometer[7,8,9] was used here to record rotational spectra of the molecules under investigation. Taking advantage of the low temperature of the supersonically expanded gas samples, this spectrometer has been proven to be a well-suited tool for the study of unstable, short-lived molecular species, such as weakly bound van der Waals complexes.[10,11,12,13,14] The theory of FTMW spectroscopy, based on the time-dependent Schrödinger equation in the density matrix formalism,[15,16] has been reviewed in Refs. 8, 9, 17, 18, 19, and 20. Briefly, this theory describes the interaction of microwave

(MW) radiation with the electric dipole moments of a molecular ensemble. A coherent MW pulse, which aligns the molecular dipole moments with the MW field, excites the molecular ensemble and generates an appreciable macroscopic polarization. Subsequently, the spontaneous coherent molecular emission signal containing information about one or more resonant frequencies is detected as a function of time. This time-domain detection technique leads to higher sensitivity and resolution compared to detection in the frequency-domain using modulation techniques.[21] To obtain the molecular transition frequencies, the time-domain signal is Fourier-transformed to give the frequency-domain spectrum. The FTMW spectrometer used for this study has been described in details in Ref. 22. Only the basic principles of the instrument operation are discussed in this section.

2.1.2.1 Formation of van der Waals complexes

A gas sample is prepared in a gas reservoir at room temperature. It contains a few percent of each component of the van der Waals complex under investigation. Ne is typically used as the backing gas to keep the sample pressure at about 3-7 atm. A supersonic expansion is generated by expanding a short pulse of the gas mixture from the high pressure gas reservoir into a stainless-steel vacuum chamber (diameter 50 cm, length 70 cm) through a pulsed nozzle (General Valve, Series 9, orifice diameter 0.8 mm). A 12 inch 2000 *l*/min diffusion pump, backed by an 800 *l*/min mechanical pump, is used to evacuate the chamber and keep the chamber pressure at $\sim 10^{-6}$ torr.

The supersonic expansion can be considered as a rapid adiabatic process. The dynamics of such a process has been discussed in details in Refs. 7, 9, and 11. During

the expansion, the random thermal energy of the molecules is converted into directed kinetic energy through binary collisions. This leads to a narrow velocity distribution (see Figure 1 of Ref. 23) and therefore a very low translational temperature. The cold translational bath cools the rotational and vibrational degrees of freedom by collisional energy transfer. As the gas sample expands, the temperature drops and the molecular density decreases. After the gas pulse enters the phase where the molecular density is so low that no further collisions occur, the temperature of the expansion reaches the lowest point and will no longer change. In a typical experiment, the rotational temperature of complexes in a Ne expansion is estimated to be 1-2 K, depending on the rotational constants of the van der Waals complex under investigation. Due to the low temperature of the molecular expansion, all rotational transitions measured in this PhD work are in the ground vibrational states of the complexes.

Van der Waals complexes are characterized by very low binding energies (a few hundred cm^{-1}) compared to chemical bonds (on the order of 10,000 cm^{-1}). At room temperature, the high thermal energy kT prevents stabilization of such a complex by collisions with surrounding molecules. The low temperature and collisionless environment of supersonic expansion provide a definite advantage for generating and stabilizing van der Waals complexes. The formation of a van der Waals complex occurs during the initial phase of the expansion, and the complex will then persist in the collisionless environment. It is generally accepted that the dimer formation proceeds via a three-body collision. For example,

$$Xe + H_2O + Ne = Xe\text{-}H_2O + Ne^*$$

where the third body, here Ne, is necessary to carry away the excess kinetic energy.[7,10,24, 25,26,27,28] The detailed mechanism for trimer formation is not entirely clear. There are two possible mechanisms. For example, the Xe-$(H_2O)_2$ complex can be formed in one step via a four-body collision,

$$Xe + H_2O + H_2O + Ne = Xe\text{-}(H_2O)_2 + Ne^*$$

or two successive three-body collisions,

$$Xe + H_2O + Ne = Xe\text{-}H_2O + Ne^*$$

$$Xe\text{-}H_2O + H_2O + Ne = Xe\text{-}(H_2O)_2 + Ne^*$$

2.1.2.2 Spectrometer design and its operating principle

The mechanical setup of our spectrometer is schematically shown in Figure 2-3. The sample cell is a MW cavity of Fabry-Pérot type, in which the MW excitation pulse interacts with the molecular ensemble. The MW cavity consists of two spherical aluminum mirrors (diameter of 260 mm and radius of curvature of 380 mm) mounted inside the vacuum chamber described in section 2.1.1 (see Figure 2-3). One of the mirrors is fixed and mounted into the flange cover of the chamber. A wire hook antenna is placed at the center of this mirror to couple the external MW pulse into the cavity and the molecular emission signals out of the cavity. The pulsed nozzle, which expands the molecular pulse into the cavity, is located closely above the antenna. The other mirror is mounted on two linear bearings, and can be moved with a computer controlled Motor Mike drive in order to tune the cavity into resonance with the external MW radiation to generate a standing wave pattern. A diode MW detector is

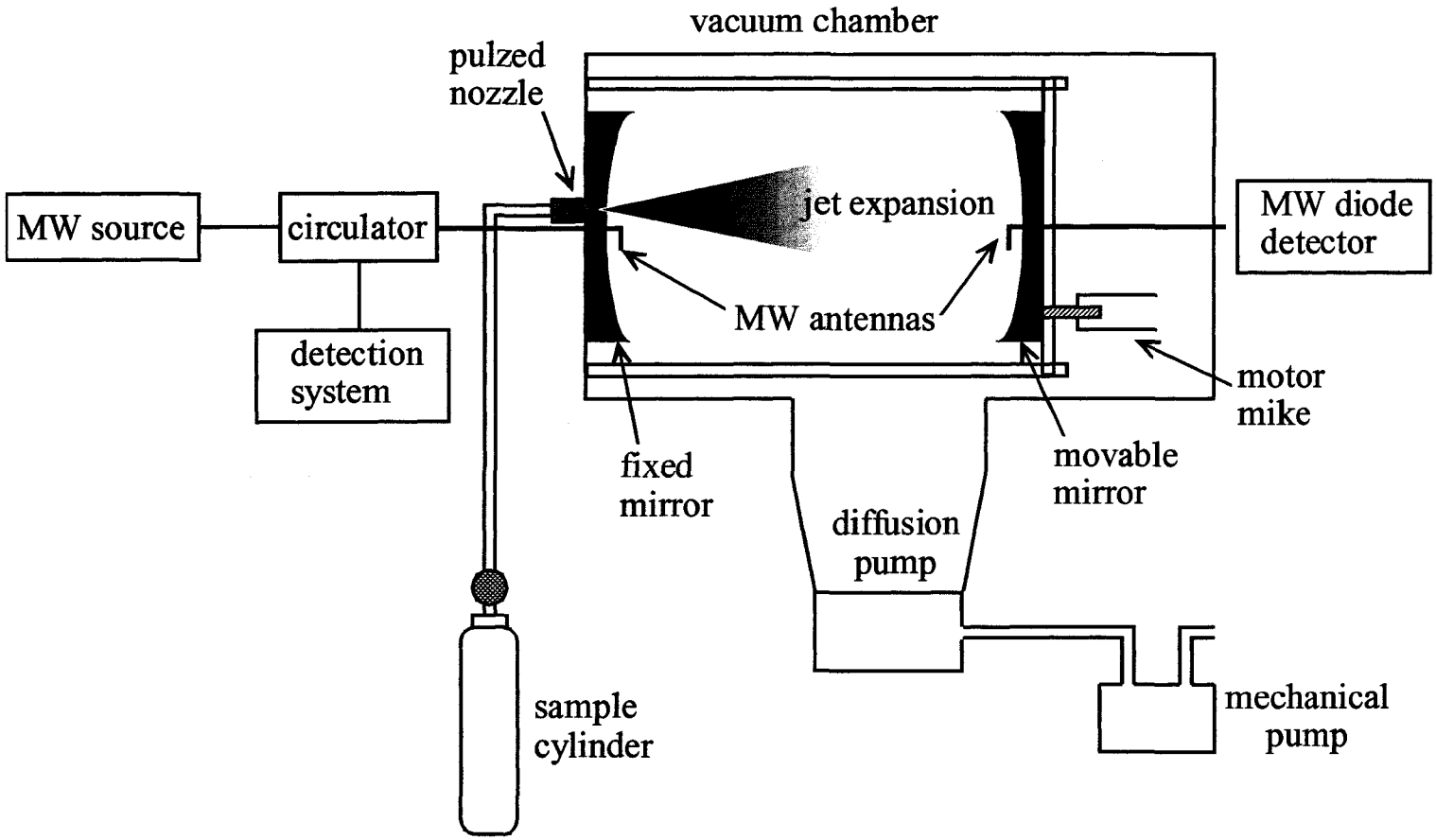

Figure 2-3: A simplified diagram of the mechanical setup of the FTMW spectrometer.

connected to a second antenna at the center of the moveable mirror to monitor the throughput of the cavity.

A schematic diagram of the electrical circuit for the MW excitation and superheterodyne detection system is shown in Figure 2-4. MW radiation at frequency ν is generated by a Hewlett Packard MW synthesizer, which operates in the range of 1-20 GHz. The radiation passes through a power divider and is divided into two components, one of which is used to create the excitation pulse and the other serves as reference frequency for superheterodyne detection. The excitation pulse is generated with two MW *p-i-n* diode switches. A double-balanced mixer and an optional power amplifier are placed between the two diode switches. The mixer uses a 20 MHz local signal to produce two sidebands at ν-20 and ν+20 MHz. The power amplifier is necessary to achieve appreciable macroscopic polarization for the investigation of molecules with small dipole moments (0.1 D or less), for example the Xe-N_2, Xe-CH_4, Xe-H_2O, and Xe-O_2 dimers described in this thesis.

The MW pulse is coupled into the cavity through a wire hook antenna to excite the molecular ensemble. The cavity is tuned into resonance with the ν-20 MHz sideband signal prior to each experiment. If one or more rotational transition frequencies are within the bandwidths of the excitation pulse and the MW cavity, an appreciable macroscopic polarization will be achieved, which corresponds to a phase coherent oscillation of molecular dipole moments induced by the radiation. Such oscillation results in a spontaneous emission signal at the molecular resonance frequency ν_m. As the expansion travels parallel to the direction of the microwave propagation, the signal for each transition contains two components due to the Doppler

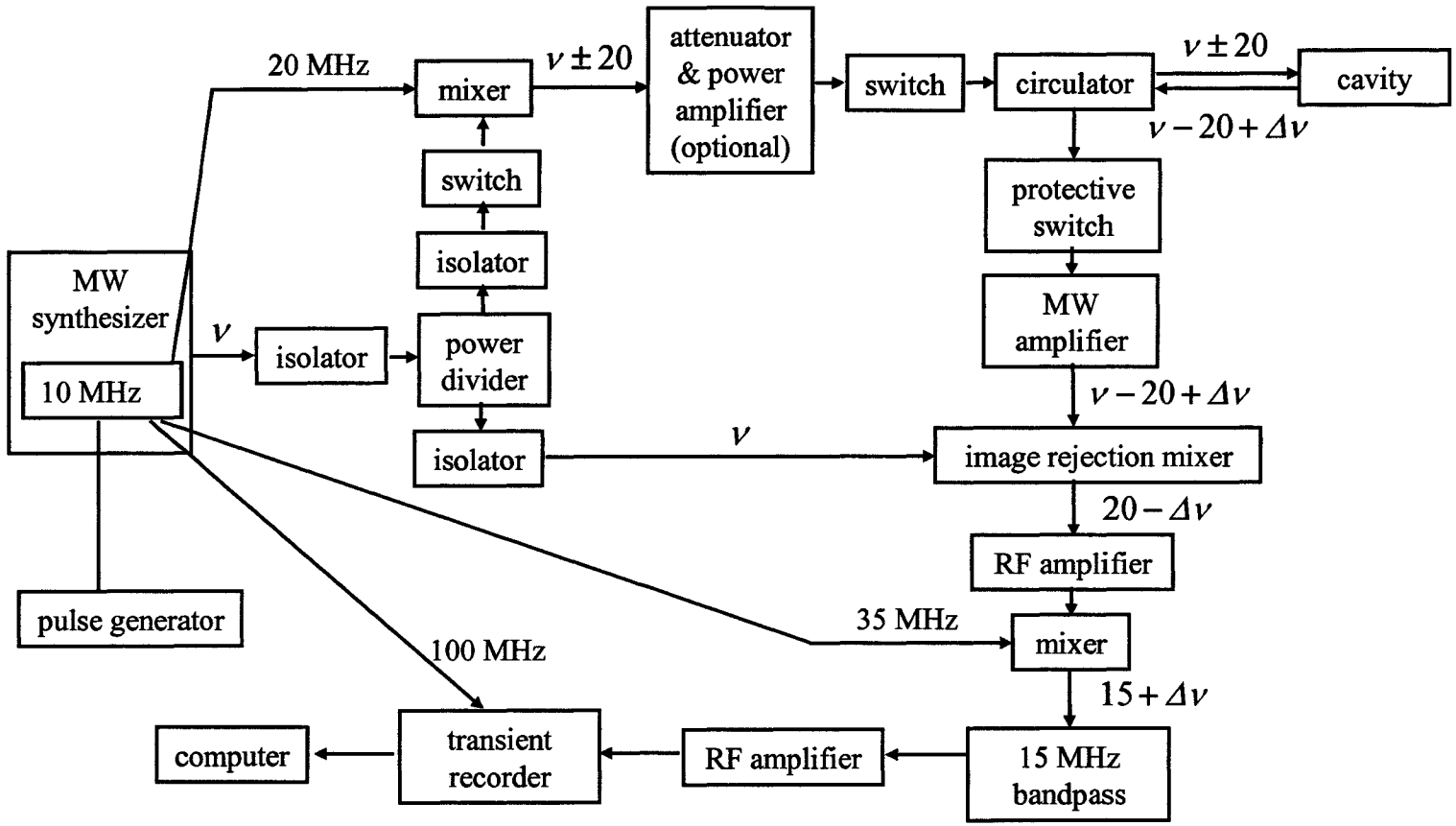

Figure 2-4: A schematic diagram of the electrical circuit for MW excitation and superheterodyne detection system.

effect. The line position is taken as the average frequency of these two components for the analyses. For a Ne expansion, a typical line width (full-width at half-height) of 7 kHz and an estimated accuracy of ±1 kHz were achieved for most well-resolved transitions.[29]

The molecular emission signal, at frequency ν_m, is coupled out of the cavity through the antenna in the fixed mirror and directed to the superheterodyne detection system by a circulator. In order to prevent damage of the detection system from the MW excitation radiation, a protective switch is placed behind the circulator and kept closed until most of the excitation pulse has dissipated. After the molecular signal is amplified and double superheterodyned, it is digitized and sampled by a transient recorder at 10 nsec intervals. For most transitions, 8k data points are recorded and 16k data points for spectra containing narrow hyperfine splittings. All the data points are stored in a personal computer for signal averaging.

As a pulsed experiment, the timing sequence of all the events is extremely important. A pulse generator is used to produce various TTL pulses, as shown in Figure 2-5. First, a short molecular pulse of about 1 msec is generated to open the nozzle and expand the gas sample into the cavity. After a suitable delay, a MW pulse (on the order of μsec) is coupled into the cavity and excites the molecular ensemble. During the same time, a TTL pulse is generated to keep the protective switch closed until a trigger is sent to the transient recorder to start data acquisition. The timing of the trigger pulse is critical because it must ensure that the main part of the excitation radiation has dissipated while it is still early enough to capture the molecular emission signal. In the above sequence, all the pulse durations and delays can be adjusted to

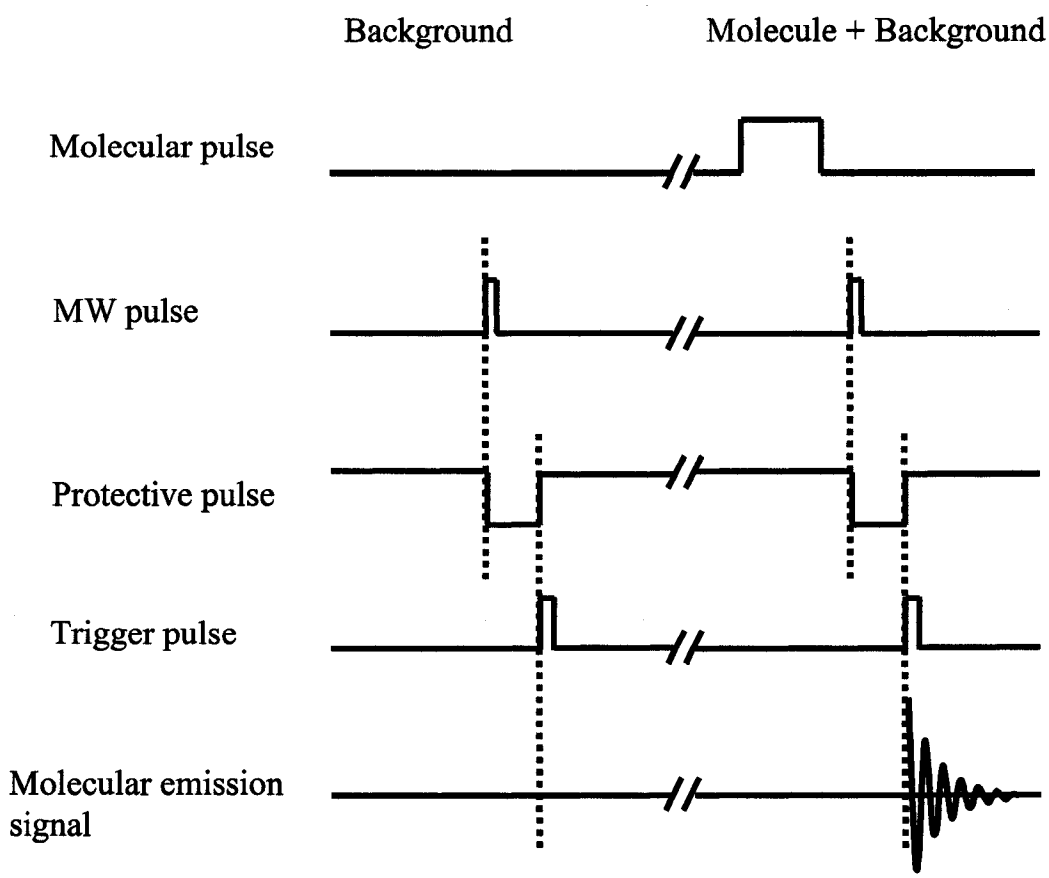

Figure 2-5: Pulse sequence of a single FTMW experiment. The molecular emission signal is recorded as the difference between "molecule + background" signal and "background" signal. The entire pulse sequence is repeated for signal averaging.

achieve optimal experimental conditions. A background signal is obtained by repeating the above sequence without the molecular pulse. Such background signal is subtracted from the above background + molecular signal to eliminate the effect of the intense background.

In most cases, the signal of a single experiment is very weak, and phase coherent signal averaging of a number of experiments is used to improve the signal-to-noise ratio. In this experiment, the internal 10 MHz crystal of the MW synthesizer is used to phase correlate all events, including generating the 20 MHz and 35 MHz signals used in the MW excitation and detection systems, the 100 MHz signal used by the transient recorder as the clock for data acquisition. It is also used as a clock for the pulse generator to produce the various TTL pulses. 8k or 16k data points are recorded for a time-domain signal and the same amount of zero data is added to the end before being Fourier transformed to the frequency domain spectrum. The process of adding zeros, called zero filling, can better utilize the resolution in the time-domain spectrum. An example of the time-domain and frequency-domain spectra is given in Figure 2-6.

2.2 *Ab initio* calculations

Accurate *ab initio* electronic structure calculations are very effective to obtain information about the structure and electronic properties of molecules, especially to explore the potential energy surface (PES) of a van der Waals complex.[30,31,32,33,34,35] In particular, comparison of such theoretical information with spectroscopic experimental results has significantly increased our understanding of the nature of intermolecular forces. In this thesis, a number of *ab initio* calculations were performed, including construction of intermolecular PESs, dipole moment calculations, and geometry optimizations. These calculations have provided guidance for the spectral searches, and have complemented and facilitated interpretations of the spectroscopic results.

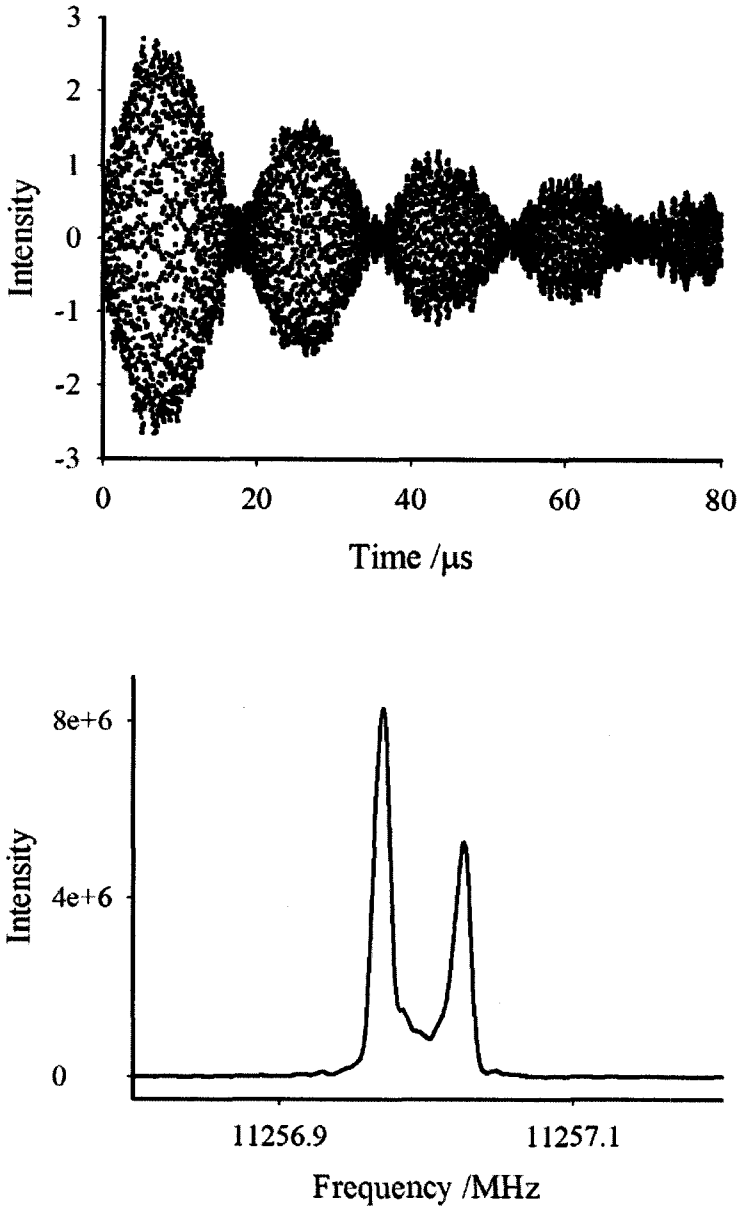

Figure 2-6: Time domain and frequency domain signals of the $J = 3\text{-}2$, $\Pi 1_{1s}$ transition of the $^{132}Xe\text{-}^{15}NH_3$. The signals were recorded using 5 averaging cycles. The transition is split into two components in the frequency domain spectrum due to the Doppler effect. The transition frequency is recorded as the average frequency of these two components.

2.2.1 Potential energy surface and dipole moment calculations

The PESs for five Xe atom containing van der Waals dimers, Xe-N_2, Xe-CH_4, Xe-H_2O, Xe-NH_3, and Xe-O_2, were constructed using the MOLPRO 2002.6 package of *ab initio* programs.[36] The interacting molecules were frozen at their experimental equilibrium structures. Therefore, the calculated PESs depend only on the intermolecular degrees of freedom. The interaction energy ΔE_{AB} was calculated using the supermolecule approach as the difference between the energy of the dimer AB and the sum of the energies of the monomers A and B:[31]

$$\Delta E_{AB} = E_{AB} - (E_A + E_B) \qquad (2\text{-}1)$$

Such an approach requires the employed calculation methods to be size-consistent, i.e., the dimer energy at infinite separation must be equal to the sum of the constituent monomer energies. In addition, a high level description of electron correlation is required for weakly bound van der Waals complexes because the binding energies in such systems are dominated by dispersion interactions which are an electron correlation effect. Based on these two considerations, the size-consistent comprehensive coupled cluster level of theory with single, double, and perturbatively included triple excitations [CCSD(T)] [37,38,39] was selected for the construction of PESs of the five dimers mentioned above. It is generally accepted that the CCSD(T) method can provide "meaningful descriptions of intermolecular forces".[35] For the open-shell Xe-O_2 van der Waals complex, the restricted open-shell Hartree-Fock (ROHF) function was used as reference wavefunction and the spin unrestricted coupled cluster theory [UCCSD(T)] was applied to calculate the interaction energies.[38]

To capture the dispersion energy, it is necessary to employ large basis sets, containing a number of polarization and diffuse functions. Dunning's augmented correlation-consistent aug-cc-pVTZ basis set[40] was chosen for the H, O, C, and N atoms. It is difficult to find a large enough basis set to account for the large number of electrons in the Xe atom. The Well-Tempered basis set (WTBS)[41] augmented by a number of basis functions with high angular quantum numbers, d, f, g, h, and the small-core pseudopotential and correlation-consistent aug-cc-pVXZ-PP (X = Q, 5) basis sets[42] were selected for calculating the PESs. In the Xe-N_2 study, two surfaces were constructed with WTBS and aug-cc-pV5Z-PP basis sets respectively. These two surfaces have similar features and are of reasonable spectroscopic accuracy. The overall goal of calculating the PESs for the other four dimers was to capture the main features of the interactions. A highly accurate quantitative comparison with the spectroscopic results was not intended. Therefore, the aug-cc-pVQZ-PP basis set was selected for the Xe atom to reduce the computational cost. In all the calculations, additional sets of basis functions were placed at the midpoint of the van der Waals bond. These functions, called midbond functions, help to provide an accurate description of the dispersion interaction.[43,44,45,46,47] The employment of bond functions increases the computational efficiency because nucleus-centered highly diffuse and polarized functions must be included otherwise. In the supermolecule approach, the monomer energy E_A (E_B) is calculated with the basis set of monomer A (B) while the basis sets for both A and B are used to calculate the complex energy E_{AB}. As a result, compared with the calculated E_A or E_B value, each monomer leads to a lower energy to E_{AB} by virtue of the basis set of its partner, and this artificially lowers the obtained

interaction energy ΔE_{AB}. This effect is a consequence of the incompleteness of the employed basis sets and is termed basis set superposition error (BSSE).[48] In order to remove the BSSE, the full counterpoise correction method developed by Boys and Bernardi[49] was applied in all the PES calculations. In this method, all energies E_{AB}, E_A, E_B are calculated with the basis sets for both A and B present. The computational details for each PES calculation will be described in the respective chapters.

In addition to PES calculations, dipole moments of the Xe-CH_4 dimer were computed at various configurations. These calculations were performed to help interpret some of the experimental observations (see Chapter 4 for detailed discussions). The employed basis sets and level of theory were the same as for the PES calculation. The finite difference approximation[50] was used to calculate the dipole moment as the first derivative of the energy with respect to the applied electric field. At each configuration, I chose two finite electric fields with the same field strength and opposite directions. Two energy calculations were performed with these two electric fields applied to the system respectively. The dipole moment was then obtained as the ratio of the energy difference to the electric field difference.

2.2.2 Geometry optimization

An *ab initio* PES probes the entire region of the intermolecular interaction potential, and can therefore advance our knowledge about the intermolecular forces. However, its computational cost increases rapidly with increasing number of intermolecular degrees of freedom. For example, if one computer can calculate one data point per hour and a PES is calculated on a grid of 10 data points for each

intermolecular degree of freedom, it will take the computer 10^3 hours (41.7 days) to calculate the Xe-H_2O (3 intermolecular degrees of freedom) surface, and 10^7 hours (416666.7 days) for the Xe-$(H_2O)_2$ (7 intermolecular degrees of freedom) surface. Therefore, it is computationally too expensive to study the intermolecular interactions within the Xe-$(H_2O)_2$ complex through PES calculations. Instead, a full geometry optimization procedure was performed in this thesis to search for the equilibrium structures of the Xe-$(H_2O)_2$ complex. This was accomplished by using the GAUSSIAN03 software package [51] at the level of second-order Møller-Plesset perturbation theory (MP2).[52] Prior to this calculation, the performance of a variety of basis sets was tested against partial geometry optimizations of the Xe-H_2O complex (the H_2O monomer was fixed at its experimental equilibrium structure[1]). The structural parameters of the Xe-H_2O complex are defined in Figure 2-7. The optimized parameters obtained using different basis sets are given in Table 2-1 and compared with those of the global minimum from the *ab initio* PES (see section 2.2.1). The optimizations using the aug-cc-pVTZ[40] basis set for the O atom, the 6-311++G(d,p)[53] basis set for the H atoms, and without midbond functions give the best agreement with the *ab initio* PES. The inclusion of midbond functions results in shorter optimized van der Waals bonds compared with the *ab initio* global minimum from the PES calculation. Optimizations with two different sizes of basis sets [ECP46MWB ECP(6s6p3d1f) [54] and aug-cc-pVQZ-PP(14s11p12d2f1g)[42]] for the Xe atom were tested and show similar behavior. The aug-cc-pVQZ-PP[42] basis set was eventually selected for the Xe-$(H_2O)_2$ optimization because this basis set was also used in the PES calculations of Xe-H_2O and the resulting PES is consistent with the spectroscopic data.

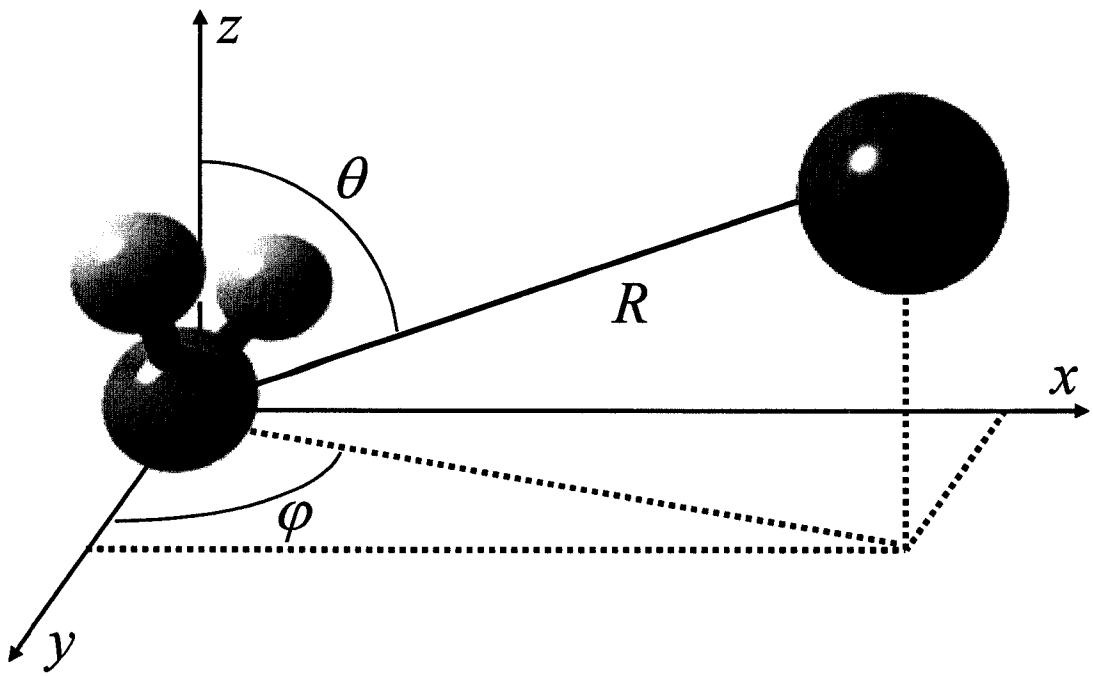

Figure 2-7: Molecule fixed axes frame for the Xe-H_2O complex. The origin of the coordinate system is at the center-of-mass of the H_2O unit, and the C_2 axis of H_2O is chosen as the z-axis. The H_2O unit lies in yz-plane. The position of the Xe atom is described by spherical coordinates (R, θ, φ). R is the distance between Xe and the origin, θ is the angle between the R vector and the z-axis. $\theta = 0°$ corresponds to the C_{2v} geometry where the hydrogen atoms point to the xenon atom. φ is the angle for the H_2O out-of-plane rotation about its C_2 axis. $\varphi = 0°$ if all four atoms are coplanar. $\theta = 0°$, $\varphi = 0°$ corresponds to the symmetric Xe-H_2O geometry, and $\theta = 180°$, $\varphi = 0°$ corresponds to the symmetric Xe-OH_2 geometry. $\theta = 53°$, $\varphi = 0°$ corresponds to an L-shaped Xe-HOH structure with a linear Xe-HO arrangement.

The counterpoise correction used to remove BSSE in single point calculation was not employed in the geometry optimization procedure because of the high computational cost. It has been demonstrated that results from geometry optimization procedures at the MP2 level including counterpoise correction lead to larger deviation from experiment than those without correction.[55] The results of the optimization procedure will be discussed in Chapter 5.

Table 2-1: A comparison of the structural parameters of the equilibrium geometry of the Xe-H_2O complex obtained from an *ab initio* geometry optimization (MP2 level of theory) and PES calculation [CCSD(T) level of theory].

	Basis sets				Structural parameters of the equilibrium geometry [a]		
	Xe	O	H	midbond function [b]	R	θ	φ
Geometry optimization	ECP46MWB ECP	6-311++G(d,p)	6-311++G(d,p)	no	4.1 Å	50.4°	10.0°
	ECP46MWB ECP	aug-cc-pVTZ	6-311++G(d,p)	no	4.1 Å	59.0°	0.0°
	ECP46MWB ECP	aug-cc-pVTZ	aug-cc-pVTZ	no	3.8 Å	61.2°	0.0°
	ECP46MWB ECP	aug-cc-pVTZ	aug-cc-pVTZ	yes	3.4 Å	60.8°	0.0°
	aug-cc-pVQZ-PP	aug-cc-pVTZ	6-311++G(d,p)	no	3.9 Å	62.1°	0.0°
	aug-cc-pVQZ-PP	aug-cc-pVTZ	aug-cc-pVTZ	no	3.8 Å	64.4°	0.1°
	aug-cc-pVQZ-PP	aug-cc-pVTZ	6-311++G(d,p)	yes	3.7 Å	59.7°	0.2°
	aug-cc-pVQZ-PP	aug-cc-pVTZ	aug-cc-pVTZ	yes	3.7 Å	58.4°	0.0°
PES calculation	aug-cc-pVQZ-PP	aug-cc-pVTZ	aug-cc-pVTZ	yes	4.0 Å	60.0°	0.0°

[a] Structural parameters are defined in Figure 2-7.

[b] Midbond functions (3s3p2d2f1g) were placed at the midpoint of the van der Waals bond, with the exponents α_s, α_p = 0.94, 0.34, 0.12; α_d, α_f = 0.64, 0.23; α_g = 0.35.[47]

References

[1] *CRC Handbook of Chemistry and Physics*, 84th Ed. (CRC Press, Boca Raton, 2003).

[2] C. N. Banwell and E. M. McCash, *Fundamentals of Molecular Spectroscopy*, 4th ed. (McGraw-Hill, London, 1994).

[3] W. Gordy and R. L. Cook, *Microwave Molecular Spectra*, 3rd ed. (Wiley, London, 1984).

[4] C. H. Townes and A. L. Schawlow, *Microwave Spectroscopy*, (Dover, New York, 1975).

[5] J. K. G. Watson, in *Vibrational Spectra and Structure: A Series of Advances*, edited by J. R. Durig (Elsevier, Amsterdam, 1977).

[6] J. Michaud and M. C. L. Gerry, J. Am. Chem. Soc. **128**, 7613 (2006).

[7] T. J. Balle and W. H. Flygare, Rev. Sci. Instrum. **52**, 33 (1981).

[8] E. J. Campbell, L. W. Buxton, T. J. Balle, and W. H. Flygare, J. Chem. Phys. **74**, 813 (1981).

[9] E. J. Campbell, L. W. Buxton, T. J. Balle, M. R. Keenan, and W. H. Flygare, J. Chem. Phys. **74**, 829 (1981).

[10] A. C. Legon, Ann. Rev. Phys. Chem. **34**, 275 (1983).

[11] M. R. Keenan, E. J. Campbell, T. J. Balle, L. W. Buxton, T. K. Minton, P. D. Soper, and W. H. Flygare, J. Chem. Phys. **72**, 3070 (1980).

[12] R. K. Thomas, Proc. R. Soc. London Ser. A **344**, 579 (1975).

[13] M. R. Keenan, L. W. Buxton, E. J. Campbell, A. C. Legon, and W. H. Flygare, J. Chem. Phys. **74**, 2133 (1981).

[14] W. G. Read and E. J. Campbell, Phys. Rev. Lett. **49**, 1146 (1982).

[15] R. C. Tolman, *The Principles of Statistical Mechanics* (Oxford University Press, London, 1962).

[16] K. Blum, *Density Matrix Theory and Application* (Plenum Press, 1981).

[17] H. Dreizler, Mol. Phys. **59**, 1 (1986).

[18] J. C. McGurk, T. G. Schmalz, and W. H. Flygare, Adv. Chem. Phys. **25**, 1 (1974).

[19] R. L. Shoemaker, *Laser and Coherence Spectroscopy* (Plenum Press, New York, 1978).

[20] H. Dreizler, Ber. Bunsenges. Phys. Chem. **99**, 1451 (1995).

[21] J. Ekkers and W. H. Flygare, Rev. Sci. Instrum. **47**, 448 (1976).

[22] Y. Xu and W. Jäger, J. Chem. Phys. **106**, 7968 (1997).

[23] R. E. Smalley, L. Wharton, and D. H. Levy, Acc. Chem. Res. **10**, 139 (1977).

[24] O. F. Hagena and W. O. Gert, J. Chem. Phys. **56**, 1793 (1972).

[25] D. Golomb, R. E. Good, and R. F. Brown, J. Chem. Phys. **52**, 1545 (1970).

[26] D. Golomb, R. E. Good, A. B. Bailey, M. R. Busby, and R. Dawbarn, J. Chem. Phys. **57**, 3844 (1972).

[27] J. M. Calo, J. Chem. Phys. **62**, 4904 (1975).

[28] T. A. Milne, A. E. Vandegrift, and F. T. Greene, J. Chem. Phys. **52**, 1552 (1970).

[29] V. N. Markov, Y. Xu, and W. Jäger, Rev. Sci. Instrum. **69**, 4061 (1998).

[30] A. D. Buckingham, P. W. Fowler, and J. M. Hutson, Chem. Rev. **88**, 963 (1988).

[31] G. Chałasiński and M. Gutowski, Chem. Rev. **88**, 943 (1988).

[32] P. Hobza and R. Zahradnik, Int. J. Quantum Chem. **42**, 581 (1992).

[33] G. Chałasiński and M. M. Szczęśniak, Chem. Rev. **94**, 1723 (1994).

[34] B. Brutschy and P. Hobza, Chem. Rev. **100**, 3861 (2000).

[35] G. Chałasiński and M. M. Szczęśniak, Chem. Rev. **100**, 4227 (2000).

[36] MOLPRO, a package of *ab initio* programs designed by H.-J. Werner and P. J. Knowles, version 2002.6, R. D. Amos, A. Bernhardsson, A. Berning, P. Celani, D. L. Cooper, M. J. O. Deegan, A. J. Dobbyn, F. Eckert, C. Hampel, G. Hetzer, P. J. Knowles, T. Korona, R. Lindh, A. W. Lloyd, S. J. McNicholas, F. R. Manby, W. Meyer, M. E. Mura, A. Nicklass, P. Palmieri, R. Pitzer, G. Rauhut, M. Schütz, U. Schumann, H. Stoll, A. J. Stone, R. Tarroni, T. Thorsteinsson, and H.-J. Werner.

[37] C. Hampel, K. Peterson, and H.-J. Werner, Chem. Phys. Lett. **190**, 1 (1992).

[38] P. J. Knowles, C. Hampel, and H.-J. Werner, J. Chem. Phys. **99**, 5219 (1993).

[39] M. J. O. Deegan and P. J. Knowles, Chem. Phys. Lett. **227,** 321 (1994).

[40] T. H. Dunning, Jr., J. Chem. Phys. **90**, 1007 (1989).

[41] S. Huzinaga and M. Klobukowski, Chem. Phys. Lett. **212**, 260 (1993).

[42] K. A. Peterson, D. Figgen, E. Goll, H. Stoll, and M. Dolg, J. Chem. Phys., **119**, 11113 (2003).

[43] F.-M. Tao and Y.-K. Pan, Chem. Phys. Lett. **194**, 162 (1992).

[44] F.-M. Tao and Y.-K. Pan, J. Chem. Phys. **97**, 4989 (1992).

[45] F.-M. Tao, J. Chem. Phys. **98**, 3049 (1992).

[46] T. B. Pederson, B. Fernández, H. Koch, and J. Makarewicz, J. Chem. Phys. **115**, 8431 (2001).

[47] S. M. Cybulski and R. R. Toczylowski. J. Chem. Phys. **111**, 10520 (1999).

[48] B. Liu and A. D. Mclean, J. Chem. Phys. **59**, 4557 (1973).

[49] S. F. Boys and F. Bernardi, Mol. Phys. **19**, 553 (1970).

[50] H.-J. Werner and P. J. Knowles, *MOLPRO User's Manual Version 2002.6* (University of Birmingham, 2003).

[51] Gaussian 03, Revision B.01, M. J. Frisch, G. W. Trucks, H. B. Schlegel, G. E. Scuseria, M. A. Robb, J. R. Cheeseman, J. A. Montgomery, Jr., T. Vreven, K. N. Kudin, J. C. Burant, J. M. Millam, S. S. Iyengar, J. Tomasi, V. Barone, B. Mennucci, M. Cossi, G. Scalmani, N. Rega, G. A. Petersson, H. Nakatsuji, M. Hada, M. Ehara, K. Toyota, R. Fukuda, J. Hasegawa, M. Ishida, T. Nakajima, Y. Honda, O. Kitao, H. Nakai, M. Klene, X. Li, J. E. Knox, H. P. Hratchian, J. B. Cross, C. Adamo, J. Jaramillo, R. Gomperts, R. E. Stratmann, O. Yazyev, A. J. Austin, R. Cammi, C. Pomelli, J. W. Ochterski, P. Y. Ayala, K. Morokuma, G. A. Voth, P. Salvador, J. J. Dannenberg, V. G. Zakrzewski, S. Dapprich, A. D. Daniels, M. C. Strain, O. Farkas, D. K. Malick, A. D. Rabuck, K. Raghavachari, J. B. Foresman, J. V. Ortiz, Q. Cui, A. G. Baboul, S. Clifford, J. Cioslowski, B. B. Stefanov, G. Liu, A. Liashenko, P. Piskorz, I. Komaromi, R. L. Martin, D. J. Fox, T. Keith, M. A. Al-Laham, C. Y. Peng, A. Nanayakkara, M. Challacombe, P. M. W. Gill, B. Johnson, W. Chen, M. W. Wong, C. Gonzalez, and J. A. Pople, Gaussian, Inc., Pittsburgh PA, 2003.

[52] J. S. Binkley, J. A. Pople, Int. J. Quantum Chem. **9**, 229 (1975).

[53] R. Krishman, J. S. Binkley, R. Seeger, and J. A. Pople, J. Chem. Phys. **72,** 650 (1980).

[54] A. Niklass, M. Dolg, H. Stoll, and H. Preuss, J. Chem. Phys., **102**, 8942 (1995).

[55] K. S. Kim, P. Tarakeshwar, and J. Y. Lee, Chem. Rev. **100**, 4145 (2000).

CHAPTER 3

Microwave Spectra of the Xe-N_2 van der Waals Complex: A Comparison of Experiment and Theory

3.1 Introduction

Accurate Xe-molecule interaction potential energy surfaces (PESs) need to be constructed to provide necessary information for the investigation of more complex Xe-host site interactions and the interpretation of the ^{129}Xe (nuclear spin $I = 1/2$) nuclear magnetic resonance results. The Xe-N_2 complex was chosen as the first test case because of the relatively small number of electrons of N_2 and the high (C_{2v}) symmetry of its equilibrium structure. A semi-empirical PES of the Xe-N_2 system based on the Tang-Toennies (BTT) model was previously determined by Bowers *et al.*[1] Subsequently, an *ab initio* potential at the Hartree-Fock level of theory and the corresponding magnetic shielding surface were determined by de Dios *et al.*[2] High resolution spectroscopic studies of the Xe-N_2 complex can be used to gauge and improve the semi-empirical and *ab initio* potentials.

Earlier spectroscopic and *ab initio* work on complexes of N_2 with other rare gas atoms include the microwave spectra of Ar-N_2,[3,4] Kr-N_2,[5] and Ne-N_2 (Ref. 6) and semi-empirical PESs of Ar-N_2 (Ref. 4) and Ne-N_2 (Ref. 6). Both experimental and

theoretical studies are in agreement with T-shaped equilibrium geometries for these complexes. In the microwave studies, it was possible to resolve the ^{14}N nuclear quadrupole hyperfine structures of the rotational transitions. The resulting nuclear quadrupole coupling constants were found to be K_a dependent as a result of the large amplitude bending motions within the complexes[7] and were used to test the angular anisotropy of the PES in the case of Ne-N_2. It is instructive to see whether similar behavior will be found for the Xe-N_2 complex.

In the following, I describe a combined theoretical and experimental approach that was used to measure and assign rotational transitions of the Xe-N_2 complex and to construct PESs for the Xe-N_2 interaction. Previous studies of the Ne-N_2 (Ref. 6) and Ar-N_2 (Ref. 4) systems have shown that the calculated spectra derived from *ab initio* and semi-empirical PESs could differ significantly from the experimental ones. In these cases, a morphing procedure was applied to the PESs to achieve satisfactory agreement with the experimental data.[8,9] For the Ne-N_2 (Ref. 6) and Ar-N_2 (Ref. 4) systems, satisfactory agreement with experiment has been achieved by changing one or more parameters of the PESs, such as well depths and intermolecular separations. In the present work, high quality *ab initio* PESs were constructed for the Xe-N_2 system. A simple scaling procedure was used to achieve spectroscopic accuracy for these surfaces.

3.2 Spectral search, assignments, and analyses

The sample mixtures consisted of 1% Xe and 2% N_2 in Ne at about 3 atm backing pressure. Enriched $^{15}N_2$ (98%, Cambridge Isotope Laboratories) was used to

investigate the spectrum of the ^{131}Xe-$^{15}N_2$ isotopomer. The initial rotational constants for the Xe-N_2 complex were estimated by assuming a T-shaped structure with C_{2v} symmetry, similar to other Rg-N_2 complexes [Rg = Ne,[6] Ar,[3,4] and Kr[5]]. The separation between the Xe atom and the center-of-mass of N_2 was estimated to be 4.21 Å. This value was obtained by comparison of the separations in Ne-N_2, Ar-N_2, and Kr-N_2 with those in Ar-CO,[10] Ne-CO, Kr-CO, and Xe-CO (Ref. 11) and extrapolation to Xe-N_2. Several lines were soon found based on the resulting rotational constants and confirmed to be the hyperfine pattern of the $J_{KaKc} = 2_{02}$-1_{01} transition of ^{132}Xe-$^{14}N_2$. The corresponding lines of the ^{129}Xe isotopomer were soon located by extrapolation from ^{132}Xe-$^{14}N_2$ using a pseudodiatomic approach.

3.2.1 Xe-$^{14}N_2$

Twelve *a*-type transitions with J ranging from 1 to 5 and with K_a from 0 to 1 were recorded for the ^{132}Xe-$^{14}N_2$ (26.89% natural abundance) and ^{129}Xe-$^{14}N_2$ (26.44% natural abundance) isotopomers. In addition, the nuclear quadrupole hyperfine structures due to the presence of two ^{14}N ($I = 1$) nuclei were observed and assigned. All the measured frequencies are listed in Table 3-1 together with the quantum number assignments. An example spectrum of the 2_{12}-1_{11} transition of ^{132}Xe-$^{14}N_2$ is shown in Figure 3-1 to demonstrate the sensitivity and resolution achieved. The coupling scheme $\boldsymbol{I}_1 + \boldsymbol{I}_2 = \boldsymbol{I}$ and $\boldsymbol{I} + \boldsymbol{J} = \boldsymbol{F}$ was used, where $\boldsymbol{I}_1$ and $\boldsymbol{I}_2$ are the nuclear spin vectors of the two ^{14}N nuclei and $\boldsymbol{J}$ is the total angular momentum vector of the complex excluding the nuclear spin.

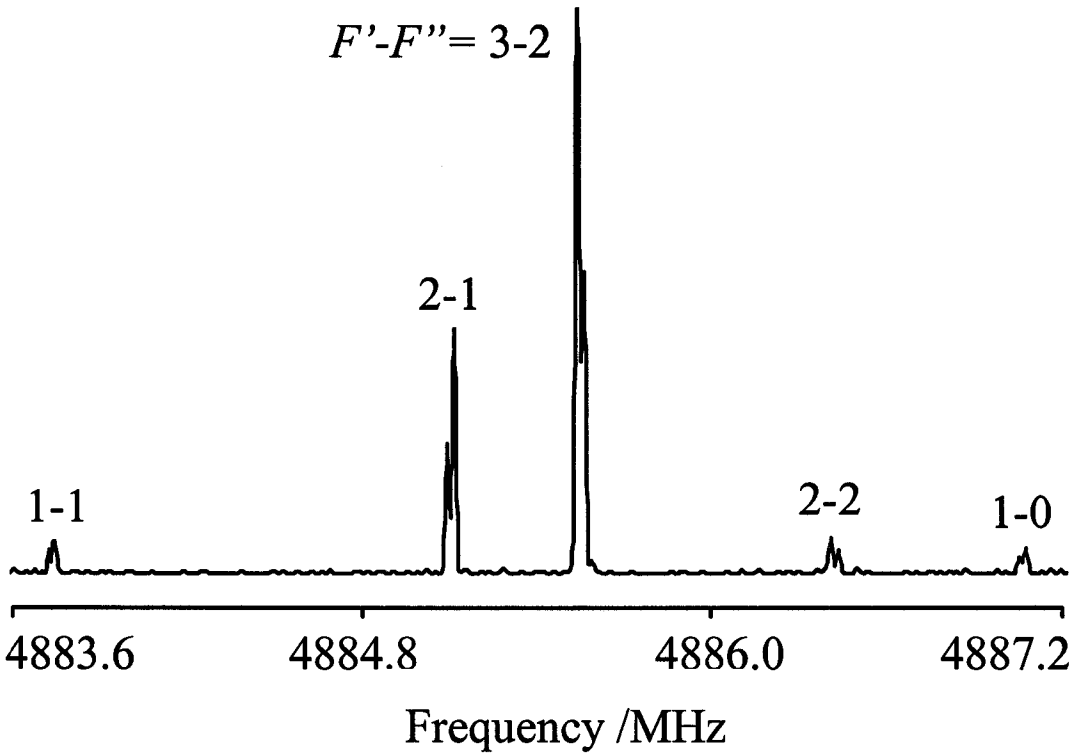

Figure 3-1: A composite spectrum of the $J_{KaKc} = 2_{12}$-1_{11} transition of ^{132}Xe-$^{14}N_2$. Each hyperfine component appears as a narrow doublet due to the Doppler effect. Each doublet was recorded individually using 200 averaging cycles.

Pickett's SPFIT/SPCAT suite of programs[12] was used to fit spectroscopic parameters to the measured transition frequencies. Initially, all the measured frequencies were used to fit rotational, centrifugal distortion, ^{14}N nuclear quadrupole coupling, and spin-rotation constants together. However, differences between the observed and measured frequencies of up to 26 kHz resulted, significantly exceeding the estimated measurement uncertainty of about 1 kHz. Following the procedure previously used for the cases of Ne-,[6] Ar-,[3,4] and Kr-N_2,[5] three separate hyperfine structure fits for the individual K_a stacks were done which gave satisfactory results.

Table 3-2 gives the resulting hypothetical hyperfine-free unsplit line positions ν_{center} and their experimental uncertainties $\Delta\nu_{center}$ for the ^{132}Xe-$^{14}N_2$ and ^{129}Xe-$^{14}N_2$ isotopomers. These frequencies were used to compare with those calculated from the *ab initio* PESs (see discussions below). The resulting nuclear quadrupole coupling and spin-rotation constants of ^{14}N nuclei are given in Table 3-3, together with the standard deviations of the individual fits. For the $K_a = 0$ stacks only the nuclear quadrupole coupling constants χ_{aa} are well determined; in the cases of the $K_a = 1$ stacks, three nuclear quadrupole coupling constants, χ_{aa}, χ_{bb}, χ_{cc}, and the spin-rotation constant M_{aa} need to be included in the fitting procedures.

Watson's *A*-reduction Hamiltonian in its I^r representation[13] was used to fit the rotational and centrifugal distortion constants to the hypothetical unsplit center frequencies. The rotational constants *B* and *C*, three quartic centrifugal distortion constants Δ_J, Δ_{JK} and δ_J, and one sextic centrifugal distortion constant Φ_{JK} are well-determined (see Table 3-4). The rotational constant *A* and the quartic centrifugal distortion constants Δ_K and δ_K could not be determined because only *a*-type transitions were measured for this near prolate asymmetric top. During the fitting procedure, the *A* constant was fixed at the values derived from spectroscopic fits of both *a*- and hypothetical *b*-type transitions calculated from the scaled PES as described below.

3.2.2 ^{131}Xe-$^{15}N_2$

The initial search for ^{131}Xe-$^{15}N_2$ lines was based on the prediction using the scaled *ab initio* PES and the transitions were found within 0.5 MHz of the calculated frequencies. Nuclear quadrupole hyperfine structures due to the ^{131}Xe nucleus ($I = 3/2$)

were partly resolved in four rotational transitions. The measured transition frequencies and determined spectroscopic constants are given in Table 3-5. An example spectrum of the 2_{11}-1_{10} transition is shown in Figure 3-2. Quantum number assignments could be achieved for the observed hyperfine components, and ^{131}Xe nuclear quadrupole coupling constants were obtained and given in Table 3-5.

3.3 Discussion of experimental results

The ^{14}N nucleus ($I = 1$) is a boson. If the two ^{14}N nuclei in the Xe-$^{14}N_2$ complex are equivalent, the total wavefunction of the system must be symmetric with respect to an exchange of the two ^{14}N nuclei. For the ground state, where both vibrational and electronic wave functions are symmetric, the total nuclear spin function must be antisymmetric (total nuclear spin quantum number I_{tot} = 1) for levels with antisymmetric rotational wavefunction ($K_a = 1$) and symmetric ($I_{tot} = 0$ and 2) for levels with symmetric rotational wavefunction ($K_a = 0$). The observed nuclear quadrupole hyperfine structures of Xe-$^{14}N_2$ complexes are in accord with the above spin statistics, suggesting two equivalent ^{14}N nuclei in the system and therefore a T-shaped structure of the complex. This is consistent with the behavior of other Rg-N_2 complexes (Rg =Ar,[3,4] Kr,[5] and Ne[6]). The van der Waals bond length R between Xe and the center of mass of the N_2 unit was calculated to be 4.208 Å using $R = \left(\frac{h}{8\pi^2 \mu \overline{B}}\right)$ with $\overline{B} = (B + C)/2$. μ is the pseudodiatomic reduced mass of the complex.

Like in other Rg-N_2 (Refs. 3,4,5,6) systems, the ^{14}N nuclear quadrupole coupling constants in Xe-$^{14}N_2$ are K_a dependent because the electric field gradient

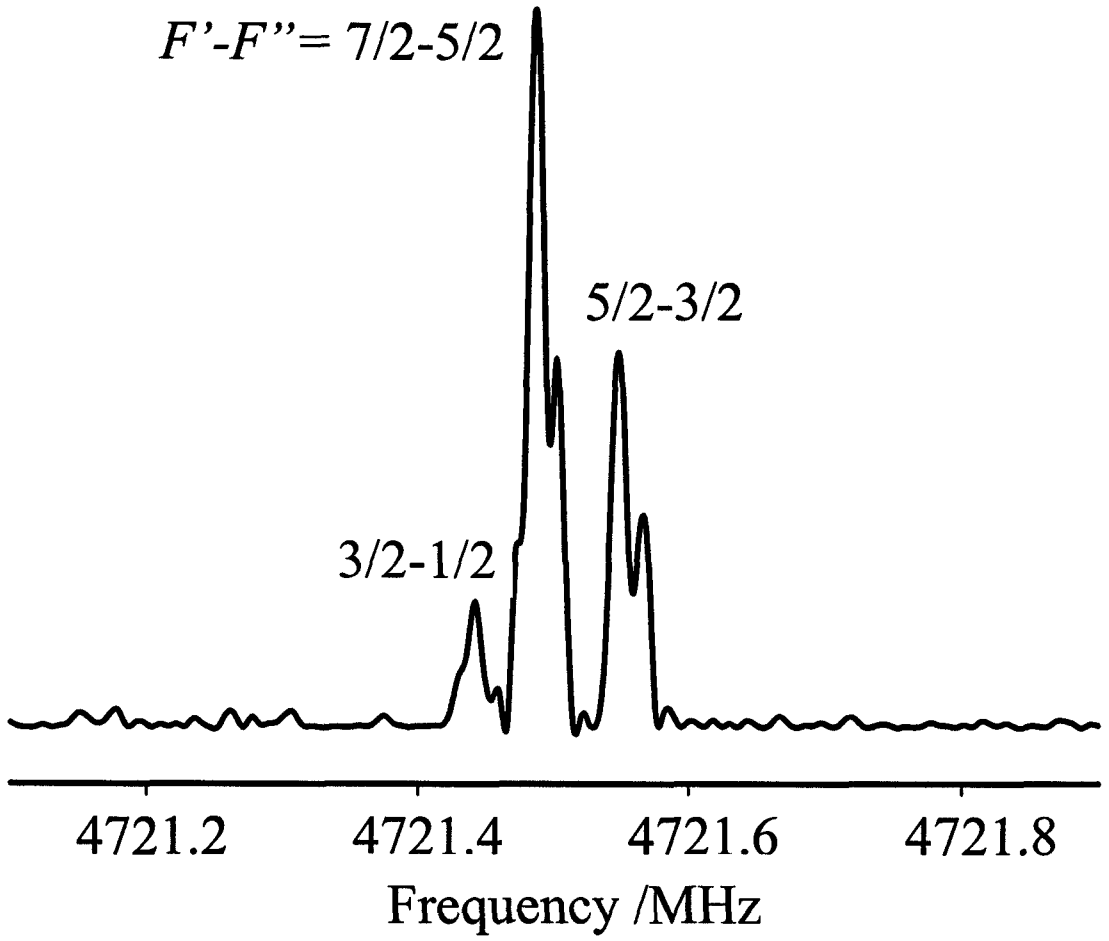

Figure 3-2: A composite spectrum of the $J_{KaKc} = 2_{11}$-1_{10} transition of ^{131}Xe-$^{15}N_2$. Each ^{131}Xe nuclear quadrupole hyperfine component appears as a doublet due to the Doppler effect. The spectrum was obtained from two individual experiments with 400 averaging cycles each.

tensor depends on the large amplitude van der Waals motions. This behavior has been investigated theoretically by Hutson for the case of Ar-N_2.[7] For weakly bound rare gas-linear molecule complexes with a quadrupolar nucleus in the molecular monomer, the nuclear quadrupole coupling constants χ_{gg} of the complex have often been used to obtain information about an average orientation of the molecular monomer with respect to the principal inertial axes g of the complex. Equation (3-1) has been applied, under the assumption that the nuclear quadrupole coupling constant of the linear monomer, χ_0, remains essentially unchanged after formation of the complex.

$$\chi_{gg} = \frac{\chi_0}{2}\left\langle 3\cos^2\theta_{gg} - 1\right\rangle \text{ with } g = a, b, c. \tag{3-1}$$

Here, θ_{gg} is the angle between the linear molecule axis and the g-principal inertial axis of the complex. Values of 0.1342 ($K_a = 0$ stack), 0.1228 (lower $K_a = 1$ stack), 0.1221 (upper $K_a = 1$ stack) were obtained for $\left\langle \cos^2\theta_a \right\rangle$, corresponding to angles θ_a of 68.5°, 69.5°, and 69.5° respectively. The nuclear quadrupole coupling constants, χ_0, of homonuclear diatomics, such as Cl_2 (Ref. 14) or N_2,[4,5,6] may be difficult to obtain directly. Instead, χ_0 can be calculated from the complex coupling constant using equation (3-1) and the assumption that the out-of-plane coupling constant χ_{cc} is independent of the large amplitude motions. From the coupling constant of the upper $K_a = 1$ stacks, which depends only on χ_{cc} (Ref. 7), we arrive at a value of χ_0= -5.367(2) MHz for free N_2. This value agrees with the values of -5.372(2), -5.370(3), and -5.371(4) derived from the χ_{cc} coupling constants (upper $K_a = 1$ stack) of the Ne-,[6] Ar-,[3] and Kr-N_2 (Ref. 5) complexes, respectively, within the error limits.

The observed nuclear quadrupole hyperfine structures in ^{131}Xe-^{15}N$_2$ due to the presence of the ^{131}Xe nucleus arise from the non-zero electric field gradient at the Xe nucleus. There are two mechanisms responsible for this electric field gradient. One is the induction interaction between the electric multipole moments of the partner molecule and the Xe electron cloud.[15] The ^{131}Xe nuclear quadrupole coupling constants of several Xe-molecule complexes, such as Xe-HCl,[15,16] Xe-HF,[17] and Xe-CO_2 (Ref. 18) have been interpreted in terms of this mechanism. The ^{131}Xe nuclear quadrupole coupling constant contributed by this mechanism can be calculated in terms of electric multipole moments of N_2 using the following expressions:[15]

$$q_0 = -6Q\left\langle \frac{3\cos^2\theta - 1}{R^5} \right\rangle - \cdots$$

$$\chi_{ind} = -eq_0(1-\gamma)Q_{Xe}/h \qquad (3\text{-}2)$$

Here, R is the van der Waals bond length, θ is the angle between the R vector and the N_2 molecular axis. q_0 is the component of the electric field gradient along the R vector generated by the multipole moments of the N_2 monomer at the site of Xe nucleus. As electric dipole and octupole moments of N_2 are zero, only the electric quadrupole moment Q = -1.47 D Å (Ref. 19) of N_2 was considered here, and higher order electric moments were neglected. The brackets indicate averaging over the large amplitude angular motions. With R = 4.208 Å, a Sternheimer shielding factor γ = -152 (Ref. 15), and the ^{131}Xe nuclear quadrupole moment Q_{Xe} = -0.12 b,[20] the χ_{ind} of ^{131}Xe-^{15}N$_2$ is predicted to be -0.894 MHz for a T-shaped configuration (θ = 90°). Assuming an average angle θ of 69° between the N_2 axis and R vector, to account for the large amplitude bending motions, a value of -0.538 MHz is obtained. A second mechanism

responsible for the distortion of the Xe electron cloud is the dispersion interaction. For example, in the ^{131}Xe-Rg (Rg = Ne, Ar and Kr) dimers,[21] ^{131}Xe nuclear quadrupole hyperfine structures were observed even though the electric multipole moments of the binding partners vanish. In these cases, the following values for the ^{131}Xe nuclear quadrupole coupling constants were obtained: ^{131}Xe-^{20}Ne, χ_{aa} = 0.3878(9) MHz; ^{131}Xe-Ar, χ_{aa} = 0.7228(36) MHz; ^{131}Xe-Kr, χ_{aa} = 0.7079(86) MHz.[21] Sign and magnitude of these values are in accord with the value from the extrapolation of the ^{131}Xe coupling constants of the Xe-HCl and Xe-HF complexes to the limit of zero electric multipole moments in Figure 3 of Ref. 22. The experimental value of 0.290 MHz for the ^{131}Xe quadrupole coupling constant in ^{131}Xe-$^{15}N_2$ indicates that the dispersion interaction has a larger and opposite contribution to the electric field gradient at the ^{131}Xe nucleus. The contribution of the dispersion interaction to the nuclear quadrupole coupling constant χ_{dis} can be estimated as a difference between the experimental χ_{aa} (0.290 MHz) and predicted χ_{ind} (-0.538 MHz) values, and a value of 0.828 MHz is resulted. This is in accord with the χ_{aa} values of ^{131}Xe-Rg (Rg = Ne, Ar and Kr) dimers.[21]

3.4. Potential energy surfaces and bound states calculations

3.4.1 Computational details

Two PESs were calculated at the CCSD(T) level of theory[23,24] using the MOLPRO 2002.6 package of *ab initio* programs.[25] For the first surface (PES I), the Well-Tempered Basis Set (28s23p17d)[26] augmented by 3d, 4f, 3g, and 2h functions, totaling 274 basis functions, was used for the Xe atom. Some of the exponents for

these additional polarization functions were taken from Ref. 27 and others were varied to reach the lowest Xe-N_2 binding energy. The exponents are 0.716, 0.32, 0.135 (d functions), 1.622, 0.507, 0.158, 0.3 (f functions), 1.007, 0.315, 0.3 (g functions), and 0.4, 0.3 (h functions). In the second surface (PES II), the aug-cc-pV5Z-PP basis set,[28] totalling 206 basis functions, was used for the Xe atom. For both these surfaces, the aug-cc-pVTZ basis set[29] was used for the N atoms, and the basis sets were supplemented with (3s3p3d1f1g) midbond functions. The exponents for (3s3p2d1f1g) were taken from Ref. 30, and a 1d function was added to reach a lower Xe-N_2 binding energy. The exponents are 0.9, 0.3, 0.1 for s and p functions, 0.6, 0.2, 0.1 for d functions and 0.3 for f and g functions. The interaction energies were calculated using the supermolecule approach and full counterpoise correction[31] was applied to eliminate basis-set superposition error. The Xe-N_2 geometry was defined in a Jacobi coordinate system (r, R, θ). Here, r is the N-N distance which was fixed at the equilibrium value of 1.095 Å.[32] R and θ are the polar coordinates of the Xe atom with respect to the center-of-mass of the N_2 unit; $\theta = 0°$ corresponds to a linear configuration with $C_{\infty v}$ symmetry and $\theta = 90°$ corresponds to a T-shaped configuration with C_{2v} symmetry. The Xe-N_2 PESs were calculated on a grid of 294 points for PES I and 273 points for PES II. The radial grid includes 42 points for PES I and 39 points for PES II from 3.5 to 10 Å and the angular grid consists of 7 equally spaced cuts with θ from 0° to 90° in steps of 15°. The calculated interaction energies are given in Tables 3-6 and 3-7.

The *ab initio* potentials were interpolated using the JACOBI code by Song *et al.*[33] A contour plot of the interpolated potential PES I is given in Figure 3-3. The deviation of the interpolated potential from the *ab initio* points is smaller than 0.001

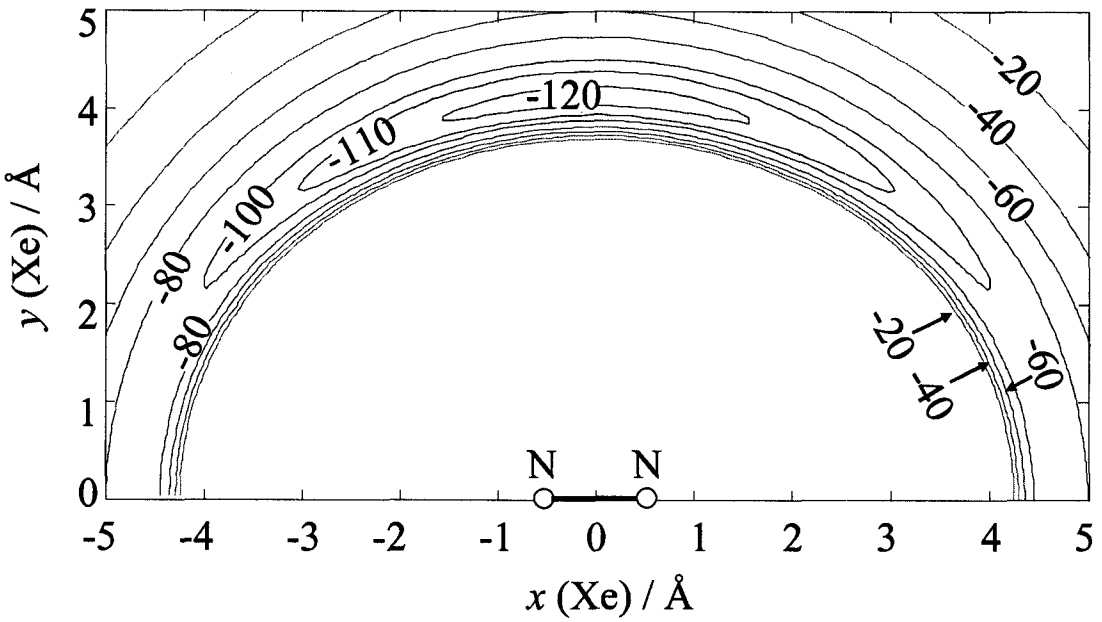

Figure 3-3: Contour diagram of the interpolated Xe-N_2 unscaled PES I. Potential energies are given in cm^{-1}.

cm^{-1}. This small error in the fit is within the accuracy of the *ab initio* calculations. The energies of bound ro-vibrational energy levels with rotational quantum number J up to 5 and vibrational quantum number υ up to 11 were then determined using the JACOBI code by Song *et al.*[33] A radial basis set consisting of 80 tri-diagonal Morse functions and an angular basis set of 80 Legendre polynomials were used. The basis sets were large enough to obtain energies of ro-vibrational levels that were converged to within $0.00001 cm^{-1}$. The resulting rotational transition frequencies are given in Table 3-8.

3.4.2 *Ab initio* potential energy surfaces

Both calculated PESs have a single minimum at a T-shaped geometry at R = 4.10Å, θ = 90°, with well depths of 122.4 cm^{-1} (PES I) and 119.3 cm^{-1} (PES II),

respectively. The overall topologies of PES I and PES II are similar and consistent with those of the *ab initio* surface by de Dios *et al.*[2] and the semi-empirical BTT surface (Table 3-9).[1,2] By comparison, our results give a well depth at the T-shaped configuration about 34% deeper than the previous *ab initio* surface[2] but about 29% shallower than that from the BTT surface.[1,2] At the saddle point, which corresponds to the linear configuration, our well depth is about 38% deeper than that of the *ab initio* surface[2] and about 24% lower than that from BTT surface.[1,2] The distances at the minimum energy configuration and at the saddle point are 1-3% shorter compared to the *ab initio* surface,[2] and 5-6% longer compared to the BTT surface.[1,2]

3.4.3 Scaled potential energy surfaces

The microwave transition frequencies obtained from bound state calculation are compared with the experimental ones in Table 3-8. For the ^{132}Xe-$^{14}N_2$ isotopomer, the calculated line frequencies from PES I are about 2.5% lower than the measured values, while those from PES II are within 1% of the experimental values. For example, for the 4_{04}-3_{03} transition of ^{132}Xe-$^{14}N_2$ (9881.8 MHz), the deviation of calculated frequencies from experimental values are 245.8 MHz for PES I and 80.0 MHz for PES II. These deviations are much larger than the experimental measurement uncertainty, which is estimated to be 1 kHz. In order to achieve a better agreement with experiment data, we have attempted to scale the potential energy and the radial coordinate of the *ab initio* surfaces.

The goal was to achieve a better agreement between experimental rotational constants and centrifugal distortion constants and those determined from the energy

levels supported by the PESs. The calculated transition frequencies were used to fit rotational and centrifugal distortion constants, analogous to the procedure with the experimental data, and are given in Table 3-10. The molecular constants can give more physical insight into the global features of the PES than the line positions alone. The Xe-N_2 complex can be approximated as a linear pseudo-diatomic rotor. In this picture, the linear combination $(B+C)/2$ is inversely proportional to the intermolecular separation, while Δ_J provides a measure of the radial anisotropy of the PES. The linear combination B-C and Δ_{Jk} indicate the deviation from linearity of the complex. These parameters are a measure of the angular anisotropy of the surface and are related to the energy difference of the global minimum and the saddle point.

The calculated constants from both PES I and II are closer to experimental values compared to those obtained from BTT surface[1,2] and *ab initio* surface by de Dios *et al.*[2] (see Table 3-10). A comparison between PES I and II shows that although PES II predicts more accurate transition frequencies, the spectroscopic constants of PES I are closer to the experimental values [except for $(B+C)/2$]. For example, the value for Δ_{Jk} from PES II is almost five times the experimental value while PES I gives a value about 20% less (see Table 3-10). The Δ_J values from both surfaces agree very well with the experimental value, indicating that the radial anisotropies of the surfaces are in accord with the experimental spectra. However, the calculated $(B+C)/2$ value for PES I is 2.5% smaller than the experimental value and 0.8% larger for PES II, which suggests that an intermolecular equilibrium separation R is too large for PES I and too small for PES II. For B-C and Δ_{JK}, PES I gives values that are too low by 11% and 20%, respectively, and the results from PES II are too large by 22% and 370%,

respectively. This, in turn, means that the angular anisotropy of PES I is too large and that of PES II too small. In order to achieve a better agreement with experiment data, I scaled both of these two surfaces by potential and radial scaling. The first potential was scaled mainly to reduce the intermolecular separation R and to reduce the energy difference between the global minimum (T-shaped) and the saddle point (linear configuration). The best agreement was achieved by reducing the separation R by 0.058 Å and lowering the potential energy of the whole surface by 3.8% * $\cos\theta$. The energies along the minimum energy path in the angular coordinate are shown in Figure 3-4 for both the unscaled and scaled PES I. The spectroscopic constants from experimental data and unscaled and scaled PES I are compiled in Table 3-10. The experimental line positions are reproduced to within ± 0.01% (see Table 3-8). The scaled PES I has double minima at $\theta = 80°$ and 100° respectively, both with energies of 122.9 cm^{-1} and $R = 4.08$ Å. A transition state at $R = 4.07$ Å and $\theta = 90°$ lies 0.3 cm^{-1} above the global minima. These double minima, although very distinct from the unscaled PES I, have little effect on the calculated rotational spectra because the ground state of the Xe-N_2 lies 18 cm^{-1} above the transition state at $\theta = 90°$. This scaled PES I was also used to determine the line frequencies and rotational and centrifugal distortion constants for the ^{129}Xe-$^{14}N_2$ isotopomer (see Tables 3-8 and 3-10). Excellent agreement with the experimental data was found; the largest deviation is only 0.15%. In addition, the A rotational constant was determined by using both a-type and hypothetical b-type transitions calculated from the scaled PES I in a fitting procedure. This value was used in the fits of the experimental constants. PES II was scaled by increasing the separation R and lowering the potential energies. However, the simple

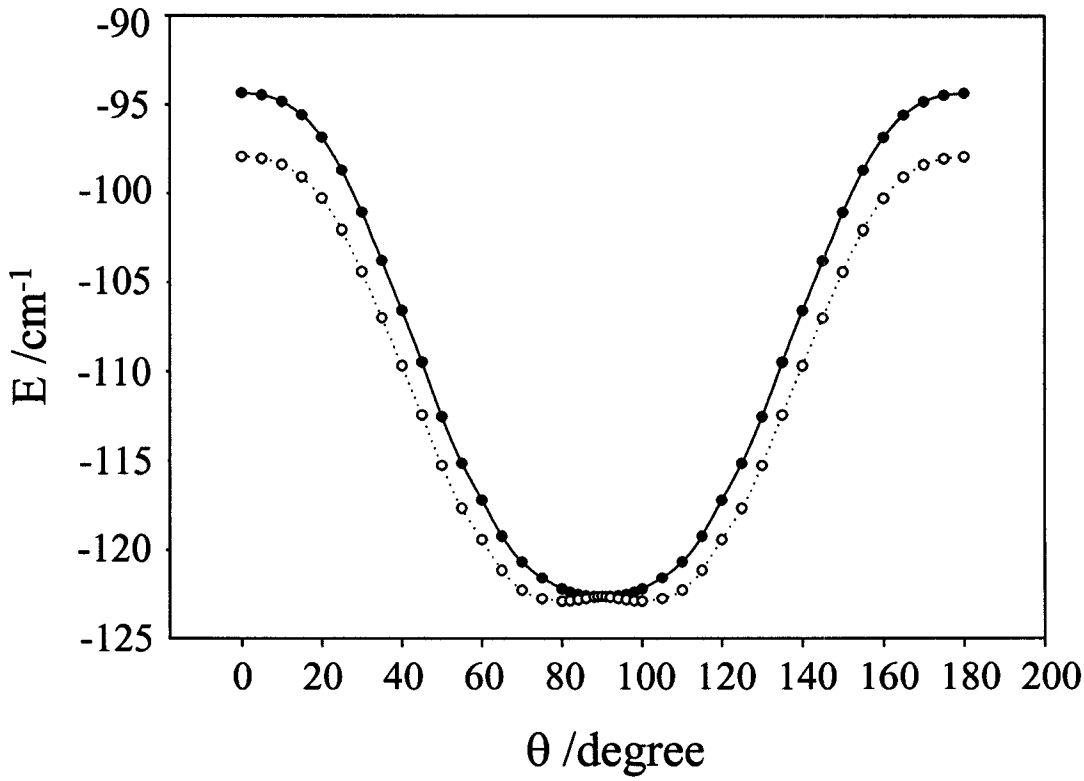

Figure 3-4. Plot of the minimum energies of Xe-N_2 as a function of polar angle θ for unscaled (solid line) and scaled (dotted line) PES I.

potential and radial scaling of this surface did not result in as good an agreement with the experimental data as the scaled PES I. The Δ_J and Δ_{Jk} values are always in poor agreement (see Table 3-10). The best agreement was achieved by increasing the separation R by 0.024 Å and lowering the whole surface by 45.5%. The global minimum of this scaled PES II has a well depth of 171.4 cm^{-1} at R = 4.21 Å, θ = 90°. The experimental information can be reproduced to within ± 0.3% (see Table 3-8).

3.5 Summary

Rotational transitions for three isotopomers of the Xe-N_2 complex were measured and assigned. Nuclear quadrupole hyperfine structures due to the interaction of the nuclear spins of the ^{14}N and ^{131}Xe nuclei with the overall rotation were detected and analyzed. The spectra are in accord with a T-shaped complex having C_{2v} symmetry, with two equivalent N atoms.

Two high level *ab initio* Xe-N_2 PESs were determined and a single minimum, corresponding to a T-shaped configuration, was obtained for both surfaces. These two surfaces were compared with other existing *ab initio* and semi-empirical PESs. In addition, our two surfaces were used to calculate the rotational energy levels and to determine rotational transition frequencies. Both calculated line frequencies and the spectroscopic parameters were compared with the experimental data. The line frequencies from PES I deviate from the experimental ones by about 2.5% for the ^{132}Xe-$^{14}N_2$ isotopomer, and the frequencies from PES II deviate from the experimental data by about 1%. However, PES I has a better overall shape since the calculated spectroscopic parameters are closer to the experimental values than those from PES II [except for $(B+C)/2$]. After appropriate potential and radial scaling, the deviations in transition frequencies were reduced to within 0.01% for PES I. The scaled PES I reproduces the transition frequencies of the ^{129}Xe-$^{14}N_2$ isotopomer to within 0.15%.

Table 3-1: Measured frequencies of the ^{14}N hyperfine structure of Xe-$^{14}N_2$ isotopmers.

		^{132}Xe-$^{14}N_2$		^{129}Xe-$^{14}N_2$	
$J'_{Ka'Kc'}$-$J''_{Ka''Kc''}$	F' I'-F'' I''	ν_{obs} (MHz)	$\Delta\nu_{HFS}$ [a] (kHz)	ν_{obs} (MHz)	$\Delta\nu_{HFS}$ (kHz)
2_{02}-1_{01}	1 2-1 2	4943.0435	1.5	4962.7860	1.3
	3 2-3 2	4943.0098	0.1	4962.7517	-1.1
	2 0-1 2	4942.9176	0.8	4962.6598	0.1
	0 2-1 2	4942.6459	4.2		
	2 2-1 0	4942.6004	0.9	4962.3422	-1.0
	2 2-2 2	4942.5259	-1.7	4962.2699	-1.6
	4 2-3 2	4942.3250	1.8	4962.0673	0.4
	3 2-2 2	4942.2866	-1.4	4962.0294	-2.7
	1 2-1 0	4941.5010	-0.7	4961.2432	-3.3
	1 2-2 2	4941.4301	0.2	4961.1737	-1.1
	2 0-1 0	4941.3774	0.8	4961.1211	0.6
	2 0-2 2	4941.3062	1.5	4961.0491	-0.7
	0 2-1 0	4941.1037	2.3		
3_{03}-2_{02}	4 2-4 2	7413.2949	-1.2	7442.9020	-1.8
	2 2-2 0	7413.0379	4.7	7442.6364	-4.5
	3 2-3 2	7412.9556	-2.8	7442.5688	2.2
	2 2-1 2	7412.9076	-0.4	7442.5149	-0.9
	1 2-0 2	7412.8299	1.3	7442.4316	-4.7
	3 0-2 0	7412.7379	0.2	7442.3434	-2.1
	3 2-2 2	7412.7190	0.2	7442.3250	-2.2
	5 2-4 2	7412.6302	0.4	7442.2361	-1.7
	4 2-3 2	7412.6118	2.2	7442.2152	-2.8
	1 2-1 2	7412.4228	-5.6	7442.0359	-0.5
	2 2-2 2	7411.8102	-0.1	7441.4207	1.6
	3 0-3 2	7411.7534	-1.0	7441.3625	-0.7
4_{04}-3_{03}	3 2-2 2	9881.9402	-1.1	9921.4004	-0.1
	2 2-1 2	9881.9071	-1.2	9921.3684	1.4
	4 0-3 0	9881.8618	-1.3	9921.3246	2.6
	6 2-5 2	9881.8136	-1.3	9921.2781	4.2
	5 2-4 2	9881.8024	1.2	9921.2672	6.5
5_{05}-4_{04}	4 2-3 2	12349.5959	4.2	12398.8752	-2.0
	3 2-2 2	12349.5747	0.5	12398.8574	-1.8
	5 0-4 0	12349.5451	-1.9	12398.8311	-1.0
	6 2-5 2	12349.5074	-1.2	12398.7944	0.0
2_{12}-1_{11}	1 1-0 1	4887.0540	1.3	4906.2588	-0.3
	2 1-2 1	4886.4086	-1.0	4905.6139	3.2
	3 1-2 1	4885.5384	2.6	4904.7436	1.8
	2 1-1 1	4885.0942	-2.6	4904.3000	2.2
	1 1-1 1	4883.7237	4.8	4902.9282	-0.9

Table 3-1: (Continued).

$J'_{Ka'Kc'}$-$J''_{Ka''Kc''}$	$F'\ I'$-$F''\ I''$	^{132}Xe-$^{14}N_2$		^{129}Xe-$^{14}N_2$	
		ν_{obs} (MHz)	$\Delta\nu_{HFS}$ (kHz)	ν_{obs} (MHz)	$\Delta\nu_{HFS}$ (kHz)
3_{13}-2_{12}	3 1-3 1	7328.0510	1.3	7356.8408	-4.1
	2 1-1 1	7327.5057	1.7	7356.3052	0.6
	4 1-3 1	7327.2839	3.1	7356.0828	0.4
	3 1-2 1	7327.1756	-0.3	7355.9755	-0.5
	2 1-2 1	7326.1217	-4.5		
4_{14}-3_{13}	3 1-2 1	9767.9370	-2.2	9806.3232	-1.3
	5 1-4 1	9767.8559	1.0	9806.2383	-2.6
	4 1-3 1	9767.8178	1.1	9806.2029	0.9
5_{15}-4_{14}	4 1-3 1	12206.8906	-0.5	12254.8386	-0.0
	6 1-5 1			12254.7935	-1.3
	5 1-4 1	12206.8294	-0.9	12254.7797	1.8
2_{11}-1_{10}	1 1-1 1	4983.1167	-0.4	5003.1109	1.5
	3 1-2 1	4981.5255	-0.2	5001.5209	2.2
	1 1-0 1	4981.1094	-1.2	5001.1063	1.0
	2 1-1 1	4980.9293	-1.0	5000.9247	3.2
	2 1-2 1	4980.1083	-0.4	5000.1069	5.5
3_{12}-2_{11}	2 1-2 1	7473.1936	0.2	7503.1802	-0.6
	4 1-3 1	7471.2257	1.0	7501.2102	-0.8
	3 1-2 1	7471.0328	-1.1	7501.0184	-1.3
	2 1-1 1	7471.0098	3.1	7500.9943	1.3
	3 1-3 1	7469.6172	0.3	7499.5977	-4.6
4_{13}-3_{12}	5 1-4 1	9959.9164	1.3	9999.8861	-1.0
	4 1-3 1	9959.8215	-1.0	9999.7951	0.8
	3 1-2 1	9959.7960	3.5	9999.7643	-0.2
5_{14}-4_{13}	6 1-5 1	12447.1998	-4.6	12497.1410	-3.8
	5 1-4 1	12447.1510	0.8	12497.0939	3.4
	4 1-3 1	12447.1276	1.3	12497.0671	0.5

[a] $\Delta\nu_{HFS} = \nu_{obs} - \nu_{cal}$.

Table 3-2. Microwave center frequencies for Xe-$^{14}N_2$ isotopomers.

$J'_{Ka'Kc'}$-$J''_{Ka''Kc''}$	^{132}Xe-$^{14}N_2$		^{129}Xe-$^{14}N_2$	
	ν_{center} (MHz)	$\Delta\nu_{center}$ (kHz) [a]	ν_{center} (MHz)	$\Delta\nu_{center}$ (kHz)
2_{02}-1_{01}	4942.3925	0.9	4962.1345	-0.9
2_{12}-1_{11}	4885.5142	1.1	4904.7191	1.3
2_{11}-1_{10}	4981.3488	-0.6	5001.3448	2.7
3_{03}-2_{02}	7412.6673	-0.2	7442.2741	-1.5
3_{13}-2_{12}	7327.2786	-1.2	7356.0802	-0.6
3_{12}-2_{11}	7471.1378	-0.7	7501.1221	-2.5
4_{04}-3_{03}	9881.8376	-0.8	9921.3006	3.0
4_{14}-3_{13}	9767.8584	0.3	9806.2431	-0.7
4_{13}-3_{12}	9959.8658	1.7	9999.8363	0.2
5_{05}-4_{04}	12349.5351	0.4	12398.8190	-1.2
5_{15}-4_{14}	12206.8508	0.0	12254.7989	0.4
5_{14}-4_{13}	12447.1702	-0.7	12497.1114	0.3

[a] $\Delta\nu_{center} = \nu_{obs} - \nu_{cal}$.

Table 3-3: ^{14}N nuclear quadrupole coupling constants and spin-rotation constants of Xe-$^{14}N_2$ isotopomers.

		$K_a = 0$	Lower $K_a = 1$	Upper $K_a = 1$
^{132}Xe-$^{14}N_2$	χ_{aa} /MHz	1.6037(6)	1.6886(18)	1.6984(18)
	χ_{bb} /MHz	-3.66(60)	-4.4335(12)	-4.3835(12)
	χ_{cc} /MHz	2.06(60)	2.7449(12)	2.6851(12)
	M_{aa} /MHz	-	0.0173(10)	0.0157(10)
	σ /kHz [a]	2.0	2.3	1.8
^{129}Xe-$^{14}N_2$	χ_{aa} /MHz	1.6015(7)	1.7017(22)	1.7038(18)
	χ_{bb} /MHz	-2.73(62)	-4.4294(15)	-4.3855(12)
	χ_{cc} /MHz	1.13(62)	2.7277(15)	2.6817(12)
	M_{aa} /MHz	-	0.0160(11)	0.0153(10)
	σ /kHz	2.3	1.8	2.5

[a] Standard deviation of the fit.

Table 3-4: Rotational and centrifugal distortion constants of Xe-$^{14}N_2$ isotopomers.

Constant	^{132}Xe-$^{14}N_2$	^{129}Xe-$^{14}N_2$
A /MHz [a]	75088.256	75094.418
B /MHz	1259.6638(4)	1264.7970(4)
C /MHz	1211.7734(4)	1216.5135(4)
Δ_J /MHz	0.01435(2)	0.01442(2)
Δ_{Jk} /MHz	2.2377(2)	2.2744(2)
δ_J /MHz	0.000868(3)	0.000895(3)
Φ_{JK} /MHz	-0.001026(6)	-0.000988(6)
σ /kHz [b]	0.8	1.6

[a] Fixed at a value derived from a fit of both *a*- and hypothetical *b*-type transitions determined from the scaled PES I.
[b] Standard deviation of the fit.

Table 3-5: Measured frequencies and determined spectroscopic constants of ^{131}Xe-$^{15}N_2$ isotopmer.

$J'_{Ka'Kc'}$ - $J''_{Ka''Kc''}$	F' - F''	ν_{obs} (MHz)	$\Delta\nu_{HFS}$ [a] (kHz)
2_{02}-1_{01}	1.5-0.5	4685.6132	-2.0
	2.5-2.5	4685.6089	-0.2
	2.5-1.5	4685.5376	0.9
	3.5-2.5	4685.5376	1.0
	1.5-1.5	4685.4862	1.3
2_{12}-1_{11}	2.5-1.5	4632.0568	6.4
	1.5-1.5	4632.0033	-4.0
	3.5-2.5	4631.9828	4.8
	0.5-0.5	4631.9182	-7.1
2_{11}-1_{10}	2.5-1.5	4721.5514	-6.6
	3.5-2.5	4721.4901	4.5
	1.5-0.5	4721.4428	2.1
3_{03}-2_{02}	3.5-3.5	7027.5682	1.6
	2.5-1.5	7027.5105	-1.6
	1.5-0.5	7027.5105	-1.6
	3.5-2.5	7027.4942	-0.0
	4.5-3.5	7027.4942	0.0

A /MHz [b]	69392.188
B /MHz	1193.8686(3)
C /MHz	1149.1169(3)
Δ_J /MHz	0.01269(2)
Δ_{Jk} /MHz	2.2039(2)
χ_{aa} /MHz	0.290(2)
χ_{bb} /MHz	0.048(7)
χ_{cc} /MHz	-0.242(7)
σ /kHz [c]	3.9

[a] $\Delta\nu_{HFS} = \nu_{obs} - \nu_{cal}$.
[b] Fixed at a value derived from a fit of both *a*- and hypothetical *b*-type transitions determined from the scaled PES I.
[c] Standard deviation of the fit.

Table 3-6: *Ab initio* Xe-N_2 potential energies (in cm^{-1}) of PES I.

R / Å	0°	15°	30°	45°	60°	75°	90°
3.5000	2166.83	1919.42	1352.71	790.46	419.24	242.21	193.86
3.5500	1787.40	1577.74	1097.70	622.19	310.23	162.81	122.84
3.6000	1465.54	1288.16	882.60	481.68	220.22	97.89	65.25
3.6500	1193.28	1043.69	701.66	364.33	146.02	45.15	18.48
3.7000	963.27	837.38	550.07	266.99	85.33	2.70	-18.68
3.7500	770.42	664.35	423.28	186.75	36.30	-30.68	-48.09
3.8000	608.16	519.50	318.02	120.89	-3.20	-57.55	-71.00
3.8500	473.03	398.79	230.54	67.07	-34.44	-78.00	-88.45
3.9000	360.44	298.44	159.08	23.81	-59.13	-93.58	-101.68
3.9500	267.08	215.90	100.19	-11.06	-78.15	-104.69	-110.70
4.0000	190.22	147.69	52.43	-38.47	-92.22	-112.63	-117.02
4.1000	75.70	47.48	-16.24	-76.38	-109.72	-120.60	-122.44
4.2000	1.10	-17.44	-59.26	-97.62	-116.58	-121.17	-121.26
4.2500	-25.24	-39.94	-73.57	-103.35	-117.18	-119.75	-119.17
4.3000	-45.67	-57.30	-83.82	-107.17	-116.80	-117.07	-116.30
4.4000	-73.44	-80.33	-96.55	-109.45	-112.70	-110.57	-109.12
4.5500	-91.56	-94.31	-100.94	-104.36	-102.25	-97.95	-96.20
4.7000	-93.94	-94.42	-95.89	-94.59	-89.79	-85.18	-83.40
4.8500	-88.34	-87.66	-86.63	-83.09	-77.58	-72.93	-71.04
5.0000	-79.49	-78.15	-75.59	-71.44	-66.13	-61.76	-60.27
5.1500	-69.29	-67.86	-64.96	-61.01	-56.10	-52.15	-50.92
5.3000	-59.39	-58.16	-55.13	-51.55	-47.32	-43.96	-42.91
5.4500	-50.26	-49.36	-46.44	-43.35	-39.79	-36.89	-35.88
5.6000	-42.40	-41.44	-39.22	-36.37	-33.21	-31.19	-30.07
5.8000	-33.56	-32.66	-31.01	-28.73	-26.23	-24.58	-23.94
6.0000	-26.32	-26.01	-24.63	-22.89	-20.98	-19.58	-19.09
6.2500	-19.71	-19.40	-18.41	-17.21	-15.58	-14.55	-14.22
6.5000	-14.75	-14.81	-14.09	-12.82	-12.01	-11.22	-11.04
6.7500	-11.37	-11.19	-10.71	-9.85	-9.31	-8.71	-8.43
7.0000	-8.67	-8.52	-8.38	-7.73	-7.11	-6.74	-6.67
7.2500	-6.76	-6.83	-6.43	-6.19	-5.64	-5.27	-5.27
7.5000	-5.33	-5.38	-5.07	-4.81	-4.41	-4.08	-4.13
7.7500	-4.50	-4.28	-3.99	-3.75	-3.73	-3.31	-3.18
8.0000	-3.56	-3.53	-3.20	-3.12	-2.92	-2.77	-2.61
8.2500	-2.85	-2.70	-2.74	-2.48	-2.28	-2.30	-2.15
8.5000	-2.33	-2.30	-2.22	-1.91	-1.93	-1.71	-1.76
8.7500	-1.98	-1.91	-1.62	-1.71	-1.60	-1.58	-1.38
9.0000	-1.67	-1.43	-1.51	-1.38	-1.16	-1.16	-1.16
9.2500	-1.32	-1.29	-1.05	-1.23	-0.97	-1.01	-0.99
9.5000	-1.10	-1.05	-1.01	-0.92	-0.83	-0.92	-0.68
9.7500	-0.97	-0.97	-0.75	-0.92	-0.83	-0.70	-0.68
10.0000	-0.72	-0.79	-0.79	-0.64	-0.53	-0.61	-0.57

Table 3-7: *Ab initio* Xe-N_2 potential energies (in cm^{-1}) of PES II.

R / Å	0°	15°	30°	45°	60°	75°	90°
3.5000	2003.22	1771.70	1240.47	715.03	370.49	207.88	164.16
3.6000	1345.75	1180.34	801.12	427.90	186.50	75.40	46.32
3.7000	877.65	760.33	491.87	229.63	63.10	-10.98	-29.65
3.8000	548.09	465.58	277.37	95.48	-17.17	-64.96	-76.32
3.8500	423.02	354.06	197.17	46.54	-45.29	-83.01	-91.61
3.9000	319.17	261.72	131.34	7.16	-67.13	-96.45	-102.77
3.9500	233.36	185.63	77.65	-24.19	-83.74	-106.10	-110.54
4.0000	162.77	123.28	34.22	-48.82	-96.06	-112.64	-115.54
4.1000	58.20	31.46	-28.23	-82.25	-110.66	-118.61	-119.26
4.2000	-9.69	-27.42	-66.44	-100.20	-115.74	-117.97	-117.19
4.2500	-33.45	-47.85	-78.91	-105.03	-115.81	-116.01	-114.73
4.3000	-51.92	-63.37	-87.97	-107.78	-114.68	-113.26	-111.62
4.4000	-76.45	-83.55	-98.24	-108.57	-109.82	-106.20	-104.07
4.5500	-92.06	-95.09	-100.58	-102.36	-98.84	-93.64	-91.27
4.7000	-92.98	-93.81	-94.38	-91.85	-86.30	-80.74	-78.44
4.8500	-86.67	-86.36	-84.49	-80.08	-73.98	-68.69	-66.60
5.0000	-77.34	-76.49	-73.59	-68.61	-62.73	-57.98	-56.16
5.1500	-67.27	-66.22	-63.04	-58.18	-52.86	-48.74	-47.19
5.3000	-57.61	-56.55	-53.49	-49.07	-44.42	-40.92	-39.61
5.4500	-48.90	-47.91	-45.15	-41.28	-37.30	-34.37	-33.26
5.6000	-41.31	-40.43	-38.04	-34.71	-31.36	-28.89	-27.99
5.8000	-32.91	-32.19	-30.26	-27.61	-24.97	-23.04	-22.33
6.0000	-26.25	-25.68	-24.14	-22.05	-19.97	-18.48	-17.94
6.2500	-19.90	-19.48	-18.33	-16.79	-15.25	-14.16	-13.76
6.5000	-15.23	-14.92	-14.06	-12.90	-11.78	-10.97	-10.67
6.7500	-11.77	-11.53	-10.88	-10.03	-9.19	-8.59	-8.36
7.0000	-9.19	-9.00	-8.52	-7.88	-7.25	-6.79	-6.62
7.2500	-7.24	-7.11	-6.74	-6.25	-5.77	-5.42	-5.29
7.5000	-5.77	-5.67	-5.39	-5.01	-4.64	-4.37	-4.27
7.7500	-4.64	-4.56	-4.34	-4.05	-3.76	-3.54	-3.47
8.0000	-3.76	-3.70	-3.53	-3.30	-3.07	-2.90	-2.84
8.2500	-3.07	-3.02	-2.89	-2.70	-2.52	-2.38	-2.34
8.5000	-2.53	-2.38	-2.38	-2.23	-2.09	-1.98	-1.94
8.7500	-2.10	-2.06	-1.98	-1.85	-1.74	-1.65	-1.61
9.0000	-1.75	-1.72	-1.65	-1.55	-1.45	-1.38	-1.35
9.2500	-1.46	-1.44	-1.38	-1.30	-1.22	-1.16	-1.14
9.5000	-1.24	-1.22	-1.17	-1.10	-1.04	-0.99	-0.97
9.7500	-1.05	-1.03	-0.99	-0.94	-0.88	-0.84	-0.82
10.0000	-0.89	-0.88	-0.85	-0.80	-0.75	-0.72	-0.70

Table 3-8: Comparison of rotational transition frequencies (in MHz) of Xe-$^{14}N_2$ isotopomers from experiment and potentials.

Isotopomer	$J'_{Ka'Kc'}$-$J''_{Ka''Kc''}$	Experiment	PES I	Scaled PES I[a]	PES II	Scaled PES II
^{132}Xe-$^{14}N_2$	2_{02}-1_{01}	4942.393	4819.40 (-2.49)[b]	4942.21 (-0.004)	4982.50 (0.81)	4949.31 (0.14)
	2_{12}-1_{11}	4885.514	4769.58 (-2.37)	4885.89 (+0.008)	4881.99 (-0.07)	4875.21 (-0.21)
	2_{11}-1_{10}	4981.349	4854.94 (-2.54)	4981.82 (+0.009)	4999.09 (0.36)	4969.90 (-0.22)
	3_{03}-2_{02}	7412.667	7228.26 (-2.49)	7412.07 (-0.008)	7472.75 (0.81)	7423.41 (0.14)
	3_{13}-2_{12}	7327.279	7153.50 (-2.37)	7327.50 (+0.003)	7322.20 (-0.07)	7312.40 (-0.20)
	3_{12}-2_{11}	7471.138	7281.61 (-2.54)	7471.51 (+0.005)	7497.72 (0.35)	7454.35 (-0.22)
	4_{04}-3_{03}	9881.838	9636.00 (-2.49)	9881.21 (-0.006)	9961.76 (0.81)	9896.71 (0.15)
	4_{14}-3_{13}	9767.858	9536.24 (-2.37)	9768.32 (+0.005)	9761.41 (-0.07)	9784.92 (-0.19)
	4_{13}-3_{12}	9959.866	9707.18 (-2.54)	9960.55 (+0.007)	9995.20 (0.35)	9938.04 (-0.22)
	5_{05}-4_{04}	12349.535	12042.43 (-2.49)	12348.43 (-0.009)	12448.87 (0.80)	12368.62 (0.15)
	5_{15}-4_{14}	12206.851	11917.60 (-2.37)	12207.08 (+0.002)	12199.04 (-0.06)	12184.24 (-0.19)
	5_{14}-4_{13}	12447.170	12131.48 (-2.54)	12447.71 (+0.004)	12490.90 (0.35)	12420.40 (-0.22)
^{129}Xe-$^{14}N_2$	2_{02}-1_{01}	4962.135	4831.86 (-2.63)	4954.99 (-0.14)		
	2_{12}-1_{11}	4904.719	4781.75 (-2.51)	4898.32 (-0.13)		
	2_{11}-1_{10}	5001.345	4867.55 (-2.68)	4994.76 (-0.13)		
	3_{03}-2_{02}	7442.274	7246.95 (-2.62)	7431.24 (-0.15)		
	3_{13}-2_{12}	7356.080	7171.74 (-2.51)	7346.14 (-0.14)		
	3_{12}-2_{11}	7501.122	7300.53 (-2.67)	7490.93 (-0.14)		
	4_{04}-3_{03}	9921.301	9660.91 (-2.62)	9906.76 (-0.15)		
	4_{14}-3_{13}	9806.243	9560.55 (-2.51)	9793.17 (-0.13)		
	4_{13}-3_{12}	9999.836	9732.39 (-2.67)	9986.43 (-0.13)		
	5_{05}-4_{04}	12398.819	12073.55 (-2.62)	12380.34 (-0.15)		
	5_{15}-4_{14}	12254.799	11947.97 (-2.51)	12238.12 (-0.14)		
	5_{14}-4_{13}	12497.111	12162.98 (-2.67)	12480.04 (-0.14)		

[a] See text.

[b] The numbers in brackets are the differences between experimental frequencies and those from the potentials in percent.

Table 3-9: Comparison of well depths of the Xe-N_2 potentials of this work with literature potentials.

	T-shaped ($\theta = 90°$)		Linear ($\theta = 0°$)	
Reference	D_e / cm^{-1}	R_e / Å	D_e / cm^{-1}	R_e / Å
PES I [a]	122.4	4.10	93.9	4.70
scaled PES I [a]	122.6	4.07	97.9	4.60
PES II [a]	119.3	4.10	93.0	4.70
scaled PES II [a]	171.4	4.21	135.4	4.72
de Dios *et al.*[b]	91.2	4.22	67.6	4.76
BTT[c]	171.7	3.89	124.1	4.45

[a] This work.
[b] Reference 2.
[c] References 1 and 2.

Table 3-10: Comparison of rotational and centrifugal distortion constants (in MHz) of Xe-$^{14}N_2$ isotopomers from experiment and potentials.

Isotopomer	Constant	Experiment	PES I	Scaled PES I [b]	PES II	Scaled PES II	BTT[c]	de Dios *et al.*[c]
^{132}Xe-$^{14}N_2$	A[a]	75088.256	73475.813(1)	75088.256(1)	80260.557(1)	74949.324(1)	65293(282)	90.2(36)×10^3
	B	1259.6638(4)	1226.3018(4)	1259.6141(4)	1275.0625(4)	1261.1104(4)	1354.1(11)	1140.27(60)
	C	1211.7734(4)	1183.6419(3)	1211.6809(3)	1216.4676(3)	1213.7317(3)	1325.6(10)	1121.83(58)
	$(B+C)/2$	1235.7186	1204.9719	1235.6475	1245.7650	1237.4209	1339.85	1131.05
	$B-C$	47.89	42.66	47.93	58.59	47.37	28.5	18.44
	Δ_J	0.01435(2)	0.01414(1)	0.01441(1)	0.01501(1)	0.00825(1)		
	Δ_{Jk}	2.2377(2)	1.7830(2)	2.0860(2)	10.5142(2)	6.7077(2)		
	δ_J	0.000868(3)	0.000576(3)	0.000969(3)	-0.001122(3)	-0.000735(3)		
	Φ_{JK}	-0.001026(6)	-0.000713(4)	-0.001093(4)	0.001515(4)	0.000903(4)		
^{129}Xe-$^{14}N_2$	A	75094.418	73481.001(1)	75094.418(1)				
	B	1264.7970(4)	1229.5312(4)	1262.9377(4)				
	C	1216.5135(4)	1186.6445(3)	1214.7476(3)				
	$(B+C)/2$	1240.6553	1208.0878	1238.8422				
	$B-C$	48.28	42.89	48.19				
	Δ_J	0.01442(2)	0.01419(1)	0.01443(1)				
	Δ_{Jk}	2.2743(2)	1.8013(2)	2.1089(2)				
	δ_J	0.000895(3)	0.000578(3)	0.000969(3)				
	Φ_{JK}	-0.000988(6)	-0.000721(4)	-0.001106(1)				

[a] Fixed at a value derived from a fit of both *a*- and hypothetical *b*-type transitions calculated from the scaled PES I.
[b] See text.
[c] Ref. 1 and 2, from quantum diffusion Monte Carlo solution of the van der Waals vibrational motion.

References

[1] M. S. Bowers, K. T. Tang, and J. P. Toennies, J. Chem. Phys., **88**, 5465(1988).

[2] A. C. de Dios and C. J. Jameson, J. Chem. Phys. **107**, 4253 (1997).

[3] W. Jäger and M. C. L. Gerry, Chem. Phys. Lett. **196**, 274 (1992).

[4] W. Jäger, M. C. L. Gerry, C. Bissonnette, and F. R. W. McCourt, Faraday Discuss. **97**, 105 (1994).

[5] W. Jäger, Y. Xu, N. Heineking, and M. C. L. Gerry, J. Chem. Phys. **99**, 7510 (1993).

[6] W. Jäger, Y. Xu, G. Armstrong, M. C. L. Gerry, F. Y. Naumkin, F. Wang, and F. R. W. McCourt, J. Chem. Phys. **109**, 5420 (1998).

[7] J. M. Hutson, Mol. Phys. **84**, 185 (1995).

[8] J. M. M. Howson and J. M. Hutson, J. Chem. Phys. **115**, 5059 (2001).

[9] M. Meuwly and J. M. Hutson, J. Chem. Phys. **110**, 8338 (1999).

[10] T. Ogata, W. Jäger, I. Ozier, and M. C. L. Gerry, J. Chem. Phys. **98**, 9399 (1993).

[11] K. A. Walker, T. Ogata, W. Jäger, M. C. L. Gerry, and I. Ozier, J. Chem. Phys. **106**, 7519 (1997).

[12] H. M. Pickett, J. Mol. Spectrosc. **148**, 371 (1991).

[13] J. K. G. Watson, in *Vibrational Spectra and Structure: A Series of Advances*, edited by J. R. Durig (Elsevier, Amsterdam, 1977).

[14] Y. Xu, W. Jäger, I. Ozier, and M. C. L. Gerry, J. Chem. Phys. **98**, 3726 (1993).

[15] E. J. Campbell, L. W. Buxton, M. R. Keenan, and W. H. Flygare, Phys. Rev. A **24**, 812 (1981).

[16] M. R. Keenan, L. W. Buxton, E. J. Campbell, T. J. Balle, and W. H. Flygare, J. Chem. Phys. **73**, 3523 (1980).

[17] F. A. Baiocchi, T. A. Dixon, C. H. Joyner, and W. Klemperer, J. Chem. Phys. **75**, 2041 (1981).

[18] M. Iida, Y. Ohshima, and Y. Endo, J. Phys. Chem. **97**, 357 (1993).

[19] A. D. Buckingham, C. Graham, and J. H. Williams, Mol. Phys. **49**, 703 (1983).

[20] W. L. Faust and M. N. McDermott, Phys. Rev. **123**, 198 (1961).

[21] W. Jäger, Y. Xu, and M. C. L. Gerry, J. Chem. Phys. **99**, 919 (1993).

[22] E. J. Campbell, L. W. Buxton, and A. C. Legon, J. Chem. Phys. **78**, 3483 (1983).

[23] C. Hampel, K. Peterson, and H.-J. Werner, Chem. Phys. Lett. **190**, 1 (1992).

[24] M. J. O. Deegan and P. J. Knowles, Chem. Phys. Lett. **227**, 321 (1994).

[25] MOLPRO, a package of ab initio programs designed by H.-J. Werner and P. J. Knowles, version 2002.6, R. D. Amos, A. Bernhardsson, A. Berning, P. Celani, D. L. Cooper, M. J. O. Deegan, A. J. Dobbyn, F. Eckert, C. Hampel, G. Hetzer, P. J. Knowles, T. Korona, R. Lindh, A. W. Lloyd, S. J. McNicholas, F. R. Manby, W. Meyer, M. E. Mura, A. Nicklass, P. Palmieri, R. Pitzer, G. Rauhut, M. Schütz, U. Schumann, H. Stoll, A. J. Stone, R. Tarroni, T. Thorsteinsson, and H.-J. Werner.

[26] S. Huzinaga and M. Klobukowski, Chem. Phys. Lett. **212**, 260 (1993).

[27] C. C. Lovallo and M. Klobukowski, private communication.

[28] K. A. Peterson, D. Figgen, E. Goll, H. Stoll, and M. Dolg, J. Chem. Phys. **119**, 11113 (2003).

[29] T. H. Dunning, Jr., J. Chem. Phys. **90**, 1007 (1989).

[30] T. B. Pederson, B. Fernández, H. Koch, and J. Makarewicz, J. Chem. Phys. **115**, 8431 (2001).

[31] S. F. Boys and F. Bernardi, Mol. Phys. **19**, 553 (1970).

[32] K. P. Huber and G. Herzberg, *Constants of Diatomic Molecules* (Van Nostrand Reinhold, New York, 1979).

[33] X. G. Song, Y. Xu, P.-N. Roy, and W. Jäger, J. Chem. Phys. **121**, 12308 (2004).

※※※※※※※※※※※※※※※※※※※※※※※※※※※※※

CHAPTER 4 Microwave and *ab initio* Studies of the Xe-CH_4 van der Waals Complex

※※※※※※※※※※※※※※※※※※※※※※※※※※※※※

4.1 Introduction

The Xe-CH_4 dimer is of interest for the study of Xe-molecule interactions because it can be consider as a building block for interactions between Xe and larger hydrocarbons. An empirical intermolecular potential of this complex has been constructed previously by Pirani *et al.*[1] at three basic configurations (see Figure 4-1, "edge": Xe atom sits on a C_2 axis of CH_4; "vertex": Xe atom sits on a C_3 axis and approaches a H atom; and "face": Xe atom sits on a C_3 axis and approaches a three H face center). The face configuration was determined to be the one with the lowest energy, similar to the cases of Kr-CH_4 and Ar-CH_4,[2,3] where it was found to be the equilibrium configuration. A more recent potential, which was constructed at the same configurations using molecular dynamics methods, has the same global features as the former but a slightly smaller intermolecular separation and a deeper well.[4]

More detailed insight into the structure and dynamics of the Xe-CH_4 complex can be obtained from high resolution spectra of the complex. Previous spectroscopic studies of CH_4-containing dimers, such as HX-CH_4 (X = CN,[5,6] Cl,[7,8] Br,[9] and F[7]), CO-CH_4,[10,11] Rg-CH_4 (Rg =Kr,[2,12,13] Ar,[2,12,13] and Ne[12]), H_2O-CH_4,[14,15] O_3-CH_4,[16] N_2O-CH_4,[17] *para*H_2-CH_4,[18] and OCS-CH_4[19] indicate that the methane monomer undergoes

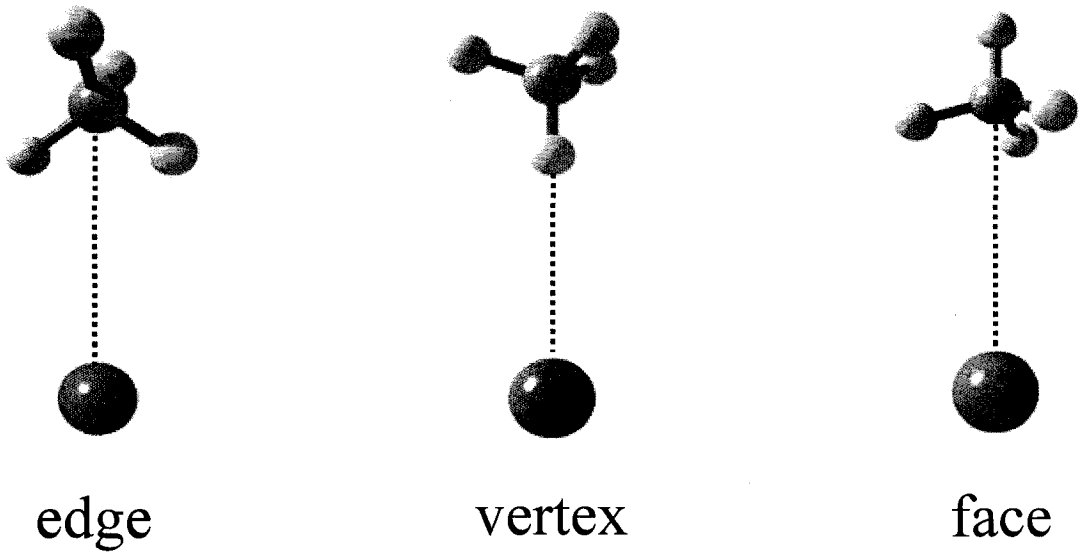

Figure 4-1: Three special configurations of the Xe-CH_4 complex.

large amplitude internal rotation motions within the complexes. The general features of the microwave spectra are governed by the angular anisotropy of the corresponding interaction potential. Figure 4-2 shows a schematic energy correlation diagram for a CH_4-containing complex as a function of methane internal rotation barrier.[6,8] Each internal rotor state is labeled by j, the total angular momentum quantum number of the CH_4 monomer, and K, the projection of angular momentum $\boldsymbol{j}$ onto the intermolecular axis. In the free rotor limit, the energy level pattern of the complex is identical to that of the free methane monomer and degenerate in the K quantum number. When the system approaches the rigid rotor limit, the pattern approaches that of an ordinary symmetric top. The molecular symmetry group for the CH_4-containing complexes is designated as $T_d(M)$, which is isomorphic to the point group of free methane, T_d. A molecular symmetry group[20] analysis predicts the occurrence of internal rotor states with A_1, E, and F_2 symmetries of the nuclear spin functions. In the following, the

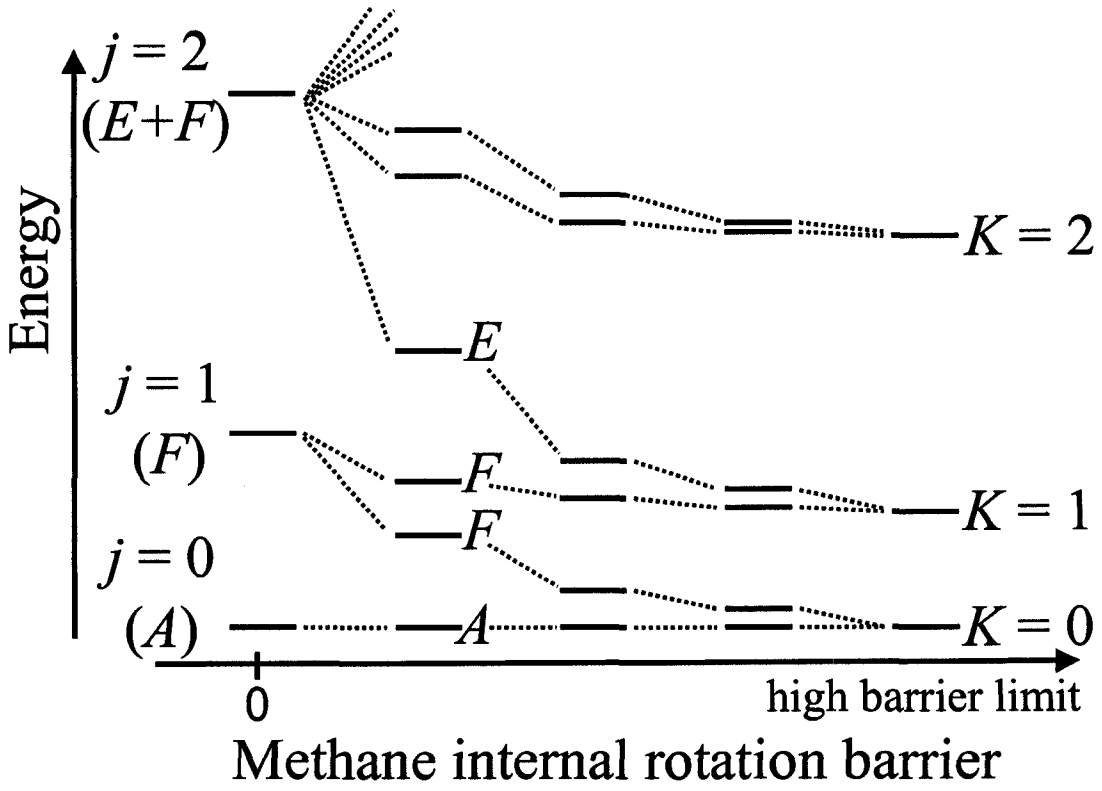

Figure 4-2: A schematic energy correlation diagram for a CH_4-containing complex as a function of the methane internal rotation barrier. The energy level pattern is identical to that of free methane at zero internal rotation barrier, and to that of a symmetric top at the high barrier limit (redrawn from Refs. 6 and 8).

subscript ('1'or '2') of symmetry species is omitted because the symmetry operations containing E^* in T_d (M) bring no additional distinction to the internal-rotation wavefunctions. Relaxation between states with different symmetries of nuclear spin wave function is a forbidden process in a molecular expansion. Only the lowest states, associated with the three different spin symmetries, are well populated at the low rotational temperature (1-2 K) of the molecular expansion. In most cases, the three lowest internal rotor states associated with three different spin symmetries respectively

could be observed in the microwave spectra. These are the $j = 0$, $K = 0$ state of A symmetry, the $j = 1$, $K = 0$ state of F symmetry, and the $j = 2$, $K = 1$ state of E symmetry. The $j = 1$, $K = 1$ state is well populated only when the gap between the $K = 0$ and $K = 1$ stacks of F symmetry is sufficiently small, which corresponds to a low angular anisotropy of the potential. In the case of CH_4-HCN,[5,6] it was possible to record spectra within this $j = 1$, $K = 1$ state. For CH_4-HF,[7] only transitions within one $K = 0$ stack were observed. This suggests that the CH_4 internal rotation is quenched by the higher anisotropy of the potential and the CH_4-HF complex is rather close to the semirigid rotor limit.[7]

In the following, I report both experimental and theoretical studies of the Xe-CH_4 complex. Microwave spectra of Xe-CH_4 within three internal rotor states were recorded, assigned, and analyzed. The spectroscopic results were used to derive structural and dynamical information about the complex. An *ab initio* potential energy surface for the Xe-CH_4 dimer was constructed, and the dipole moments were calculated at various configurations. The *ab initio* results can explain qualitatively some of the spectroscopic observations and provide further insight into the molecular structure and internal rotation motions of the methane unit within the complex.

4.2 *Ab initio* potential energy and dipole moment calculations

4.2.1 Computational details

Potential energy calculations were performed at the CCSD(T) level of theory[21,22] using the MOLPRO 2002.6 package of *ab initio* programs.[23] The aug-cc-pVQZ-PP basis set[24] was used for the Xe atom and the aug-cc-pVTZ basis set[25] for C

and H atoms. The basis sets were supplemented with (3s3p2d2f1g) midbond functions. The exponents are 0.94, 0.34, 0.12 for s and p functions, 0.64, 0.23 for d and f functions, and 0.35 for g functions.[26] The potential energies were calculated using the supermolecule approach. Full counterpoise correction[27] was applied to eliminate basis-set superposition error. The geometry of Xe-CH_4 is described by a set of spherical polar coordinates (R, θ, φ), as shown in Figure 4-3. The CH_4 monomer was frozen at the experimental equilibrium structure, with a C-H bond length of 1.0870 Å.[28] The potential energy surface was constructed as functions of R, θ, and φ. R was varied from 3.7 Å to 4.7 Å in steps of 0.1 Å, θ from 0° to 180° in steps of 15°, and φ from 0° to 90° in steps of 30°. Extra points were calculated at the edge (Xe atom sits on a C_2 axis of CH_4, $\theta = 0°$, $\varphi = 0°$), vertex (Xe atom sits on a C_3 axis and approaches a H atom, $\theta = 54.74°$, $\varphi = 0°$), and face (Xe atom sits on a C_3 axes and approaches a three H face center, $\theta = 125.26°$, $\varphi = 0°$) configurations (see Figure 4-1). The calculated interaction energies are given in Table 4-1.

Dipole moments for Xe-CH_4 were computed with the same basis sets and at the same level of theory as was used for the potential energy calculations. Calculations were performed at $\varphi = 0°$, and R and θ were varied from 3.7 Å to 4.7 Å in steps of 0.1 Å and from 0° to 180° in steps of 15°, respectively. Extra points were calculated at edge, vertex, and face configurations. The finite difference approximation[29] was used to calculate the dipole moment as the first derivative of the energy with respect to the applied electric field. At each configuration, I chose two finite electric fields with the same field strength and opposite directions. Two energy calculations were performed

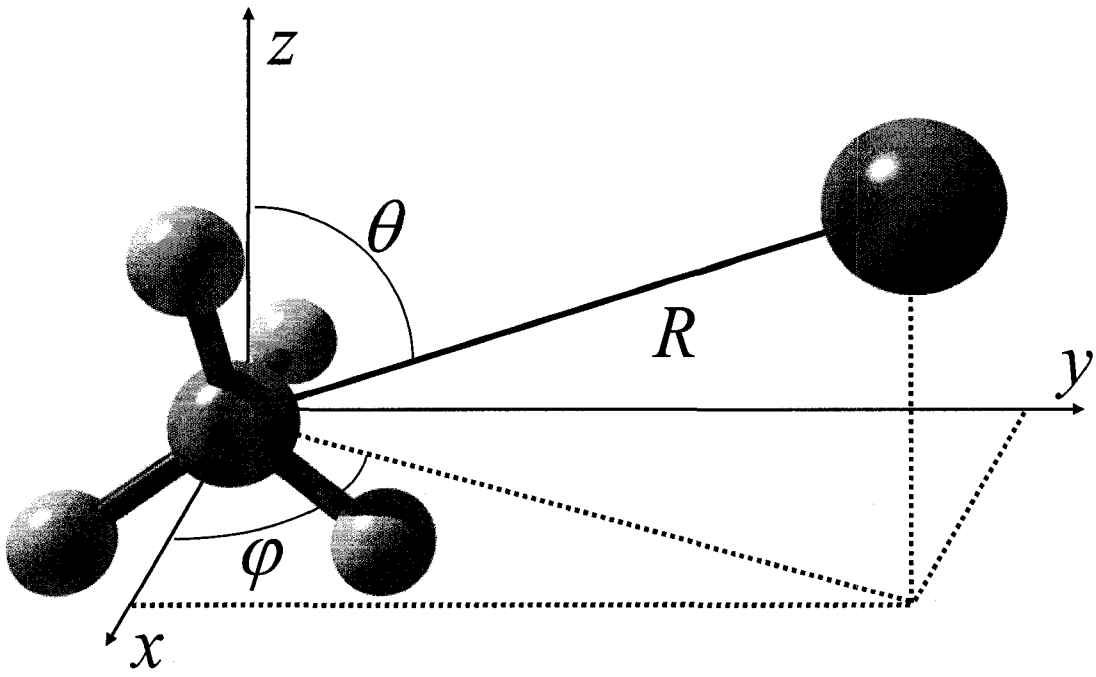

Figure 4-3: Molecule fixed axes frame for the Xe-CH_4 complex. The C atom is located at the origin, and a C_2 axis of methane is chosen as the z-axis. Two hydrogens with positive z values are in the xz-plane, and those with negative z values are in the yz-plane. The position of the Xe atom is described by spherical coordinates (R, θ, φ). R is the distance between Xe and C atoms, θ is the angle between the R vector and the z-axis, φ is the azimuthal angle. $\theta = 0°$, $\varphi = 0°$ corresponds to the edge configuration with the Xe atom sitting on a C_2 axis; $\theta = 54.74°$, $\varphi = 0°$ corresponds to the vertex configuration where the Xe atom sits on a C_3 axis and approaches a H atom; $\theta = 125.26°$, $\varphi = 0°$ corresponds to the face configuration where the Xe atom is on a C_3 axis and approaches the center of a three H face.

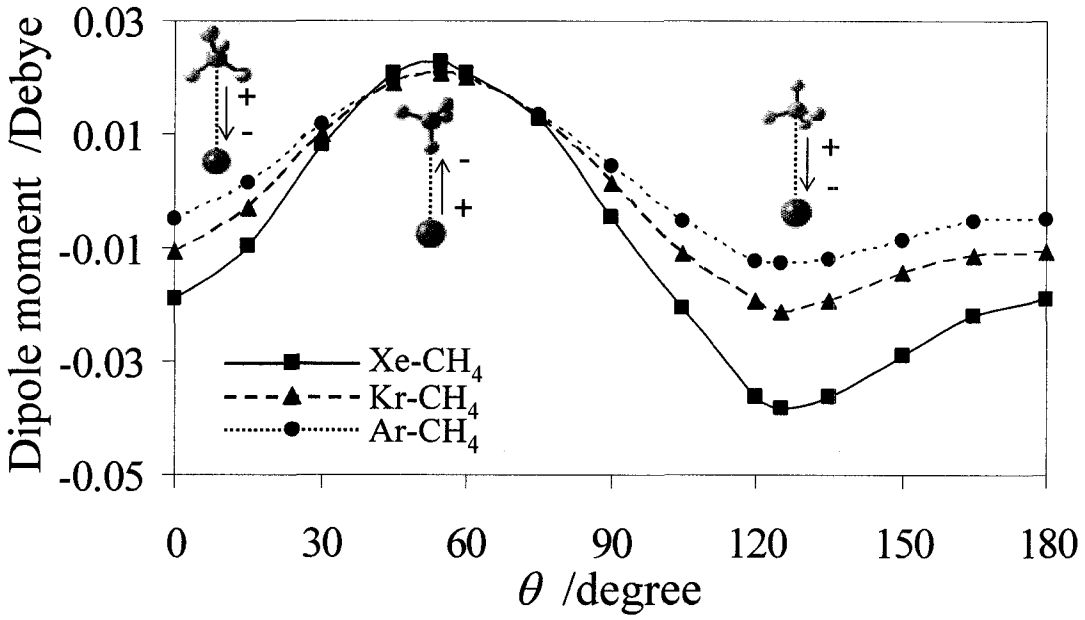

Figure 4-4: Angular dependence of the *ab initio* dipole moments of Ar-, Kr-, and Xe-CH_4. The solid line is for Xe-CH_4 from this work, the dashed and dotted lines are for Kr-CH_4 and Ar-CH_4, respectively (Ref. 2).

with these two electric fields applied to the system respectively. The dipole moment was then obtained as the ratio of the energy difference to the electric field difference. The obtained values are listed in Table 4-2. The angular dependence of the calculated dipole moment is plotted in Figure 4-4 and compared with those for Ar-, and Kr-CH_4.[2] At each angle θ, R was fixed at the value which gives the lowest interaction energy. A positive dipole moment points from the Xe atom to the C atom.

4.2.2 Discussion of the calculation results

The calculated 3-dimensional potential energy surface has a global minimum at the face configuration (R = 4.05 Å, θ = 125.26°, φ = 0°) with a well depth of 183.9

cm^{-1}. A first order saddle point is located at the edge configuration (R = 4.25 Å, θ = 0°, φ = 0°) and has energy of -151.8 cm^{-1}. A second order saddle point is at the vertex configuration (R = 4.55 Å, θ = 54.74°, φ = 0°, -121.2 cm^{-1}). The minimum energy path was constructed by varying R at each θ and φ configuration to locate the lowest energy. A contour plot of this minimum energy path is shown in Figure 4-5. To follow the minimum energy path, R changes from 4.05 Å at the global minimum to 4.55 Å at the second order saddle point. This significant variation is an indication of a strong coupling between the van der Waals stretching and bending motions of the complex. The overall topology of this potential is similar to those of the Ar-CH_4 and Kr-CH_4 potentials.[2] The energy barrier between the global minimum and the second order saddle point is 62.7 cm^{-1}, slightly larger than for Ar-CH_4 (50.5 cm^{-1}) and Kr-CH_4 (55.9 cm^{-1}).[2] The angular anisotropy of the interaction potential increases from Ar-, Kr- to Xe-CH_4, implying that the CH_4 internal rotation motion is more hindered by a larger, more polarizable rare gas electron cloud.

The angular dependence of the calculated dipole moment is shown in Figure 4-4. The dipole moment oscillates as θ changes from 0° to 180°. It reaches its positive maximum at the vertex (θ = 54.74°) configuration (second order saddle point) and the negative maximum at the face (θ = 125.26°) configuration (global minimum). Since CH_4 has no permanent dipole moment, the main contribution to the dipole moment of the complex comes from the distortion of electron densities of the Xe and CH_4 subunits. Compared with *ab initio* dipole moments of Ar-CH_4 and Kr-CH_4,[2] the oscillation amplitude of the Xe-CH_4 dipole moment is larger, because of the higher

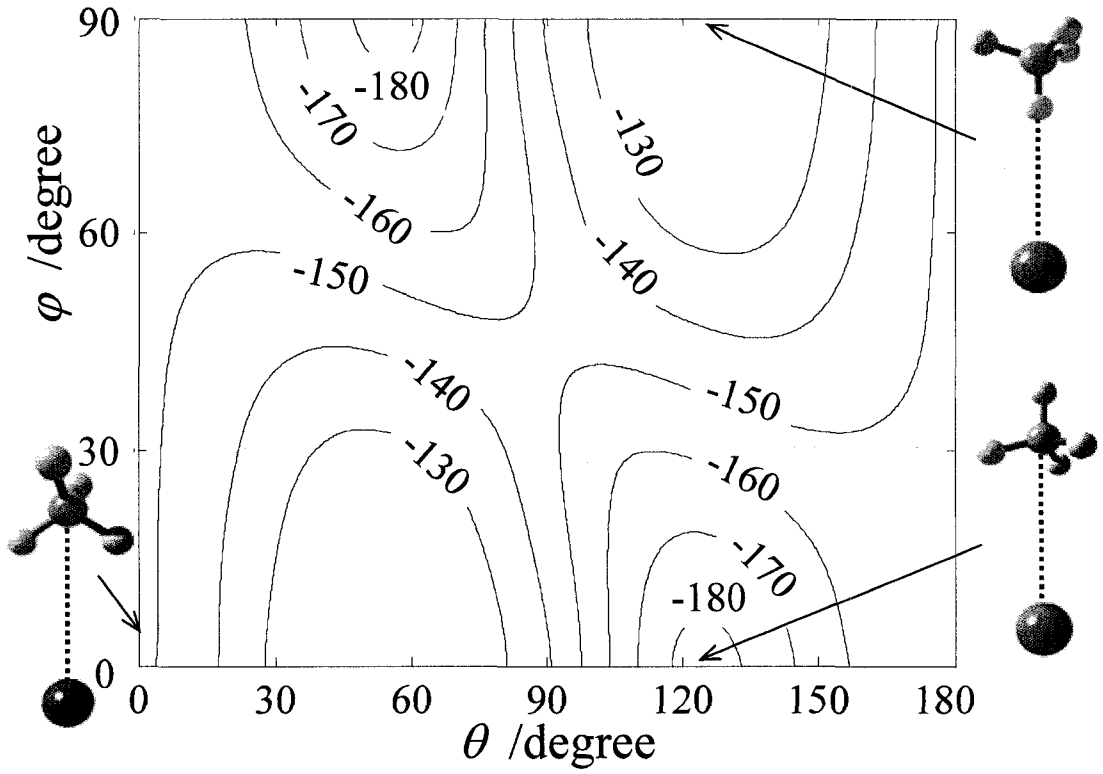

Figure 4-5: Contour diagram of the *ab initio* minimum energy path of Xe-CH_4 as function of θ and φ coordinates. R was varied at each θ and φ combination until the lowest energy was found. Potential energy values are given in cm^{-1}.

sensitivity of the Xe electron cloud polarization to the orientation of the CH_4 unit. In the dipole moment calculations, the CH_4 monomer was kept rigid, but one should keep in mind that contributions from the distortion of the CH_4 geometry may not be negligible because of the relatively large C-H bond dipole moment (0.339D).[30]

4.3 Spectral search, assignments, and analyses

The sample mixture consisted of 0.7% Xe and 1% CH_4 in Ne at a pressure of ~6 atm. Five isotopes of Xe were studied in their natural isotopic abundances (^{136}Xe:

8.87%, ^{134}Xe: 10.44%, ^{132}Xe: 26.89%, ^{131}Xe: 21.18%, ^{129}Xe: 26.44%). Isotopically enriched samples were used to investigate isotopomers containing $^{13}CH_4$, CD_4, CH_3D, and CHD_3 ($^{13}CH_4$, CH_3D, and CHD_3: 99% ^{13}C and 98% D, respectively, Cambridge Isotope Laboratories Inc; CD_4: 98% D, Merck Sharp & Dohme of Canada).

The rotational states of the Xe-CH_4 complex are labeled using the (*JjK*) scheme. Here, J is the total angular momentum quantum number of the complex. Similar to other CH_4-containing van der Waals complexes, the internal rotor states of Xe-CH_4 are associated with A, E, and F symmetries of the nuclear spin functions. The three lowest states, namely $j = 0$, $K = 0$ state of A symmetry, the $j = 1$, $K = 0$ state of F symmetry, and the $j = 2$, $K = 1$ state of E symmetry, are expected to be well populated at the low rotational temperature (1-2 K) of the molecular expansion. The population for each internal rotor state is proportional to the state density for the corresponding symmetry and the spin statistical weight (see Table 4-3). The state density ratio for the free CH_4 molecule is approximately $A:F:E = 1:3:1$.[8,31] Therefore, the relative populations for the $j = 0$, 1, and 2 internal rotor states are $A:F:E = 5:9:2$ for Xe-CH_4 and Xe-$^{13}CH_4$ and $A:F:E = 5:18:4$ for Xe-CD_4. As outlined below, the $j = 1$, $K = 0$ state is perturbed by a Coriolis interaction. This interaction couples the $j = 1$, $K = 0$ state to one component of the $j = 1$, $K = 1$ states and removes their degeneracy (see Figure 3 of Ref. 2). The degree of this perturbation depends on the energy gap between $K = 0$ and $K = 1$ stacks, i.e., it is determined by the angular anisotropy of the corresponding potential energy surface (see Figure 4-2). The Coriolis interaction is more pronounced as the angular anisotropy decreases.

4.3.1 Xe-CH_4

An effective separation between the Xe and C atoms of the Xe-CH_4 complex of 4.29 Å was estimated by comparison of the corresponding separations in Kr-CO_2 and Xe-CO_2 (Ref. 32) with that in Kr-CH_4 (Ref. 2) and extrapolation to Xe-CH_4. The J = 2-1, j = 0, K = 0 transition for the ^{132}Xe-CH_4 isotopomer was predicted at 7699 MHz. A transition at 7757.58 MHz was located and assigned to be the j = 2, K = 1 transition because a corresponding J = 1-0 transition could not be found. The j = 0, K = 0 transition was found at 7778.10 MHz, about 80 MHz away from the prediction. The K = 0 assignment was confirmed by finding the corresponding J = 1-0 transition at the approximately half the J = 2-1 transition frequency. The transitions of other isotopomers were located utilizing a pseudodiatomic model which considers CH_4 as a pseudoatom with mass 16 amu. Four transitions within the j = 0, K = 0 state, with J ranging from 0 to 4, and three transitions within the j = 2, K = 1 state, with J ranging from 1 to 4, were measured for the ^{136}Xe-CH_4, ^{134}Xe-CH_4, ^{132}Xe-CH_4, ^{131}Xe-CH_4, and ^{129}Xe-CH_4 isotopomers, respectively. Nuclear quadrupole hyperfine structures due to the presence of the ^{131}Xe (I = 3/2) nucleus were observed. The different hyperfine patterns for the K = 0 and K = 1 stacks confirmed the assignments (see Figure 4-6).

Compared with Kr-CH_4, the angular anisotropy of the Xe-CH_4 potential was expected to be larger because of the more polarizable Xe atom. As a result, the separations of Xe-CH_4 transitions for different internal rotor states were expected to be smaller. This was confirmed by the smaller J = 2-1 transition frequency difference of the j = 0, K = 0 and j = 2, K = 1 states for Xe-CH_4 (20.5211 MHz) compared to Kr-CH_4 (90.873 MHz).[2] The search for the J = 2-1, j = 1, K = 0 transition was based on

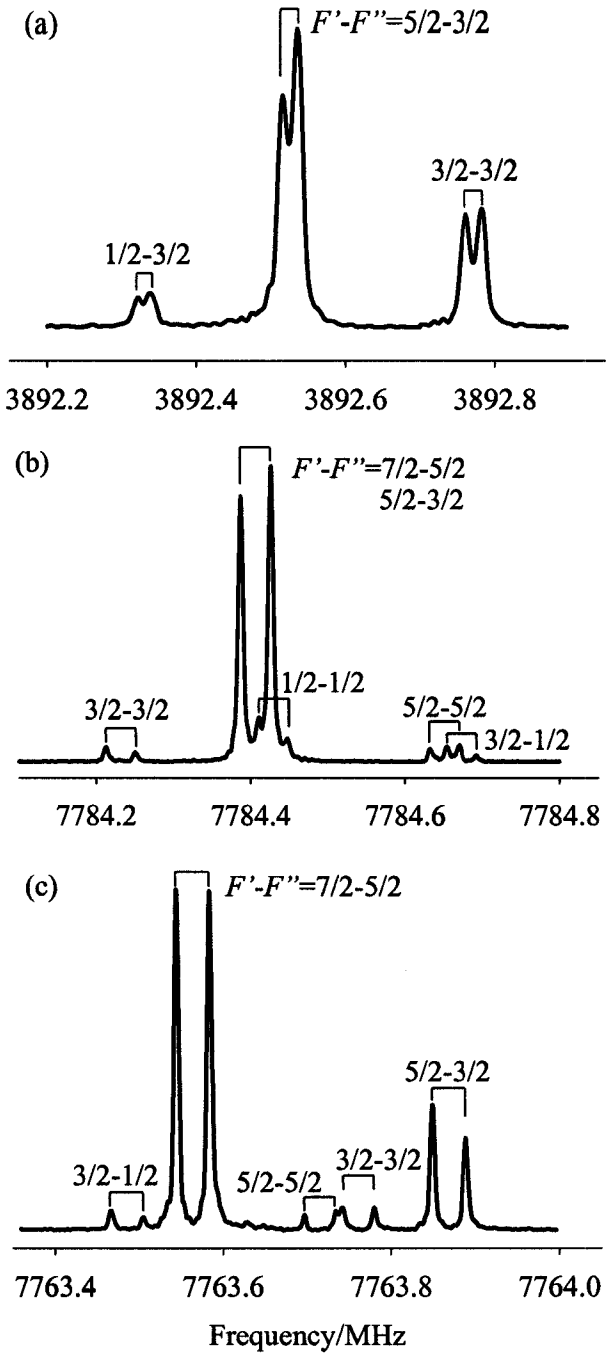

Figure 4-6: Composite spectra of the $J = 1\text{-}0$ (a), 2-1 (b) transitions in the $j = 0$, $K = 0$ state and the $J = 2\text{-}1$ transition in the $j = 2$, $K = 1$ state (c) of $^{131}Xe\text{-}CH_4$. Spectrum (a) was recorded using 3000 averaging cycles and spectra (b) and (c) using 800 averaging cycles.

this assumption, and it was found 535 MHz lower than the J = 2-1, j = 0, K = 0 transition. The corresponding difference in Kr-CH_4 is ~1 GHz.[2] The j = 1 transitions of other Xe isotopomers were located straightforwardly. The searches for other J transitions involved wide frequency range scanning because of the Coriolis interaction with the nearby K = 1 stack.

According to spin statistical weights and state densities, the relative populations of the j = 0, K = 0, the j = 1, K = 0, and the j = 2, K = 1 states should be 5, 9 and 2. This is roughly consistent with the observed intensity ratio of the j = 0, K = 0 and the corresponding j = 1, K = 0 transitions. However, the j = 2, K =1 transitions are relatively stronger than expected. The same behavior was previously reported for Kr-CH_4 (Ref. 2) and CO-CH_4 (Ref. 10). This increased intensity is possibly due to an increased effective dipole moment of the j = 2, K = 1 state, as suggested by Liu and Jäger (see discussions below).[2,10]

All measured transition frequencies are listed in Tables 4-4 and 4-5. Example spectra of the ^{131}Xe nuclear quadrupole hyperfine structure are shown in Figure 4-6. Pickett's SPFIT/SPCAT suite of programs[33] was used to fit spectroscopic parameters to the measured transition frequencies. The rotational constant B and centrifugal distortion constant D_J for each internal rotor state were determined individually using a pseudodiatomic model (see Table 4-4 and 4-5). As a result of the Coriolis interaction, the fitting procedure for the j = 1, K = 0 transitions gave a negative centrifugal distortion constant and a large standard deviation. The ^{131}Xe nuclear quadrupole coupling constants χ_{aa} of ^{131}Xe-CH_4 were also determined for all internal rotor states and are given in Table 4-5. For the j = 1, K = 0 state of ^{131}Xe-CH_4, the rotational and

distortion constants B and D_J and the ^{131}Xe nuclear quadrupole coupling constant χ_{aa} could not be determined in a single fitting procedure because of the irregular spectroscopic pattern. Instead, the ^{131}Xe nuclear quadrupole coupling constant χ_{aa} was determined using only the hyperfine components of the J = 2-1 transition and the center frequencies of the three J transitions were used to fit the rotational constant B and centrifugal distortion constant D_J.

4.3.2 Xe-$^{13}CH_4$ and Xe-CD_4

Using the spectroscopic constants of Xe-CH_4 as a guide, the analogous transitions of Xe-$^{13}CH_4$ and Xe-CD_4 were measured for the three internal rotor states. The j = 2, K = 1 transitions are relatively stronger than expected from the spin statistical weight and state densities, similar to the case of Xe-CH_4. For Xe-$^{13}CH_4$, the relative intensities of the j = 0, K = 0 and j = 1, K = 0 transitions are in good agreement with the expected ratio. However, the j = 1, K = 0 transitions of Xe-CD_4 are weaker than expected from the ratio of 54:15 for the j = 0, K = 0 and j = 1, K = 0 transitions. This can be rationalized by the observation of narrow splittings in the j = 1, K = 0 transitions (see Figure 4-7), which are possibly due to nuclear quadrupole interaction of the four spin I = 1 deuterium nuclei with the overall rotation of the complex. The frequency of the most intense component was recorded as the transition frequency. All measured transition frequencies are listed in Tables 4-6, 4-7, 4-8 and 4-9, along with the fitted spectroscopic constants. The same fitting procedure as for Xe-CH_4 was applied for Xe-$^{13}CH_4$ and Xe-CD_4.

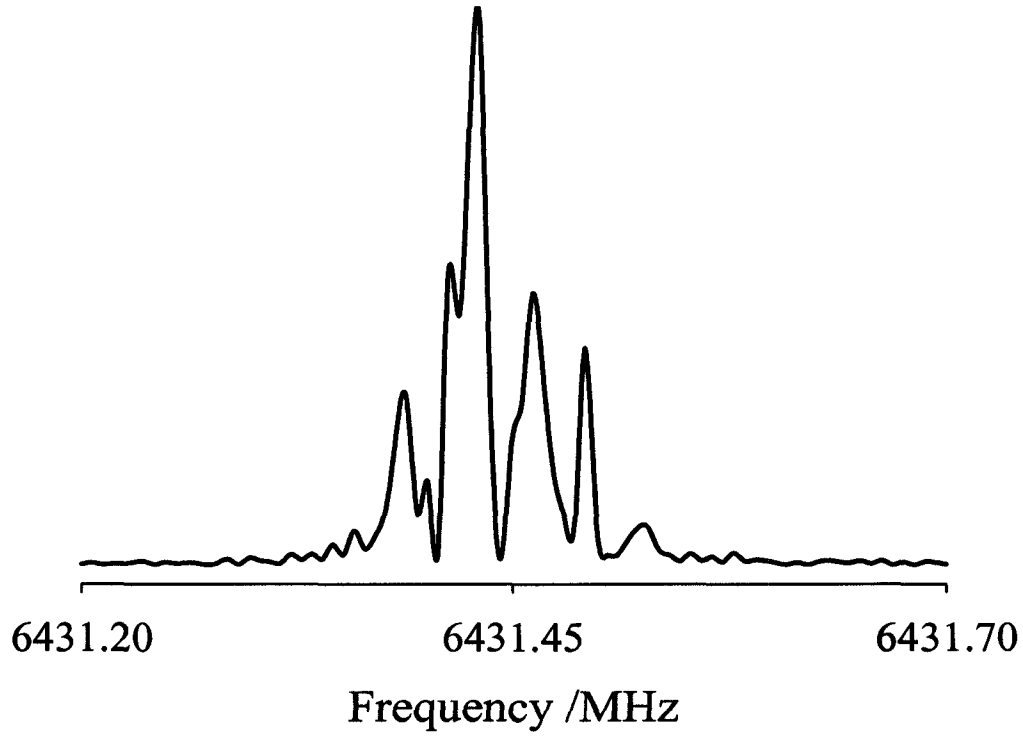

Figure 4-7: A spectrum of the $J = 2\text{-}1$ transition of ^{132}Xe-CD_4 in the $j = 0$, $K = 0$ state. 400 averaging cycles were used to record the spectrum. Seven of the visible components could be reproduced in different experiments.

4.3.3 Xe-CH_3D and Xe-CHD_3

The isotopomers containing Xe-CH_3D and Xe-CHD_3 have C_{3v}(M) symmetry (see Table 4-3) since the partial substitution reduces the symmetry of the methane monomer. Therefore, relaxation from the $j = 2$, $K = 1$ state to lower states is no longer a nuclear spin forbidden process, and only the $j = 0$, $K = 0$ state of A symmetry and the $j = 1$, $K = 0$ state of E symmetry are observable. These two states correlate to the $j_k = 0_0$ and 1_1 states, respectively, of free CH_3D and CHD_3 (the k subscript denotes the projection of j onto the C_3 axis of CH_3D and CHD_3 and is omitted below). The observed relative transition intensities are consistent with the ratio expected from spin

statistical weights and state densities, 4 and 4 for Xe-CH_3D and 11 and 16 for Xe-CHD_3. The measured transition frequencies and fitted spectroscopic constants are listed in Tables 4-10, 4-11 and 4-12. The nuclear quadrupole hyperfine structures of ^{131}Xe were recorded and the frequencies and assignments are given in Table 4-12. No deuterium hyperfine structure was resolved.

4.4 Discussion of the experimental results

4.4.1 Structural parameters and force constants

In a pseudodiatomic approximation, the van der Waals bond length R, the van der Waals stretching frequency ν_s, and the corresponding stretching force constant k_s can be calculated from the rotational and centrifugal distortion constants:[34]

$$B = h/8\pi^2\mu R^2$$

$$\nu_s = \left(\frac{4B^3}{D_J}\right)^{1/2}$$

$$k_s = 4\pi^2\nu_s^2\mu \qquad (4\text{-}1)$$

Here, μ is the pseudodiatomic reduced mass of the complex. The resulting values of R, ν_s, and k_s of the individual isotopomers are listed in Table 4-13 for the $j = 0$, $K = 0$ and $j = 2$, $K = 1$ states. Calculations were not done for the $j = 1$, $K = 0$ state because of the involved Coriolis interaction. The values for the $j = 0$, $K = 0$ state of ^{132}Xe-CH_4 are R = 4.264 Å, ν_s = 33.19 cm^{-1}, and k_s = 0.928 Nm^{-1}. Compared with the values of ^{84}Kr-CH_4 (R = 4.097 Å, ν_s = 32.31 cm^{-1}, and k_s = 0.828 N m^{-1}),[2] ^{132}Xe-CH_4 has a longer and more rigid van der Waals bond. For the $j = 2$, $K = 1$ state, there is a slightly longer van

der Waals bond (4.269 Å) and a smaller stretching force constant (0.866 N m^{-1}). The van der Waals bond length decreases upon substitution with a heavier isotope, consistent with a regular isotope effect. The force constant for the ^{132}Xe-CD_4 isotopomer (1.047 N m^{-1} for $j = 0$, $K = 0$ state) was found to be significantly larger than that of ^{132}Xe-CH_4 (0.928 N m^{-1} for $j = 0$, $K = 0$ state) while partially deuterated isotopomers, surprisingly, have smaller force constants than both, 0.734 Nm^{-1} ($j = 0$, $K = 0$ state) for ^{132}Xe-CH_3D and 0.832 N m^{-1} ($j = 0$, $K = 0$ state) for ^{132}Xe-CHD_3. Similar behavior has been found previously in Ar-NH_3 (Ref. 35), Kr-NH_3 (Ref. 36), Kr-CH_4 (Ref. 2), and CO-CH_4 (Ref. 10). It may be a result of an inadequacy of the pseudodiatomic approximation, which neglects the internal degrees of freedom of CH_4. For example, orientations where the deuterons are bounded to Xe will be slightly preferred, and may lead, in turn, to a higher anisotropy in the internal rotation coordinate.[35]

In an attempt to compare the spectroscopic and *ab initio* data, the computer program LEVEL7.5 (Ref. 37) was used to determine the bound states supported by the *ab initio* potential curves along selected radial coordinates using a pseudodiatomic model. The bound states supported by the *ab initio* potential curves of ^{132}Xe-CH_4 were determined for three different configurations (face, edge, vertex) separately, and then the corresponding parameters R, ν_s, and k_s were calculated. The obtained R, ν_s and k_s values are given in Table 4-14 together with the experimental values for the $j = 0$, $K = 0$ and $j = 2$, $K = 1$ states. By comparison, the theoretical values are on the same order of magnitude as the experimental values. Interestingly, there are relatively large discrepancies for R (+8%), ν_s (+27%), and k_s (+62%) values for the potential curve at

the face configuration, which corresponds to the *ab initio* equilibrium geometry. The best agreement for R is found at the edge configuration (+1%) and for ν_s and k_s at the vertex configuration (+3% and +5%, respectively). We take these variations of discrepancies among the states as further indication for rather delocalized wavefunctions and strong radial angular coupling.

4.4.2 Hyperfine structure and angular information

The observed ^{131}Xe nuclear quadrupole hyperfine structures contain dynamical information about the angular coordinate of the Xe-CH_4 complex. The presence of the CH_4 molecule distorts the spherically symmetric electron distribution of the free Xe atom in the complex. This leads to a non-zero field gradient at the Xe nucleus, and in turn to a nonzero ^{131}Xe nuclear quadrupole coupling constant χ_{aa}. Utilizing this quadrupole coupling constant χ_{aa}, an average orientation of the CH_4 subunit can be determined. The main contributions to the non-zero field gradient at the Xe nucleus are the dispersion interaction and the induction interaction between the nonzero electric multipole moments of CH_4 and the Xe electron cloud. Below, we use χ_{dis} and χ_{ind}, respectively, to represent the contributions to the quadrupole coupling constant from these two interactions. The dispersion interaction has been neglected in accounting for the nuclear quadrupole coupling constants in, for example, the Xe-HX (X = F and Cl) complexes,[38,39] but this is not acceptable if the electric moments of the monomer are small. For example, the observed quadruple coupling constant for ^{131}Xe-$^{15}N_2$ is 0.290 MHz, while the χ_{ind} value obtained using the electric multipole moments of N_2 is -0.538 MHz. The difference, 0.828 MHz, is attributed to χ_{dis}, and this value is in

accord with the χ_{aa} value for the Ar-Xe complex, 0.723 MHz,[40] which has no contribution from χ_{ind}. Assuming the same magnitude of contribution from χ_{dis} in ^{131}Xe-CH_4, we can obtain an estimate for the χ_{ind} value by subtracting 0.723 MHz from the observed quadrupole coupling constants. The resulting χ_{ind} values of the ^{131}Xe-CH_4 isotopomer are 0.256 MHz, 0.355 MHz, and 0.499 MHz, for the $j = 0$, $j = 1$, and $j = 2$ states, respectively. These values can, in turn, be interpreted in terms of the multipole moments of the methane monomer using the expressions:[38]

$$q_0 = -20\Omega\left\langle \frac{P_3(\cos(\theta - 54.74))}{R^6} \right\rangle - 30\Phi\left\langle \frac{P_4(\cos\theta)}{R^7} \right\rangle - \cdots$$

$$\chi_{ind} = -eq_0(1-\gamma)Q_{Xe}/h \qquad (4\text{-}2)$$

Here, q_0 is the electric field gradient tensor along the intermolecular a-axis generated by the multipole moments of the CH_4 monomer at the site of the Xe nucleus. Ω and Φ are the electric octopole and hexadecapole moments of CH_4, respectively. $\Omega = 2.22$ D Å^2 is along the direction with $\theta = 54.74°$, $\varphi = 0°$, and $\Phi = 4.8$ D Å^3 is along $\theta = 0°$, $\varphi = 0°$ (Refs. 41 and 42). θ and φ are defined in Figure 4-3. Higher order electric moments were neglected here. The brackets indicate averaging over the large amplitude motions. With the van der Waals bond length $R = 4.27$ Å, the ^{131}Xe nuclear quadrupole moment $Q_{Xe} = -0.12$ b,[43] and the Sternheimer shielding factor $\gamma = -152$ (Ref. 38), values for the average angle $\langle\theta\rangle$, were determined to be 106.6°/142.2°, 109.2°/140.0°, and 113.5°/136.2° for the $j = 0$, 1, and 2 states, respectively. The two sets of angles for each j state arise from the two solutions for $\langle\theta\rangle$ obtained using equation (4-2). Equation (4-2) was also used to determine χ_{ind} as a function of $\langle\theta\rangle$.

Extreme values for χ_{ind} of -1.141 MHz and 0.685 MHz were found to occur at angular orientations of $\theta = 176.5°$ and 125.26° respectively. The orientation with $\theta = 176.5°$ is close to the edge configuration and the $\theta = 125.26°$ orientation corresponds to the equilibrium geometry determined by the *ab initio* calculations. The χ_{ind} value of the $j = 2$, $K = 1$ state, 0.499 MHz, lies rather close to the value determined at the equilibrium geometry, which suggests that the $j = 2$ state may be more localized near the equilibrium structure compared to the other two states. Further support comes from the transition intensity enhancement in the $j = 2$ state (see discussion below).

4.4.3 Coriolis interaction in the $j = 1$ state

Large standard deviations of spectroscopic fits and negative values for the centrifugal distortion constant D_J were determined for the $j = 1$, $K = 0$ state, similar to the cases of Kr-CH_4 (Ref. 2) and CO-CH_4 (Ref. 10). This is a result of a Coriolis interaction between the $j = 1$, $K = 0$ state and one component of $j = 1$, $K = 1$ state. This interaction couples states of the same total parity and thus removes the degeneracy of the even and odd parity $K = 1$ states. As a result, the $K = 0$ stack is compressed and gives a smaller B rotational constant (see Figure 3 of Ref. 2). As the angular anisotropy of the intermolecular potential increases, the energy gap between the two interacting stacks also increases (see Figure 4-2), and the Coriolis effect is less pronounced. The frequency difference $\Delta = (\nu_{J=3-2}) - 1.5(\nu_{J=2-1})$ was used as a measure of the magnitude of this perturbation. The Δ value for ^{132}Xe-CH_4 is 23.3 MHz, much smaller than that for ^{84}Kr-CH_4 (94.4 MHz), indicating a less pronounced Coriolis interaction in the Xe-CH_4 complex. This is consistent with the larger angular anisotropy of the *ab*

initio Xe-CH_4 potential compared to that of Kr-CH_4.[2] The Δ values for other isotopomers, ^{132}Xe-$^{13}CH_4$, ^{132}Xe-CD_4, ^{132}Xe-CH_3D and ^{132}Xe-CHD_3, are 17.8, -0.6, 32.3, and -0.2 MHz, respectively. For heavier isotopomers, the perturbation is smaller, which is consistent with the smaller standard deviations from the corresponding fits. A similar trend was observed in Kr-CH_4 (Ref. 2) and CO-CH_4 (Ref. 10) before, and was attributed to the lower zero-point energy and a resulting slightly larger angular anisotropy for the heavier isotopomers.

4.4.4 Intensity enhancement of the $j = 2, K = 1$ transitions

Like for the Kr-CH_4 (Ref. 2) and CO-CH_4 (Ref. 10) complexes, a pronounced intensity enhancement of $j = 2, K = 1$ transitions, compared to the $j = 0, K = 0$ and $j = 1, K = 0$ transitions, was observed. Liu and Jäger[2,10] suggested that this may be the result of an increased effective dipole moment in this state. The *ab initio* calculations show that the dipole moment oscillates along the angular coordinate and reaches its maximum magnitude value at the global minimum ($\theta = 125.26°$). A wavefunction of the $j = 2, K = 1$ state that is more localized near the potential energy minimum was already proposed in the discussion of the nuclear quadrupole coupling constants and may also be responsible for the increased intensity of the corresponding transitions. The contour plots of the wavefunctions for Ar-CH_4 indicate that $j = 2$ state has a rather localized wavefunction at the global minimum, while those for $j = 0$ and 1 states are quite delocalized (see Figure 1 of Ref. 44). This may also be the case for Xe-CH_4, in particular since the Xe-CH_4 and Ar-CH_4 *ab initio* potentials have similar angular characteristics (see discussions about *ab initio* potential energy surface). Therefore, the

observation of significant intensity enhancement of the $j = 2$ transitions can be rationalized in terms of an increased effective dipole moment compared to the other two internal rotor states.

4.5 Summary

Rotational transitions within three internal rotor states, namely the $j = 0$, $K = 0$; $j = 1$, $K = 0$; and $j = 2$, $K = 1$ states, for the Xe-CH_4 complex were observed and assigned. Nuclear quadrupole hyperfine structures due to the presence of the ^{131}Xe nucleus were detected and analyzed. The observed spectra indicate large amplitude internal motions of the methane monomer within the complex. Compared with Kr-CH_4 (Ref. 2), this internal motion is slightly more hindered by the larger, more polarizable Xe atom. The $j = 1$, $K = 0$ state is perturbed by a Coriolis interaction with one component of the nearby $j = 1$, $K = 1$ states. This interaction is less pronounced compared to that found in Kr-CH_4 (Ref. 2). An *ab initio* potential energy surface of the Xe-CH_4 complex was constructed at the CCSD(T) level of theory and the global minimum was found at the face configuration. This potential has a greater angular anisotropy than those for Ar-CH_4 and Kr-CH_4 (Ref. 2). This is in agreement with the observation of more hindered internal motions of the methane monomer and a less pronounced Coriolis interaction. The observed intensity ratio of the $j = 0$, $K = 0$ and $j = 1$, $K = 0$ transitions agrees with the ratio expected from spin statistical weights and state densities. A pronounced intensity enhancement was observed for the $j = 2$, $K = 1$ transitions. This can possibly be attributed to an increased effective dipole moment in

this state as a result of a wavefunction that is more localized near the equilibrium geometry. The *ab initio* dipole moment calculations supported this statement.

Table 4-1: *Ab initio* interaction energies (in cm^{-1}) of Xe-CH_4.

R/Å	$\varphi = 0°$					
	$\theta = 0°$	15°	30°	45°	60°	75°
3.7	81.25	179.8	428.2	670.3	709.8	504.9
3.8	-22.16	46.92	221.1	391.1	418.8	275.1
3.9	-87.03	-39.33	81.08	198.8	218.0	118.5
4.0	-125.0	-92.28	-10.96	69.19	82.30	14.53
4.1	-144.4	-123.1	-68.99	-15.59	59.98	-52.02
4.2	-151.5	-137.9	-103.2	-68.74	-63.07	-92.22
4.3	-150.5	-142.3	-121.1	-99.87	-96.36	-114.3
4.4	-144.5	-140.0	-128.1	-115.9	-113.9	-124.1
4.5	-135.5	-133.5	-127.9	-121.8	-120.8	-125.9
4.6	-125.1	-124.7	-123.2	-121.2	-120.8	-122.5
4.7	-114.2	-114.8	-115.9	-116.4	-116.5	-116.0
	$\theta = 90°$	105°	120°	135°	150°	165°
3.7	211.6	-7.848	-100.9	-90.06	-21.93	50.66
3.8	69.55	-83.76	-148.6	-141.0	-93.81	-43.43
3.9	-23.38	-128.7	-173.0	-167.9	-135.8	-101.5
4.0	-81.53	-152.4	-182.0	-178.6	-157.3	-134.6
4.1	-115.5	-161.8	-180.9	-178.7	-165.2	-150.6
4.2	-132.7	-161.8	-173.5	-172.2	-164.1	-155.2
4.3	-138.9	-155.9	-162.5	-161.9	-157.4	-152.6
4.4	-137.7	-146.6	-149.8	-149.5	-147.6	-145.4
4.5	-132.1	-135.5	-136.4	-136.4	-136.1	-135.7
4.6	-123.9	-120.1	-123.2	-123.3	-124.1	-124.8
4.7	-114.3	-112.0	-110.5	-110.7	-112.2	-113.6

	Edge: $\theta = 0°$		Vertex: $\theta = 54.7°$		Face: $\theta = 125.26°$	
	$R = 4.15$	-149.2	$R = 4.3$	-94.84	$R = 3.8$	-152.7
	4.25	-151.8	4.35	-105.5	3.85	-166.6
			4.4	-113	3.9	-175.8
			4.45	-117.8	3.95	-181.4
			4.5	-120.4	4.0	-183.8
			4.55	-121.2	4.05	-183.9
			4.6	-120.7	4.1	-182
			4.65	-119	4.15	-178.7
			4.7	-116.6	4.2	-174.2
			4.75	-113.4	4.25	-168.9
			4.8	-109.8	4.3	-162.9

Table 4-1: (Continued).

R /Å			$\varphi = 30°$			
	$\theta = 0°$	15°	30°	45°	60°	75°
3.7		146.0	296.5	417.7	405.2	268.8
3.8		23.29	128.9	213.9	205.1	109.3
3.9		-55.6	17.39	76.22	70.03	3.747
4.0		-103.6	-54.12	-14.16	-18.42	-63.41
4.1		-130.3	-97.46	-71.0	-73.9	-103.8
4.2		-142.5	-121.4	-104.4	-106.3	-125.5
4.3		-145.0	-132.2	-121.7	-123.0	-134.8
4.4		-141.4	-134.2	-128.3	-129.1	-135.8
4.5		-134.1	-130.7	-127.9	-128.3	-131.6
4.6		-124.8	-123.9	-123.0	-123.2	-124.2
4.7		-114.5	-115.2	-115.6	-115.7	-115.3
	$\theta = 90°$	105°	120°	135°	150°	165°
3.7	113.3	24.06	13.65	44.42	72.67	81.47
3.8	0.359	-61.89	-68.9	-47.29	-27.72	-21.87
3.9	-71.39	-114.1	-118.7	-103.7	-90.45	-86.7
4.0	-114.3	-143.0	-145.8	-135.7	-126.9	-124.6
4.1	-137.3	-156.0	-157.6	-150.9	-145.3	-144.1
4.2	-146.9	-158.5	-159.3	-155.0	-151.7	-151.1
4.3	-147.6	-154.4	-154.6	-152.0	-150.2	-150.2
4.4	-142.8	-146.2	-146.1	-144.6	-143.9	-144.1
4.5	-134.7	-135.9	-135.5	-134.9	-134.8	-135.2
4.6	-124.8	-124.6	-124.1	-123.9	-124.3	-124.8
4.7	-114.2	-113.1	-112.5	-112.7	-113.3	-113.9

R /Å			$\varphi = 60°$			
	$\theta = 0°$	15°	30°	45°	60°	75°
3.7		81.47	72.67	44.42	13.65	24.06
3.8		-21.87	-27.72	-47.29	-68.89	-61.89
3.9		-86.7	-90.45	-103.7	-118.7	-114.1
4.0		-124.6	-126.9	-135.7	-145.8	-143.0
4.1		-144.1	-145.3	-150.9	-157.6	-155.9
4.2		-151.1	-151.7	-155.0	-159.3	-158.5
4.3		-150.2	-150.2	-152.0	-154.6	-154.4
4.4		-144.1	-143.9	-144.6	-146.1	-146.2
4.5		-135.2	-134.8	-134.9	-135.5	-135.9
4.6		-124.8	-124.3	-123.9	-124.1	-124.6
4.7		-113.9	-113.3	-112.7	-112.5	-113.1

Table 4-1: (Continued).

R /Å	$\varphi = 60°$					
	$\theta = 90°$	105°	120°	135°	150°	165°
3.7	113.3	268.8	405.2	417.7	296.5	146.0
3.8	0.364	109.3	205.1	213.9	128.9	23.29
3.9	-71.39	3.749	70.03	76.22	17.39	-55.6
4.0	-114.3	-63.41	-18.42	-14.16	-54.12	-103.6
4.1	-137.3	-103.8	-73.9	-71.0	-97.46	-130.3
4.2	-146.9	-125.5	-106.3	-104.4	-121.4	-142.5
4.3	-147.6	-134.8	-123.0	-121.7	-132.2	-145.0
4.4	-144.4	-135.8	-129.1	-128.4	-134.2	-141.4
4.5	-134.7	-131.6	-128.3	-127.9	-130.7	-134.1
4.6	-124.8	-124.2	-123.2	-123.0	-123.9	-124.8
4.7	-114.2	-115.3	-115.7	-115.6	-115.2	-114.5

R /Å	$\varphi = 90°$					
	$\theta = 0°$	15°	30°	45°	60°	75°
3.7		50.66	-21.93	-44.02	-100.9	-7.84
3.8		-43.43	-93.81	-141.0	-148.6	-83.76
3.9		-101.5	-135.9	-167.9	-173.0	-128.7
4.0		-134.6	-157.3	-178.6	-182.0	-152.4
4.1		-150.6	-165.2	-178.7	-180.9	-161.8
4.2		-155.3	-164.1	-172.2	-173.5	-161.8
4.3		-152.6	-157.4	-161.8	-162.5	-155.9
4.4		-145.4	-147.6	-149.5	-149.8	-146.6
4.5		-135.7	-136.1	-136.4	-136.4	-135.5
4.6		-124.8	-124.1	-123.3	-123.2	-123.7
4.7		-113.6	-112.2	-110.7	-110.5	-112.0
	$\theta = 90°$	105°	120°	135°	150°	165°
3.7	211.6	504.9	709.8	670.3	428.2	179.8
3.8	69.6	275.1	418.8	391.1	221.1	46.95
3.9	-23.34	118.5	218.0	198.9	81.08	-39.31
4.0	-81.53	14.53	82.30	69.19	-10.96	-92.64
4.1	-115.5	-51.99	-6.838	-15.59	-68.99	-123.1
4.2	-132.7	-92.22	-63.07	-68.74	-103.2	-137.9
4.3	-138.9	-114.3	-96.36	-99.87	-121.1	-142.3
4.4	-137.7	-124.1	-113.9	-115.9	-128.1	-140.0
4.5	-132.1	-125.8	-120.8	-121.8	-127.9	-133.5
4.6	-124.0	-122.4	-120.8	-121.2	-123.2	-124.7
4.7	-114.3	-116	-116.5	-116.4	-115.9	-114.8

Table 4-2: *Ab initio* dipole moment values (in Debye) of Xe-CH_4 ($\varphi = 0°$).

R /Å	$\varphi = 0°$					
	$\theta = 0°$	15°	30°	45°	60°	75°
3.7	-0.0703	-0.0515	-0.0022	0.0476	0.0558	0.016
3.8	-0.0558	-0.0401	0.00081	0.0421	0.0489	0.0158
3.9	-0.0441	-0.031	0.00317	0.0374	0.0431	0.0156
4.0	-0.0347	-0.0235	0.00495	0.0335	0.0382	0.0153
4.1	-0.0273	-0.0179	0.00625	0.0302	0.0341	0.0149
4.2	-0.0214	-0.013	0.00716	0.0274	0.0307	0.0144
4.3	-0.0168	-0.0098	0.00773	0.0249	0.0277	0.0139
4.4	-0.0131	-0.0071	0.00804	0.0227	0.0251	0.0133
4.5	-0.0103	-0.005	0.00813	0.0208	0.0228	0.0126
4.6	-0.008	-0.0034	0.00805	0.019	0.0208	0.0119
4.7	-0.0063	-0.0022	0.00785	0.0174	0.0189	0.0112
	$\theta = 90°$	105°	120°	135°	150°	165°
3.7	-0.0342	-0.0633	-0.0715	-0.0713	-0.0704	-0.0702
3.8	-0.026	-0.0506	-0.05779	-0.0576	-0.0564	-0.0559
3.9	-0.0194	-0.0405	-0.04679	-0.0465	-0.0452	-0.0444
4.0	-0.0142	-0.0323	-0.03799	-0.0377	-0.0363	-0.0351
4.1	-0.0275	-0.0252	-0.03098	-0.0307	-0.0291	-0.0278
4.2	-0.007	-0.0208	-0.02539	-0.0251	-0.0234	-0.022
4.3	-0.0046	-0.0167	-0.02095	-0.0216	-0.0189	-0.0174
4.4	-0.0027	-0.0135	-0.01742	-0.0171	-0.0154	-0.0138
4.5	-0.0014	-0.011	-0.01458	-0.0143	-0.0126	-0.0109
4.6	-0.0004	-0.009	-0.01232	-0.0121	-0.0104	-0.0087
4.7	0.0003	-0.0075	-0.01051	-0.0103	-0.0086	-0.007

Edge: $\theta = 0°$		Vertex: $\theta = 54.7°$		Face: $\theta = 125.26°$	
$R = 4.15$	-0.0242	$R = 4.3$	0.0289	$R = 3.8$	-0.0581
4.25	-0.0189	4.35	0.0274	3.85	-0.0523
		4.4	0.0261	3.9	-0.0471
		4.45	0.0249	3.95	-0.0424
		4.5	0.0237	4.0	-0.0382
		4.55	0.0226	4.05	-0.0345
		4.6	0.0215	4.1	-0.0312
		4.65	0.0205	4.15	-0.0282
		4.7	0.0196	4.2	-0.0256
		4.75	0.0187	4.25	-0.0232
		4.8	0.0178	4.3	-0.0211

Table 4-3: Symmetry labels of nuclear spin wavefunctions and nuclear spin statistical weights (in parentheses) of the three lowest internal rotor states of Xe-CH_4 isotopomors from symmetry group analyses (Ref. 2).

		$j = 0$	$j = 1$	$j = 2$
Xe-CH_4	T_d(M)	A (5)	F (3)	E (2)
Xe-$^{13}CH_4$	T_d(M)	A (5)	F (3)	E (2)
Xe-CD_4	T_d(M)	A (15)	F (18)	E (12)
Xe-CH_3D	C_{3v}(M)	A (4)	E (4)	
Xe-CHD_3	C_{3v}(M)	A (11)	E (16)	

Table 4-4: Measured transition frequencies and spectroscopic constants of Xe-CH_4 isotopomers.

J'-J''	^{136}Xe-CH_4		^{134}Xe-CH_4		^{132}Xe-CH_4		^{129}Xe-CH_4	
	ν_{obs} (MHz)	$\Delta\nu$[a] (kHz)	ν_{obs} (MHz)	$\Delta\nu$ (kHz)	ν_{obs} (MHz)	$\Delta\nu$ (kHz)	ν_{obs} (MHz)	$\Delta\nu$ (kHz)
				$j = 0, K = 0$				
1-0	3877.2053	0.3	3883.2194	2.5	3889.4078	0.2	3899.0479	0.4
2-1	7753.7012	-0.2	7765.7210	-1.7	7778.1016	-0.6	7797.3777	-0.5
3-2	11628.7808	0.0	11646.8066	0.2	11665.3713	0.6	11694.2755	0.2
4-3	15501.7346	0.0	15525.7570	0.1	15550.4999	-0.2	15589.0219	-0.1
B /MHz	1938.6615(2)		1941.6677		1944.7632(2)		1949.5834(2)	
D_J /kHz	29.522(9)		29.628(9)		29.710(9)		29.867(9)	
σ /kHz[b]	0.2		1.5		0.4		0.3	
				$j = 1, K = 0$				
2-1	7222.7156	-691.9	7232.6785	-699.0	7242.9340	-706.5	7258.8910	-719.6
3-2	10857.0325	790.7	10872.1540	798.8	10887.7225	807.5	10911.9493	822.4
4-3	14514.1858	-247.1	14534.6301	-249.6	14555.6824	-252.3	14588.4397	-257.0
B/MHz	1803.0344(3)		1805.5058(3)		1808.0496(3)		1812.0078(3)	
D_J/kHz	-352.18(1)		-354.82(1)		-357.57(1)		-361.85(1)	
σ/kHz	623.1		629.5		636.3		648.1	
				$j = 2, K = 1$				
2-1	7734.2072	0.03	7745.7226	0.1	7757.5805	-0.3	7776.0367	-0.8
3-2	11599.4284	-0.03	11616.6952	-0.1	11634.4772	0.4	11662.1545	0.9
4-3	15462.3909	0.01	15485.4021	0.04	15509.0995	-0.1	15545.9864	-0.3
B /MHz	1933.8028(3)		1936.6824(3)		1939.6478(3)		1944.2630(3)	
D_J /kHz	31.37(1)		31.47(1)		31.57(1)		31.71(1)	
σ /kHz	0.02		0.1		0.3		0.7	

[a] $\Delta\nu = \nu_{obs} - \nu_{cal}$.
[b] Standard deviation of the fit.

Table 4-5: Measured transition frequencies and spectroscopic constants of ^{131}Xe-CH_4.

		$j=0, K=0$		$j=1, K=0$			$j=2, K=1$	
J'-J''	F'-F''	ν_{obs} (MHz)	$\Delta\nu$[a] (kHz)	ν_{obs} (MHz)	$\Delta\nu$ (kHz)	F'-F''	ν_{obs} (MHz)	$\Delta\nu$ (kHz)
1-0	1.5-1.5	3892.7659	0.2					
	2.5-1.5	3892.5209	0.03					
	0.5-1.5	3892.3255	0.5					
2-1	1.5-0.5	7784.6694	-0.8	7248.4405	0.8	2.5-1.5	7763.8666	-0.2
	2.5-2.5	7784.6496	0.4	7248.4155	-1.1	1.5-1.5	7763.7583	0.6
	0.5-0.5	7784.4267	1.4			2.5-2.5	7763.7131	-0.9
	2.5-1.5	7784.4040	-0.4	7248.1471	-0.0	3.5-2.5	7763.5609	-0.3
	3.5-2.5	7784.4040	-0.4	7248.1471	-0.0	1.5-0.5	7763.4830	0.3
	1.5-1.5	7784.2286	-0.9	7247.9555	0.8			
	0.5-1.5			7247.6847	-0.5			
3-2	2.5-1.5	11674.9006	-0.6	10895.7268		3.5-2.5	11643.6006	0.7
	1.5-0.5	11674.9006	-0.6	10895.7268		4.5-3.5	11643.5240	0.5
	3.5-2.5	11674.8409	0.3	10895.6581				
	4.5-3.5	11674.8409	0.3	10895.6581				
4-3	3.5-2.5	15563.1575	0.4	14566.4514		3.5-2.5	15521.2307	1.5
	2.5-1.5	15563.1575	0.4	14566.4514		4.5-3.5	15521.2125	-0.8
	4.5-3.5	15563.1285	-0.2	14566.4199		5.5-4.5	15521.1816	-1.2
	5.5-4.5	15563.1285	-0.2	14566.4199				
B /MHz		1946.3444(1)		1809.3487(3)			1941.1618(1)	
D_J /kHz		29.763(5)		-358.96(1)			31.615(2)	
χ_{aa} /MHz		0.979(2)		1.0779(2)			1.222(2)	
σ /kHz[b]		0.6					0.8	

[a] $\Delta\nu = \nu_{obs} - \nu_{cal}$.

[b] Standard deviation of the fit.

Table 4-6: Measured transition frequencies and spectroscopic constants of Xe-$^{13}CH_4$ isotopomers.

	^{136}Xe-$^{13}CH_4$		^{134}Xe-$^{13}CH_4$		^{132}Xe-$^{13}CH_4$		^{129}Xe-$^{13}CH_4$	
J'-J''	ν_{obs} (MHz)	$\Delta\nu$[a] (kHz)	ν_{obs} (MHz)	$\Delta\nu$ (kHz)	ν_{obs} (MHz)	$\Delta\nu$ (kHz)	ν_{obs} (MHz)	$\Delta\nu$ (kHz)
				$j = 0, K = 0$				
2-1	7351.7578	-0.2	7363.7962	-0.4	7376.1948	0.02	7395.4978	-0.2
3-2	11026.0455	0.2	11044.0979	0.5	11062.6904	-0.03	11091.6365	0.3
4-3	14698.4226	-0.06	14722.4812	-0.1	14747.2640	0.01	14785.8414	-0.08
B /MHz	1838.1517(3)		1841.1621(3)		1844.2623(3)		1849.0893(3)	
D_J /kHz	26.53(1)		26.62(1)		26.70(1)		26.85(1)	
σ /kHz[b]	0.2		0.4		0.02		0.2	
				$j = 1, K = 0$				
2-1	6887.2243	-476.0	6897.3439	-481.9	6907.7625	-487.6	6923.9744	-497.1
3-2	10348.3807	544.0	10363.7070	550.7	10379.4874	557.2	10404.0438	568.2
4-3	13827.3469	-170.0	13848.0158	-172.1	13869.3023	-174.1	13902.4242	-177.6
B /MHz	1719.7535(3)		1722.2674(3)		1724.8552(3)		1728.8821(3)	
D_J /kHz	-271.44(1)		-273.63(1)		-275.92(1)		-279.47(1)	
σ /kHz	428.7		434.0		439.1		447.8	
				$j = 2, K = 1$				
2-1	7348.3479	-0.1	7359.9323	0.8	7371.8595	-0.4	7390. 4279	-0.3
3-2	11020.8244	0.1	11038.1930	-0.9	11056.0809	0.5	11083.9244	0.4
4-3	14691.2631	-0.05	14714.4125	0.3	14738.2495	-0.2	14775.3579	-0.1
B /MHz	1837.3134(3)		1840.2100(3)		1843.1929(3)		1847.8362(3)	
D_J /kHz	28.30(1)		28.39(1)		28.49(1)		28.64(1)	
σ /kHz	0.1		0.7		0.4		0.3	

[a] $\Delta\nu = \nu_{obs} - \nu_{cal}$.
[b] Standard deviation of the fit.

Table 4-7: Measured transition frequencies and spectroscopic constants of Xe-CD_4 isotopomers.

	^{136}Xe-CD_4		^{134}Xe-CD_4		^{132}Xe-CD_4		^{129}Xe-CD_4	
J'-J''	ν_{obs} (MHz)	$\Delta\nu$[a] (kHz)	ν_{obs} (MHz)	$\Delta\nu$ (kHz)	ν_{obs} (MHz)	$\Delta\nu$ (kHz)	ν_{obs} (MHz)	$\Delta\nu$ (kHz)
				$j = 0, K = 0$				
2-1	6519.5096	0.05	6531.7481	-1.1	6544.3554	0.1	6563.9808	-0.02
3-2	9778.1261	-0.06	9796.4827	1.3	9815.3861	-0.1	9844.8179	0.02
4-3	13035.3770	0.02	13059.8423	-0.4	13085.0411	0.04	13124.2709	-0.01
B /MHz	1630.0291(3)		1633.0896(3)		1636.2417(3)		1641.1490(3)	
D_J /kHz	18.97(1)		19.04(1)		19.11		19.22(1)	
σ /kHz[b]	0.05		1.0		0.09		0.02	
				$j = 1, K = 0$				
2-1	6407.8477	-5.0	6419.4708	-5.2	6431.4394	-4.9	6450.0685	-5.2
3-2	9611.1441	5.7	9628.5809	6.0	9646.5364	5.6	9674.4848	6.0
4-3	12813.6534	-1.8	12836.9050	-1.9	12860.8526	-1.8	12898.1240	-1.9
B /MHz	1602.0486(3)		1604.9542(3)		1607.9458(3)		1612.6027(3)	
D_J /kHz	10.68		10.65(1)		10.60(1)		10.53(1)	
σ /kHz	4.5		4.7		4.4		4.7	
				$j = 2, K = 1$				
2-1	6463.5189	-0.9	6475.3180	-0.2	6487.4664	-0.3	6506.3766	-0.1
3-2	9694.0824	1.1	9711.7738	0.2	9729.9925	0.4	9758.3510	0.2
4-3	12923.2044	-0.3	12946.7846	0.06	12971.0680	-0.1	13008.8678	-0.05
B /MHz	1616.0397(3)		1618.9900(3)		1622.0277(3)		1626.7561(3)	
D_J /kHz	19.97(1)		20.06(1)		20.13(1)		20.24(1)	
σ /kHz	0.8		0.2		0.3		0.1	

[a] $\Delta\nu = \nu_{obs} - \nu_{cal}$.
[b] Standard deviation of the fit.

Table 4-8: Measured transition frequencies and spectroscopic constants of ^{131}Xe-$^{13}CH_4$.

		$j=0, K=0$		$j=1, K=0$			$j=2, K=1$	
J'-J''	F'-F''	ν_{obs} (MHz)	$\Delta\nu$[a] (kHz)	ν_{obs} (MHz)	$\Delta\nu$ (kHz)	F'-F''	ν_{obs} (MHz)	$\Delta\nu$ (kHz)
2-1	1.5-0.5	7382.7708	-2.4	6913.3503	-1.4	2.5-1.5	7378.1825	0.2
	2.5-2.5	7382.7526	0.5	6913.3322	3.7	1.5-1.5	7378.0739	1.3
	0.5-0.5			6913.0763	-4.7	2.5-2.5	7378.0234	-5.3
	2.5-1.5	7382.5059	-0.1	6913.0594	1.7	3.5-2.5	7377.8763	1.2
	3.5-2.5	7382.5059	-0.1	6913.0594	1.7	1.5-0.5	7377.7972	1.0
	1.5-1.5	7382.3295	-0.8	6912.8639	-0.4	0.5-0.5	7377.6418	-0.8
	0.5-1.5	7382.0841	-0.2	6912.5947	1.2			
3-2	2.5-1.5	11072.2393	4.0	10387.6001		3.5-2.5	11065.2598	2.5
	1.5-0.5	11072.2393	4.0	10387.6001		4.5-3.5	11065.1807	0.2
	3.5-2.5	11072.1739	-0.5	10387.5298				
	4.5-3.5	11072.1739	-0.5	10387.5298				
4-3	3.5-2.5	14759.9410	0.2	13880.1948		3.5-2.5	14750.4543	2.2
	2.5-1.5	14759.9410	0.2	13880.1948		4.5-3.5	14750.4361	-0.04
	4.5-3.5	14759.9110	-1.3	13880.1596		5.5-4.5	14750.4024	-3.0
	5.5-4.5	14759.9110	-1.3	13880.1596				
B /MHz		1845.8457(1)		1726.1763(3)			1844.7156(1)	
D_J /kHz		26.742(6)		-277.09(1)			28.520(5)	
χ_{aa} /MHz		0.984(2)		1.0832(2)			1.229(3)	
σ /kHz[b]		1.6					2.2	

[a] $\Delta\nu = \nu_{obs} - \nu_{cal}$.
[b] Standard deviation of the fit.

Table 4-9: Measured transition frequencies and spectroscopic constants of ^{131}Xe-CD_4.

		$j = 0, K = 0$		$j = 1, K = 0$			$j = 2, K = 1$	
J'-J''	F'-F''	ν_{obs} (MHz)	$\Delta\nu$[a] (kHz)	ν_{obs} (MHz)	$\Delta\nu$ (kHz)	F'-F''	ν_{obs} (MHz)	$\Delta\nu$ (kHz)
2-1	1.5-0.5	6551.0925	-1.1	6437.8808	-0.5	2.5-1.5	6493.9200	0.1
	2.5-2.5	6551.0695	1.3			1.5-1.5	6493.8010	-1.4
	2.5-1.5	6550.7678	-0.2	6437.5239	2.7	2.5-2.5	6493.7565	1.2
	3.5-2.5	6550.7678	-0.2	6437.5239	2.7	3.5-2.5	6493.5896	-1.2
	1.5-1.5	6550.5503	-0.4	6437.2828	-1.6	1.5-0.5	6493.5054	-0.7
3-2	2.5-1.5	9825.0993	-0.6	9655.7702				
	1.5-0.5	9825.0993	-0.6	9655.7702		3.5-2.5	9739.3422	0.5
	3.5-2.5	9825.0260	0.9	9655.6908		4.5-3.5	9739.2613	1.9
	4.5-3.5	9825.0260	0.9	9655.6908				
4-3	3.5-2.5	13097.9303	-2.7	12873.1006				
	2.5-1.5	13097.9303	-2.7	12873.1006		3.5-2.5	12983.4952	-0.5
	4.5-3.5	13097.9017	2.6	12873.0703		4.5-3.5	12983.4756	-3.0
	5.5-4.5	13097.9017	2.6	12873.0703		5.5-4.5	12983.4483	2.7
B /MHz		1637.8512(2)		1609.4738(3)			1623.5792(1)	
D_J /kHz		19.146(6)		10.59(1)			20.189(5)	
χ_{aa} /MHz		1.208(2)		1.328(3)			1.317(4)	
σ /kHz[b]		1.5					1.6	

[a] $\Delta\nu = \nu_{obs} - \nu_{cal}$.
[b] Standard deviation of the fit.

Table 4-10: Measured transition frequencies and spectroscopic constants of Xe-CH_3D.

J'-J''	ν_{obs} (MHz)	$\Delta\nu$[a] (kHz)	ν_{obs} (MHz)	$\Delta\nu$ (kHz)	ν_{obs} (MHz)	$\Delta\nu$ (kHz)	ν_{obs} (MHz)	$\Delta\nu$ (kHz)
				$j = 0, K = 0$				
	^{136}Xe-CH_3D		^{134}Xe-CH_3D		^{132}Xe-CH_3D		^{129}Xe-CH_3D	
2-1	7390.6081	-0.9	7402.6939	-0.5	7415.1409	-1.2	7434.5180	-1.0
3-2	11083.8693	1.1	11101.9888	0.6	11120.6542	1.4	11149.7094	1.1
4-3	14774.6723	-0.4	14798.8197	-0.2	14823.6909	-0.4	14862.4129	-0.4
B /MHz	1847.9250(3)		1850.9473(3)		1854.0602(3)		1858.9058(3)	
D_J /kHz	34.09(1)		34.21(1)		34.34(1)		34.50(1)	
σ /kHz[b]	0.90		0.48		1.06		0.90	
				$j = 1, K = 0$				
	^{136}Xe-CH_3D		^{134}Xe-CH_3D		^{132}Xe-CH_3D		^{129}Xe-CH_3D	
2-1	6881.4896	-1285	6891.3825	-1299	6901.5655	-1315	6917.4092	-1338
3-2	10353.9581	1469	10369.0580	1485	10384.6060	1502	10408.7978	1529
4-3	13855.7377	-459	13876.2612	-464	13897.3978	-470	13930.2879	-478
B /MHz	1716.9167(3)		1719.3637(3)		1721.8822(3)		1725.8006(3)	
D_J /kHz	-472.12(1)		-475.84(1)		-479.72(1)		-485.79(1)	
σ /kHz	1157.5		1170.2		1184.0		1205.3	

[a] $\Delta\nu = \nu_{obs} - \nu_{cal}$.
[b] Standard deviation of the fit.

Table 4-11: Measured transition frequencies and spectroscopic constants of Xe-CHD_3.

J'-J''	ν_{obs} (MHz)	$\Delta\nu$ [a] (kHz)	ν_{obs} (MHz)	$\Delta\nu$ (kHz)	ν_{obs} (MHz)	$\Delta\nu$ (kHz)	ν_{obs} (MHz)	$\Delta\nu$ (kHz)
			$j = 0, K = 0$					
	^{136}Xe-CHD_3		^{134}Xe- CHD_3		^{132}Xe- CHD_3		^{129}Xe- CHD_3	
2-1	6780.0444	-0.08	6792.2394	0.0	6804.7992	-0.04	6824.3496	-0.18
3-2	10168.5279	0.09	10186.8140	-0.0	10205.6477	0.05	10234.9661	0.21
4-3	13555.1643	-0.03	13579.5345	0.0	13604.6346	-0.01	13643.7114	-0.06
B /MHz	1695.2163(3)		1698.2659(3)		1701.4066(3)		1706.2953(3)	
D_J /kHz	25.65(1)		25.75(1)		25.85(1)		25.98(1)	
σ /kHz [b]	0.07		0.003		0.13		0.16	
			$j = 1, K = 0$					
	^{136}Xe-CHD_3		^{134}Xe- CHD_3		^{132}Xe- CHD_3		^{129}Xe- CHD_3	
2-1	6620.7508	-9.5	6632.2199	-9.5	6644.0314	-9.8	6662.4163	-9.4
3-2	9930.9274	10.8	9948.1363	10.8	9965.8595	11.2	9993.4446	10.8
4-3	13240.8010	-3.4	13263.7560	-3.4	13287.3960	-3.5	13324.1928	-3.4
B /MHz	1655.2199(3)		1658.0865(3)		1661.0387(3)		1665.6337(3)	
D_J /kHz	3.73(1)		3.64(1)		3.55(1)		3.41(1)	
σ /kHz	8.5		8.5		8.8		8.5	

[a] $\Delta\nu = \nu_{obs} - \nu_{cal}$.
[b] Standard deviation of the fit.

Table 4-12: Measured transition frequencies and spectroscopic constants of ^{131}Xe-CH_3D and ^{131}Xe-CHD_3.

		$j=0, K=0$		$j=1, K=0$	
J'-J''	F'-F''	ν_{obs} (MHz)	$\Delta\nu$(kHz) [a]	ν_{obs} (MHz)	$\Delta\nu$(kHz)
			^{131}Xe-CH_3D		
2-1	1.5-0.5	7421.7559	-2.4	6907.0408	-2.0
	2.5-2.5	7421.7369	0.9	6907.0211	2.2
	2.5-1.5	7421.4742	-1.0	6906.7396	-0.4
	3.5-2.5	7421.4742	-1.0	6906.7396	-0.4
	1.5-1.5	7421.2886	-0.4	6906.5410	0.2
3-2	2.5-1.5	11130.2387	3.0	10392.6070	
	1.5-0.5	11130.2387	3.0	10392.6070	
	3.5-2.5	11130.1709	-0.2	10392.5295	
	4.5-3.5	11130.1709	-0.2	10392.5295	
4-3	3.5-2.5	14836.4181	1.6	13908.2128	
	2.5-1.5	14836.4181	1.6	13908.2128	
	4.5-3.5	14836.3839	-2.3	13908.1779	
	5.5-4.5	14836.3839	-2.3	13908.1779	
B /MHz		1855.6494(1)		1723.1685(3)	
D_J /kHz		34.380(4)		-481.69(1)	
χ_{aa} /MHz		1.0431(3)		1.115(3)	
σ /kHz [b]		1.8			
			^{131}Xe-CHD_3		
2-1	1.5-0.5	6811.5002	-0.2	6650.3778	-0.9
	2.5-2.5	6811.4759	0.2		
	2.5-1.5	6811.1865	-1.1	6650.0347	2.4
	3.5-2.5	6811.1865	-1.1	6650.0347	2.4
	1.5-1.5	6810.9823	0.5	6649.8030	-1.4
3-2	2.5-1.5	10215.3244	2.1	9974.9664	
	1.5-0.5	10215.3244	2.1	9974.9664	
	3.5-2.5	10215.2497	-1.3	9974.8973	
	4.5-3.5	10215.2497	-1.3	9974.8973	
4-3	3.5-2.5	13617.4765	-0.8	13299.4848	
	2.5-1.5	13617.4765	-0.8	13299.4848	
	4.5-3.5	13617.4445	0.6	13299.4575	
	5.5-4.5	13617.4445	0.6	13299.4575	
B /MHz		1703.0102(2)		1662.5481(3)	
D_J /kHz		25.896(6)		3.51(1)	
χ_{aa} /MHz		1.153(3)		1.276(3)	
σ /kHz		1.0			

[a] $\Delta\nu = \nu_{obs} - \nu_{cal}$.

[b] Standard deviation of the fit.

Table 4-13: Van der Waals bond lengths, stretching frequencies, and force constants of Xe-CH_4 isotopomers.

	$j = 0, K = 0$ state				
	^{136}Xe-CH_4	^{134}Xe-CH_4	^{132}Xe-CH_4	^{131}Xe-CH_4	^{129}Xe-CH_4
R (Å)	4.264	4.264	4.264	4.264	4.264
ν_s (cm^{-1})	33.14	33.16	33.19	33.20	33.23
k_s (N m^{-1})	0.928	0.928	0.928	0.928	0.928
	^{136}Xe-$^{13}CH_4$	^{134}Xe-$^{13}CH_4$	^{132}Xe-$^{13}CH_4$	^{131}Xe-$^{13}CH_4$	^{129}Xe-$^{13}CH_4$
R (Å)	4.262	4.262	4.262	4.262	4.262
ν_s (cm^{-1})	32.28	32.30	32.34	32.35	32.37
k_s (N m^{-1})	0.929	0.929	0.929	0.930	0.929
	^{136}Xe-CD_4	^{134}Xe-CD_4	^{132}Xe-CD_4	^{131}Xe-CD_4	^{129}Xe-CD_4
R (Å)	4.212	4.212	4.212	4.212	4.212
ν_s (cm^{-1})	31.88	31.91	31.94	31.96	31.99
k_s (N m^{-1})	1.046	1.046	1.047	1.047	1.047
	^{136}Xe-CH_3D	^{134}Xe-CH_3D	^{132}Xe-CH_3D	^{131}Xe-CH_3D	^{129}Xe-CH_3D
R (Å)	4.250	4.250	4.250	4.250	4.250
ν_s (cm^{-1})	28.70	28.72	28.74	28.76	28.79
k_s (N m^{-1})	0.735	0.735	0.734	0.735	0.735
	^{136}Xe-CHD_3	^{134}Xe-CHD_3	^{132}Xe-CHD_3	^{131}Xe-CHD_3	^{129}Xe-CHD_3
R (Å)	4.224	4.224	4.224	4.224	4.224
ν_s (cm^{-1})	29.07	29.10	29.12	29.13	29.17
k_s (N m^{-1})	0.832	0.832	0.832	0.832	0.832
	$j = 2, K = 1$ state				
	^{136}Xe-CH_4	^{134}Xe-CH_4	^{132}Xe-CH_4	^{131}Xe-CH_4	^{129}Xe-CH_4
R (Å)	4.269	4.269	4.269	4.270	4.270
ν_s (cm^{-1})	32.03	32.05	32.07	32.09	32.12
k_s (N m^{-1})	0.867	0.867	0.866	0.867	0.867
	^{136}Xe-$^{13}CH_4$	^{134}Xe-$^{13}CH_4$	^{132}Xe-$^{13}CH_4$	^{131}Xe-$^{13}CH_4$	^{129}Xe-$^{13}CH_4$
R (Å)	4.263	4.263	4.263	4.263	4.264
ν_s (cm^{-1})	31.23	31.26	31.28	31.30	31.31
k_s (N m^{-1})	0.870	0.870	0.870	0.870	0.869
	^{136}Xe-CD_4	^{134}Xe-CD_4	^{132}Xe-CD_4	^{131}Xe-CD_4	^{129}Xe-CD_4
R (Å)	4.230	4.230	4.231	4.231	4.231
ν_s (cm^{-1})	30.67	30.68	30.72	30.72	30.77
k_s (N m^{-1})	0.969	0.968	0.968	0.967	0.968

Table 4-14: Comparison of *ab initio* and experimental values of derived parameters for $^{132}Xe\text{-}CH_4$.

		R (Å)	ν_s (cm^{-1})	k_s ($N\ m^{-1}$)
experimental values	$j = 0, K = 0$ state	4.264	33.2	0.928
	$j = 2, K = 1$ state	4.269	32.1	0.866
ab initio values	face	4.082	40.9	1.410
	edge	4.293	36.4	1.118
	vertex	4.620	32.9	0.912

References

[1] F. Pirani, D. Cappelletti, and G. Liuti, Chem. Phys. Lett. **350**, 286 (2001).

[2] Y. Liu and W. Jäger, J. Chem. Phys. **120**, 9047 (2004).

[3] T. G. A. Heijimen, T. Korona, R. Moszynski, P. E. S. Wormer, and A. van der Avoird, J. Chem. Phys. **107**, 902 (1997).

[4] F. Pirani, M. Albertí, A. Castro, M. Moix Teixidor, and D. Cappelletti, Chem. Phys. Lett. **394**, 37 (2004).

[5] A. C. Legon and A. L. Wallwork, J. Chem. Soc., Chem. Commun. 588 (1989).

[6] A. C. Legon and A. L. Wallwork, J. Chem. Soc., Faraday Trans. **88**, 1 (1992).

[7] A. C. Legon, B. P. Roberts, and A. L. Wallwork, Chem. Phys. Lett. **173**, 107 (1990).

[8] Y. Ohshima and Y. Endo, J. Chem. Phys. **93**, 6256 (1990).

[9] M. J. Atkins, A. C. Legon, and A. L. Wallwork, Chem. Phys. Lett. **192**, 368 (1992).

[10] Y. Liu and W. Jäger, J. Chem. Phys. **121**, 6240 (2004).

[11] C. Xia, K. A. Walker, and A. R. W. Mckellar, J. Chem. Phys. **114**, 4824 (2001).

[12] A. R. W. McKellar, Faraday Discuss. Chem. Soc. **97**, 69 (1994).

[13] I. Pak, D. A. Roth, M. Hepp, G. Winnewisser, D. Scouteris, B. J. Howard, and K. M. T. Yamada, Z. Naturforsch., A: Phys. Sci. **53**, 725 (1998).

[14] R. D. Suenram, G. T. Fraser, F. J. Lovas, and Y. Kawashima, J. Chem. Phys. **101**, 7230 (1994).

[15] L. Dore, R. C. Cohen, C. A. Schmuttenmaer, K. L. Busarow, M. J. Elrod, J. G. Loeser, and R. J. Saykally, J. Chem. Phys. **100**, 863 (1994).

[16] A. R. Hight Walker, G. T. Fraser, R. D. Suenram, and F. J. Lovas, J. Chem. Phys. **113**, 2139 (2000).

[17] D. Scouteris, D. Phil. thesis, Oxford University, 1998.

[18] A. R. W. Mckellar, D. A. Roth, I. Pak, and G. Winnewisser, J. Chem. Phys. **110**, 9989 (1999).

[19] J. P. I. Hearn and B. J. Howard, Mol. Phys. **100**, 2679 (2002).

[20] P. R. Bunker and P. Jensen, *Fundamentals of Molecular Symmetry* (Institute of Physics, Bristol, 2005).

[21] C. Hampel, K. Peterson, and H.-J. Werner, Chem. Phys. Lett. **190**, 1 (1992).

[22] M. J. O. Deegan and P. J. Knowles, Chem. Phys. Lett. **227**, 321 (1994).

[23] MOLPRO, a package of ab initio programs designed by H.-J. Werner and P. J. Knowles, version 2002.6, R. D. Amos, A. Bernhardsson, A. Berning, P. Celani, D. L. Cooper, M. J. O. Deegan, A. J. Dobbyn, F. Eckert, C. Hampel, G. Hetzer, P. J. Knowles, T. Korona, R. Lindh, A. W. Lloyd, S. J. McNicholas, F. R. Manby, W. Meyer, M. E. Mura, A. Nicklass, P. Palmieri, R. Pitzer, G. Rauhut, M. Schütz, U. Schumann, H. Stoll, A. J. Stone, R. Tarroni, T. Thorsteinsson, and H.-J. Werner.

[24] K. A. Peterson, D. Figgen, E. Goll, H. Stoll, and M. Dolg, J. Chem. Phys. **119**, 11113 (2003).

[25] T. H. Dunning, Jr., J. Chem. Phys. **90**, 1007 (1989).

[26] S. M. Cybulski and R. R. Toczylowski, J. Chem. Phys. **111**, 10520 (1999).

[27] S. F. Boys and F. Bernardi, Mol. Phys. **19**, 553 (1970).

[28] *CRC Handbook of Chemistry and Physics* 84th Ed. (CRC Press, Boca Raton, 2003).

[29] H. –J. Werner and P. J. Knowles, *MOLPRO User's Manual Version 2002.6* (University of Birmingham, 2003).

[30] P. Lazzeretti, R. Zanasi, and W. T. Raynes, J. Chem. Phys. **87**, 1681 (1987).

[31] J. T. Hougen, in *International Review of Science*, edited by D. A. Ramsay (Butterworths, London, 1976), Ser. 2, Vol. 3.

[32] M. Iida, Y. Ohshima, and Y. Endo, J. Phys. Chem. **97**, 357 (1993).

[33] H. M. Pickett, J. Mol. Spectrosc. **148**, 371 (1991).

[34] W. Gordy and R. L. Cook, *Microwave Molecular Spectra,* 3rd ed. (Wiley, London, 1984).

[35] J. van Wijngaarden and W. Jäger, J. Chem. Phys. **114**, 3968 (2001).

[36] J. van Wijngaarden and W. Jäger, Mol. Phys. **99**, 1215 (2001).

[37] R. J. LeRoy, "LEVEL7.5, A Computer Program for Solving the Radial Schrödinger Equation for Bound and Quasibound Levels," University of Waterloo, Chemical Physics Research Report No. CP-655 2002 (unpublished).

[38] E. J. Campbell, L. W. Buxton, M. R. Keenan, and W. H. Flygare, Phys. Rev. A **24**, 812 (1981).

[39] F. A. Baiocchi, T. A. Dixon, C. H. Joyner, and W. Klemperer, J. Chem. Phys. **75**, 2041 (1981).

[40] W. Jäger, Y. Xu, and M. C. L. Gerry, J. Chem. Phys. **99**, 919 (1993).

[41] C. G. Gray and K. E. Gubbins, *Theory of Molecular Fluid* (Clarendon, Oxford, 1984), Vol. 1.

[42] G. Birnbaum and E. G. Cohen, J. Chem. Phys. **62**, 3807 (1975).

[43] W. L. Faust and M. N. McDermott, Phys. Rev. **123**, 198 (1961).

[44] T. G. A. Heijimen, P. E. S. Wormer, A. van der Avoird, R. E. Miller, and R. Moszynski, J. Chem. Phys. **110**, 5639 (1999).

CHAPTER 5 Rotational and *Ab Initio* Studies of the Xe-$(H_2O)_N$ ($N = 1, 2$) van der Waals Complexes: Xenon as a Probe of Electronic Structure and Dynamics

5.1 Introduction

As introduced in Chapter 1, hyperpolarized ^{129}Xe is used as a sensitive atomic probe to characterize, for example, porous materials and biological tissues with nuclear magnetic resonance (NMR) and magnetic resonance imaging (MRI) methods. A detailed interpretation of ^{129}Xe NMR/MRI results requires a fundamental understanding of Xe-molecule interactions. The study of Xe-water interactions is of particular importance with regards to *in vivo* MRI studies, as water is a main constituent of the human body. The interactions of water molecules with Xe atoms determine the traveling paths of Xe in the human body and contribute significantly to background signals of *in vivo* images. As a result of the hydrophobic Xe-water interaction, a bio-compatible gas carrier, for example the recently reported water soluble cryptophanes,[1] is necessary to increase the solubility of Xe and to deliver it into the target tissues. A detailed characterization of the Xe-water interactions might help to improve hyperpolarized ^{129}Xe *in vivo* delivery methods and to interpret the phenomena observed in the NMR/MRI studies. In addition, detailed knowledge about

interactions of Xe with water, a prototypical model of hydrophobic interactions, will contribute to a better understanding of more complicated interactions in biological systems. A number of experimental and theoretical NMR studies have been carried out in an attempt to understand these interactions.[2,3,4] In this Chapter, I give details about microwave and *ab initio* studies of the Xe-$(H_2O)_N$ (N = 1, 2) complexes.

A number of interaction potentials for the Ar-,[5,6,7,8,9,10] and Kr-H_2O[11] complexes have been previously reported. These potentials all predict an equilibrium geometry in which all four atoms are coplanar. However, the angle θ between the intermolecular axis and the C_2 axis of the H_2O unit (see Figure 5-1) is not consistent among the different studies. For Ar-H_2O, an anti-hydrogen bonded orientation of the H_2O unit was found in a MP2 potential reported by Chałasiński *et al.*[8] and a semiempirical potential by Bulski *et al.*,[9] with θ = 100° and 129.5°, respectively. In contrast, Cohen *et al.*[7] determined an intermolecular potential using spectroscopic data, and a hydrogen bonded H_2O orientation (θ = 74.3°) was found. This is in agreement with the MP4 potential energy surface (θ = 75°) reported by Tao *et al.*[10] A similar equilibrium geometry was also found in the MP2 calculation of the Kr-H_2O (θ = 80°) potential by Chałasiński *et al.*[11]

Extensive spectroscopic studies have been carried out on the Ar-,[12,13,14,15,16,17,18,19,20,21] Kr-H_2O,[22] and Ar-$(H_2O)_2$ (Ref. 23 and 24) complexes. For Ar-, and Kr-H_2O, two tunneling states were observed in the microwave spectra,[12,13,22] in accord with computational studies.[7,10,11] For example, the Ar-H_2O potential by Cohen *et al.*[7] predicts that the H_2O in-plane rotation is hindered by barriers at θ = 0° (26.3 cm^{-1}) and θ = 180° (17.2 cm^{-1}), corresponding to the symmetric Ar-H_2O and

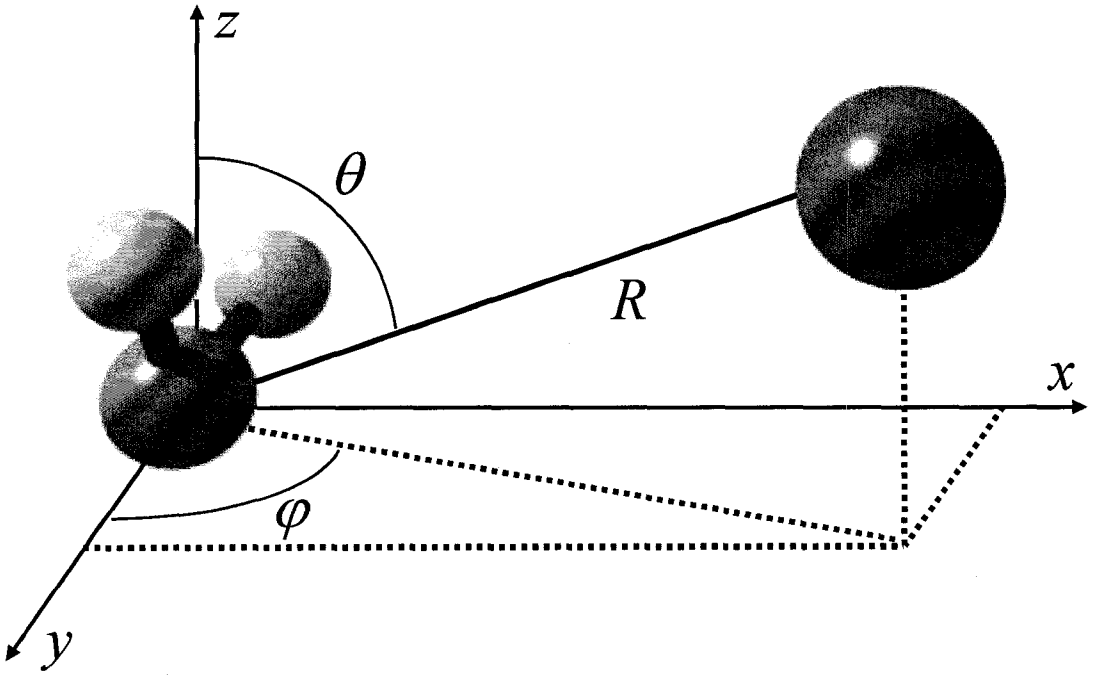

Figure 5-1: Molecule fixed axes frame for the Xe-H_2O complex. The origin of the coordinate system is at the center-of-mass of the H_2O unit, and the C_2 axis of H_2O is chosen as the z-axis. The H_2O unit lies in yz-plane. The position of the Xe atom is described by spherical coordinates (R, θ, φ). R is the distance between Xe and the origin, θ is the angle between the R vector and the z-axis. $\theta = 0°$ corresponds to the C_{2v} geometry where the hydrogen atoms point to the xenon atom. φ is the angle for the H_2O out-of-plane rotation about its C_2 axis. $\varphi = 0°$ if all four atoms are coplanar. $\theta = 0°$, $\varphi = 0°$ corresponds to the symmetric Xe-H_2O geometry, and $\theta = 180°$, $\varphi = 0°$ corresponds to the symmetric Xe-OH_2 geometry. $\theta = 53°$, $\varphi = 0°$ corresponds to an L-shaped Xe-HOH structure with a linear Xe-HO arrangement.

Ar-OH_2 configurations, respectively. The out-of-plane rotation of H_2O is hindered by a barrier of 54.2 cm^{-1} at $\theta = 90°$ and $\varphi = 90°$ (φ is the angle for the H_2O out-of-plane rotation about its C_2 axis. $\varphi = 0°$ if all four atoms coplanar; see Figure 5-1). The microwave studies could determine effective structures of, and H_2O dynamics in, these complexes. In both the Ar- and Kr-H_2O cases, the microwave data show that the H atoms point towards Ar or Kr in both observed states, and a large amplitude H_2O out-of-plane motion is present despite the relatively high energy barrier.[12,13,22] In the Ar-$(H_2O)_2$ studies,[23,24] the structure was described as an isosceles triangle, treating the water molecules as spheres. The experimental results suggest that Ar approaches the water dimer from an axis perpendicular to the plane of the water molecule that acts as a proton donor. The presence of Ar shows little effect on the intermolecular distance in the water dimer. It is instructive to see how the structure and hydrogen bonding interaction of the water dimer are affected by a larger and more polarizable Xe atom.

In this work, rotational transitions within two tunneling states, namely the $\Sigma 0_{00}$ and $\Sigma 1_{01}$ states, were measured and assigned for the Xe-H_2O dimer. Nine *a*- type and twelve *b*- type transitions were measured for the Xe-$(H_2O)_2$ trimer. The ^{131}Xe ($I = 3/2$), D ($I = 1$), and ^{17}O ($I = 5/2$) nuclear quadrupole hyperfine structures were resolved and analyzed in case of Xe-H_2O. For Xe-$(H_2O)_2$, only the ^{131}Xe nuclear quadrupole hyperfine structure could be detected. The determined spectroscopic constants, including nuclear quadrupole coupling constants, were used to obtain information about the structure and intermolecular dynamics of these two complexes. Experimental data were complemented by the construction of an *ab initio* potential energy surface (PES) of Xe-H_2O at the CCSD(T) level of theory and geometry optimization of Xe-

$(H_2O)_2$ at the MP2 level of theory. The variations in structure and dynamics in going from the dimer to the trimer are elucidated and interpreted in terms of non-additive three-body effects. The studies of the Xe-$(H_2O)_N$ (N = 1, 2) complexes constitutes a step towards the understanding of how the Xe electron distribution is affected by successive solvation with water molecules.

5.2 *Ab initio* calculations

5.2.1 Potential energy surface of the Xe-H_2O dimer

Potential energies of the Xe-H_2O dimer were calculated at the CCSD(T) level of theory[25,26] using the MOLPRO 2002.6 package of *ab initio* programs.[27] The aug-cc-pVQZ-PP[28] basis set was chosen for the Xe atom and the aug-cc-pVTZ[29] basis set for O and H atoms. The basis sets were supplemented with (3s3p2d2f1g) midbond functions, with the exponents α_s, α_p = 0.94, 0.34, 0.12; α_d, α_f = 0.64, 0.23; α_g = 0.35.[30] The interaction energies were calculated using the supermolecule approach and counterpoise correction[31] was applied to eliminate basis-set superposition error. The Xe-H_2O geometry is defined by a set of spherical polar coordinates (R, θ, φ), with the origin of the coordinate system at the center-of-mass (c.m.) of the H_2O unit, as shown in Figure 5-1. The H_2O unit was kept rigid at its equilibrium structure, with a O-H bond length of 0.9575 Å and a H-O-H angle of 104.51 degree.[32] R is the Xe-c.m.(H_2O) distance and θ is the angle between the R vector and the C_2 axis of the H_2O unit. $\theta = 0°$ corresponds to C_{2v} geometry with the H atoms pointing towards the Xe atom. φ is the angle for the H_2O out-of-plane rotation about its C_2 axis. $\varphi = 0°$ corresponds to the geometry with all four atoms coplanar. The PES was constructed on a grid of 630

points. R was varied from 3.5 Å to 4.3 Å in steps of 0.1 Å, θ from 0° to 180° in steps of 10°, and φ from 0° to 90° in steps of 30°. The calculated interaction energies are given in Table 5-1.

5.2.2 Geometry optimization of the Xe-$(H_2O)_2$ trimer

A complete geometry optimization was performed at the MP2 level of theory[33] using the GAUSSIAN03 package of *ab initio* programs.[34] The aug-cc-pVQZ-PP[28] basis set was used for the Xe atom, aug-cc-pVTZ[29] for the O atoms, and 6-311++G(d,p)[35] for the H atoms. Figure 5-2 shows the obtained minimum energy configurations. A comparison of their structural parameters with the effective structure obtained from the experimental results is given in Table 5-2. Their minimum nature was confirmed by the absence of imaginary frequencies in the harmonic frequency calculation. The calculated counterpoise corrected binding energies (D_e), zero-point vibrational energy (ΔZPE) corrections and van der Waals stretching frequencies for the minima are given in Table 5-3. The calculated stretching frequencies were compared with those obtained from harmonic force field analysis of experimental data.

5.3 Spectral search, assignments, and analyses

The Xe-H_2O [Xe-$(H_2O)_2$] complex was studied using sample mixtures that contained 0.4% (0.6%) Xe and 0.1% (0.15%) H_2O. Ne was used as backing gas to keep the pressure at about 5 atm for the Xe-H_2O study and 6 atm for Xe-$(H_2O)_2$. Several Xe isotope containing complexes were studied in their natural isotopic abundances (^{136}Xe: 8.87%, ^{134}Xe: 10.44%, ^{132}Xe: 26.89%, ^{131}Xe: 21.18%, ^{129}Xe:

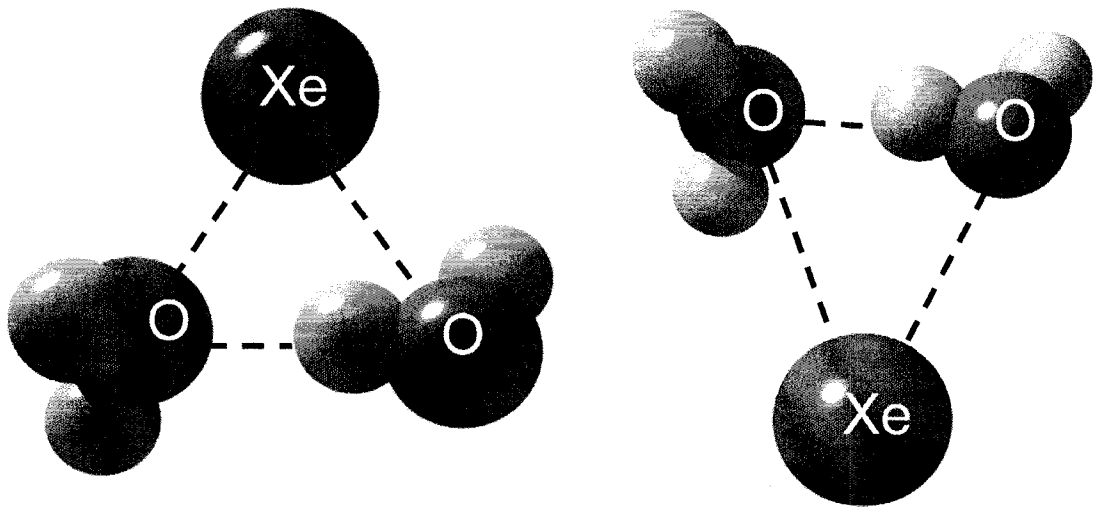

Figure 5-2: Geometries of Minimum I (left) and Minimum II (right) of the Xe-$(H_2O)_2$ trimer optimized at the MP2 level of theory. The unlabeled elements are H atoms.

26.44%). For the Xe-H_2O dimer, isotopically enriched samples were used to investigate isotopomers containing D_2O (99.8%), $H_2{}^{17}O$ (35-40% ^{17}O, Cambridge Isotope Laboratories), and $H_2{}^{18}O$ (70% ^{18}O, Cambridge Isotope Laboratories). Xe-HDO was studied using the same sample mixtures as for Xe-D_2O because HDO was present through the fast exchange between D_2O and residual H_2O in the sample system. The intensities of Xe-HDO transitions were found to increase significantly after conditioning the sample system for 1-2 hours.

5.3.1 Xe-H_2O

The H_2O unit was anticipated to undergo large amplitude internal rotation motions within the Xe-H_2O dimer. As a consequence, transitions within different tunneling states were expected to occur. Following the labeling scheme developed by

Hutson[5] and Cohen *et al.*,[15] the two lowest energy tunneling states correlate with the $j_{kakc} = 0_{00}$ and 1_{01} rotational states of free water, and are designated as $\Sigma 0_{00}$ and $\Sigma 1_{01}$ states, respectively. Σ represents $K = 0$ where K is the projection of the internal rotational angular momentum of the H_2O monomer, j, onto the intermolecular axis, R. Fermi-Dirac statistics applies to the isotopomers containing H_2O, requiring the total wavefuction to be antisymmetric with respect to exchange of the two H nuclei ($I = ½$). This results in the antisymmetric spin function ($I = 0$, *para*H_2O) to be associated with the symmetric $\Sigma 0_{00}$ tunneling state and the symmetric spin function ($I = 1$, *ortho*H_2O) with the antisymmetric $\Sigma 1_{01}$ state. The isotopomers containing D_2O obey Bose-Einstein spin statistics and the total wavefunction must be symmetric with respect to exchange of the two D nuclei ($I = 1$). Consequently, the $\Sigma 0_{00}$ state can have total D nuclear spin of 0 or 2 (*ortho*D_2O), while $\Sigma 1_{01}$ state has total D nuclear spin of 1 (*para*D_2O). The spin statistical weights for the $\Sigma 0_{00}$ and $\Sigma 1_{01}$ states are 1 and 3 for Xe-H_2O, and 6 and 3 for Xe-D_2O, respectively. For Xe-H_2O and Xe-D_2O, the $\Sigma 1_{01}$ state is populated because relaxation from the $\Sigma 1_{01}$ to $\Sigma 0_{00}$ state is a nuclear-spin-forbidden process. As a result, transitions within both these two states were expected to be observed. For Xe-HDO, the $\Sigma 1_{01}$ state is no longer metastable because of the lower symmetry for HDO unit, and only $\Sigma 0_{00}$ ground state transitions were expected.

I started the spectral search for Xe-H_2O with the $J = 2$-1 transitions around 8 GHz. Initial transition frequencies were predicted based on a pseudodiatomic approximation. The Xe-c.m.(H_2O) distance was estimated to be 3.97 Å by comparison of the corresponding distances in Kr-CO_2 and Xe-CO_2 (Ref. 36) with that in Kr-H_2O

(Ref. 22) and extrapolation to Xe-H_2O. The J = 2-1 transition for the ^{132}Xe- H_2O isotopomer was predicted at 8104 MHz and two transitions were soon located at 8181 MHz and 8022 MHz, with an intensity ratio of approximately 1:3. This intensity ratio is consistent with the spin statistical weights of 1 and 3 for the $\Sigma 0_{00}$ and $\Sigma 1_{01}$ states and transitions were assigned accordingly. The assignments were further supported by the observation of proton hyperfine splittings in the J = 1-0, $\Sigma 1_{01}$ transition, but not in the corresponding transition within the $\Sigma 0_{00}$ state. These hyperfine splittings could arise from nuclear spin-spin, or spin-rotation interactions, which are expected only for the $\Sigma 1_{01}$ state (I = 1). The hyperfine structure extends over about 50 kHz, the same order of magnitude as was observed for Ar-H_2O.[13] A lot of efforts were made to resolve the hyperfine structure of the J = 1-0, $\Sigma 1_{01}$ transition for ^{132}Xe-H_2O, but without success. The rotational transition appears to be split into four or possibly five hyperfine components (see Figure 5-3) instead of the predicted three, which is similar to the observation in Ar-H_2S.[37] Other J transitions and transitions of complexes containing the five main Xe isotopes were located straightforwardly. Nuclear quadrupole hyperfine structures due to the presence of the ^{131}Xe nucleus were also observed, which confirmed the assignment to the Xe-containing species. All measured transition frequencies are listed in Tables 5-4 and 5-5. Example spectra showing ^{131}Xe nuclear quadrupole hyperfine structure are given in Figure 5-4. Pickett's SPFIT/SPCAT suite of programs[38] was used to determine the spectroscopic constants. Each tunneling state was analyzed using a pseudodiatomic approach and the determined rotational constant B, centrifugal distortion constant D_J, and ^{131}Xe nuclear quadrupole coupling constants χ_{aa} are given in Tables 5-4 and 5-5.

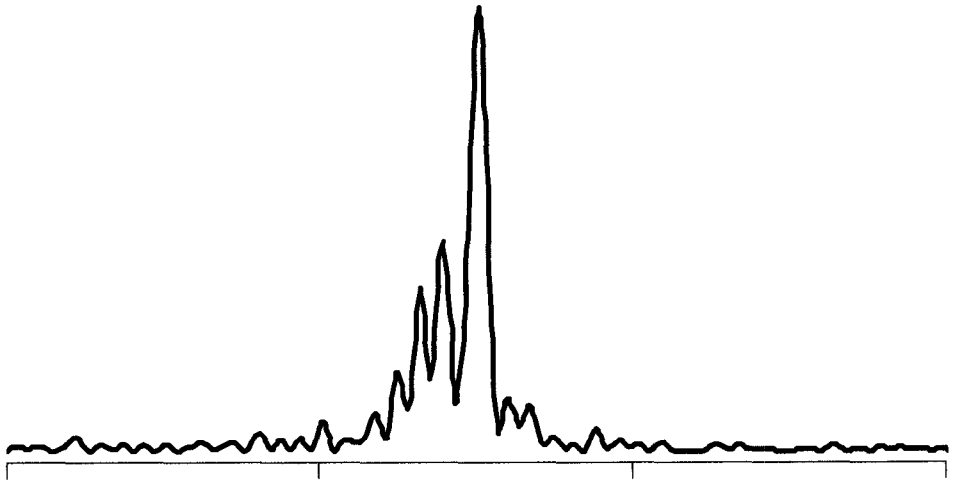

Figure 5-3: A spectrum of the J = 1-0 transition of the $\Sigma 1_{01}$ state of $^{132}Xe\text{-}H_2O$. 400 averaging cycles were used to record the spectrum. Seven of the visible components could be reproduced in different experiments.

The locations of $Xe\text{-}H_2{}^{18}O$ and $Xe\text{-}H_2{}^{17}O$ transitions were predicted using a pseudodiatomic approach with scaled reduced mass. The measured transition frequencies within the $\Sigma 0_{00}$ and $\Sigma 1_{01}$ states are listed in Tables 5-6, 5-7 and 5-8. The transition intensity ratio within these two states stays the same as for $Xe\text{-}H_2O$ because their spin statistics are analogous. Because the $H_2{}^{18}O$ and $H_2{}^{17}O$ samples were only partially enriched, the observed transitions were less intense than those of isotopomers with normal H_2O. The transition intensities of $Xe\text{-}H_2{}^{17}O$ were further reduced by ^{17}O (I = 5/2) nuclear quadrupole hyperfine splittings, causing significant difficulties to measure and resolve the spectra. Therefore, only the J = 2-1 hyperfine transition

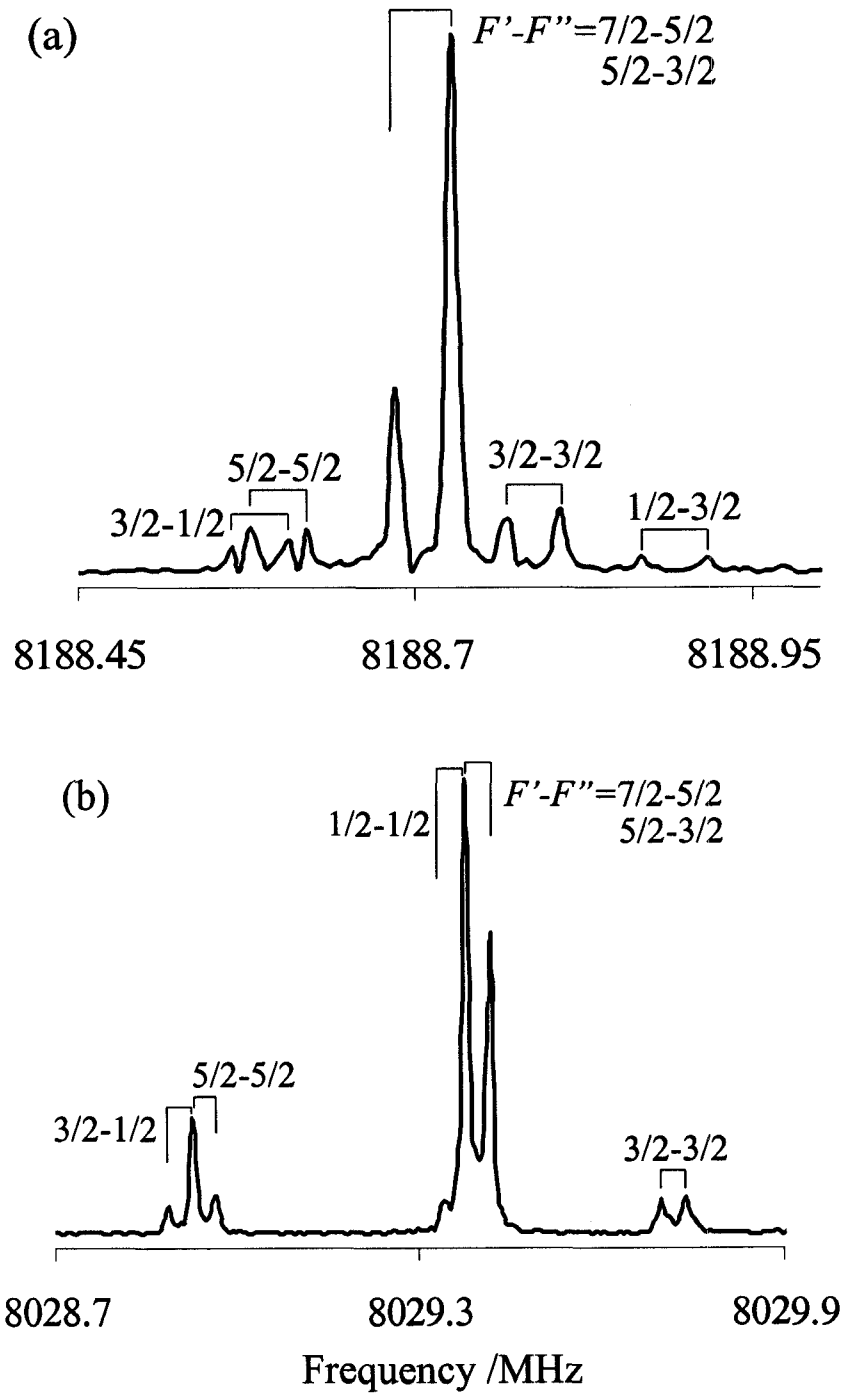

Figure 5-4: Composite spectra of the $J = 2\text{-}1$ transitions of the $\Sigma 0_{00}$ (a) and $\Sigma 1_{01}$ states (b) of $^{131}Xe\text{-}H_2O$. Spectrum (a) was recorded using 800 averaging cycles and spectrum (b) using 100 averaging cycles.

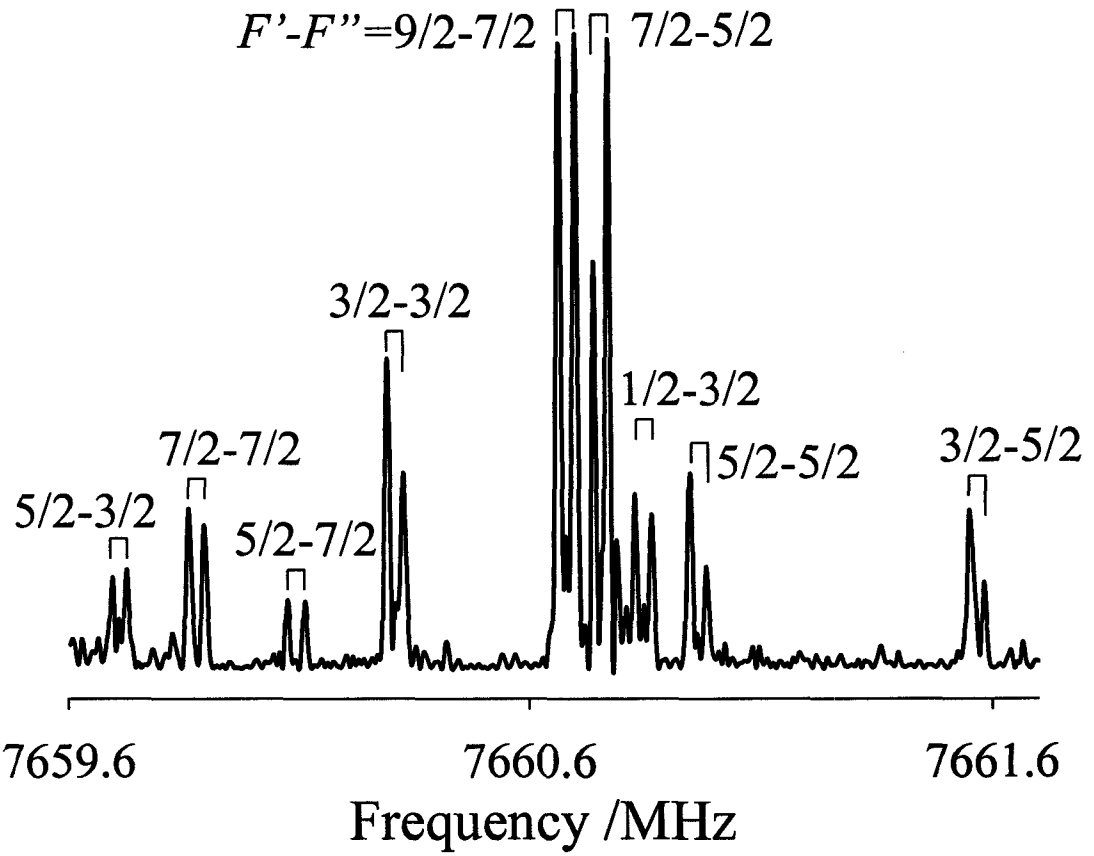

Figure 5-5: A composite spectrum the J = 2-1 transition of the $\Sigma 1_{01}$ state of ^{132}Xe-$H_2{}^{17}O$. 2000 averaging cycles were used to record the spectrum.

frequencies within each tunneling state of Xe-$H_2{}^{17}O$ were measured for the two main Xe isotopes (^{132}Xe and ^{129}Xe). The ^{17}O nuclear quadruple hyperfine structures were partially resolved and assigned. Figure 5-5 shows an example spectrum of the ^{132}Xe-$H_2{}^{17}O$ isotopomer in the $\Sigma 1_{01}$ state to demonstrate the signal-to-noise ratio achieved. The spectroscopic constants of Xe-$H_2{}^{18}O$, including the ^{131}Xe nuclear quadrupole coupling constants, are shown in Tables 5-6 and 5-7. For Xe-$H_2{}^{17}O$, the rotational constant B and the ^{17}O nuclear quadrupole coupling constant χ_{aa} were obtained (see Table 5-8). As only one transition was measured for each tunneling state, the

centrifugal distortion constant D_J was fixed at the average value of the corresponding constants for the Xe-$H_2{}^{16}O$ and Xe-$H_2{}^{18}O$ isotopomers.

Two tunneling components were also observed for the Xe-D_2O complexes. The higher frequency component was found more intense and was assigned to the $\Sigma 0_{00}$ state based on the predicted spin statistical weights (6 and 3 for the $\Sigma 0_{00}$ and $\Sigma 1_{01}$ states, respectively). Both tunneling components show hyperfine structures due to the D nuclear quadrupole interactions. The partially resolved hyperfine structures for the two tunneling states of the $J = 2\text{-}1$ transition are shown in Figure 5-6. Following Bose-Einstein statistics, the $\Sigma 0_{00}$ state requires a total D nuclear spin, I_D, of 0 or 2, while the $\Sigma 1_{01}$ state requires I_D to be 1. The hyperfine structure in the lower frequency component matches the $I_D = 1$ hyperfine pattern better, which further supports the assignment of the two tunneling states. All measured transition frequencies are listed in Tables 5-9 and 5-10, together with the determined spectroscopic constants including the D nuclear quadrupole coupling constants. For ^{131}Xe-D_2O, several hyperfine components due to the ^{131}Xe nucleus were measured for the $\Sigma 0_{00}$ state. For the $\Sigma 1_{01}$ state, only the strongest component for each transition was observed due to the low signal-to-noise ratio achieved. However, the information was sufficient to determine the ^{131}Xe nuclear quadrupole coupling constants for both states (see Table 5-10).

Only transitions within the $\Sigma 0_{00}$ ground state were observed for Xe-HDO because the partial deuteration reduces the symmetry of the water, and as a result, relaxation from the $\Sigma 1_{01}$ to the $\Sigma 0_{00}$ state is now an allowed process. All measured transition frequencies are listed in Tables 5-11 and 5-12. The nuclear quadrupole

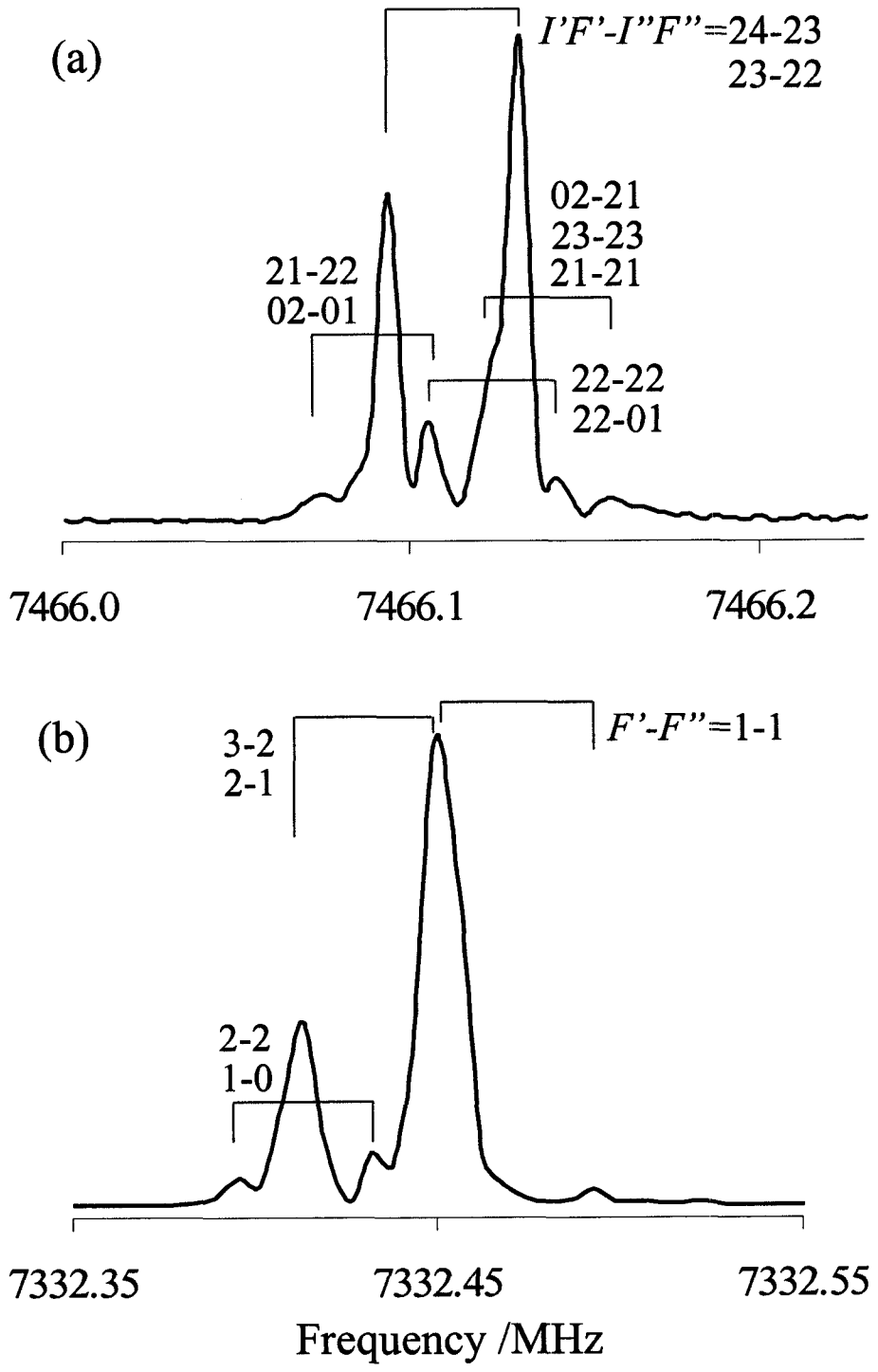

Figure 5-6: Composite spectra of the $J = 2\text{-}1$ transitions of the $\Sigma 0_{00}$ (a) and $\Sigma 1_{01}$ states (b) of $^{132}Xe\text{-}D_2O$. 200 averaging cycles were used in each case.

hyperfine structures due to the ^{131}Xe and D nuclei were observed and assigned. The determined spectroscopic constants, including the ^{131}Xe and D nuclear quadrupole coupling constants, are given in Tables 5-11 and 5-12.

5.3.2 Xe-$(H_2O)_2$

Based on the geometry of Ar-$(H_2O)_2$,[23,24] the rotational constants *A*, *B*, and *C* of Xe-$(H_2O)_2$ were predicted by assuming a simple isosceles triangular structure of the trimer with two water spheres and a Xe atom. Using the structures of the Ar-H_2O,[12] Ar-$(H_2O)_2$,[23,24] and Xe-H_2O complexes as a guide, I predicted a Xe-c.m.(H_2O) distance of 3.90 Å, and a c.m.(H_2O)-c.m.(H_2O) distance of 3.00 Å. With an estimated inertial defect Δ = 1.0 amu Å^2, the *A*, *B*, and *C* rotational constants of ^{132}Xe-$(H_2O)_2$ were then calculated to be 6253, 1377, and 1126 MHz respectively. These predictions are within 20 MHz of the experimental values determined later in this work.

Nine [nine] *a*-type and twelve [eleven] *b*-type transitions with rotational quantum number *J* ranging from 0 to 5 and K_a from 0 to 2 were measured for the ^{132}Xe-$(H_2O)_2$ [^{129}Xe-$(H_2O)_2$] isotopomer. All measured transition frequencies are listed in Table 5-13 together with the quantum number assignments. Rotation-tunneling spectra of Xe-$(H_2O)_2$ that could arise from the internal rotation of the H_2O molecules were not observed. In the case of Ar-$(H_2O)_2$,[23,24] two components were detected for each *a*-type transition with tunneling splittings in the range from 50 to 600 kHz. Possible reasons for only one detected component in Xe-$(H_2O)_2$ could be too low a transition intensity (for spin statistical reasons) for the second component to be observed, or quenching of the tunneling splitting as a result of the increased angular

anisotropy of the Xe-$(H_2O)_2$ potential compared to that of Ar-$(H_2O)_2$. In a number of transitions, narrow splittings of about 20 kHz were observed. The origin of these splittings could be the tunneling motion or proton hyperfine structures arising from H-H spin-spin or H spin-rotation interactions. However, these hyperfine structures could only be partially resolved, and no attempt was made to fit and interpret them. In those cases, the frequency of the most intense component was recorded as the transition frequency in Table 5-13. The rotational constants A, B, and C, and five quartic centrifugal distortion constants D_J, D_{JK}, D_K, d_1, and d_2 were determined in a fitting procedure and are given in Table 5-14.

The rotational transitions of ^{131}Xe-$(H_2O)_2$ are complicated by nuclear quadrupole hyperfine structures due to the presence of the ^{131}Xe nucleus. The hyperfine structures of four a-type and seven b-type transitions were partially resolved. Figure 5-7 gives an example spectrum to demonstrate the signal-to-noise ratio and resolution achieved. All measured frequencies are summarized in Table 5-15 and were used to fit the rotational, centrifugal distortion, and ^{131}Xe nuclear quadrupole coupling constants simultaneously. The determined spectroscopic constants are given in Table 5-14. Inclusion of the off-diagonal nuclear quadrupole coupling constant χ_{ab} was necessary for the hyperfine analysis because of perturbations caused by the near degeneracy of the 1_{10} and 2_{02} energy levels (~80 MHz energy difference). The contribution from χ_{ab} to each transition frequency was calculated using Pickett's SPCAT program[38] and is included in Table 5-15. This contribution was found to be significant (30 to 65 kHz) for transitions involving the 1_{10} and 2_{02} energy levels, while it was negligible for other transitions.

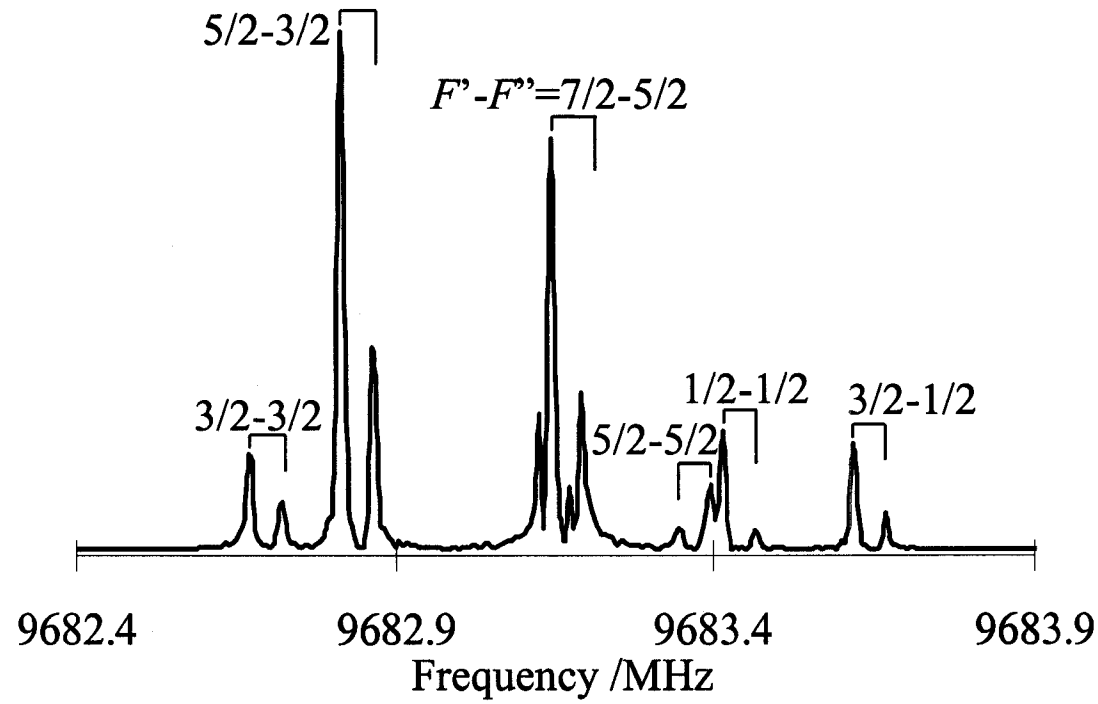

Figure 5-7: A composite spectrum of the $J_{KaKc} = 2_{12} - 1_{01}$ transition of ^{131}Xe-$(H_2O)_2$. A total of 2000 averaging cycles was used to record the spectrum.

5.4 Discussion of the Xe-H_2O results

5.4.1 *Ab initio* potential energy surface

A 3-dimensional PES for Xe-H_2O complex was constructed as function of R, θ, and φ coordinates (see Figure 5-1 for a definition). The global minimum was found at a planar, hydrogen bonded configuration with R = 4.0 Å, θ = 60°, φ = 0°, with a well depth of 191.7 cm^{-1}. This configuration is rather close to an L-shaped Xe-HOH structure with a linear Xe-HO arrangement. Two first order saddle points have symmetric Xe-H_2O geometry (R = 3.95 Å, θ = 0°, φ = 0°, -169.1 cm^{-1}) and symmetric Xe-OH_2 geometry (R = 3.85 Å, θ = 180°, φ = 0°, -161.5 cm^{-1}), respectively. A second

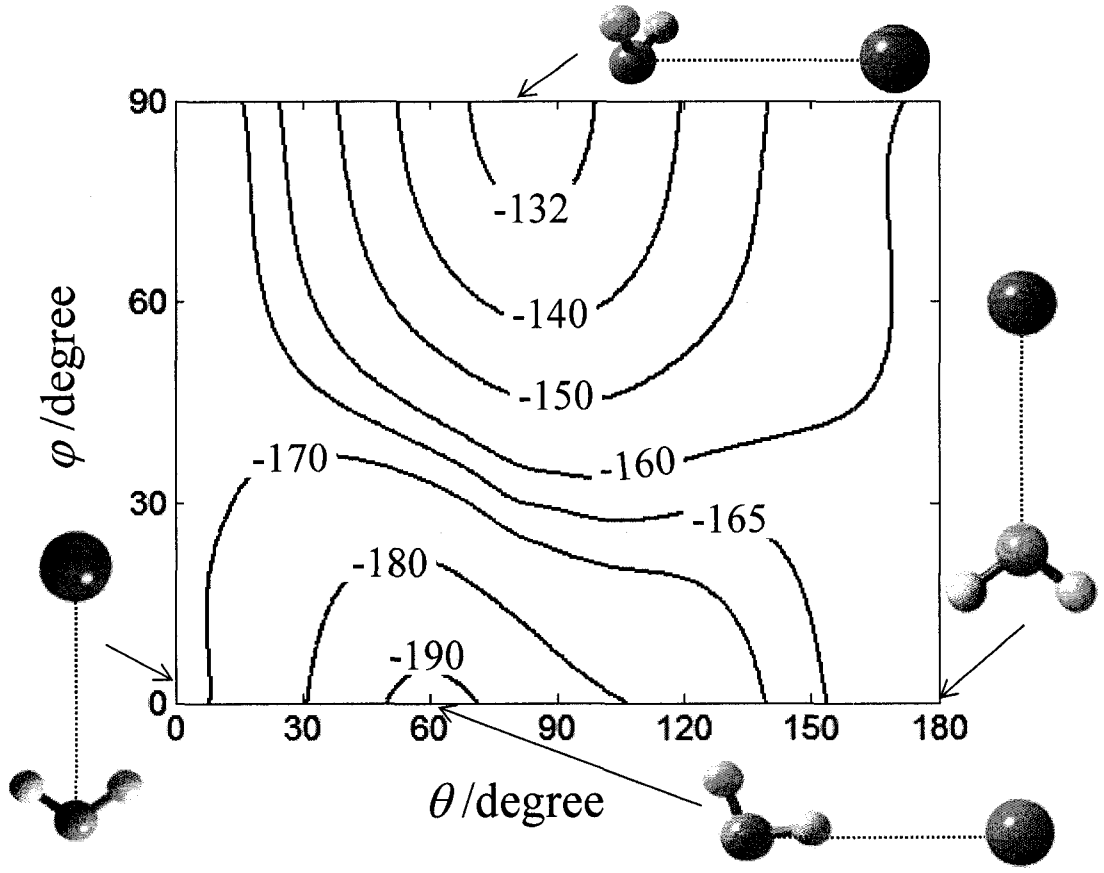

Figure 5-8: Contour diagram of the *ab initio* minimum energy path of Xe-H_2O as function of θ and φ coordinates. R was varied at each θ and φ combination until the lowest energy was found. Potential energies are given in cm^{-1}.

order saddle point corresponds to a non-planar configuration with R = 4.0 Å, θ = 80°, φ = 90° and has an energy of -130.1 cm^{-1}. A minimum energy path was constructed as function of θ and φ coordinates. At each θ and φ configuration, R was varied to locate the lowest energy. A contour plot of this minimum energy path is shown in Figure 5-8. This potential has similar overall features as the Ar-H_2O potentials by Cohen *et al.*,[7] Tao *et al.*,[10] and the Kr-H_2O potential by Chałasiński *et al.*[11] Compared with Ar-,[7,10,

and Kr-H_2O,[11] the Xe-H_2O equilibrium structure adopts a more hydrogen bonded position (the equilibrium structure of Ar-H_2O: $\theta = 74.3°$ in Ref. 7 and $\theta = 75°$ in Ref. 10, and Kr-H_2O: $\theta = 80°$ in Ref. 11), and its potential is slightly more anisotropic in the angular coordinate, implying a more hindered H_2O internal rotation within the Xe-H_2O complex. The potential barrier for the H_2O in-plane rotation is 22.6 cm^{-1} at the symmetric Xe-H_2O geometry ($\theta = 0°$, $\varphi = 0°$) and 30.2 cm^{-1} at the symmetric Xe-OH_2 geometry ($\theta = 180°$, $\varphi = 0°$). The barrier for the H_2O out-of-plane rotation about the C_2 axis is 61.6 cm^{-1} ($\theta = 80°$, $\varphi = 90°$).

5.4.2 Structural parameters and force constants

The rotational constant B and the centrifugal distortion constant D_J were used to calculate the van der Waals bond length R, the van der Waals stretching frequency ν_s, and the corresponding force constant k_s using the pseudodiatomic model:[39]

$$B = h/8\pi^2\mu R^2$$

$$\nu_s = \left(\frac{4B^3}{D_J}\right)^{1/2}$$

$$k_s = 4\pi^2\nu_s^2\mu \qquad (5\text{-}1)$$

where μ is the pseudodiatomic reduced mass of the complex. The results for the individual isotopomers are listed in Table 5-16. Values of R = 3.9485 Å, ν_s = 34.85 cm^{-1}, and k_s = 1.134 N m^{-1} were determined for the $\Sigma 0_{00}$ ground state of ^{132}Xe-H_2O. This indicates that the van der Waals bond of ^{132}Xe-H_2O is slightly longer and more rigid compared to that of ^{84}Kr-H_2O (R = 3.7897 Å, ν_s = 34.8 cm^{-1}, and k_s = 1.06

N m^{-1}).[22] Shorter van der Waals bond lengths and larger force constants were obtained for the deuterated species (R = 3.9453 Å, ν_s = 34.71 cm^{-1}, and k_s = 1.180 N m^{-1} for the $\Sigma 0_{00}$ state of ^{132}Xe-HDO; R = 3.9463 Å, ν_s = 34.84 cm^{-1}, and k_s = 1.243 N m^{-1} for the $\Sigma 0_{00}$ state of ^{132}Xe-D_2O). For the $\Sigma 1_{01}$ state, there is an increased van der Waals bond length and a larger force constant compared to the ground state.

An approximate isotopic substitution analysis was used to derive information about the H_2O orientation with respect to the Xe atom by applying Kraitchman's equations.[40] The assumption that the isotopic substitutions are on the intermolecular a-axis has to be made because of the absence of separated B and C values. This is a good approximation for the ^{18}O substitution because the O atom is rather close to the c.m.(H_2O). Using the rotational constants of the ^{132}Xe containing species, a distance along the a-axis between the c.m. of the complex and the O atom was obtained, with values of 3.458 Å and 3.453 Å, for the $\Sigma 0_{00}$ and $\Sigma 1_{01}$ states, respectively. The H atoms are further off the a-axis, so that the substitution analysis of their a-coordinates is less accurate. An analysis using data from ^{132}Xe-H_2O and ^{132}Xe-D_2O gives distances along the a-axis between the c.m. of the complex and the H atoms of 3.452 Å and 3.455 Å, for the $\Sigma 0_{00}$ and $\Sigma 1_{01}$ states, respectively. The differences between the a-coordinates of the O and H atoms is 0.006 Å for the $\Sigma 0_{00}$ state and 0.002 Å for the $\Sigma 1_{01}$ state, much smaller compared to the corresponding values in ^{84}Kr-H_2O (~0.05 Å)[22] and Ar-H_2O (~0.1 Å).[12,13] In the latter cases, it was determined that the H atoms point on average towards the respective rare gas atom. In the Xe-H_2O case, the difference in the a-coordinates of H and O atoms is so small that it can not decide whether the H atoms point towards or away from the Xe atom. However, it is still worthwhile to point out

that these rather small differences in the *a*-coordinates may imply that the anti-hydrogen bonded orientations and non-planar configurations have more significant contributions to the Xe-H_2O wavefuctions compared to the cases of Kr- and Ar-H_2O.

More information about the motion in the angular coordinates of the Xe-H_2O complex can be obtained from a comparison of spectroscopic and *ab initio* data. The computer program LEVEL7.5 (Ref. 41) was used to determine the bound states of ^{132}Xe-H_2O that are supported by the *ab initio* potential curves along radial coordinates at four selected angular configurations (global minimum, two first order saddle points, and one second order saddle point), using a pseudodiatomic model. The molecular parameters, R, ν_s, and k_s, were then calculated and are compared with the experimental values in Table 5-17. Those calculated values are on the same order of magnitude as the experimental data. The best agreement with the experimental values for the $\Sigma 0_{00}$ state was found at the symmetric Xe-OH_2 geometry (θ = 180°, φ = 0°) for R (Δ = -1.3%) and the second order saddle point (θ = 80°, φ = 90°) for ν_s (Δ = -6.3%) and k_s (Δ = -12.1%). For the $\Sigma 1_{01}$ state, the second order saddle point (θ = 80°, φ = 90°) gives the R value (Δ = +0.9%) closest to the experimental values and the global minimum (θ = 60°, φ = 0°) gives the closet ν_s (Δ = +5.8%) and k_s (Δ = +11.8%) values. These variations of discrepancies among different configurations can be considered as a further indication of a rather delocalized Xe-H_2O ground state wavefunction. The symmetric Xe-OH_2 geometry (θ = 180°, φ = 0°) and the second order saddle point (θ = 80°, φ = 90°), corresponding to an anti-hydrogen bonded orientation and a non-planar configuration respectively, give values that are relatively close to the

experimental ones. This supports what was found in the isotopic substitution analysis, namely that there is a significant contribution to the wavefunctions in each state from the anti-hydrogen bonded and non-planar configurations. However, these two methods only give qualitative information about the H_2O angular motion; more information can be extracted from the hyperfine structural analyses, as discussed in the next section.

5.4.3 Hyperfine structure and angular information

The observed nuclear quadrupole hyperfine structures due to the presence of the ^{131}Xe, D, and ^{17}O nuclei can be used to deduce dynamical information about the internal angular coordinates of the Xe-H_2O complex. As a result of the large amplitude H_2O internal motions, the orientation of the H_2O unit that can be obtained from the nuclear quadrupole coupling constants χ_{aa} is an effective orientation, averaged over these motions. Because H_2O is an asymmetric top, two angles (the angle θ between the C_2 axis of H_2O and the intermolecular a-axis, and the angle φ for the H_2O out-of-plane rotation about its C_2 axis, see Figure 5-1) are used to describe its orientation within the complex. To determine both angles, two nuclear quadrupole coupling constants are needed. Therefore, the $\chi_{aa}(^{131}Xe)$ value of the ^{131}Xe-H_2O isotopomer and $\chi_{aa}(^{17}O)$ of the ^{132}Xe-$H_2{}^{17}O$ isotopomer were utilized to determine two effective angles, θ_{eff} and φ_{eff} in Xe-H_2O, and $\chi_{aa}(^{131}Xe)$ of the ^{131}Xe-D_2O isotopomer and $\chi_{aa}(D)$ of the ^{132}Xe-D_2O isotopomer to obtain the effective angles in Xe-D_2O. In this procedure, the isotopic substitutions at the Xe and O positions were assumed to have negligible effect on the dynamics of the complex. The details of the derivation of the effective angles and interpretation of the results are discussed as follows.

(a) Xe-H_2O

The non-zero value of the ^{131}Xe nuclear quadrupole coupling constant, $\chi_{aa}(^{131}Xe)$, of ^{131}Xe-H_2O arises because of the non-zero electric field gradient at the Xe nucleus due to the presence of the H_2O molecule. There are two main contributions to the electric field gradient at the Xe nucleus. One is the dispersion interaction, and the other is the induction interaction between the nonzero electric multipole moments of H_2O and the Xe electron cloud. The labels χ_{dis} and χ_{ind} will be used below to represent the contributions to the quadrupole coupling constants from these two interactions, respectively. The magnitude of χ_{ind} depends largely on the electric moments of the binding partners of Xe. In many cases, for example, the ^{131}Xe-HX (X=F and Cl) complexes,[42,43,44] χ_{dis} has been neglected in interpreting the nuclear quadrupole coupling constants because HX (X=F and Cl) has large electric moments so that χ_{dis} is relatively small compared to χ_{ind}. The electric moments of H_2O are not necessarily smaller than those of HF and HCl. The dipole moment of H_2O (1.855 D) is slightly larger than those of HF (1.826 D) and HCl (1.109 D). However, compared with the $\chi_{aa}(^{131}Xe)$ values of ^{131}Xe-HF (-8.54 MHz)[44] and ^{131}Xe-HCl (-4.9 MHz),[42,43] the values for ^{131}Xe-H_2O (-0.445 MHz for the $\Sigma 0_{00}$ state and -1.814 MHz for the $\Sigma 1_{01}$ state) are much smaller. Similar behavior has been found previously in ^{83}Kr-H_2O.[22] A possible reason is that the electric field gradient at the ^{131}Xe nucleus is reduced by averaging over the large amplitude H_2O internal rotation. The $\chi_{aa}(^{131}Xe)$ value for the $\Sigma 0_{00}$ state is approximately one-fourth of that of the $\Sigma 1_{01}$ state, which suggests that H_2O

experiences different vibrational dynamics within these two states, and might undergo more free internal rotation in the $\Sigma 0_{00}$ state.

The magnitude of $\chi_{aa}(^{131}Xe)$ for ^{131}Xe-H_2O is not much larger than those for ^{131}Xe-^{20}Ne (0.3878 MHz), ^{131}Xe-Ar (0.7228 MHz), and ^{131}Xe-^{84}Kr (0.7079 MHz), in which cases $\chi_{ind}(^{131}Xe) = 0$.[45] Therefore, $\chi_{dis}(^{131}Xe)$ can not be neglected in the ^{131}Xe-H_2O case. The $\chi_{aa}(^{131}Xe)$ value of ^{131}Xe-Ar, 0.723 MHz[45] was used as an estimate for $\chi_{dis}(^{131}Xe)$ in ^{131}Xe-H_2O. In the case of ^{131}Xe-$^{15}N_2$, $\chi_{dis}(^{131}Xe)$ was estimated to be 0.828 MHz by taking the difference between the experimental $\chi_{aa}(^{131}Xe)$ value and the calculated $\chi_{ind}(^{131}Xe)$ value, and was found to be in accord with the $\chi_{aa}(^{131}Xe)$ value of ^{131}Xe-Ar, 0.723 MHz (see Chapter 3). The $\chi_{ind}(^{131}Xe)$ values for ^{131}Xe-H_2O can be estimated by subtracting $\chi_{dis}(^{131}Xe)$ from the observed $\chi_{aa}(^{131}Xe)$ values, and the resulting values are -1.168 MHz for the $\Sigma 0_{00}$ state and -2.537 MHz for the $\Sigma 1_{01}$ state. These values can be interpreted in terms of the multipole moments of the H_2O monomer using the expressions:[43]

$$q_0 = -6\mu\left\langle\frac{\cos\theta}{R^4}\right\rangle - 12\left\langle\frac{Q_{xx}\sin^2\theta\sin^2\varphi + Q_{yy}\sin^2\theta\cos^2\varphi + Q_{zz}\cos^2\theta}{R^5}\right\rangle - \cdots$$

$$\chi_{ind} = -eq_0(1-\gamma)Q_{Xe}/h \qquad (5\text{-}2)$$

In the above expressions, q_0 is the component of the electric field gradient tensor along the a-axis generated by the multipole moments of the H_2O monomer at the site of the Xe nucleus. μ and Q are the electric dipole and quadrupole moments of H_2O, respectively. Higher order electric moments were not considered here. For free H_2O, μ = 1.8546 D[46] and the principal components of the molecular electric quadrupole tensor

Q_{xx} = -2.50 D Å, Q_{yy} = 2.63 D Å, and Q_{zz} = -0.13 D Å.[47] The brackets indicate averaging over the large amplitude angular motions. The van der Waals bond length R is 3.9485 Å for the $\Sigma 0_{00}$ state and 3.9876 Å for the $\Sigma 1_{01}$ state. The ^{131}Xe nuclear quadrupole moment Q_{Xe} = -0.12 b,[48] and the Sternheimer shielding factor γ = -152.[43]

Because it is impossible to solve for two effective angles θ_{eff} and φ_{eff} only by equation (2), the $\chi_{aa}(^{17}O)$ values of the complex were used to determine an effective orientation of the H_2O unit within the complex. The principal components of the ^{17}O nuclear quadrupole coupling tensor in $H_2{}^{17}O$ are χ_{xx} = 10.169 MHz, χ_{yy} = -8.899 MHz, χ_{zz} = -1.269 MHz.[49] The $\chi_{aa}(^{17}O)$ values for the complex can be expressed as the projection of the monomer constants onto the a-axis of the complex, under the assumption that the monomer constants remain unchanged upon complex formation:

$$\chi_{aa}(^{17}O) = \chi_{xx}\langle \sin^2\theta \sin^2\varphi \rangle + \chi_{yy}\langle \sin^2\theta \cos^2\varphi \rangle + \chi_{zz}\langle \cos^2\theta \rangle \qquad (5\text{-}3)$$

For ^{132}Xe-$H_2{}^{17}O$, the $\chi_{aa}(^{17}O)$ values are -1.372 MHz and -4.184 MHz for the $\Sigma 0_{00}$ and $\Sigma 1_{01}$ states, respectively. These quite different $\chi_{aa}(^{17}O)$ values are further evidence for different vibrational dynamics in the two states. Similar observations were reported previously, for CO-H_2O,[50] Ar-H_2O,[12,13] Kr-H_2O,[22] and Ne-H_2S.[51] In the limit of free rotation of the H_2O monomer, the $\chi_{aa}(^{17}O)$ value is zero. A smaller $\chi_{aa}(^{17}O)$ value in the $\Sigma 0_{00}$ state than the $\Sigma 1_{01}$ state suggests more free H_2O internal rotation in the $\Sigma 0_{00}$ state, also consistent with the observed smaller $\chi_{aa}(^{131}Xe)$ value in the $\Sigma 0_{00}$ state. Equations (5-2) and (5-3) can be solved for the effective angles θ_{eff} and φ_{eff} by neglecting the averaging brackets. The obtained values are θ_{eff} = 88.5°, φ_{eff} = 38.9° for the $\Sigma 0_{00}$ state and θ_{eff} = 86.2°, φ_{eff} = 29.8° for the $\Sigma 1_{01}$ state. These orientations are

between hydrogen bonded and anti-hydrogen bonded orientations. This might suggest that the hydrogen bonded and anti-hydrogen bonded orientations have similar contributions to the Xe-H_2O wavefunction in each state. This is further supported by the similar energy barriers at the symmetric Xe-H_2O geometry (hydrogen bonded orientation, 22.6 cm^{-1}) and the Xe-OH_2 geometry (anti-hydrogen bonded orientation, 30.2 cm^{-1}) in the *ab initio* potential. The large amplitude out-of-plane motion is evident from the obtained φ_{eff} values, and this is consistent with the structural parameters and force constants obtained from the rotational and distortion constants.

(b) Xe-D_2O and Xe-HDO

Assuming that the nuclear quadrupole coupling constants for free D_2O and HDO are not affected by complex formation, the determined χ_{aa}(D) constants for the complex can also be interpreted in terms of projection of the monomer constants. Different from the ^{17}O case, the D nuclear quadrupole coupling tensors in D_2O and HDO are quite symmetric (asymmetry parameter $\eta = |\chi_{bb}-\chi_{cc}|/\chi_{aa}$ is 0.06 for D_2O and 0.11 for HDO), and the following expressions can be used under the assumption that the nuclear quadrupole interaction is cylindrically symmetric about the O-D bond:

$$\chi_{aa}(D) = \frac{1}{2}\chi_0\left\langle 3\cos^2\beta - 1\right\rangle \qquad (5\text{-}4)$$

Here, β is the angle between the O-D bond axis and the *a*-axis of the complex. χ_0 is the principal component of the D nuclear quadrupole coupling tensor along the O-D bond, $\chi_0(D_2O)$ = 0.330 MHz[50] and χ_0(HDO) = 0.313 MHz.[50, 52] The brackets indicate averaging over the large amplitude angular motions. From equation (5-4), I calculated

the $\langle\cos^2\beta\rangle$ values to be 0.437 for the $\Sigma 0_{00}$ state [χ_{aa}(D) = 0.0513(12) MHz] and 0.479 for the $\Sigma 1_{01}$ state [χ_{aa}(D) = 0.0726(14) MHz] of ^{132}Xe-D_2O and 0.432 for ^{132}Xe-HDO [χ_{aa}(D) = 0.0464(16) MHz]. These values are relatively close to the $\langle\cos^2\beta\rangle$ value of 0.333 in the free rotor limit, which may indicate that the D_2O and HDO units undergo only slightly hindered internal rotation within the complexes. The obtained effective angles β_{eff} are 48.6°, 131.4° for the $\Sigma 0_{00}$ state and 46.2°, 133.8° for the $\Sigma 1_{01}$ state of ^{132}Xe-D_2O and 48.9°, 131.1° for ^{132}Xe-HDO. At first glance, the two tunneling states of ^{132}Xe-D_2O have similar dynamics because the difference in β_{eff} is only 2.4°. This is similar to the CO-H_2O,[50] Ar-H_2O, [12,13] Kr-H_2O,[22] and Ne-H_2S[51] cases. However, this appears to contradict the findings from the ^{131}Xe hyperfine structures in ^{131}Xe-D_2O. The χ_{aa}(^{131}Xe) values are -1.449 MHz for the $\Sigma 0_{00}$ state and -2.76 MHz for the $\Sigma 1_{01}$ state and imply different dynamics for the two states, consistent with the observations in the ^{131}Xe-H_2O complex. A possible reason for this contradiction is that the χ_{aa}(D) values are primarily sensitive to the projection of the O-D bond onto the *a*-axis of the complex, and insensitive to the D_2O out-of-plane motion, as suggested by Yaron *et al.*[50] for the case of CO-H_2O.

To better understand the dynamics of Xe-D_2O, the effective angles θ_{eff} and φ_{eff} can be determined from both the χ_{aa}(D) and χ_{aa}(^{131}Xe) constants. The χ_{ind}(^{131}Xe) values of ^{131}Xe-D_2O were obtained by following the same procedure as for ^{131}Xe-H_2O and the estimated χ_{dis}(^{131}Xe) value, 0.723 MHz, was used. Equation (5-2) is still applicable here to relate the χ_{ind}(^{131}Xe) values to the respective angles, with μ = 1.8545 D,[46] Q_{xx} = -2.402 D Å, Q_{yy} = 2.724 D Å, and Q_{zz} = -0.321 D Å,[47] and R = 3.9463 Å

($\Sigma 0_{00}$ state) and 3.9823 Å ($\Sigma 1_{01}$ state). Because the angles θ and φ are not included in equation (5-4), they cannot be obtained directly by solving equations (5-2) and (5-4). Instead, the θ_{eff} and φ_{eff} were determined by looking for the orientations that satisfy equation (5-2) and can also reproduce the angle β_{eff} obtained from equation (5-4). This yields values of $\theta_{eff} = 89.9°$, $\varphi_{eff} = 31.9°$ for the $\Sigma 0_{00}$ state and $\theta_{eff} = 87.2°$, $\varphi_{eff} = 21.9°$ for the $\Sigma 1_{01}$ state. Note that there is more than one pair of θ_{eff} and φ_{eff} values obtained for each state, but only the values closest to those for Xe-H_2O are reported here under the assumption that the vibrational dynamics does not change dramatically upon deuteration. The resulting φ_{eff} value has a 10.0° difference for the two states, similar to the Xe-H_2O case. This result also supports that the χ_{aa}(D) value is not sensitive to the out-of-plane motion of H_2O.

5.5 Discussion of the Xe-$(H_2O)_2$ results

5.5.1 Structural analysis

The rotational constants of Xe-$(H_2O)_2$ can be used to estimate the structural parameters of the trimer, such as the Xe-c.m.(H_2O) distance, R, and the c.m.(H_2O)-c.m.(H_2O) distance, r, by treating the H_2O molecules as spheres. The A rotational constant of the Xe-$(H_2O)_2$ trimer (6267.6 MHz) is rather close to the $(B+C)/2$ value of the $(H_2O)_2$ (6160.7 MHz),[53] consistent with the initially assumed isosceles triangular structure. The small inertial defect (Δ = 1.34 amu Å^2) and relatively small quartic centrifugal distortion constants of ^{132}Xe-$(H_2O)_2$ (see Table 5-14) suggest that a semirigid model can be applied here, with the following inertial equations:

$$I_a = \frac{1}{2} mr^2 \qquad (5\text{-}5)$$

$$I_b = \mu l^2 \qquad (5\text{-}6)$$

$$I_c = \mu l^2 + \frac{1}{2} mr^2 \qquad (5\text{-}7)$$

Here, m is the mass of water, $\mu = m_{Xe} m_{(H_2O)_2} / (m_{Xe} + m_{(H_2O)_2})$, and l is the Xe-c.m.[$(H_2O)_2$] distance [see Figure 5-9(a)]. By solving equations (5-5) and (5-6), I obtained r = 2.992 Å and l = 3.579 Å. From these values, the Xe-c.m.(H_2O) distance R was calculated to be 3.879 Å. An angle α of 67.3° between the Xe-c.m.(H_2O) bond and the c.m.(H_2O)-c.m.(H_2O) bond was obtained. Compared with the corresponding separations in the Xe-H_2O dimer (3.949 Å), the Xe-c.m.(H_2O) distance R is shortened by 0.07 Å in the trimer. In other instances, for example, the rare gas trimers Ne_2-Kr and Ne_2-Xe,[54] the van der Waals bond distances were found to be longer than in the corresponding dimers due to the repulsive, non-additive triple-dipole dispersion term.[55] A possible explanation for the shrinkage of the Xe-H_2O bond in the Xe-$(H_2O)_2$ trimer is that a H_2O molecule induces dipole moments on Xe and the other H_2O molecule with the result of an attractive, non-additive electrostatic interaction. The shrinkage of the Xe-H_2O bond indicates that this attractive interaction affects the Xe-H_2O bond length more than the repulsive triple-dipole dispersion term. This electrostatic interaction is expected to be less pronounced between two H_2O molecules because the non-polar Xe atom cannot induce a significant dipole moment on H_2O molecules. This is also consistent with a slightly longer H_2O-H_2O bond length found in the Xe-$(H_2O)_2$ trimer (2.992 Å) compared to the $(H_2O)_2$ (2.98 Å).[53,56]

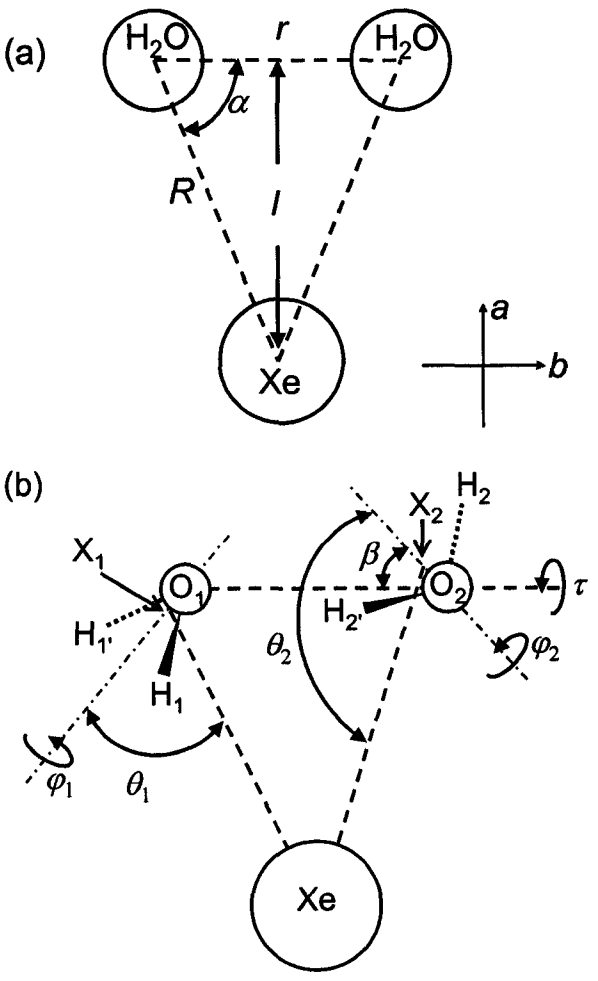

Figure 5-9: Definition of structural parameters for the Xe-$(H_2O)_2$ complex. The *a*- and *b*-axes are the principal inertial axes of the complex. The parameters defined in (a) were used for the structural analysis: r = c.m.(H_2O)-c.m.(H_2O) distance, R = Xe-c.m.(H_2O) distance, l = Xe-c.m.[$(H_2O)_2$] distance, and α = ∠[Xe-c.m.(H_2O)-c.m.(H_2O)]. Additional parameters defined in (b) were used in the ^{131}Xe nuclear quadrupole hyperfine structure analysis: $\theta_1 = 180°-\angle(Xe\text{-}X_1\text{-}O_1)$, $\varphi_1 = \angle(Xe\text{-}O_1\text{-}X_1\text{-}H_1)$, $\theta_2 = 180°-\angle(Xe\text{-}X_2\text{-}O_2)$, $\varphi_2 = \angle(Xe\text{-}O_2\text{-}X_2\text{-}H_2)$, $\beta = \angle(O_1\text{-}O_2\text{-}X_2)$, and $\tau = \angle(X_1\text{-}O_1\text{-}O_2\text{-}X_2)$.

5.5.2 Harmonic force field analysis

The ASYM20PC program of Hedberg and Mills[57] was used to perform a harmonic force field analysis for the Xe-$(H_2O)_2$ complex to extract information about van der Waals vibrational frequencies and corresponding force constants. The H_2O molecules were considered as pseudo atoms and C_s point group symmetry was used for the analysis. Three vibrational modes were considered for this complex, i.e. the H_2O-H_2O stretch (ν_1), and the symmetric (ν_2) and asymmetric (ν_3) H_2O-Xe-H_2O stretches. The force constant matrix $\boldsymbol{F}$ is then a 3×3 matrix with diagonal force constants F_{11}, F_{22}, and F_{33} corresponding to the three vibrational modes respectively. The centrifugal distortion constants of the ^{132}Xe-$(H_2O)_2$, ^{131}Xe-$(H_2O)_2$, and ^{129}Xe-$(H_2O)_2$ isotopomers listed in Table 5-14 were used to refine the diagonal force constants. All off-diagonal terms were fixed at zero during the fit. The corresponding harmonic frequencies were then calculated from the obtained force constants using Wilson's GF matrix method.[58] This analysis could reproduce the D_J, D_{JK}, and d_1, d_2 centrifugal distortion constants within 5% of the experimental values, especially good agreement was found for the D_J and D_{JK} constants. The D_K constants deviate by up to 32% from the experimental values but the deviations are on the same order of the magnitude as the experimental uncertainties. All obtained force constants and harmonic frequencies are summarized in Table 5-18. A comparison of the experimental and calculated centrifugal distortion constants is provided in Table 5-19. The values of the F_{22} (1.489 N m^{-1}) and F_{33} (1.508 N m^{-1}) force constants are 30-40% larger than that of the Xe-H_2O stretching force constant (1.134 N m^{-1}) in the dimer, while the F_{11} value, 10.76 N m^{-1}, is nearly identical to the corresponding value (10.8 N m^{-1}) of the $(H_2O)_2$.[53,56] The increase of the

Xe-H_2O stretching force constant in going from the dimer to the trimer can also be attributed to an attractive electrostatic interaction as a result of the induced dipoles. This attractive force lowers the Xe-H_2O binding potential and leads to a stronger van der Waals bond. The H_2O-H_2O stretch force constant is less affected because of the smaller non-additive electrostatic effect caused by the non-polar Xe atom.

5.5.3 ^{131}Xe nuclear quadrupole coupling constants

The main contribution to the electric field gradient at the Xe nucleus comes from the electric multipole moments of two H_2O molecules. It is therefore sensitive to the H_2O orientations, and I was able to obtain dynamical information about the internal angular coordinates of the Xe-$(H_2O)_2$ complex, and determine effective orientations of the two H_2O molecules from the experimental nuclear quadrupole coupling constants. For example, the surprisingly large value of the off-diagonal constant χ_{ab} (±8.446 MHz) is an indication of high asymmetry of the Xe electron distribution with respect to the *ac*- and *bc*-inertial planes. The two H_2O molecules adopt distinct effective orientations relative to the Xe atom, and as a result, contribute differently to the electric field gradient at the Xe nucleus. From the experimentally determined constants, I calculated the components of the principal quadrupole coupling axis system (*a'b'c'*). The resulting $\chi_{a'a'}$, $\chi_{b'b'}$ and $\chi_{c'c'}$ values are 9.020, -8.212 and -0.808 MHz, respectively. The *c'*-axis coincides with inertial *c*-axis and the *a'*- and *b'*-axes are rotated by 39.3° from the *a*- and *b*-inertial axes. The nuclear quadrupole coupling constants along each Xe-c.m.(H_2O) bond were also determined by projecting the principal axis components onto the corresponding Xe-c.m.(H_2O) intermolecular axis.

The obtained values are 7.614 and -4.414 MHz, respectively. The absolute values are larger by an order of magnitude than the corresponding constant of the ^{131}Xe-H_2O dimer (χ_{aa} = -0.445 MHz), which indicates that the H_2O internal motions are largely hindered in the trimer by interaction with a second H_2O molecule. This also provides evidence for the sensitivity of the electronic structure of the Xe atom upon its surrounding, and the nuclear quadrupole coupling constants can be used to identify the number of surrounding H_2O molecules and their relative positions.

To obtain further information about the effective H_2O orientations, I predicted the nuclear quadrupole coupling constants for different H_2O orientations to search for a geometry that can reproduce the experimental nuclear quadrupole coupling constants. In these calculations, the H_2O monomers were kept rigid at the experimental structure.[59] The intermolecular structural parameters, r, R, and α, were fixed at the values estimated from the rotational constants. Six additional angles are necessary to describe the H_2O orientations, as defined in Figure 5-9(b). θ_1(180°-$\angle$Xe-X_1-O_1), φ_1($\angle$Xe-O_1-X_1-H_1), θ_2(180°-$\angle$Xe-X_2-O_2), and φ_2($\angle$Xe-O_2-X_2-H_2) describe the orientations of two H_2O molecules, relative to the Xe atom. X_1 and X_2 are the c.m. of the two H_2O molecules, respectively. β ($\angle$$O_1$-$O_2$-$X_2$) and τ ($\angle$$X_1$-$O_1$-$O_2$-$X_2$) are used to define the relative orientations of two H_2O molecules.

I first calculated the electric field gradient tensor at the Xe nucleus contributed by the electric multipole moments of each H_2O molecule individually. In each calculation, I considered the dipole[46] and quadrupole moment[47] of H_2O and neglected the higher order electric moments. Four point charges of equal magnitude, two positive and two negative, were used to reproduce the dipole and quadrupole moment of H_2O.

The positive charges lie near the two H atoms, and the negative charges sit on the two sides of the H_2O plane and near the O atom.[60] The electric field gradient tensor at the Xe nucleus was then calculated as a summation over contributions from four point charges.[61] The determined two electric field gradient tensors contributed by two H_2O molecules were summed up to generate the corresponding tensor in the Xe-$(H_2O)_2$ complex. This tensor was then used to obtain the ^{131}Xe nuclear quadrupole coupling constants,[43] according to equation (5-8). The experimental ^{131}Xe nuclear quadrupole coupling constants of the Ne_2-^{131}Xe complex, χ_{aa} (0.564 MHz) and χ_{bb} (-0.256 MHz),[54] were used to approximate the effect of the dispersion interaction.

$$\begin{pmatrix} \chi_{aa} & \chi_{ab} & \chi_{ac} \\ \chi_{ab} & \chi_{bb} & \chi_{bc} \\ \chi_{ac} & \chi_{bc} & \chi_{cc} \end{pmatrix} = -\frac{e(1-\gamma)Q_{Xe}}{h} \begin{pmatrix} q_{aa} & q_{ab} & q_{ac} \\ q_{ab} & q_{bb} & q_{bc} \\ q_{ac} & q_{bc} & q_{cc} \end{pmatrix} + \begin{pmatrix} 0.564 & 0 & 0 \\ 0 & -0.256 & 0 \\ 0 & 0 & -0.308 \end{pmatrix} \quad (5\text{-}8)$$

Here, q_{ij} and χ_{ij} ($i, j = a, b, c$) are the components of the electric field gradient and nuclear quadrupole coupling tensor in the inertial axis system. Q_{Xe} = -0.12 b is the ^{131}Xe nuclear quadrupole moment,[48] and γ = -152 is the Sternheimer shielding factor.[43]

The best agreement between the calculated and experimental constants was found in the structure with $\theta_1 = 148°$, $\varphi_1 = 90°$, $\theta_2 = 43°$, $\varphi_2 = 41°$, $\beta = 30°$, and $\tau = 151°$. The calculated values are χ_{aa} = 2.858 MHz, χ_{bb} = -1.045 MHz, and χ_{ab} = 7.694 MHz, which differ from the experimental ones by 0.7, 0.3, and -0.7 MHz, respectively. It is interesting to note that the χ_{ab} value is more sensitive to the dipole moment of H_2O than the χ_{aa} and χ_{bb} values. For example, if the dipole moment increases by 10%, the χ_{ab} value (8.347 MHz) increases by 0.65 MHz, while the changes in the χ_{aa} (2.941 MHz) and χ_{bb} values (-1.096 MHz) are about 0.1 MHz. This

improvement of the χ_{ab} value without too large an effect on χ_{aa} and χ_{bb} could be viewed as further evidence of the large three-body effect from the non-additive electrostatic interactions as a result of induced dipoles, which supports the above suggestion in the structural and harmonic force field analyses. This calculation can not be viewed as a highly accurate structure determination because of an insufficient description of the dispersion interactions, three-body effects, and large amplitude vibrational motions of the complex. However, this still can be regarded as a reasonable first approximation to generate a picture of the electric field gradient at the Xe nucleus and predict the H_2O orientation within the complex. A more accurate model describing the intermolecular interactions in the complex will improve the structure calculation.

To rationalize the determined effective structure, I performed a complete geometry optimization as described in section 5.2.2. Two minimum energy configurations were located and both configurations have triangular geometries, which are consistent with the experimental results. In Minimum I, the Xe atom approaches the H side of the proton donor water molecule and the 'backside' of the acceptor water. The situation is reversed in Minimum II (see Figure 5-2). The remaining structural parameters, other than the position of the Xe atom, of these two minima agree with each other, and are consistent with the effective, experimental structure obtained from structural and nuclear quadrupole hyperfine analyses (see Table 5-2), considering large amplitude vibrational and internal rotation motions. The experimental position of the Xe atom agrees better with Minimum I, which has a higher zero-point corrected binding energy than Minimum II by ~1 kJ/mol (see Table 5-3). This suggests that the effective structure is highly averaged over the internal

angular coordinates of the complex as a result of a rather delocalized ground state wavefunction. The van der Waals stretching frequencies from the harmonic force field analysis are on the same order of magnitude as the corresponding *ab initio* frequencies (see Table 5-3).

5.5 Summary

A 3-dimensional *ab initio* PES of Xe-H_2O dimer was constructed at the CCSD(T) level of theory. The global minimum corresponds to a planar, hydrogen bonded configuration, close to an L-shaped Xe-HOH structure with a linear Xe-HO arrangement. The potential barrier was found to be lower for the H_2O in-plane rotation compared to the out-of-plane motion. Rotational transitions of the Xe-H_2O dimer within two tunneling states, namely the $\Sigma 0_{00}$ and $\Sigma 1_{01}$ states, were measured and assigned. Nuclear quadrupole hyperfine structures arising from the ^{131}Xe, D, and ^{17}O nuclei were observed and analyzed. The determined structural parameters and force constants suggest that the ground state wavefunction for Xe-H_2O is rather delocalized in the angular coordinates and that the anti-hydrogen bonded orientations and non-planar configurations have significant contribution to the wavefunction. The hyperfine structure analyses were used to derive the information about the vibrational dynamics of the Xe-H_2O and Xe-D_2O complex. The nuclear quadrupole coupling constants of ^{131}Xe and ^{17}O indicate that the two observed tunneling states have different dynamics and that the H_2O unit undergoes less hindered internal motion in the $\Sigma 0_{00}$ state. The obtained effective H_2O orientation also supports that there are significant contributions to the wavefunctions in each state from the anti-hydrogen bonded orientations and

non-planar configurations, and agrees with the structural parameters and force constants obtained from the rotational and centrifugal distortion constants.

Several *a*- type and *b*- type rotational transitions of the ground state were measured for the Xe-$(H_2O)_2$ trimer. The spectroscopic results provide detailed information about structure and vibrational dynamics of the complex. The analyses suggest that an attractive electrostatic interaction as a result of induced dipole moments makes crucial contributions to non-additive three-body effects. Nuclear quadrupole hyperfine structures due to the presence of the ^{131}Xe nucleus were detected and provide detailed insight into the electronic structure of the Xe atom. The coupling constants are therefore an exquisite probe of the electrostatic environment of the Xe atom. In particular, the large value of the off-diagonal nuclear quadrupole coupling constant, χ_{ab}, provides evidence for different contributions to the electronic environment of the Xe nucleus by the two H_2O molecules. An effective structure of the trimer, based on reproducing the experimental ^{131}Xe nuclear quadrupole coupling constants, is supported by *ab initio* calculations. The information provided into the variations of structure and vibrational dynamics in going from the Xe-H_2O dimer to the Xe-$(H_2O)_2$ trimer constitutes a step towards the understanding of "macroscopic" Xe-water surroundings interactions. The interpretation of the ^{131}Xe nuclear quadrupole coupling constants can shed light on the effect of the surrounding water distribution upon the electronic structure of the Xe atom.

Table 5-1: *Ab initio* interaction energies (in cm^{-1}) of Xe-H_2O.

R / Å	$\varphi = 0°$						
	$\theta = 0°$	10°	20°	30°	40°	50°	60°
3.5	28.95	40.34	71.26	112.0	147.7	162.1	144.9
3.6	-65.71	-59.43	-42.60	-20.91	-2.966	2.381	-10.15
3.7	-122.5	-119.6	-112.0	-102.6	-95.80	-95.76	-104.5
3.8	-153.5	-152.7	-150.9	-149.2	-149.1	-151.9	-157.7
3.9	-167.0	-167.5	-169.2	-172.0	-175.9	-180.1	-183.6
4	-169.1	-170.3	-174.0	-179.4	-185.2	-189.9	-191.7
4.1	-164.1	-165.6	-170.3	-176.9	-183.6	-188.1	-188.8
4.2	-154.8	-156.5	-161.5	-168.4	-175.2	-179.42	-179.2
4.3	-143.1	-145.0	-149.9	-156.6	-163.1	-166.8	-166.0
	$\theta = 70°$	80°	90°	100°	110°	120°	130°
3.5	97.47	34.33	-27.76	-76.95	-108.4	-122.8	-123.6
3.6	-39.24	-76.00	-110.8	-137.3	-153.3	-159.3	-157.5
3.7	-121.0	-140.0	-156.7	-168.3	-174.1	-174.8	-171.8
3.8	-165.7	-173.0	-177.9	-180.0	-179.4	-177.0	-173.6
3.9	-185.8	-185.7	-183.3	-179.5	-175.1	-171.0	-167.6
4	-190.3	-185.6	-178.8	-171.7	-165.3	-160.4	-157.1
4.1	-185.1	-177.8	-168.7	-159.9	-152.5	-150.0	-144.5
4.2	-174.2	-165.7	-155.7	-146.1	-138.6	-133.6	-131.1
4.3	-160.5	-151.5	-141.3	-131.8	-124.6	-120.0	-117.8
	$\theta = 140°$	150°	160°	170°	180°		
3.5	-115.3	-103.0	-90.78	-82.08	-78.94		
3.6	-150.9	-142.3	-134.2	-128.6	-126.6		
3.7	-166.7	-161.0	-155.9	-152.5	-151.3		
3.8	-169.7	-166.2	-163.2	-161.3	-160.7		
3.9	-164.9	-162.8	-161.4	-160.6	-160.3		
4	-155.3	-154.4	-154.0	-153.9	-153.9		
4.1	-143.3	-143.2	-143.6	-144.0	-144.1		
4.2	-130.4	-130.9	-131.7	-132.4	-132.7		
4.3	-117.5	-118.3	-119.4	-120.3	-120.6		

R / Å	$\varphi = 30°$						
	$\theta = 0°$	10°	20°	30°	40°	50°	60°
3.5		37.15	58.90	86.09	107.5	112.7	97.06
3.6		-60.96	-48.51	-33.07	-21.15	-18.61	-28.02
3.7		-120.1	-113.8	-106.0	-100.1	-99.12	-104.1
3.8		-152.5	-150.1	-147.2	-145.1	-144.9	-146.8
3.9		-167.0	-167.0	-167.0	-167.2	-167.4	-167.1
4		-169.6	-171.0	-172.8	-174.2	-174.3	-172.8
4.1		-164.8	-167.0	-169.7	-171.6	-171.8	-169.4
4.2		-155.6	-158.1	-161.2	-163.4	-163.4	-160.6
4.3		-144.2	-146.7	-149.8	-151.9	-151.8	-148.8

Table 5-1: (continued).

R/Å	$\varphi = 30°$						
	$\theta = 70°$	80°	90°	100°	110°	120°	130°
3.5	63.39	20.36	-22.34	-57.68	-82.33	-95.99	-100.3
3.6	-47.51	-72.25	-96.51	-116.4	-130.3	-137.8	-139.9
3.7	-114.0	-126.3	-138.2	-147.9	-154.5	-158.0	-158.7
3.8	-150.3	-154.4	-158.2	-161.2	-163.1	-164.0	-164.0
3.9	-166.4	-165.3	-164.0	-162.9	-161.8	-161.2	-160.8
4	-169.6	-165.4	-161.1	-157.3	-154.6	-153.0	-152.4
4.1	-164.8	-158.8	-152.7	-147.6	-144.0	-142.0	-141.4
4.2	-155.2	-148.4	-141.7	-135.9	-131.9	-129.8	-129.2
4.3	-143.2	-136.2	-129.2	-123.4	-119.4	-117.3	-116.7
	$\theta = 140°$	150°	160°	170°	180°		
3.5	-98.00	-92.15	-85.63	-80.74			
3.6	-138.2	-134.6	-130.6	-127.6			
3.7	-157.6	-155.6	-153.4	-151.8			
3.8	-163.4	-162.5	-161.6	-160.9			
3.9	-160.6	-160.5	-160.4	-160.3			
4	-152.6	-152.9	-153.4	-153.8			
4.1	-141.7	-142.5	-143.3	-143.9			
4.2	-129.6	-130.6	-131.6	-132.4			
4.3	-117.3	-118.3	-119.5	-120.3			

R/Å	$\varphi = 60°$						
	$\theta = 0°$	10°	20°	30°	40°	50°	60°
3.5		30.87	35.70	40.91	43.57	41.64	34.61
3.6		-64.04	-59.72	-54.37	-50.06	-48.41	-50.11
3.7		-121.1	-117.3	-112.0	-106.9	-103.0	-101.4
3.8		-152.2	-148.8	-143.8	-138.3	-133.3	-129.6
3.9		-165.9	-162.8	-158.2	-152.7	-147.1	-142.3
4		-168.1	-165.4	-161.2	-155.9	-150.2	-144.9
4.1		-163.2	-160.8	-157.0	-152.0	-146.4	-141.1
4.2		-154.1	-151.9	-148.4	-143.9	-138.6	-133.4
4.3		-142.5	-140.7	-137.6	-133.4	-128.6	-123.7
	$\theta = 70°$	80°	90°	100°	110°	120°	130°
3.5	23.28	9.152	-6.140	-21.18	-34.98	-46.97	-56.96
3.6	-55.07	-62.59	-71.74	-81.56	-91.22	-100.1	-108.0
3.7	-102.2	-105.3	-110.2	-116.3	-123.0	-129.6	-135.7
3.8	-127.8	-128.0	-130.1	-133.7	-138.2	-143.0	-147.8
3.9	-139.0	-137.4	-137.7	-139.5	-142.4	-146.0	-149.7
4	-140.7	-138.1	-137.3	-138.0	-139.8	-142.4	-145.3
4.1	-136.6	-133.5	-131.8	-131.7	-132.8	-134.7	-137.0
4.2	-128.9	-125.5	-123.6	-123.0	-123.6	-125.0	-126.7
4.3	-119.3	-116.0	-113.9	-113.1	-113.3	-114.3	-115.7

Table 5-1: (continued).

R /Å				$\varphi = 60°$			
	$\theta = 140°$	150°	160°	170°	180°		
3.5	-64.98	-71.12	-75.47	-78.08			
3.6	-114.5	-119.7	-123.5	-125.8			
3.7	-141.0	-145.3	-148.6	-150.6			
3.8	-152.1	-155.7	-158.4	-160.1			
3.9	-153.2	-156.1	-158.4	-159.8			
4	-148.1	-150.5	-152.3	-153.5			
4.1	-139.2	-141.2	-142.8	-143.8			
4.2	-128.6	-130.2	-131.5	-132.4			
4.3	-117.2	-118.6	-119.7	-120.4			
R /Å				$\varphi = 90°$			
	$\theta = 0°$	10°	20°	30°	40°	50°	60°
3.5		27.78	24.8	21.07	17.51	14.59	12.17
3.6		-65.58	-65.03	-63.85	-62.12	-60.20	-58.67
3.7		-121.6	-117.7	-114.8	-109.9	-105.1	-101.2
3.8		-152.1	-148.2	-142.5	-135.9	-129.5	-124.3
3.9		-165.4	-160.9	-154.4	-147.1	-140.0	-134.3
4		-167.4	-162.8	-156.2	-148.6	-141.4	-135.7
4.1		-162.5	-158.0	-151.5	-144.1	-137.2	-131.5
4.2		-153.2	-149.0	-142.9	-135.9	-129.4	-124.2
4.3		-141.7	-137.8	-132.2	-125.9	-119.9	-115.1
	$\theta = 70°$	80°	90°	100°	110°	120°	130°
3.5	9.699	6.4375	1.6885	-5.013	-13.87	-24.63	-36.73
3.6	-58.20	-59.36	-62.51	-67.74	-74.93	-83.69	-93.44
3.7	-98.98	-98.8	-100.8	-104.9	-110.7	-117.7	-125.5
3.8	-121.1	-120.1	-121.3	-124.4	-129.0	-134.7	-140.9
3.9	-130.6	-129.1	-129.7	-132.1	-135.8	-140.4	-145.2
4	-131.8	-130.1	-130.4	-132.2	-135.2	-138.8	-142.6
4.1	-127.7	-126.0	-126.0	-127.4	-129.7	-132.6	-135.6
4.2	-120.6	-118.8	-118.7	-119.7	-121.6	-123.9	-126.2
4.3	-111.8	-110.1	-109.8	-110.7	-112.1	-114.0	-115.8
	$\theta = 140°$	150°	160°	170°	180°		
3.5	-49.21	-60.88	-70.45	-76.75			
3.6	-103.4	-112.5	-120.0	-124.9			
3.7	-133.3	-140.4	-146.2	-150.0			
3.8	-147.0	-152.5	-156.8	-159.7			
3.9	-150.0	-154.1	-157.5	-159.6			
4	-146.2	-149.4	-151.9	-153.4			
4.1	-138.4	-140.8	-142.6	-167.1			
4.2	-128.4	-130.2	-131.5	-132.4			
4.3	-117.4	-118.8	-119.8	-120.4			

Table 5-2: The structures of *ab initio* local minima of the Xe-$(H_2O)_2$ complex and comparison with the effective structure obtained from experimental rotational constants and ^{131}Xe nuclear quadrupole coupling constants.

	Minimum I	Minimum II	Effective structure [a]
r (O_1···H_1) /Å	0.9673	0.9668	0.9724
r (O_1···$H_{1'}$) /Å	0.9673	0.9679	0.9724
∠ $H_{1'}O_1H_1$ /°	104.48	104.49	104.50
r (O_2···H_2) /Å	0.9652	0.9653	0.9724
r (O_2···$H_{2'}$) /Å	0.9734	0.9740	0.9724
∠ $H_{2'}O_2H_2$ /°	104.31	104.61	104.50
r (X_1···X_2) /Å	2.923	2.907	2.992
r (Xe···X_1) /Å	3.756	3.777	3.879
r (Xe···X_2) /Å	3.884	3.609	3.879
∠ $X_1O_1O_2$ /°	120	119	145
∠ $O_1O_2X_2$ /°	58	61	30
∠ $X_1O_1O_2X_2$ /°	180	158	151
∠ $H_{1'}X_1O_1O_2$ /°	90	77	90
∠ $H_{2'}X_2O_2O_1$ /°	0	3	0
∠ $XeO_1O_2X_2$ /°	0	157	331

[a] The water monomer was fixed at its experimental structure from Ref. 59.

Table 5-3: Calculated counterpoise corrected binding energies (D_e) and zero-point vibrational energy corrections (ΔZPE) in units of kJ/mol for the *ab initio* local minima of the Xe-$(H_2O)_2$ complex and comparison of van der Waals stretching frequencies (in cm^{-1}) from *ab initio* calculations and harmonic force field analysis.

	Minimum I	Minimum II	Harmonic force field analysis
D_e	-22.24	-23.63	
ΔZPE	10.56	10.93	
$D_0 = D_e + \Delta ZPE$	-11.68	-12.70	
H_2O-H_2O stretch	157.5	168.3	143.2
H_2O-Xe-H_2O symmetric stretch	45.8	56.1	38.4
H_2O-Xe-H_2O asymmetric stretch	47.4	47.9	38.8

Table 5-4: Measured transition frequencies and determined spectroscopic constants for Xe-H_2O isotopomers.

	^{136}Xe-H_2O		^{134}Xe-H_2O		^{132}Xe-H_2O		^{129}Xe-H_2O	
J'-J''	ν_{obs} (MHz)	$\Delta\nu$[a] (kHz)	ν_{obs} (MHz)	$\Delta\nu$ (kHz)	ν_{obs} (MHz)	$\Delta\nu$ (kHz)	ν_{obs} (MHz)	$\Delta\nu$ (kHz)
				$\Sigma 0_{00}$				
1-0	4076.7294	-0.06	4083.7680	-0.8	4091.0195	-1.0	4102.3064	-0.8
2-1	8152.7126	0.05	8166.7894	0.6	8181.2879	-0.5	8203.8596	0.7
3-2	12227.2029	-0.01	12248.3110	-0.2	12270.0524	1.3	12303.8994	-0.2
4-3					16356.5556	-0.5	16401.6739	0.02
B /MHz	2038.4269 (4)		2041.9468 (4)		2045.5730 (2)		2051.2166 (2)	
D_J /kHz	31.10(2)		31.20(2)		31.358(9)		31.479(9)	
σ /kHz[b]	0.04		0.6		0.9		0.5	
				$\Sigma 1_{01}$				
1-0	3997.6954	0.2	4004.4375	-2.2	4011.3860	-0.8	4022.2011	-0.3
2-1	7994.8759	-1.4	8008.3659	0.2	8022.2580	-0.7	8043.8850	-0.6
3-2	11991.0344	1.4	12011.2659	1.4	12032.1023	1.4	12064.5365	0.9
4-3	15985.6487	-0.4	16012.6218	-0.6	16040.3978	-0.5	16083.6340	-0.3
B /MHz	1998.8904 (2)		2002.2626 (2)		2005.7363 (2)		2011.1438 (2)	
D_J /kHz	21.382(9)		21.402(9)		21.454(9)		21.547(9)	
σ /kHz	1.0		1.3		0.9		0.6	

[a] $\Delta\nu = \nu_{obs} - \nu_{cal}$.
[b] Standard deviation of the fit.

Table 5-5: Measured transition frequencies and determined spectroscopic constants of ^{131}Xe-H_2O.

		$\Sigma 0_{00}$		$\Sigma 1_{01}$	
J'-J''	F'-F''	ν_{obs} (MHz)	$\Delta\nu$ (kHz)[a]	ν_{obs} (MHz)	$\Delta\nu$ (kHz)
1-0	1.5-1.5	4094.6347	0.9	4014.5704	-0.9
	2.5-1.5	4094.7445	-0.6	4015.0244	-0.3
	0.5-1.5	4094.8347	0.6	4015.3863	-1.2
2-1	1.5-0.5	8188.5777	-3.4	8028.8982	-0.8
	2.5-2.5	8188.5932	2.6	8028.9381	0.3
	0.5-0.5			8029.3512	-1.2
	2.5-1.5	8188.7023	0.5	8029.3924	1.1
	3.5-2.5	8188.7023	0.5	8029.3924	1.1
	1.5-1.5	8188.7810	-0.3	8029.7144	-0.8
	0.5-1.5	8188.8924	-0.2		
3-2	2.5-1.5	12281.1340	1.1	12042.6495	0.6
	1.5-0.5	12281.1340	1.1	12042.6495	0.6
	3.5-2.5	12281.1595	-0.9	12042.7626	1.5
	4.5-3.5	12281.1595	-0.9	12042.7626	1.5
	2.5-2.5			12042.9740	1.2
4-3	4.5-3.5			16054.5924	-1.2
	5.5-4.5			16054.5924	-1.2
B /MHz		2047.4242(2)		2007.5100(2)	
D_J /kHz		31.39(1)		21.484(7)	
$\chi_{aa}(^{131}Xe)$ /MHz		-0.445(1)		-1.814(2)	
σ /kHz[b]		1.5		1.0	

[a] $\Delta\nu = \nu_{obs} - \nu_{cal}$.
[b] Standard deviation of the fit.

Table 5-6: Measured transition frequencies and determined spectroscopic constants for Xe-$H_2{}^{18}O$ isotopomers.

	^{136}Xe-$H_2{}^{18}O$		^{134}Xe- $H_2{}^{18}O$		^{132}Xe- $H_2{}^{18}O$		^{129}Xe- $H_2{}^{18}O$	
J'-J''	ν_{obs} (MHz)	$\Delta\nu$[a] (kHz)	ν_{obs} (MHz)	$\Delta\nu$ (kHz)	ν_{obs} (MHz)	$\Delta\nu$ (kHz)	ν_{obs} (MHz)	$\Delta\nu$ (kHz)
				$\Sigma 0_{00}$				
1-0			3726.2559	0.3	3733.5192	0.8	3744.8255	0.8
2-1	7437.7763	0.0	7451.8756	-0.2	7466.3985	-0.3	7489.0073	-0.3
3-2	11155.0822	0.0	11176.2252	0.05	11198.0026	-0.2	11231.9066	-0.3
4-3					14927.6926	0.1	14972.8808	0.1
B /MHz	1859.6550(5)		1863.1808(4)		1866.8124(2)		1872.4658(2)	
D_J /kHz	26.37(3)		26.48(2)		26.589(9)		26.742(9)	
σ /kHz[b]	0.0		0.2		0.4		0.4	
				$\Sigma 1_{01}$				
1-0	3654.2615	1.2	3661.0419	-1.8	3668.0320	-0.1	3678.9110	1.1
2-1	7308.0688	-0.2	7321.6357	0.6	7335.6097	-0.3	7357.3625	-0.6
3-2	10960.9739	-0.7	10981.3224	0.6	11002.2797	0.4	11034.9027	-0.2
4-3	14612.5257	0.3	14639.6512	-0.3	14667.5857	-0.1	14711.0727	0.1
B /MHz	1827.1678(2)		1830.5596(2)		1834.0539(2)		1839.4930(2)	
D_J /kHz	18.815(9)		18.847(9)		18.928(9)		19.029(9)	
σ /kHz	0.7		1.0		0.3		0.6	

[a] $\Delta\nu = \nu_{obs} - \nu_{cal}$.

[b] Standard deviation of the fit.

Table 5-7: Measured transition frequencies and determined spectroscopic constants of $^{131}Xe\text{-}H_2{}^{18}O$.

		$\Sigma 0_{00}$		$\Sigma 1_{01}$	
J'-J''	F'-F''	ν_{obs} (MHz)	$\Delta\nu$ (kHz) [a]	ν_{obs} (MHz)	$\Delta\nu$ (kHz)
1-0	2.5-1.5			3671.6889	-1.4
2-1	1.5-0.5	7473.6979	-3.5	7342.2922	1.8
	2.5-2.5	7473.7146	3.5	7342.3279	-1.4
	2.5-1.5	7473.8243	0.5	7342.7831	-0.5
	3.5-2.5	7473.8243	0.5	7342.7831	-0.5
	1.5-1.5	7473.9039	-0.5	7343.1093	1.2
3-2	2.5-1.5			11012.8908	0.4
	1.5-0.5			11012.8908	0.4
	3.5-2.5	11209.1294	0.0	11013.0022	-0.7
	4.5-3.5	11209.1294	0.0	11013.0022	-0.7
B /MHz		1868.6665(3)		1835.8376(2)	
D_J /kHz		26.62(2)		18.93(2)	
$\chi_{aa}(^{131}Xe)$ /MHz		-0.451(3)		-1.817(3)	
σ /kHz [b]		2.2		1.2	

[a] $\Delta\nu = \nu_{obs} - \nu_{cal}$.
[b] Standard deviation of the fit.

Table 5-8: Measured transition frequencies and determined spectroscopic constants of Xe-$H_2{}^{17}O$ isotopomers.

			$\Sigma 0_{00}$		$\Sigma 1_{01}$	
	J'-J''	F'-F''	ν_{obs}(MHz)	$\Delta\nu$ (kHz)[a]	ν_{obs}(MHz)	$\Delta\nu$ (kHz)
^{132}Xe-$H_2{}^{17}O$	2-1	2.5-1.5			7659.7039	-2.3
		3.5-3.5			7659.8755	2.0
		2.5-3.5			7660.0871	4.4
		1.5-1.5			7660.3029	-0.9
		4.5-3.5	7804.4223	0.3	7660.6762	-4.1
		3.5-2.5	7804.4449	-0.6	7660.7506	-1.4
		0.5-1.5	7804.4751	0.2	7660.8423	0.6
		2.5-2.5	7804.5141	0.02	7660.9609	-0.4
		1.5-2.5			7661.5610	2.1
		B /MHz	1950.8663(3)		1914.9861(1)	
		D_J /kHz[b]	28.974		20.191	
		$\chi_{aa}(^{17}O)$ /MHz	-1.372(20)		-4.1837(33)	
		σ/kHz[c]	0.4		2.4	
^{129}Xe-$H_2{}^{17}O$	2-1	1.5-1.5			7681.9989	1.7
		4.5-3.5	7827.0133	-0.5	7682.3697	-1.7
		3.5-2.5	7827.0361	-0.7	7682.4397	-3.0
		0.5-1.5	7827.0679	2.4		
		2.5-2.5	7827.1027	-1.2	7682.6536	3.0
		B /MHz	1956.5134(3)		1920.4083(1)	
		D_J /kHz	29.111		20.288	
		$\chi_{aa}(^{17}O)$ /MHz	-1.342(20)		-4.157(9)	
		σ/kHz	1.4		2.4	

[a] $\Delta\nu = \nu_{obs} - \nu_{cal}$.
[b] D_J constants are fixed at the average value of corresponding constants for Xe-$H_2{}^{16}O$ and Xe-$H_2{}^{18}O$ isotopomers.
[c] Standard deviation of the fit.

Table 5-9: Measured transition frequencies and determined spectroscopic constants of Xe-D_2O istopomers.

		$\Sigma 0_{00}$			$\Sigma 1_{01}$		
	J'-J''	$I'F'$-$I''F''$	ν_{obs}(MHz)	$\Delta\nu$ (kHz)[a]	$I'F'$-$I''F''$	ν_{obs}(MHz)	$\Delta\nu$ (kHz)
^{136}Xe-D_2O	1-0	23-22	3719.0434	-4.5			
		01-00	3719.0647	-4.0			
		01-22	3719.0647	-4.0			
		22-22	3719.0647	-6.3			
	2-1	21-22	7437.5083	1.0	12-12	7304.9191	3.2
		02-01	7437.5083	2.7	11-10	7304.9191	-0.4
		23-22	7437.5336	-1.3	12-11	7304.9362	-0.9
		24-23	7437.5336	-2.4	13-12	7304.9362	-2.5
		22-22	7437.5461	3.5	11-11	7304.9733	0.8
		22-01	7437.5461	1.2			
		02-21	7437.5625	7.4			
		23-23	7437.5625	4.4			
		21-21	7437.5625	3.4			
	3-2	03-02	11154.8863	-3.8	14-13	10956.3662	-2.3
		23-22	11154.8863	-3.3	13-12	10956.3662	-1.5
		25-24	11154.8863	-0.4	12-11	10956.3662	2.1
		24-23	11154.8863	0.3			
	4-3	23-22	14870.5350	-2.5	15-14	14606.5524	-0.7
		22-21	14870.5350	-1.4	14-13	14606.5524	-0.2
		04-03	14870.5350	0.05	13-12	14606.5524	1.4
		24-23	14870.5350	0.2			
		26-25	14870.5350	1.6			
		25-24	14870.5350	2.0			
	B /MHz		1859.5738(2)			1826.3727(2)	
	D_J /kHz		23.658(7)			17.301(8)	
	χ_{aa}(D) /MHz		0.0515(12)			0.0707(18)	
	σ /kHz[b]		3.2			1.1	
^{134}Xe-D_2O	1-0	23-22	3726.0890	0.7			
	2-1	21-22	7451.5861	0.2	12-12	7318.4611	2.0
		02-01	7451.5861	1.9	11-10	7318.4611	-1.4
		23-22	7451.6116	-1.8	12-11	7318.4793	-0.2
		24-23	7451.6116	-2.9	13-12	7318.4793	-1.7
		22-22	7451.6236	2.5	11-11	7318.5137	0.2
		22-01	7451.6236	0.2			
		02-21	7451.6370	3.5			
		23-23	7451.6370	0.5			
		21-21	7451.6370	-0.5			

Table 5-9: (continued).

		$\Sigma 0_{00}$			$\Sigma 1_{01}$		
	J'-J''	$I'F'$-$I''F''$	ν_{obs}(MHz)	$\Delta\nu$ (kHz)[a]	$I'F'$-$I''F''$	ν_{obs}(MHz)	$\Delta\nu$ (kHz)
^{134}Xe-D_2O	3-2	03-02	11175.9982	-3.9	14-13	10976.6762	-1.1
		23-22	11175.9982	-3.4	13-12	10976.6762	-0.3
		25-24	11175.9982	-0.5	12-11	10976.6762	3.1
		24-23	11175.9982	0.2			
	4-3	23-22	14898.6743	-1.8	15-14	14633.6218	-1.0
		22-21	14898.6743	-0.7	14-13	14633.6218	-0.5
		04-03	14898.6743	0.7	13-12	14633.6218	1.0
		24-23	14898.6743	0.8			
		26-25	14898.6743	2.3			
		25-24	14898.6743	2.6			
	B /MHz		1863.0942(2)			1829.7589(2)	
	D_J /kHz		23.753(7)			17.379(8)	
	χ_{aa}(D) /MHz		0.0513(14)			0.0680(18)	
	σ /kHz		1.4			0.5	
^{132}Xe-D_2O	1-0	23-22	3733.3397	-0.0	12-11	3666.4242	-2.2
		01-00	3733.3611	0.6	10-11	3666.4597	0.7
		01-22	3733.3611	0.6			
		22-22	3733.3611	-1.7			
	2-1	21-22	7466.0872	0.9	12-12	7332.4092	3.6
		02-01	7466.0872	2.6	11-10	7332.4092	-0.05
		23-22	7466.1114	-2.4	12-11	7332.4271	-0.3
		24-23	7466.1114	-3.5	13-12	7332.4271	-1.9
		22-22	7466.1234	1.9	11-11	7332.4642	0.5
		22-01	7466.1234	-0.4			
		02-21	7466.1385	4.6			
		23-23	7466.1385	1.6			
		21-21	7466.1385	0.6			
	3-2	03-02	11197.7424	-4.0	14-13	10997.5946	-2.1
		23-22	11197.7424	-3.5	13-12	10997.5946	-1.3
		25-24	11197.7424	-0.6	12-11	10997.5946	2.4
		24-23	11197.7424	0.06			
	4-3	23-22	14927.6548	-1.9	15-14	14661.5097	-0.9
		22-21	14927.6548	-0.8	14-13	14661.5097	-0.3
		04-03	14927.6548	0.7	13-12	14661.5097	1.2
		24-23	14927.6548	0.8			
		26-25	14927.6548	2.2			
		25-24	14927.6548	2.6			

Table 5-9: (continued).

			$\Sigma 0_{00}$			$\Sigma 1_{01}$	
	J'-J''	$I'F'$-$I''F''$	ν_{obs}(MHz)	$\Delta\nu$ (kHz)[a]	$I'F'$-$I''F''$	ν_{obs}(MHz)	$\Delta\nu$ (kHz)
^{132}Xe-D_2O	B /MHz		1866.7201(2)			1833.2462(2)	
	D_J /kHz		23.857(7)			17.421(8)	
	χ_{aa}(D) /MHz		0.0513(12)			0.0726(14)	
	σ /kHz		1.7			1.2	
^{129}Xe-D_2O	1-0	23-22	3744.6274	-0.9	12-11	3677.2840	0.8
		01-00	3744.6491	0.07			
		01-22	3744.6491	0.07			
		22-22	3744.6491	-2.2			
	2-1	21-22	7488.6605	0.6	12-12	7354.1199	2.2
		02-01	7488.6605	2.3	11-10	7354.1199	-1.3
		23-22	7488.6853	-2.1	12-11	7354.1385	-0.7
		24-23	7488.6853	-3.1	13-12	7354.1385	-2.2
		22-22	7488.6971	2.1	11-11	7354.1752	0.2
		22-01	7488.6971	-0.2			
		02-21	7488.7119	4.5			
		23-23	7488.7119	1.5			
		21-21	7488.7119	0.5			
	3-2	03-02	11231.5947	-3.2	14-13	11030.1580	-1.5
		23-22	11231.5947	-2.6	13-12	11030.1580	-0.6
		25-24	11231.5947	0.3	12-11	11030.1580	3.0
		24-23	11231.5947	0.9			
	4-3	23-22	14972.7733	-2.2	15-14	14704.9175	-0.9
		22-21	14972.7733	-1.1	14-13	14704.9175	-0.4
		04-03	14972.7733	0.3	13-12	14704.9175	1.2
		24-23	14972.7733	0.4			
		26-25	14972.7733	1.9			
		25-24	14972.7733	2.3			
	B /MHz		1872.3647(2)			1838.6748(2)	
	D_J /kHz		24.006(7)			17.502(8)	
	χ_{aa}(D) /MHz		0.0513(12)			0.0717(18)	
	σ /kHz		1.5			0.7	

[a] $\Delta\nu = \nu_{obs} - \nu_{cal}$.
[b] Standard deviation of the fit.

Table 5-10: Measured transition frequencies and determined spectroscopic constants of ^{131}Xe-D_2O.

	$\Sigma 0_{00}$			$\Sigma 1_{01}$		
J'-J''	$F_1', I', F' - F_1'', I'', F''$	ν_{obs}(MHz)	$\Delta\nu$[a] (kHz)	$F_1', I', F' - F_1'', I'', F''$	ν_{obs}(MHz)	$\Delta\nu$ (kHz)
1-0	1.5, 2, 2.5 - 1.5, 2, 2.5	3736.74170	-0.4			
	2.5, 2, 4.5 - 1.5, 2, 3.5	3737.11010	-2.5			
	0.5, 2, 2.5 - 1.5, 2, 3.5	3737.40910	-2.6			
2-1	1.5, 2, 3.5 - 0.5, 2, 2.5	7473.15690	0.4	3.5, 1, 2.5 - 2.5, 1, 1.5	7339.6039	0.01
	0.5, 2, 2.5 - 0.5, 2, 2.5	7473.51890	-0.6	3.5, 1, 4.5 - 2.5, 1, 3.5	7339.6039	-0.01
	3.5, 0, 3.5 - 2.5, 0, 2.5	7473.55110	-1.5			
	3.5, 2, 5.5 - 2.5, 2, 4.5	7473.55110	1.8			
	1.5, 0, 1.5 - 1.5, 2, 1.5	7473.79180	1.0			
	1.5, 2, 2.5 - 1.5, 2, 3.5	7473.81030	3.9			
3-2	4.5, 2, 6.5 - 3.5, 2, 5.5	11208.86400	-0.6	3.5, 1, 4.5 - 2.5, 1, 3.5	11008.3054	-0.7
	4.5, 0, 4.5 - 3.5, 0, 3.5	11208.86400	-0.3	4.5, 1, 5.5 - 3.5, 1, 4.5	11008.3054	0.7
4-3	5.5, 2, 6.5 - 4.5, 2, 5.5	14942.46730	-0.3	4.5, 1, 5.5 - 3.5, 1, 4.5	14675.7679	-0.3
	5.5, 0, 5.5 - 4.5, 0, 4.5	14942.46730	-0.1	5.5, 1, 6.5 - 4.5, 1, 5.5	14675.7679	0.3
	B /MHz	1868.5714(2)			1835.0250(9)	
	D_J /kHz	23.883(7)			17.40(2)	
	χ_{aa}(^{131}Xe) /MHz	-1.449(2)			-2.76(15)	
	χ_{aa}(D) /MHz	0.0689(31)			0.0726(fixed)	
	σ /kHz[b]	1.7			0.0	

[a] $\Delta\nu = \nu_{obs} - \nu_{cal}$.
[b] Standard deviation of the fit.

Table 5-11: Measured transition frequencies and determined spectroscopic constants of Xe-HDO isotopomers ($\Sigma 0_{00}$ state).

		^{136}Xe-HDO		^{134}Xe-HDO		^{132}Xe-HDO		^{129}Xe-HDO	
J'-J''	F'-F''	ν_{obs} (MHz)	$\Delta\nu$[a] (kHz)	ν_{obs} (MHz)	$\Delta\nu$ (kHz)	ν_{obs} (MHz)	$\Delta\nu$ (kHz)	ν_{obs} (MHz)	$\Delta\nu$ (kHz)
1-0	2-1					3906.9467	-2.1	3918.2476	-0.9
	1-1					3906.9633	0.6		
2-1	1-1	7784.6142	1.4	7798.7072	1.6	7813.2198	1.7	7835.8153	1.7
	2-1	7784.6324	-3.3	7798.7256	-3.3	7813.2393	-2.0	7835.8340	-3.0
	3-2	7784.6324	-2.3	7798.7256	-2.3	7813.2393	-1.0	7835.8340	-2.0
	1-0	7784.6509	3.8	7798.7445	4.0	7813.2563	3.4	7835.8527	4.0
	2-2	7784.6509	1.5	7798.7445	1.6	7813.2563	1.1	7835.8527	1.7
3-2	2-1	11675.3124	-3.2	11696.4454	-3.5	11718.2086	-3.5	11752.0924	-3.5
	3-2	11675.3124	-0.9	11696.4454	-1.1	11718.2086	-1.1	11752.0924	-1.1
	4-3	11675.3124	-0.4	11696.4454	-0.6	11718.2086	-0.6	11752.0924	-0.6
4-3	3-2	15564.0234	-0.3	15592.1887	-0.2	15621.1962	-0.3	15666.3564	-0.3
	4-3	15564.0234	0.7	15592.1887	0.8	15621.1962	0.7	15666.3564	0.7
	5-4	15564.0234	1.0	15592.1887	1.1	15621.1962	1.0	15666.3564	1.0
B /MHz		1946.3776 (2)		1949.9018 (2)		1953.5306 (2)		1959.1808 (2)	
D_J /kHz		27.337(8)		27.447(8)		27.537(7)		27.699(8)	
χ_{aa}(D) /MHz		0.0459(18)		0.0465(18)		0.0464(16)		0.0467(18)	
σ /kHz[b]		2.0		2.1		1.6		1.9	

[a] $\Delta\nu = \nu_{obs} - \nu_{cal}$.

[b] Standard deviation of the fit.

Table 5-12: Measured transition frequencies and spectroscopic constants of ^{131}Xe-HDO ($\Sigma 0_{00}$ state).

J'-J''	F_1', F' - F_1'', F''	ν_{obs}(MHz)	$\Delta\nu^a$ (kHz)
1-0	2.5, 1.5 - 1.5, 0.5	3910.7004	-0.3
	0.5, 1.5 - 1.5, 2.5	3910.9081	-0.4
2-1	1.5, 2.5 - 0.5, 1.5	7820.4020	-0.3
	2.5, 3.5 - 2.5, 3.5	7820.4257	-0.07
	2.5, 3.5 - 1.5, 2.5	7820.6739	2.3
	3.5, 4.5 - 2.5, 3.5	7820.6739	0.2
3-2	3.5, 4.5 - 2.5, 3.5	11729.3355	-0.05
	4.5, 5.5 - 3.5, 4.5	11729.3355	-0.9
4-3	4.5, 5.5 - 3.5, 4.5	15636.0180	0.3
	5.5, 6.5 - 4.5, 5.5	15636.0180	-0.1
	B /MHz	1955.3840(2)	
	D_J /kHz	27.582(8)	
	χ_{aa}(^{131}Xe) /MHz	-1.000(2)	
	χ_{aa}(D) /MHz	0.049(7)	
	σ/kHz[b]	0.5	

[a] $\Delta\nu = \nu_{obs} - \nu_{cal}$.
[b] Standard deviation of the fit.

Table 5-13: Measured transition frequencies of the ^{132}Xe-$(H_2O)_2$ and ^{129}Xe-$(H_2O)_2$ isotopomers.

	^{132}Xe-$(H_2O)_2$		^{129}Xe-$(H_2O)_2$	
$J'_{Ka'Kc'}$-$J''_{Ka''Kc''}$	ν_{obs} (MHz)	$\Delta\nu$ [a] (kHz)	ν_{obs} (MHz)	$\Delta\nu$ (kHz)
$2_{02}-1_{01}$	5052.8353	-0.2	5075.5680	-0.9
$2_{12}-1_{11}$	4805.4089	-0.9	4826.0288	3.0
$2_{11}-1_{10}$	5319.6898	0.2	5344.9182	-0.3
$3_{03}-2_{02}$	7554.2624	0.5	7587.8870	-0.7
$3_{13}-2_{12}$	7201.7783	-3.6	7232.5867	-1.2
$3_{12}-2_{11}$	7972.8358	2.5	8010.5515	1.1
$4_{04}-3_{03}$	10026.2827	1.5	10070.2542	1.1
$4_{14}-3_{13}$	9590.8868	-0.8	9631.7489	-2.6
$4_{13}-3_{12}$	10617.6036	-0.9	10667.6487	0.0
$1_{11}-0_{00}$	7404.6223	2.4	7409.2406	2.0
$2_{12}-1_{01}$	9678.5931	0.3	9692.3666	1.6
$3_{13}-2_{02}$	11827.5391	-0.1	11849.3836	-0.5
$4_{14}-3_{03}$	13864.1650	0.2	13893.2458	-2.1
$5_{15}-4_{04}$	15808.7282	0.1	15844.6020	1.8
$1_{10}-1_{01}$	5130.3492	0.2	5125.8115	-0.5
$2_{11}-2_{02}$	5397.2024	-0.6	5395.1591	-2.6
$3_{12}-3_{03}$	5815.7719	-2.5	5817.8246	0.2
$2_{20}-2_{11}$	14628.8927	-2.7	14608.5518	-1.2
$2_{21}-2_{12}$	15390.4427	0.4	15376.8324	1.1
$3_{21}-3_{12}$	14288.1987	1.4	14265.2670	0.1
$3_{22}-3_{13}$	15781.3058	0.9		

[a] $\Delta\nu = \nu_{obs} - \nu_{cal}$.

Table 5-14: Spectroscopic constants of the ^{132}Xe-$(H_2O)_2$, ^{131}Xe-$(H_2O)_2$, and ^{129}Xe-$(H_2O)_2$ isotopomers.

	^{132}Xe-$(H_2O)_2$	^{131}Xe-$(H_2O)_2$ [a]	^{129}Xe-$(H_2O)_2$
	Rotational Constants /MHz		
A	6267.5930 (6)	6267.6063 (5)	6267.6342 (7)
B	1394.3165 (2)	1396.5752 (4)	1401.2012 (2)
C	1137.1418 (1)	1137.6434 (1)	1141.7196 (1)
	Centrifugal Distortion Constants /kHz		
D_J	5.320 (5)	5.33 (1)	5.374 (5)
D_{JK}	49.15 (4)	49.25 (9)	49.37 (7)
D_K	-0.45 (12)	0.0	-0.61 (12)
d_1	-1.088 (4)	-1.095 (8)	-1.100 (4)
d_2	-0.249 (7)	0.0	-0.283 (15)
	^{131}Xe Quadrupole Coupling Constants /MHz		
χ_{aa}		2.108 (2)	
χ_{bb}		-1.300 (3)	
χ_{cc}		-0.808 (3)	
$\lvert\chi_{ab}\rvert$		8.446(29)	
	Standard Deviation /kHz		
σ	1.5	2.5	1.5

[a] D_K, d_2, and H_{JK} were fixed at 0.0 for the ^{131}Xe-$(H_2O)_2$ isotopomer.

Table 5-15: Measured transition frequencies of the ^{131}Xe-$(H_2O)_2$ isotopomer.

$J'_{Ka'Kc'} - J''_{Ka''Kc''}$	$F' - F''$	ν_{obs} (MHz)	$\Delta\nu$ (kHz)[a]	χ_{ab} contribution (kHz)
$2_{02} - 1_{01}$	1.5 – 1.5	5059.8171	-2.4	-52.8
	3.5 – 2.5	5060.2522	2.3	0.0
$3_{03} - 2_{02}$	4.5 – 3.5	7565.2745	2.6	0.0
	3.5 – 2.5	7565.2944	-4.5	32.5
	2.5 – 1.5	7565.4529	0.1	54.4
$3_{13} - 2_{12}$	4.5 – 3.5	7211.8371	0.7	0.0
$3_{12} - 2_{11}$	4.5 – 3.5	7985.1497	1.1	0.5
$1_{11} - 0_{00}$	1.5 – 1.5	7405.8708	-4.4	0.9
	2.5 – 1.5	7406.2045	5.2	0.0
	0.5 – 1.5	7406.4589	-1.6	1.3
$2_{12} - 1_{01}$	1.5 – 1.5	9682.6897	0.0	1.3
	2.5 – 1.5	9682.8336	0.2	0.5
	3.5 – 2.5	9683.1629	5.2	0.0
	2.5 – 2.5	9683.3615	1.5	0.3
	0.5 – 0.5	9683.4335	-2.5	1.0
	1.5 – 0.5	9683.6375	-1.0	1.5
$3_{13} - 2_{02}$	2.5 – 2.5	11834.4298	-0.5	31.7
	3.5 – 2.5	11834.5839	-1.1	31.3
	4.5 – 3.5	11834.7451	-0.7	0.0
	2.5 – 1.5	11834.8259	-0.1	53.8
	1.5 – 0.5	11835.0266	-2.3	65.9
$4_{14} - 3_{03}$	4.5 – 3.5	13873.6102	2.2	-1.3
	5.5 – 4.5	13873.7444	1.0	0.0
	2.5 – 1.5	13873.8459	-2.3	-2.4
$1_{10} - 1_{01}$	2.5 – 1.5	5128.5067	-4.0	31.8
	0.5 – 1.5	5128.7088	1.8	66.6
	1.5 – 2.5	5128.8611	3.7	53.7
	2.5 – 2.5	5129.0382	0.9	31.4
	1.5 – 0.5	5129.2792	-0.5	54.4
$2_{11} - 2_{02}$	3.5 – 2.5	5396.0922	-4.1	30.2
	1.5 – 2.5	5396.1904	2.1	29.5
	0.5 – 1.5	5396.2622	1.1	53.4
	2.5 – 2.5	5396.4230	1.3	30.8
	3.5 – 3.5	5396.5845	-3.8	-1.0
	2.5 – 3.5	5396.9155	1.7	-0.4
$2_{20} - 2_{11}$	2.5 – 2.5	14621.6166	2.5	1.1
	3.5 – 3.5	14622.4600	-2.6	-0.5

[a] $\Delta\nu = \nu_{obs} - \nu_{cal}$.

Table 5-16: Van der Waals bond lengths, stretching frequencies, and force constants of Xe-H_2O isotopomers.

			$\Sigma 0_{00}$ state		
	^{136}Xe-H_2O	^{134}Xe-H_2O	^{132}Xe-H_2O	^{131}Xe-H_2O	^{129}Xe-H_2O
R (Å)	3.9484	3.9484	3.9485	3.9485	3.9486
ν_s (cm^{-1})	34.82	34.85	34.85	34.88	34.93
k_s (N m^{-1})	1.136	1.136	1.134	1.135	1.136
	^{136}Xe-$H_2{}^{18}O$	^{134}Xe-$H_2{}^{18}O$	^{132}Xe-$H_2{}^{18}O$	^{131}Xe-$H_2{}^{18}O$	^{129}Xe-$H_2{}^{18}O$
R (Å)	3.9468	3.9469	3.9469	3.9470	3.9470
ν_s (cm^{-1})	32.95	32.97	33.00	33.03	33.05
k_s (N m^{-1})	1.116	1.115	1.115	1.116	1.115
			^{132}Xe-$H_2{}^{17}O$		^{129}Xe-$H_2{}^{17}O$
R (Å)			3.9481		3.9482
	^{136}Xe-D_2O	^{134}Xe-D_2O	^{132}Xe-D_2O	^{131}Xe-D_2O	^{129}Xe-D_2O
R (Å)	3.9462	3.9463	3.9463	3.9463	3.9464
ν_s (cm^{-1})	34.78	34.81	34.84	34.87	34.88
k_s (N m^{-1})	1.244	1.244	1.243	1.244	1.243
	^{136}Xe-HDO	^{134}Xe-HDO	^{132}Xe-HDO	^{131}Xe-HDO	^{129}Xe-HDO
R (Å)	3.9452	3.9452	3.9453	3.9453	3.9453
ν_s (cm^{-1})	34.65	34.67	34.71	34.73	34.76
k_s (N m^{-1})	1.180	1.179	1.180	1.180	1.180
			$\Sigma 1_{01}$ state		
	^{136}Xe-H_2O	^{134}Xe-H_2O	^{132}Xe-H_2O	^{131}Xe-H_2O	^{129}Xe-H_2O
R (Å)	3.9873	3.9874	3.9875	3.9876	3.9877
ν_s (cm^{-1})	40.77	40.85	40.91	40.94	40.99
k_s (N m^{-1})	1.558	1.561	1.563	1.563	1.564
	^{136}Xe-$H_2{}^{18}O$	^{134}Xe-$H_2{}^{18}O$	^{132}Xe-$H_2{}^{18}O$	^{131}Xe-$H_2{}^{18}O$	^{129}Xe-$H_2{}^{18}O$
R (Å)	3.9818	3.9819	3.9820	3.9821	3.9822
ν_s (cm^{-1})	37.99	38.06	38.09	38.14	38.15
k_s (N m^{-1})	1.483	1.486	1.485	1.488	1.486
			^{132}Xe-$H_2{}^{17}O$		^{129}Xe-$H_2{}^{17}O$
R (Å)			3.9849		3.9851
	^{136}Xe-D_2O	^{134}Xe-D_2O	^{132}Xe-D_2O	^{131}Xe-D_2O	^{129}Xe-D_2O
R (Å)	3.9819	3.9820	3.9822	3.9823	3.9824
ν_s (cm^{-1})	39.59	39.61	39.67	39.76	39.76
k_s (N m^{-1})	1.611	1.610	1.612	1.617	1.614

Table 5-17: Comparison of *ab initio* and experimental values of derived parameters for ^{132}Xe-H_2O.

		R (Å)	ν_s (cm^{-1})	k_s ($N\ m^{-1}$)
experimental values	$\Sigma 0_{00}$ state	3.9485	34.85	1.134
	$\Sigma 1_{01}$ state	3.9875	40.91	1.563
ab initio values	Global minimum ($\theta = 60°$, $\varphi = 0°$)	4.0647	43.27	1.748
	1st order saddle point ($\theta = 0°$, $\varphi = 0°$)	4.0251	38.36	1.374
	1st order saddle point ($\theta = 180°$, $\varphi = 0°$)	3.8988	37.28	1.297
	2nd order saddle point ($\theta = 80°$, $\varphi = 90°$)	4.0235	32.67	0.997

Table 5-18: Vibrational frequencies and force constants of Xe-$(H_2O)_2$ from a harmonic force field analysis.[a]

Vibrational force constants	Vibrational frequencies
F_{11} = 10.76 (7) N m^{-1}	ν_1 = 143.2 cm^{-1}
F_{22} = 1.489 (4) N m^{-1}	ν_2 = 38.5 cm^{-1}
F_{33} = 1.508 (4) N m^{-1}	ν_3 = 38.8 cm^{-1}

[a] All off-diagonal force constants were fixed at zero during the fit.

Table 5-19: Comparison of calculated quartic centrifugal distortion constants of Xe-$(H_2O)_2$ from harmonic force field analysis with experimental values.[a]

	^{132}Xe-$(H_2O)_2$		^{131}Xe-$(H_2O)_2$		^{129}Xe-$(H_2O)_2$	
	exp.	calc.	exp.	calc.	exp.	calc.
D_J	5.320	5.313	5.328	5.327	5.374	5.355
D_{JK}	49.15	49.09	49.25	49.23	49.37	49.52
D_K	-0.45	-0.31			-0.61	-0.78
d_1	-1.088	-1.115	-1.095	-1.120	-1.100	-1.130
d_2	-0.249	-0.237			-0.283	-0.241

[a] All constants are in kHz.

References

[1] G. Huber, T. Brotin, L. Dubois, H. Desvaux, J.-P. Dutasta, and P. Berthault, J. Am. Chem. Soc. **128**, 6239 (2006).

[2] A. Cherubini and A. Bifone, Prog. Nucl. Magn. Reson. Spectrosc. **42**, 1 (2003).

[3] C. J. Jameson, D. N. Sears, and S. Murad, J. Chem. Phys. **121**, 9581 (2004).

[4] D. Stueber and C. J. Jameson, J. Chem. Phys. **120**, 1560 (2004).

[5] J. Hutson, J. Chem. Phys. **92**, 157 (1990).

[6] R. C. Cohen and R. J. Saykally, J. Phys. Chem. **94**, 7991 (1990).

[7] R. C. Cohen and R. J. Saykally, J. Chem. Phys. **98**, 6007 (1993).

[8] G. Chałasiński, M. M. Szczęśniak, and S. Scheiner, J. Chem. Phys. **94**, 2807 (1991).

[9] M. Bulski, P. E. S. Wormer, and A. van der Avoird, J. Chem. Phys. **94**, 8096 (1991).

[10] F.-M. Tao and W. Klemperer, J. Chem. Phys. **101**, 1129 (1994).

[11] G. Chałasiński, M. M. Szczęśniak, and S. Scheiner, J. Chem. Phys. **97**, 8181 (1992).

[12] G. T. Fraser, F. J. Lovas, R. D. Suenram, and K. Matsumura, J. Mol. Spectrosc. **144**, 97 (1990).

[13] T. C. Germann and H. S. Gutowsky, J. Chem. Phys. **98**, 5235 (1993).

[14] R. C. Cohen, K. L. Busarow, K. B. Laughlin, G. A. Blake, M. Havenith, Y. T. Lee, and R. J. Saykally, J. Chem. Phys. **89**, 4494 (1988).

[15] R. C. Cohen, K. L. Busarow, Y. T. Lee, and R. J. Saykally, J. Chem. Phys. **92**, 169 (1990).

[16] R. C. Cohen and R. J. Saykally, J. Chem. Phys. **95**, 7891 (1991).

[17] S. Suzuki, R. E. Bumgarner, P. A. Stockman, P. G. Green, and G. A. Blake, J. Chem. Phys. **94**, 824 (1991).

[18] E. Zwart and W. L. Meerts, Chem. Phys. **151**, 407 (1991).

[19] M. J. Weida and D. J. Nesbitt, J. Chem. Phys. **106**, 3078 (1997).

[20] R. Lascola and D. J. Nesbitt, J. Chem. Phys. **95**, 7917 (1991).

[21] D. J. Nesbitt and R. Lascola, J. Chem. Phys. **97**, 8096 (1992).

[22] J. van Wijngaarden and W. Jäger, Mol. Phys. **98**, 1575 (2000).

[23] E. Arunan, T. Emilsson, and H. S. Gutowsky, J. Chem. Phys. **116**, 4886 (2002).

[24] E. Arunan, T. Emilsson, and H. S. Gutowsky, J. Am. Chem. Soc. **116**, 8418 (1994).

[25] C. Hampel, K. Peterson, and H.-J. Werner, Chem. Phys. Lett. **190**, 1 (1992).

[26] M. J. O. Deegan and P. J. Knowles, Chem. Phys. Lett. **227**, 321 (1994).

[27] MOLPRO, a package of *ab initio* programs designed by H.-J. Werner and P. J. Knowles, version 2002.6, R. D. Amos, A. Bernhardsson, A. Berning, P. Celani, D. L. Cooper, M. J. O. Deegan, A. J. Dobbyn, F. Eckert, C. Hampel, G. Hetzer, P. J. Knowles, T. Korona, R. Lindh, A. W. Lloyd, S. J. McNicholas, F. R. Manby, W. Meyer, M. E. Mura, A. Nicklass, P. Palmieri, R. Pitzer, G. Rauhut, M. Schütz, U. Schumann, H. Stoll, A. J. Stone, R. Tarroni, T. Thorsteinsson, and H.-J. Werner.

[28] K. A. Peterson, D. Figgen, E. Goll, H. Stoll, and M. Dolg, J. Chem. Phys., **119**, 11113 (2003).

[29] T. H. Dunning, Jr., J. Chem. Phys. **90**, 1007 (1989).

[30] S. M. Cybulski and R. R. Toczylowski. J. Chem. Phys. **111**, 10520 (1999).

[31] S. F. Boys and F. Bernardi, Mol. Phys. **19**, 553 (1970).

[32] *CRC Handbook of Chemistry and Physics*, 84th Ed. (CRC Press, Boca Raton, 2003).

[33] J. S. Binkley, J. A. Pople, Int. J. Quantum Chem. **9**, 229 (1975).

[34] Gaussian 03, Revision B.01, M. J. Frisch, G. W. Trucks, H. B. Schlegel, G. E. Scuseria, M. A. Robb, J. R. Cheeseman, J. A. Montgomery, Jr., T. Vreven, K. N. Kudin, J. C. Burant, J. M. Millam, S. S. Iyengar, J. Tomasi, V. Barone, B. Mennucci, M. Cossi, G. Scalmani, N. Rega, G. A. Petersson, H. Nakatsuji, M. Hada, M. Ehara, K. Toyota, R. Fukuda, J. Hasegawa, M. Ishida, T. Nakajima, Y. Honda, O. Kitao, H. Nakai, M. Klene, X. Li, J. E. Knox, H. P. Hratchian, J. B. Cross, C. Adamo, J. Jaramillo, R. Gomperts, R. E. Stratmann, O. Yazyev, A. J. Austin, R. Cammi, C. Pomelli, J. W. Ochterski, P. Y. Ayala, K. Morokuma, G. A. Voth, P. Salvador, J. J. Dannenberg, V. G. Zakrzewski, S. Dapprich, A. D. Daniels, M. C. Strain, O. Farkas, D. K. Malick, A. D. Rabuck, K. Raghavachari, J. B. Foresman, J. V. Ortiz, Q. Cui, A. G. Baboul, S. Clifford, J. Cioslowski, B. B. Stefanov, G. Liu, A. Liashenko, P. Piskorz, I. Komaromi, R. L. Martin, D. J. Fox, T. Keith, M. A. Al-Laham, C. Y. Peng, A. Nanayakkara, M. Challacombe, P. M. W. Gill, B. Johnson, W. Chen, M. W. Wong, C. Gonzalez, and J. A. Pople, Gaussian, Inc., Pittsburgh PA, 2003.

[35] R. Krishman, J. S. Binkley, R. Seeger, and J. A. Pople, J. Chem. Phys. **72**, 650 (1980).

[36] M. Iida, Y. Ohshima, and Y. Endo, J. Phys. Chem. **97**, 357 (1993).

[37] H. S. Gutowsky, T. Emilsson, and E. Arunan, J. Chem. Phys. **106**, 5309 (1997).

[38] H. M. Pickett, J. Mol. Spectrosc. **148**, 371 (1991).

[39] W. Gordy and R. L. Cook, *Microwave Molecular Spectra,* 3rd ed. (Wiley, London, 1984).

[40] J. Kraitchman, Am. J. Phys. **21**, 17 (1953).

[41] R. J. LeRoy, "LEVEL7.5, *A Computer Program for Solving the Radial Schrödinger Equation for Bound and Quasibound Levels*", University of Waterloo, Chemical Physics Research Report No. CP-655, 2002 (unpublished).

[42] M. R, Keenan, L. W. Buxton, E. J. Campbell, T. J. Balle, and W. H. Flygare, J. Chem. Phys. **73**, 3523 (1980).

[43] E. J. Campbell, L. W. Buxton, M. R. Keenan, and W. H. Flygare, Phys. Rev. A **24**, 812 (1981).

[44] F. A. Baiocchi, T. A. Dixon, C. H. Joyner, and W. Klemperer, J. Chem. Phys. **75**, 2041 (1981).

[45] W. Jäger, Y. Xu, and M. C. L. Gerry, J. Chem. Phys. **99**, 919 (1993).

[46] T. R. Dyke and J. S. Muenter, J. Chem. Phys. **59**, 3125 (1973).

[47] J. Verhoeven and A. Dymanus, J. Chem. Phys. **52**, 3222 (1970).

[48] W. L. Faust and M. N. McDermott, Phys. Rev. **123**, 198 (1961).

[49] F. C. De Lucia, and P. Helminger, J. Mol. Spectrosc. **56**, 138 (1975).

[50] D. Yaron, K. I. Peterson, D. Zolandz, W. Klemperer, F. J. Lovas, and R. D. Suenram, J. Chem. Phys. **92**, 7095 (1990).

[51] Y. Liu and W. Jäger, Mol. Phys. **100**, 611 (2002).

[52] H. A. Fry and S. G. Kukolich, J. Chem. Phys. **76**, 4387 (1982).

[53] T. R. Dyke, K. M. Mack, and J. S. Muenter, J. Chem. Phys. **66**, 498 (1977).

[54] Y. Xu, W. Jäger, and M. C. L. Gerry, J. Chem. Phys. **100**, 4171 (1994).

[55] B. M. Axilrod, and E. Teller, J. Chem. Phys. **11**, 299 (1943).

[56] F. J. Lovas, N. Zobov, G. T. Fraser, and R. D. Suenram, J. Mol. Spectrosc. **171**, 189 (1995).

[57] L. Hedberg and I. M. Mills, J. Mol. Spectrosc. **160**, 117 (1993).

[58] D. Kivelson and E. B. Wilson, Jr., J. Chem. Phys. **21**, 1229 (1953).

[59] R. L. Cook, F. C. De Lucia, and P. Helminger, J. Mol. Spectrosc. **53**, 62 (1974).

[60] A. J. Stone, *The Theory of Intermolecular Forces*, (Clarendon, Oxford, 1996).

[61] C. G. Gray and K. E. Gubbins, *Theory of Molecular Fluids*, (Clarendon, Oxford, 1984), Vol. 1.

CHAPTER 6 Spectroscopic Studies of the Xe-NH_3 and Ne-Xe-NH_3 van der Waals Complexes

6.1 Introduction

^{129}Xe nuclear magnetic resonance (NMR) experiments have two main applications in protein studies, namely mapping the hydrophobic cavities in proteins[1] and using Xe as a biosensor to identify ligand-protein binding processes.[2] These studies require detailed knowledge about Xe-protein interactions.[3] A first step to study these interactions is to construct the interaction potentials of Xe with each functional group in a protein, for example, a Xe-amine potential. The construction of such a potential is a complicated process because of the large number of intermolecular degrees of freedom in the Xe-amine system. Therefore, I choose the Xe-NH_3 system as a first step. The study of the Xe-NH_3 interactions may shed light on the Xe-amine interactions because weak interactions of both amine and NH_3 are largely determined by the key atom, N, whose electronegativity will contribute to the formation of hydrogen bonds.

Previous studies of NH_3 containing van der Waals dimers reveal that NH_3 can solely acts as a hydrogen acceptor in binary complexes.[4,5,6,7] This is distinct to the case of H_2O which can act as both the hydrogen donor and acceptor. Several empirical and *ab initio* interaction potentials of Rg-NH_3 (Rg = Ne, Ar, and Kr)[8,9,10,11,12,13] show that

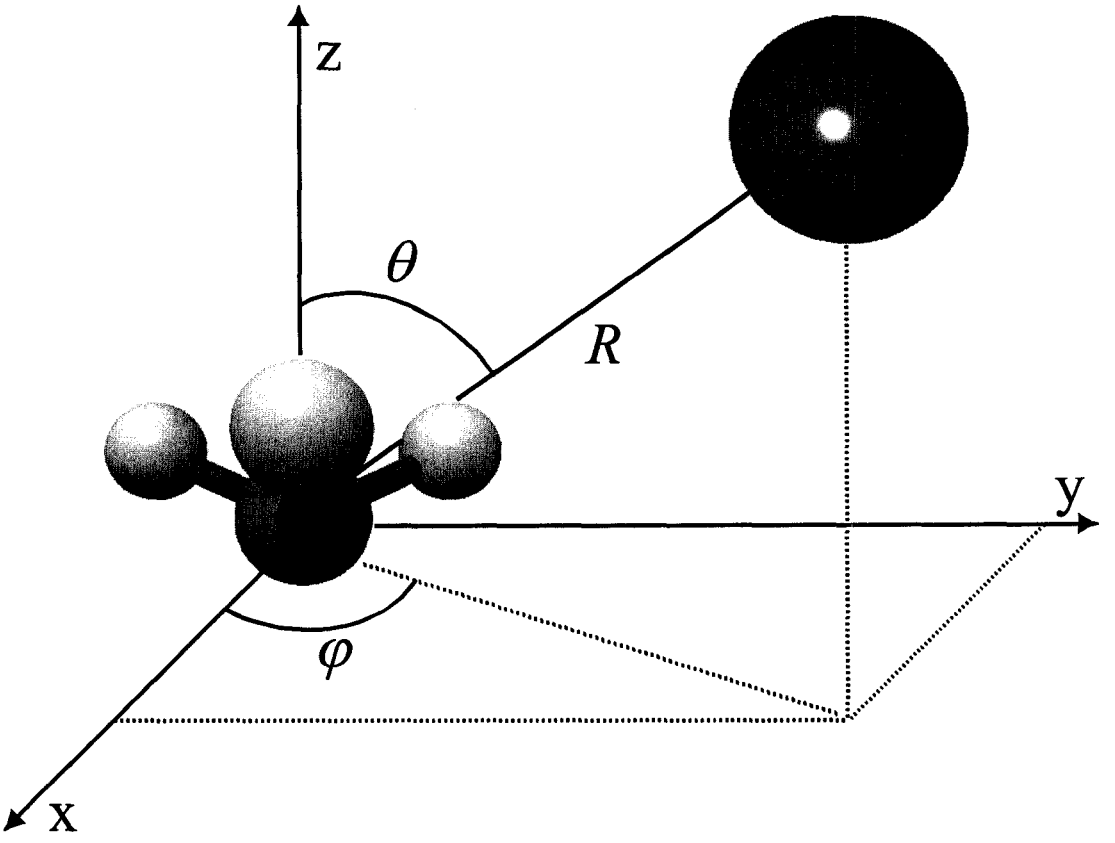

Figure 6-1: Molecule fixed axes frame for the Xe-NH_3 complex. The origin of the coordinate system is at the center-of-mass of NH_3. The C_3 axis of NH_3 is chosen as the z-axis. One H atom is in the xz-plane. The position of the Xe atom is described by spherical coordinates (R, θ, φ). R is the distance between Xe and the origin. θ is the angle between the R vector and the z-axis with $\theta = 0°$ along the axis in the direction of the H atoms. φ is the angle for the NH_3 out-of-plane rotation about its C_3 axis. $\varphi = 0°$ corresponds to the geometry with Xe in the mirror plane of NH_3 and approaching a H atom.

all these three complexes have global minima at a geometry with the rare gas atom sitting in a mirror plane of NH_3 and approaching two H atoms. The intermolecular axis is perpendicular to the C_3 axis of NH_3 or slightly tilted to the N end. The structure where the Rg atom is approaching the three H face center corresponds to a higher barrier to the NH_3 internal rotation in the θ coordinate (θ is the angle between the C_3 axis of the NH_3 and the intermolecular axis of the complex, see Figure 6-1) compared to the structure with the Rg atom at the N end. The energy difference becomes larger with increasing size of rare gas atom. These results suggest that the anti-hydrogen bonded structures are more favored in the Rg-NH_3 system, which is consistent with the notion that NH_3 only acts as a hydrogen acceptor.

Previously reported microwave and submillimeter spectra of Ne_N-, Ar_N-NH_3 (N = 1, 2, 3) and Kr-NH_3 complexes are complicated by the internal rotation and inversion tunneling motion of the NH_3 subunit.[8,14,15,16,17,18,19,20,21] Each tunneling state of a complex can be correlated with free rotor energy levels of NH_3 (j_k), as shown in Figure 6-2. Subscripts 's' and 'a' denote the symmetric and antisymmetric NH_3 inversion wavefunction, respectively. The projection of j, the total angular momentum of NH_3 monomer, onto the intermolecular axis of a complex is represented by the quantum number K. Σ stands for $K = 0$, and Π for $K = 1$, etc. Four states ($\Sigma 0_0$, $\Sigma 1_1$, two $\Pi 1_1$) of Ar-NH_3, which correlate to the lowest energy *ortho* ($j_k = 0_0$) and *para* ($j_k = 1_1$) states of the free NH_3 were observed. Only the $\Sigma 0_0$ states were found for the other six complexes, and the $\Sigma 0_0$ and $\Sigma 1_1$ states were observed for the Ne-, Ar-, and Kr-ND_3 dimers. Two inversion components were found for each state except for the $\Sigma 0_0$ states of the isotopomers containing $^{14}NH_3$ and $^{15}NH_3$. The 's' components of these

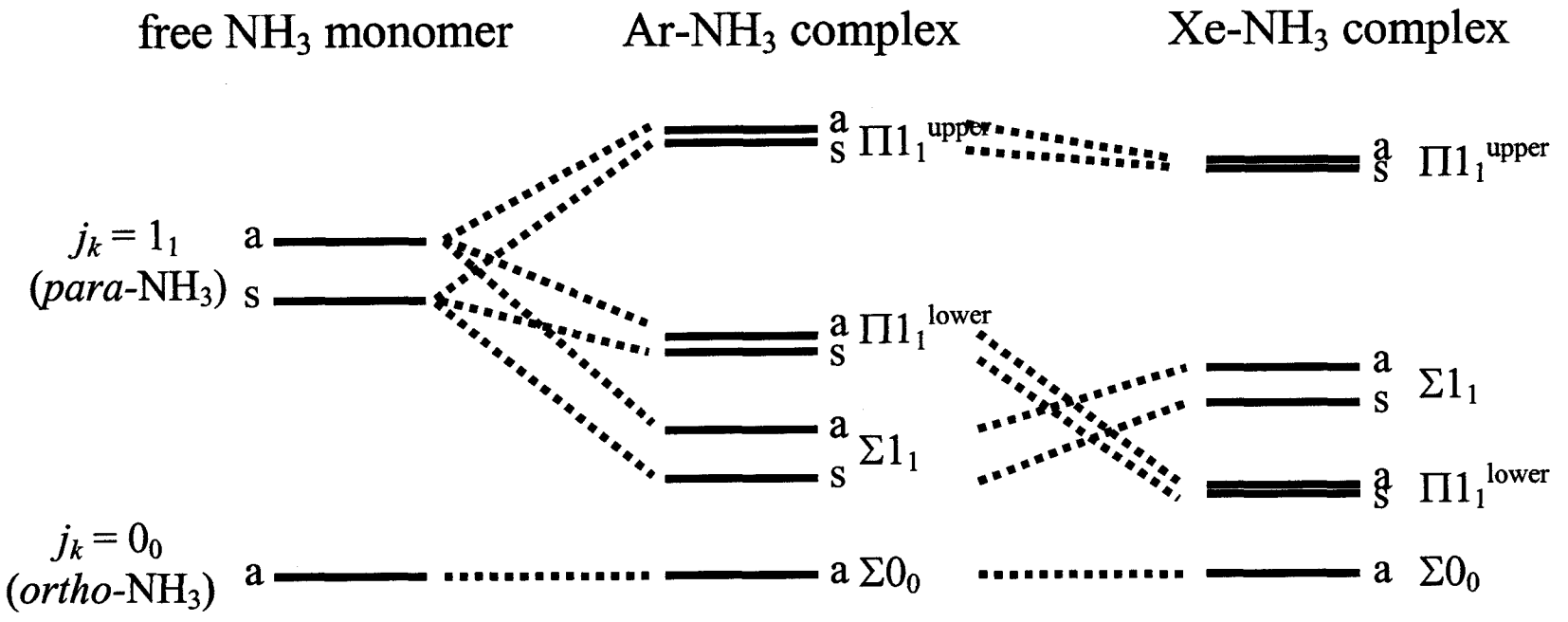

Figure 6-2: A proposed schematic energy level diagram of Xe-NH_3 correlated with those of the free NH_3 monomer and the Ar-NH_3 complex. 's' and 'a' represent symmetric and antisymmetric NH_3 inversion wavefunctions, respectively.

states were absent because they have spin statistical weight of 0. Taking Rg-NH_3 dimers [D_{3h}(M) molecular symmetry group] as an example, the total wavefunction of the system must be antisymmetric under an interchange of any two protons, i.e., must have A_2 symmetry. The combination of the spins of three H nuclei gives eight possible nuclear spin functions with the representation $4A_1 \oplus 2E$. As the electronic, vibrational, rotational, and inversion wavefunctions of the $\Sigma 0_{0s}$ state all have A_1 symmetry, no nuclear spin function with the correct symmetry can be combined with these wavefunctions to give a total wavefuction of A_2 symmetry.

The study of Ar-NH_3 suggests that the presence of the rare gas atom has little effect on the inversion tunneling splitting in the $\Sigma 1_1$ state but effectively quenches the inversion in the $\Pi 1_1$ states.[15] This is because the inversion motion in the $\Sigma 1_1$ state occurs perpendicularly to the van der Waals axis while it is parallel in the $\Pi 1_1$ states, according to the calculated tunneling wavefunctions of Ar-NH_3.[9] The inversion potential along the van der Waals axis has a larger anisotropy than the one in a perpendicular direction to the van der Waals axis because of the presence of the rare gas atom.[8] The potential anisotropy will hinder the inversion motion of NH_3 and lead to the much smaller tunneling splittings in the $\Pi 1_1$ states.

This chapter describes the microwave and *ab initio* studies of intermolecular interaction between Xe and NH_3. Rotational spectra of the Xe-NH_3 and Xe-$(NH_3)_2$ complexes were initially searched to compare their structures and dynamics with those of the Xe-H_2O and Xe-$(H_2O)_2$ complexes described in Chapter 5. Transitions within the $\Sigma 0_0$ (*ortho*) and the lower $\Pi 1_1$ (*para*) states were measured for Xe-$^{14}NH_3$ and Xe-

$^{15}NH_3$. For the deuterated isotopomers, only the *ortho* states were observed. The spectral search conducted for the Xe-$(NH_3)_2$ complex was unsuccessful, probably due to its low population in the jet expansion. Instead, rotational spectra of the Ne-Xe-NH_3 complex were found. Several *a*- type and *b*- type transitions within the ground state were measured. This extra reward provides important information about effects on the Xe-NH_3 interaction due to the presence of the structureless Ne atom. An *ab initio* potential energy surface (PES) for the Xe-NH_3 dimer was constructed and used to explain the spectroscopic observations.

6.2 *Ab initio* potential energy calculations of the Xe-NH_3 dimer

6.2.1 Computational details

Potential energies of the Xe-NH_3 dimer were calculated at the CCSD(T) level of theory[22,23] using the MOLPRO 2002.6 package of *ab initio* programs.[24] The aug-cc-pVQZ-PP basis set[25] was used for the Xe atom and the aug-cc-pVTZ basis set[26] for the N and H atoms. The basis sets were supplemented with (3s3p2d2f1g) midbond functions, with the exponents α_s, α_p = 0.94, 0.34, 0.12; α_d, α_f = 0.64, 0.23; α_g = 0.35.[27] The interaction energies were calculated using the supermolecule approach, and the basis-set superposition error was eliminated with full counterpoise correction.[28] The geometry of Xe-NH_3 is defined by a set of spherical polar coordinates (R, θ, φ), as shown in Figure 6-1, assuming a rigid NH_3 subunit. The center-of-mass (c.m.) of the NH_3 monomer was chosen as the origin of the coordinate system, and the NH_3 unit was kept rigid at its equilibrium structure, with a N-H bond length of 1.012 Å and an H-N-H angle of 106.7°.[29] R is the Xe-c.m.(NH_3) distance and θ is the angle between

the R vector and the C_3 axis of the NH_3 unit with $\theta = 0°$ along the axis in the direction of H atoms. φ is the angle for the NH_3 rotation about its C_3 axis. $\theta = 90°$, $\varphi = 0°$ corresponds to the geometry with Xe in a mirror plane of NH_3 and approaching a H atom. The Xe-NH_3 PES was constructed on a grid of 570 points. R was varied from 3.6 Å to 4.5 Å in steps of 0.1 Å, θ from 0° to 180° in steps of 15°, and φ from 0° to 60° in steps of 15°. The calculated interaction energies are given in Table 6-1.

6.2.2 Discussion of the *ab initio* potential energy surface

The calculated PES of the Xe-NH_3 dimer has similar overall features as those of the Ne/Ar/Kr analogues.[8,9,10,11,12,13] The global minimum was found at a roughly T-shaped structure with Xe in a mirror plane of NH_3 and approaching the center of two H atoms (R = 3.9 Å, $\theta = 105°$, $\varphi = 60°$, D_e = -196.0 cm^{-1}). Compared to the equilibrium structures of the Ne-, Ar-, and Kr-NH_3 complexes, this minimum has the same φ value but slightly different θ orientations [Ne-NH_3: $\theta = 90°$;[8] Ar-NH_3: $\theta = 90°$,[10] 96.6°,[9] 100°,[11] and 105°;[12] Kr-NH_3: $\theta = 100°$ (Ref. 13)]. The well of the Xe-NH_3 potential is deeper than those for Ne-, Ar-, and Kr-NH_3, as expected. From the minimum configuration, the barriers for rotation in the θ coordinate are 61.3 cm^{-1} at $\theta = 0°$ and 31.6 cm^{-1} at $\theta = 180°$. These two configurations correspond to structures with the Xe atom on the C_3 axis of NH_3 and pointing towards and away from H atoms, respectively. The barrier at $\theta = 0°$ is higher than the corresponding barriers in the Ne- (33.0 cm^{-1}),[8] Ar- (55.2 cm^{-1}),[10] and Kr-NH_3 (51.2 cm^{-1}) complexes,[13] while that at $\theta = 180°$ is comparable or even lower than in the Ne (30.9 cm^{-1}),[8] Ar (38.0 cm^{-1}),[10] and Kr

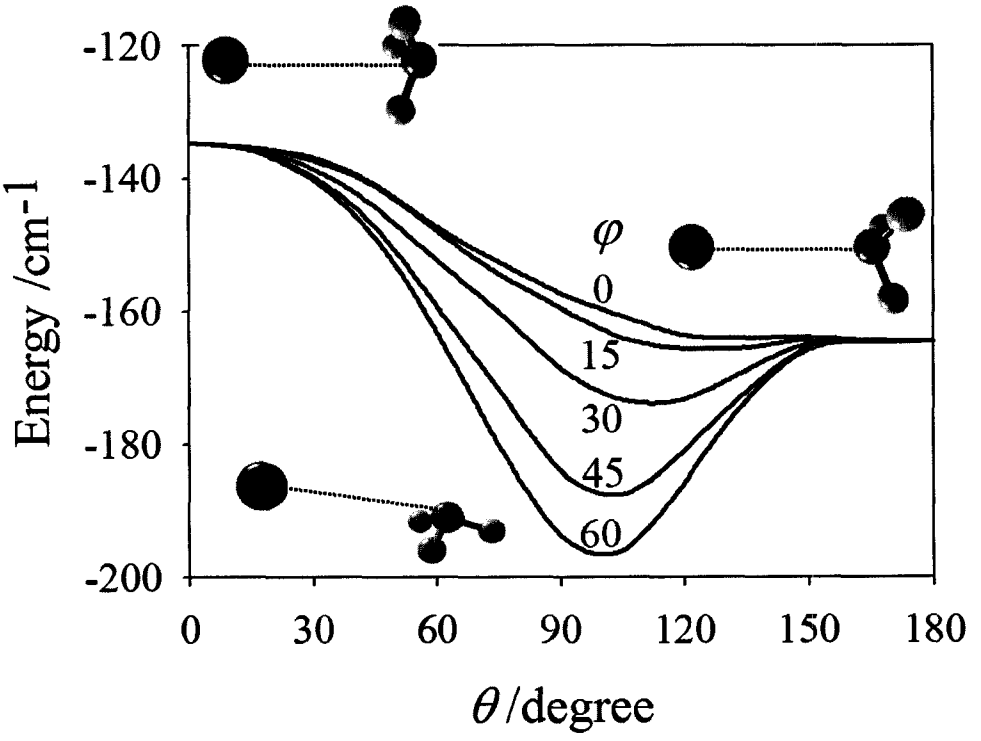

Figure 6-3: *Ab initio* minimum energy paths of Xe-NH_3 in the θ coordinate. Each curve represents a particular value of φ between 0° and 60°.

(35.2 cm^{-1})[13] analogues. This confirms that Rg-NH_3 (Rg = Ne, Ar, Kr, Xe) complexes favor anti-hydrogen bonded structures, in contrast to the Xe-H_2O case. This preference is more pronounced when NH_3 is bound to a larger and more polarizable Xe atom.

Figure 6-3 shows the minimum energy path in the θ coordinate at different φ values, ranging from 0° to 60°. R was varied to reach the lowest energy at each θ and φ combination. The φ dependence was found to be largest between θ = 60° and 130° and become smaller when close to 0° and 180°. As φ decreases, the potential well becomes broader and the minimum shifts to a larger θ value. Compared with the Ne-, Ar-, and Kr-NH_3 potentials, this shift is more pronounced in Xe-NH_3. At φ = 0°, the minimum

of the Xe-NH_3 potential occurs at θ = 180° while those of Ne-, Ar-, and Kr-NH_3 potentials are around 110°,[8] 105°,[10] and 80° (Ref. 13), respectively. As a T-shaped structure at φ = 0° corresponds to an orientation where one H atom is coplanar with, and lies between, the rare gas and N atoms, the repulsive interaction in this structure could result in the tilting of the van der Waals axis further away from the C_3 axis of NH_3. It is not surprising that this effect is larger in the Xe-NH_3 system because the larger Xe electron cloud leads to stronger repulsive interactions which push the van der Waals axis to an anti-parallel position relative to the C_3 axis of NH_3.

6.3 Spectral search, assignments, and analyses

Both the Xe-NH_3 and Ne-Xe-NH_3 complexes were generated using a sample mixture consisting of 0.5% Xe, 0.5% NH_3 and Ne as backing gas. The total pressure was kept at about 5 atm for the Xe-NH_3 study and 7 atm for Ne-Xe-NH_3. Isotopomers containing different Xe and Ne isotopes were studied in their natural abundances (^{136}Xe: 8.87%, ^{134}Xe: 10.44%, ^{132}Xe: 26.89%, ^{131}Xe: 21.18%, ^{129}Xe: 26.44%, ^{20}Ne: 90.92%, ^{22}Ne: 8.82%), while the ^{15}N- and D- substituted species were studied using isotopically enriched $^{15}NH_3$ (Cambridge Isotope Laboratories, 98% ^{15}N) and ND_3 (Cambridge Isotope Laboratories, 99% D) samples. The partially deuterated ND_2H- and NDH_2- containing isotopomers were investigated using gas mixture with ND_3 sample. In this mixture, ND_2H and NDH_2 are present due to the fast proton exchange between ND_3 and residual NH_3 in the sample system.

6.3.1 Xe-NH_3

The tunneling states of Xe-NH_3 dimer can be correlated with free rotor energy levels of NH_3 (j_k). Subscripts 's' and 'a' represent the symmetric and antisymmetric NH_3 inversion wavefunction, respectively. The angular anisotropy of the Xe-NH_3 potential removes the degeneracy of each j_k level, and an additional quantum number K is used to describe the projection of j onto the intermolecular axis. Σ stands for $K = 0$, and Π for $K = 1$, etc. Due to the low rotational temperature (1-2 K) of the molecular expansion in the experiment, only the lowest *ortho* and *para* spin states of Xe-NH_3, which correlate with $j_k = 0_0$ and 1_1 states of free NH_3 respectively were expected to be observed. Relaxation between *ortho* and *para* states is a spin-forbidden process in the expansion. The $j_k = 0_0$ *ortho* state has solely Σ components, with spin statistical weights of 0 and 4 for the $\Sigma 0_{0s}$ (A_1) and $\Sigma 0_{0a}$ (A_2) states, respectively. Therefore, the $\Sigma 0_{0s}$ (A_2) state is not observable. For the $j_k = 1_1$ *para* state, there are one Σ and two Π levels (designated by $\Pi 1_1^{lower}$ and $\Pi 1_1^{upper}$, respectively), and each level is tunneling doubled due to the NH_3 inversion. All six levels belong to the E symmetry with a spin statistical weight of 2. The relative population of these levels is expected to follow approximately a Boltzmann distribution for temperature T of 1-2 K.

By comparison of the van der Waals distances of Kr-,[30] Xe-H_2O, and Kr-NH_3,[17] the Xe-NH_3 distance was estimated to be 4.09 Å. The J = 2-1, $\Sigma 0_{0a}$ transition for the ^{132}Xe-NH_3 isotopomer was predicted to be 8028 MHz and was soon found at 8105 MHz. Additional J transitions and transitions of complexes containing the other four main Xe isotopes were located straightforwardly. Nuclear quadrupole hyperfine

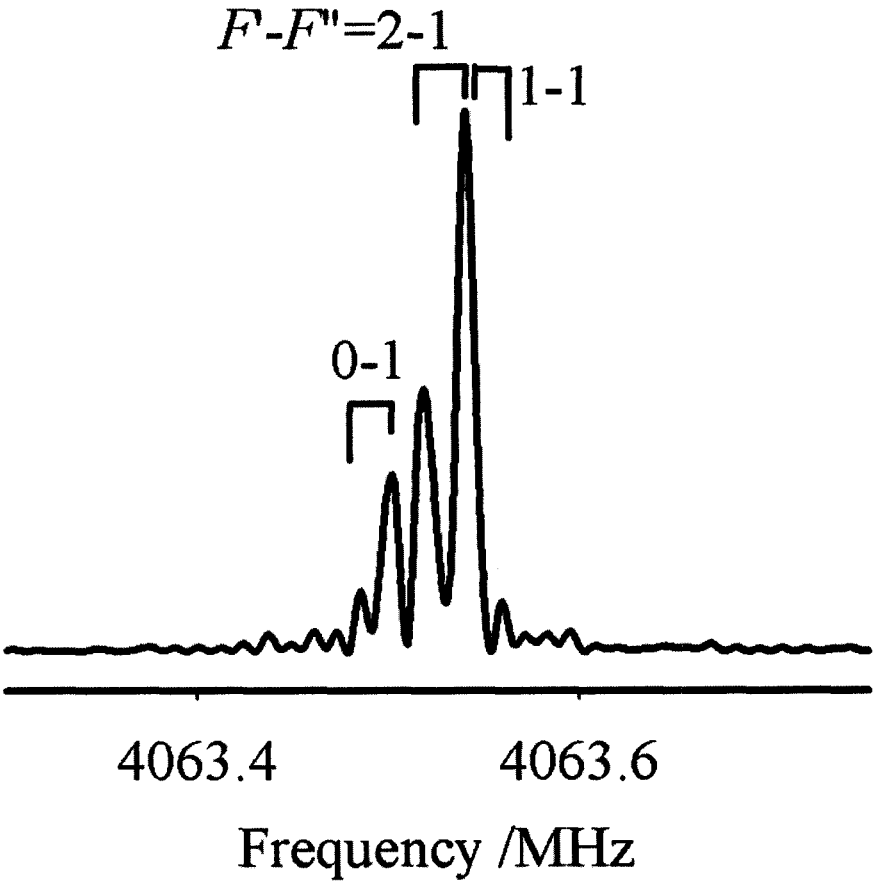

Figure 6-4: A spectrum of the $J = 1\text{-}0$ transition of the $\Sigma 0_{0a}$ state of $^{129}Xe\text{-}^{14}NH_3$. A total of 200 averaging cycles was used to record the spectrum.

structures due to the ^{14}N ($I = 1$) and ^{131}Xe ($I = 3/2$) nuclei were also detected. The magnitude of the ^{14}N hyperfine splittings was found to be only around 1/4 of the corresponding splittings in the Ne-,[8] Ar-,[14] and Kr-NH_3 (Ref. 17) complexes (see Figure 6-4). The characteristics of the ^{14}N and ^{131}Xe hyperfine patterns and the occurrence of $J = 1\text{-}0$ transition confirmed the assignment to a Σ state. The absence of the 's' tunneling component and the absence of Coriolis perturbations led the assignment of the observed transitions to the $\Sigma 0_{0a}$ state. All measured transition

frequencies are listed in Tables 6-2 and 6-3. Pickett's SPFIT/SPCAT suite of program[31] was used to determine the spectroscopic constants using a pseudodiatomic approach. The rotational constant B, the centrifugal distortion constants D_J, H_J, and the ^{14}N and ^{131}Xe nuclear quadrupole coupling constants $\chi_{aa}(^{14}N)$ and $\chi_{aa}(^{131}Xe)$, respectively, were obtained and are given in Tables 6-2 and 6-3.

The previous Ar-NH_3 study[15] revealed that the $\Sigma 1_{1s}$ and $\Sigma 1_{1a}$ states lie 45.3 and 22.6 GHz lower than the $\Pi 1_{1s}{}^{lower}$ and $\Pi 1_{1a}{}^{lower}$ states. If the internal dynamics of theXe-NH_3 complex is similar to Ar-NH_3, the $\Sigma 1_1$ states of Xe-NH_3 should be more populated than the $\Pi 1_1{}^{lower}$ states and be more easily observed. A wide range scan from 6 to 9 GHz was conducted to search for the J = 2-1 transitions within the $\Sigma 1_1$ states. Two sets of transitions of similar intensity were found and both have characteristic Xe isotopic spacing. Their transition intensities are approximately half that of the corresponding transition in the $\Sigma 0_{0a}$ state, consistent with the spin statistical weights of 2 and 4 for states with E and A_1 symmetry, respectively. Higher J transitions were located straightforwardly and the rotational spectra were found to be slightly perturbed by a Coriolis interaction. However, corresponding J = 1-0 transitions could not be found, suggesting that these two sets of transitions belong to Π states instead of Σ states. This is supported by the ^{14}N and ^{131}Xe hyperfine patterns which follow those for a Π state (see Figure 6-5). These two sets of transitions were therefore assigned to two inversion components of $\Pi 1_1{}^{lower}$ state. An even broader search was conducted for the $\Sigma 1_1$ state but without success. This might imply that the $\Pi 1_1{}^{lower}$ state has lower energy than the $\Sigma 1_1$ state in Xe-NH_3, as was found in the N_2-[32] and CO-NH_3 complexes[33] but

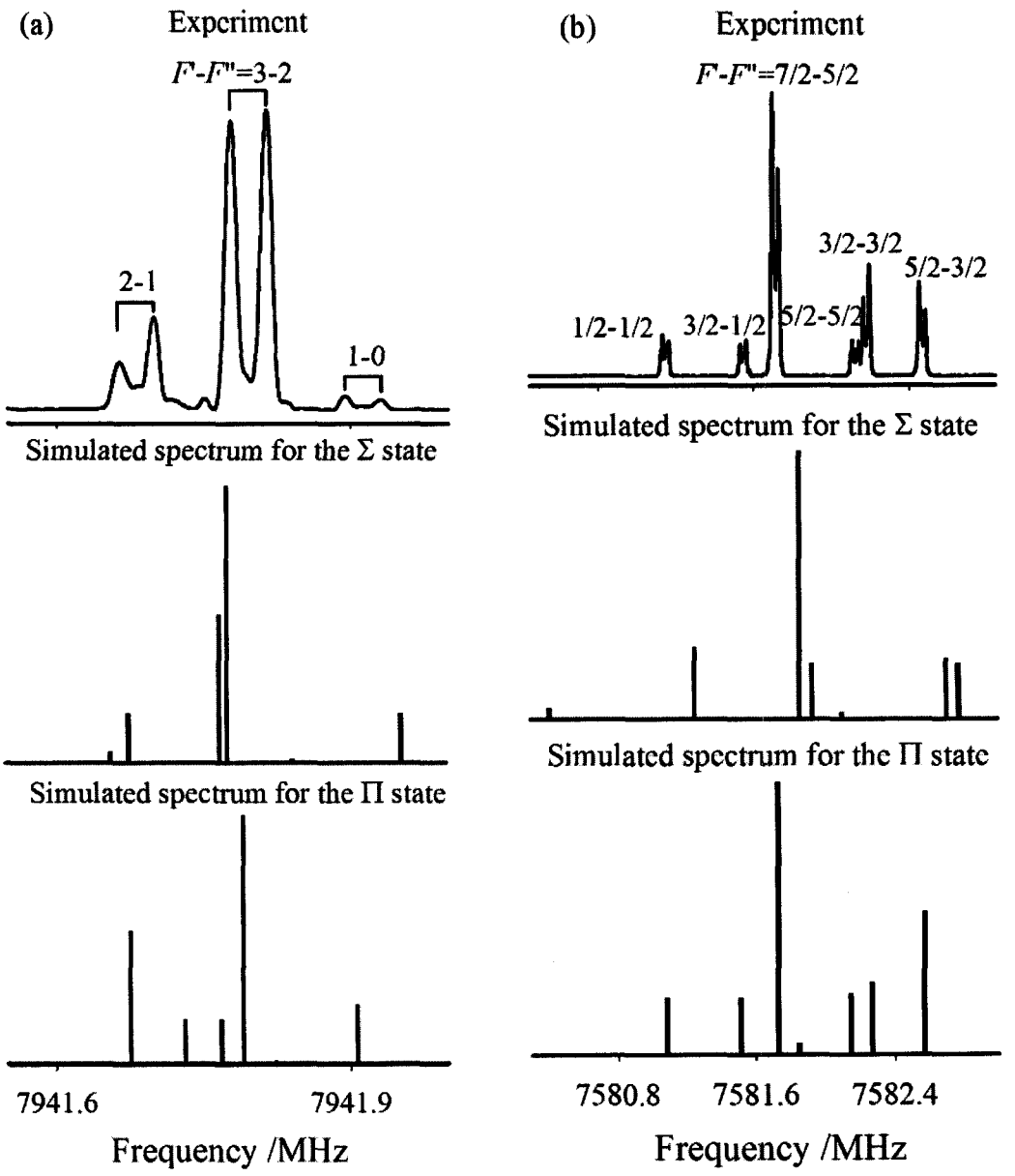

Figure 6-5: The J = 2-1 transitions of the $\Pi 1_{1a}^{lower}$ states of (a) ^{132}Xe-$^{14}NH_3$ and (b) ^{131}Xe-$^{15}NH_3$, including experimental composite spectra and simulated spectra for Σ state (b) and Π states using a pseudodiatomic approach. The experimental spectrum (a) was recorded using 5 averaging cycles and (b) using 100 averaging cycles.

different from the case of Ar-NH_3.[15] Figure 6-2 shows a proposed schematic energy level diagram which correlates the Xe-NH_3 energy levels to those of the free NH_3 monomer and the Ar-NH_3 complex. All measured frequencies of transitions assigned to the $\Pi 1_1^{lower}$ state are listed in Tables 6-4, 6-5 and 6-6. The rotational and centrifugal distortion constants were determined using a pseudodiatomic approach and are given in Tables 6-4, 6-5 and 6-7. The determined centrifugal distortion constants D_J are more negative compared to those of the unperturbed $\Sigma 0_{0a}$ state, presumably as a result of a Coriolis perturbation. The low frequency component, which is more Coriolis perturbed, was assigned to be the 's' component because the energy gap between the $\Pi 1_{1s}^{lower}$ and $\Sigma 1_{1s}$ states is expected to be smaller than that for the corresponding 'a' states according to Figure 6-2. The hyperfine analyses were not straightforward, especially for the ^{131}Xe-$^{14}NH_3$ isotopomer, which contains two quadrupolar nuclei. Initially, one quadrupole coupling constant, χ_{aa}, for each quadrupolar nucleus was included and the ^{14}N and ^{131}Xe hyperfine structures could only be poorly fit, except for the ^{14}N hyperfine structures of the $\Pi 1_{1a}^{lower}$ state. The inclusion of the $|\chi_{bb}-\chi_{cc}|$ constant was later found to be necessary in the ^{131}Xe-$^{15}NH_3$ hyperfine analysis. The ^{131}Xe constants of ^{131}Xe-$^{15}NH_3$ and the ^{14}N constants of ^{132}Xe-$^{14}NH_3$ provided guidance for the analysis of the ^{131}Xe-$^{14}NH_3$ spectra. The obtained nuclear quadrupole coupling constants for all isotopomers are given in Tables 6-4, 6-5, and 6-7.

The Xe-$^{15}NH_3$ isotopomers follow the same nuclear spin statistics as Xe-$^{14}NH_3$. The corresponding three sets of transitions were measured and assigned to the $\Sigma 0_{0a}$, $\Pi 1_{1s}^{lower}$, and $\Pi 1_{1a}^{lower}$ states, respectively. This also confirms the previous

assignments to NH_3- containing species. An example spectrum of the $J = 2$-1 transition in the $\Pi 1_{1a}^{lower}$ state of ^{131}Xe-$^{15}NH_3$ is shown in Figure 6-5(b). All measured transition frequencies and the determined spectroscopic constants, including the ^{131}Xe nuclear quadrupole coupling constants, are given in Tables 6-3, 6-8, and 6-9.

The Xe-ND_3 dimer has the same molecular symmetry as Xe-NH_3, and obeys Bose-Einstein statistics because of the three equivalent deuterons with $I = 1$. This gives spin statistical weights of 10, 1, and 8 for the $\Sigma 0_{0s}$ (A_1 symmetry), $\Sigma 0_{0a}$ (A_2 symmetry), and $\Sigma 1_1 / \Pi 1_1$ (E symmetry) states, respectively. Two sets of closely spaced transitions were measured and assigned to the two inversion components of the $\Sigma 0_0$ states. Figure 6-6 shows example spectra of the J = 2-1 transitions of ^{132}Xe-ND_3. The higher frequency component with greater intensity was assigned to the 's' component according to the spin statistical weights. The nuclear quadrupole hyperfine structure due to the ^{14}N and D nuclei could not be sufficiently resolved although some side peaks were observed. Based on the position of the side peaks, the hyperfine splittings were estimated to be at least one order of magnitude smaller than those in Ne-,[8] Ar-,[16] and Kr-ND_3 (Ref. 17). Smaller hyperfine splittings were also found in Xe-NH_3 compared to those of Ne-, Ar-, and Kr-NH_3. One possible reason for the smaller hyperfine splittings in Xe-NH_3 / ND_3 could be that the internal dynamics of the NH_3 / ND_3 subunit have changed in going from the Ne-, Ar-, and Kr- NH_3 / ND_3 complexes to the Xe-NH_3 / ND_3 complexes. For example, according to the *ab initio* calculations, Xe-NH_3 assumes a more anti-hydrogen bonded configuration than the Ne/Ar/Kr analogues, which could lead to the different angular dynamics of NH_3 / ND_3 within the Xe-NH_3 complex. This could also explain my suggestion of the different energy level

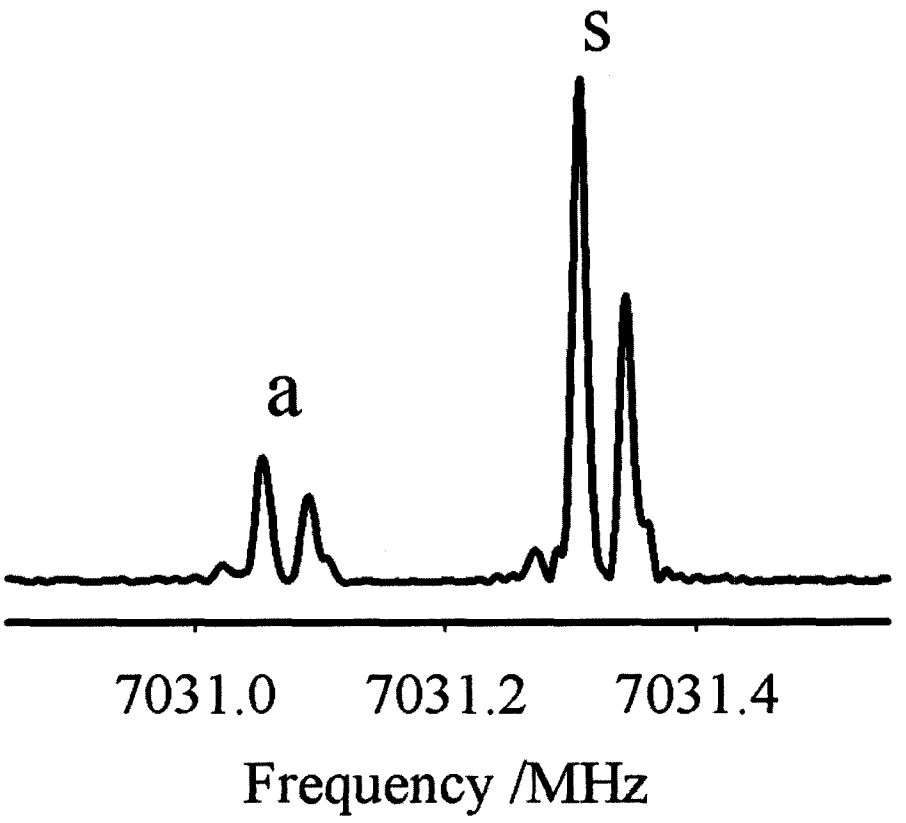

Figure 6-6: A spectrum of the $J = 2$-1 transition of the $\Sigma 0_0$ state of ^{132}Xe-$^{14}ND_3$. The labels 's' and 'a' refer to the symmetric and antisymmetric inversion components, respectively. A total of 100 averaging cycles was used to record the spectrum.

diagrams for the Xe- and Ar-NH_3 complexes. The difference in the internal dynamics complicated the prediction for other tunneling states of Xe-ND_3, and searches for the $\Sigma 1_1$ / $\Pi 1_1$ states were unsuccessful. All measured transition frequencies are listed in Tables 6-10 and 6-11. Spectroscopic fits were performed for each inversion state separately and the resulting constants are also given in Tables 6-10 and 6-11.

Both the Xe-NDH_2 and Xe-ND_2H complexes belong to C_{2v} molecular symmetry group because the partial substitution reduces the symmetry of the ammonia

monomer. As a result, the internal rotational motion in these two complexes can no longer interchange the two identical H or D atoms, and only the two inversion states ($\Sigma 0_{00s}$ and $\Sigma 0_{00a}$) of the ground internal rotor state which correlate to the $j_{kakc} = 0_{00}$ state of NDH_2 (ND_2H) are observable. The spin statistical weights for the $\Sigma 0_{00s}$ and $\Sigma 0_{00a}$ states are 1 and 3 for Xe-NDH_2, and 6 and 3 for Xe-ND_2H. Transitions within the $\Sigma 0_{00s}$ and $\Sigma 0_{00a}$ states of Xe-NDH_2 and Xe-ND_2H complexes were measured and the frequencies are listed in Tables 6-12, 6-13, 6-14, and 6-15. The inversion states were assigned by comparing the relative transition intensities with the expected spin statistical weights. Contrary to the Xe-ND_3 case, the lower frequency components for the Xe-NDH_2 and Xe-ND_2H complexes were assigned to the 's' state. The same reversal has been previously reported for other Rg-NDH_2 and Rg-ND_2H [Rg = Ne,[8] Ar,[16] and Kr (Ref. 17)] complexes. Neither ^{14}N nor D hyperfine splittings could be resolved. The transitions frequencies were fit for each inversion state separately and the resulting spectroscopic constants are given in Tables 6-12, 6-13, 6-14 and 6-15.

6.3.2 Ne-Xe-NH_3 and Xe-$(NH_3)_2$

A spectral search was conducted to find rotational transitions of the Xe-$(NH_3)_2$ complexes. An isosceles triangular structure was assumed with the Xe-c.m.[$(NH_3)_2$] axis along the *a*- inertial axis and the c.m.(NH_3)-c.m.(NH_3) axis in the direction of the *b*- axis. The Xe-c.m.(NH_3) distance, 3.69 Å, and the c.m.(NH_3)-c.m.(NH_3) distance, 3.41 Å, were estimated from the corresponding distances in the Xe-NH_3 and $(NH_3)_2$ dimers.[34] Based on this structure, the rotational constants *A*, *B*, and *C* of ^{132}Xe-$(NH_3)_2$ were predicted to be 5110, 1369, and 1080 MHz, respectively. A rotational transition

at 4740.54 MHz was first located and initially assigned to the ground state 2_{02}-1_{01} transition of ^{132}Xe-$(NH_3)_2$. This assignment resulted in laborious and unsuccessful searches for further transitions. Eventually, I assigned this transition to be the ground state 2_{02}-1_{01} transition of ^{20}Ne-^{132}Xe-NH_3. Substituting one NH_3 molecule with a 3 atomic mass units heavier Ne atom has little effect on the *B* and *C* rotational constants. However, it causes an approximately 1 GHz shift of the *A* constant. With this as a guide, 10 *a*-type and 4 *b*-type transitions were located. Transitions for ^{20}Ne-^{129}Xe-NH_3, ^{20}Ne-^{132}Xe-$^{15}NH_3$, ^{20}Ne-^{129}Xe-$^{15}NH_3$, ^{20}Ne-^{131}Xe-$^{15}NH_3$, ^{22}Ne-^{132}Xe-$^{15}NH_3$, ^{22}Ne-^{129}Xe-$^{15}NH_3$, and ^{20}Ne-^{131}Xe-$^{15}NH_3$ isotopomers were also found and support the assignment to the Ne-Xe-NH_3 complex. An example spectrum of the 3_{03}-2_{02} transition of ^{20}Ne-^{132}Xe-NH_3 is shown in Figure 6-7 to demonstrate the signal-to-noise ratio and resolution achieved. All measured transition frequencies assigned to the Ne-Xe-NH_3 complex are listed in Tables 6-16, 6-17, and 6-18. The determined spectroscopic constants, including the ^{14}N and ^{131}Xe nuclear quadrupole coupling constants, are given in Table 6-19.

Extensive searches for the Xe-$(NH_3)_2$ complex with a variety of sample conditions were conducted but no candidate was observed. Enhancing the backing pressure of the sample or increasing the percentage of NH_3 results in signal enhancement of Ne_N-NH_3 (N = 1, 2, 3) or Ne-Xe-NH_3 complexes at the expense of the Xe-NH_3 line intensities. Presumably, Ne-Xe-NH_3 succeeds in the complex formation competition with Xe-$(NH_3)_2$ taking advantage of large Ne concentration in the sample mixture. This was surprising because the spectra of the Xe-$(H_2O)_2$ complex could be observed and NH_3 has a similar dipole moment as H_2O. It was soon realized that the

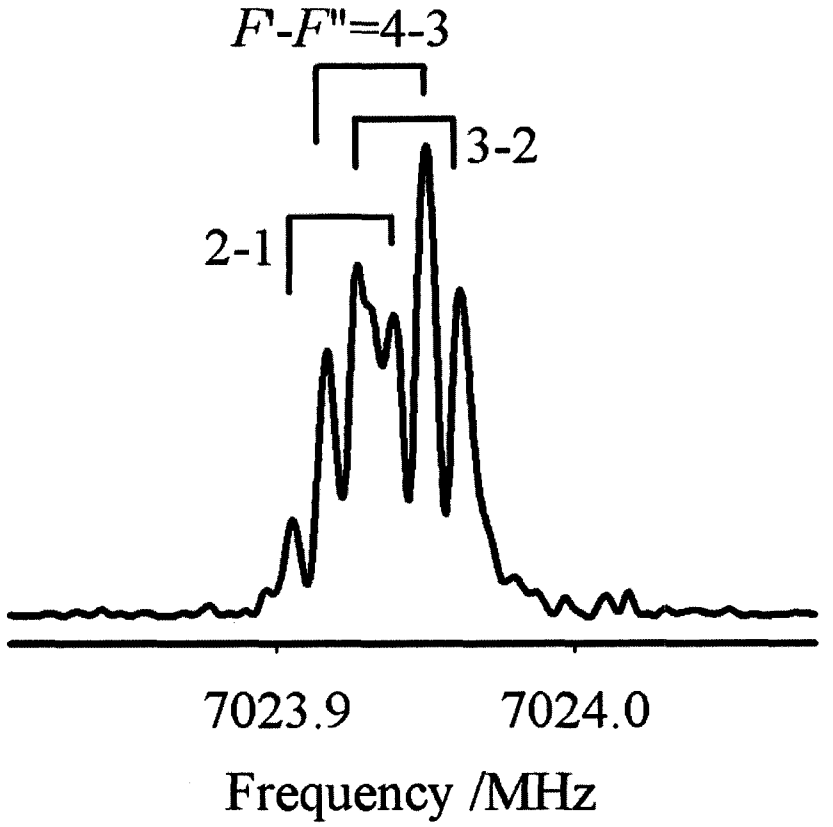

Figure 6-7: A spectrum of the $J_{KaKc} = 3_{03}$-2_{02} transition of ^{20}Ne-^{132}Xe-$^{14}NH_3$. A total of 400 averaging cycles was used to record the spectrum.

Xe-$(H_2O)_2$ complex is more strongly bound by the hydrogen bond between the two H_2O molecules. A hydrogen bond can not be formed between two NH_3 molecules because NH_3 can not act as the hydrogen donor. In the $(NH_3)_2$ dimer, a strongly bent N-H···N structure was determined experimentally instead of a nearly linear N-H···N arrangement for a hydrogen bond.[6] Further evidence that NH_3 can not act as the hydrogen donor was also found in the rotational study of NH_3-CO.[5] The structure obtained from the rotational spectra reveals that the CO approaches the N end of NH_3 with the C atom.

6.4 Discussion of the Xe-NH_3 spectroscopic results

6.4.1 Structural parameters and force constants

The van der Waals bond length R, the van der Waals stretching frequency ν_s, and the corresponding force constants k_s were estimated from the rotational constant B and the distortion constant D_J using a pseudodiatomic model:[35]

$$R = \left(\frac{h}{8\pi^2 \mu B}\right)^{1/2}$$

$$\nu_s = \left(\frac{4B^3}{D_J}\right)^{1/2}$$

$$k_s = 4\pi^2 \nu_s^2 \mu \qquad (6\text{-}1)$$

Here, μ is the pseudodiatomic reduced mass of the complex. The calculated R, ν_s, and k_s values for the $\Sigma 0_0$ / $\Sigma 0_{00}$ states are given in Table 6-20. For the $\Pi 1_1{}^{lower}$ states, the D_J constants are tainted by the Coriolis interaction, and therefore equations (6-1) are no longer applicable to calculate ν_s and k_s values. The obtained values for the $\Sigma 0_{0a}$ state of ^{132}Xe-NH_3 are R = 4.067 Å, ν_s = 36.5 cm^{-1}, and k_s = 1.18 N m^{-1}. Compared to the ground state values of ^{132}Xe-H_2O (R = 3.949 Å, ν_s = 34.9 cm^{-1}, k_s = 1.13 N m^{-1}), the Xe-NH_3 bond is 3% longer and has similar rigidity. The parameters were found to be similar for the two inversion states of the deuterated species. This could be viewed as an indication of a relatively small energy splitting of these two states. According to the regular isotope effect, the force constants are expected to increase upon deuteration, as seen in the Xe-ND_3 isotopomer (1.23 N m^{-1}). However, the partially deuterated species, Xe-ND_2H (1.14 N m^{-1}) and Xe-NDH_2 (1.08 N m^{-1}), have even smaller force constants than Xe-NH_3. Similar behavior has previously been observed in the Ne-,[8] Ar-,[16] Kr-

NH_3,[17] and Kr-,[36] Xe-, CO-CH_4 (Ref. 37) complexes. This unusual trend might indicate the inadequacy of the pseudodiatomic model applied. One can assume that orientations where Xe binds to the deuterons are slightly preferred. The result is a higher potential anisotropy in the internal rotation coordinate of the partially deuterated species, and the NH_3 internal degrees of freedom are not negligible.

In order to compare the spectroscopic and *ab initio* data, the computer program LEVEL7.5 (Ref. 38) was used to determine the bound states of ^{132}Xe-NH_3 that are supported by the *ab initio* potential curves along radial coordinates at three selected angular configurations [global minimum, symmetric Xe-H_3N (θ= 0°, φ = 0°), and symmetric Xe-NH_3 (θ = 180°, φ = 0°) geometries], using a pseudodiatomic model. The molecular parameters, R, ν_s, and k_s, were then calculated and are compared with the experimental values for the $\Sigma 0_{0a}$ state in Table 6-21. By comparison, the theoretical values are on the same order of magnitude as the experimental values. Interestingly, the best agreement with the experimental values was found at the symmetric Xe-NH_3 geometry (θ = 180°, φ = 0°) instead of the global minimum. The deviations at the symmetric Xe-NH_3 geometry are 2.2%, -1.6% and -2.5% for the R, ν_s, and k_s values, respectively. This behavior can be considered as an indication for a rather delocalized wavefunction in the $\Sigma 0_{0a}$ state. The symmetric Xe-NH_3 geometry gives values that are rather close to experimental ones, suggesting that the anti-hydrogen bonded configurations have large contribution to the ground state wavefunction.

6.4.2 Hyperfine structure and angular information

The determined ^{14}N and ^{131}Xe nuclear quadrupole coupling constants were used to extract dynamical information about the internal angular coordinates of the Xe-NH_3 complex. The obtained orientation of the NH_3 unit is an effective orientation, averaged over the large amplitude internal motions. Equation (6-2) was applied to calculate the effective angles θ_g between the C_3 axis of NH_3 and the *g*-principal inertial axes of the complex from the ^{14}N nuclear quadrupole coupling constants:

$$\chi_{gg} = \frac{\chi_0}{2}\left\langle 3\cos^2\theta_g - 1\right\rangle \text{ with } g = a, b, c. \tag{6-2}$$

The nuclear quadrupole coupling constant of the NH_3 monomer, χ_0 (-4.0898 MHz), was assumed to stay unchanged upon formation of the complex. From the χ_{aa} constants, the Legendre polynomial factors, $\left\langle P_2(\cos\theta_a)\right\rangle = \frac{1}{2}\left\langle 3\cos^2\theta_a - 1\right\rangle$, were calculated to be -0.018 ($\Sigma 0_{0a}$ state), 0.086 ($\Pi 1_{1s}^{lower}$ state), 0.091 ($\Pi 1_{1a}^{lower}$ state) for ^{132}Xe-NH_3, which correspond to effective angles θ_a of 55.5°/124.5°, 51.3°/128.7°, and 51.1°/128.9°, respectively. Two sets of angles for each complex arise from the two solutions of θ_a obtained using equation (6-2). These $\left\langle P_2(\cos\theta_a)\right\rangle$ values are rather close to the value of zero in the free rotor limit, indicating nearly free internal rotation of NH_3 within the complex. The $\left\langle P_2(\cos\theta_a)\right\rangle$ value for the $\Sigma 0_{0a}$ state was found to be smaller than the corresponding values of Ne- (-0.066),[8] Ar- (-0.086),[14] and Kr-NH_3 (-0.061)[17], which is surprising because of the anticipated more hindered internal motion of NH_3 when bound to a larger Xe atom. A careful look at the PES of Xe-NH_3 reveals that one barrier to the NH_3 internal rotation at θ_a = 180° is comparable and

even lower than the corresponding barrier in the Ne/Ar/Kr analogues. This could change the NH_3 angular dynamics within the Xe-NH_3 complex, leading to a smaller χ_{aa} constant. The magnitude of the $\langle P_2(\cos\theta_a)\rangle$ values for the $\Pi 1_1^{lower}$ states is slightly larger than that for $\Sigma 0_{0a}$ state, suggesting more hindered internal rotation in the $\Pi 1_1^{lower}$ states. The nuclear quadrupole coupling constants for the two $\Pi 1_1^{lower}$ inversion components are similar in magnitude, which could indicate similar dynamics within these two states, as is also expected from their small energy splitting.

A second, independent value for the effective angle θ_a can be calculated from the ^{131}Xe nuclear quadrupole coupling constant, χ_{aa}. Two main contributions to the electric field gradient at the Xe nucleus are the dispersion and induction interactions between the multipole moments of NH_3 and the Xe electron cloud. χ_{dis} and χ_{ind} are used to represent the contributions to the quadrupole coupling constants from these two interactions. χ_{dis} can be approximated with the experimental χ_{aa} value of ^{131}Xe-Ar, 0.723 MHz.[39] The subtraction of 0.723 MHz from the observed χ_{aa} values of ^{131}Xe-NH_3 will give an estimate of χ_{ind}, which can be further interpreted in terms of the multipole moments of NH_3 using the expressions:[40]

$$q_0 = -6\mu\left\langle\frac{\cos\theta_a}{R^4}\right\rangle - 12Q\left\langle\frac{3\cos^2\theta_a - 1}{2R^5}\right\rangle - \cdots$$

$$\chi_{ind} = -eq_0(1-\gamma)Q_{Xe}/h \qquad (6\text{-}3)$$

Here, q_0 is the electric field gradient along the intermolecular a- axis generated by the multipole moments of the NH_3 monomer at the site of the Xe nucleus. μ = 1.47 D and Q = -2.32 D Å are the electric dipole and quadrupole moments, respectively, of the free

NH_3 monomer.[41] Higher order electric moments were not considered here. The brackets indicate averaging over the large amplitude angular motions. The van der Waals bond length R is 4.067 Å for the $\Sigma 0_{0a}$ state, 4.130 Å for the $\Pi 1_{1s}$ state, and 4.108 Å for the $\Pi 1_{1a}$ state. With the ^{131}Xe nuclear quadrupole moment Q_{Xe} = -0.12 b,[42] and the Sternheimer shielding factor γ = -152 (Ref. 40), values of 119.5°, 127.6°, and 127.2° were obtained for the effective angles θ_a in the $\Sigma 0_{0a}$, $\Pi 1_{1s}^{lower}$, and $\Pi 1_{1a}^{lower}$ states, respectively. These values are in accord with the second set of values calculated from the ^{14}N nuclear quadrupole coupling constants. Equation (6-3) was also used to determine χ_{ind} as a function of θ_a. Extreme values for χ_{ind} of -2.586 MHz and 7.621 MHz were found to occur at θ_a = 65° and 180°, respectively. The χ_{ind} values (1.662 for $\Sigma 0_{0a}$ state, 2.637 for $\Pi 1_{1s}^{lower}$ state, and 2.651 for $\Pi 1_{1a}^{lower}$ state) are not close to either extreme, and presumably represent highly averaged values, analogous to the ^{14}N nuclear quadrupole coupling constants. The determined ^{131}Xe nuclear quadrupole coupling constants are similar for the two $\Pi 1_1^{lower}$ inversion states, which further supports the similarity of the internal dynamics within these two states.

6.4.3 Inversion tunneling

Similar B rotational constants were determined for the two $\Sigma 0_0$ / $\Sigma 0_{00}$ inversion states of ^{132}Xe-ND_3, ^{132}Xe-ND_2H, and ^{132}Xe-NDH_2, with differences of only 63.5 kHz, 50.2 kHz, and 460.0 kHz, respectively. This suggests relatively small inversion splittings of the energy levels, which is further supported by the similarities in the nuclear quadrupole coupling constants. In the previous studies of other Rg-NH_3 (Rg =

Ne,[8] Ar,[16] Kr[17]) complexes, the corresponding difference in B constants increases in the order of Rg-ND_3, -ND_2H, and –NDH_2, consistent with the trend for the inversion energy level splittings of the free monomers, 1.6 GHz for ND_3, 5 GHz for ND_2H and 12 GHz for NDH_2. However, the opposite order is observed for ^{132}Xe-ND_3 and ^{132}Xe-ND_2H with a slightly larger difference of the B constants for the ^{132}Xe-ND_3 isotopomer. The previously reported Ne-[8] and Ar-NH_3 (Ref. 10) PESs indicate that the anisotropy of the potential in the inversion coordinate is smallest around the global minimum and largest when the rare gas atom is located on the C_3 axis of NH_3. The $\Sigma 0_0$ / $\Sigma 0_{00}$ states are expected to be quite localized at the global minimum. However, Xe-ND_2H could adopt a slightly different angular orientation from Xe-ND_3 because Xe binding to deuterons is more favored than to hydrogen atoms. Such small preference in the angular orientation could lead to a higher anisotropy of the Xe-ND_2H potential in the inversion coordinate, and thus, quench the inversion tunneling motion of ND_2H.

The difference of B constants in the $\Pi 1_1^{lower}$ inversion states of ^{132}Xe-NH_3 and ^{132}Xe-$^{15}NH_3$ are 20.9 MHz and 17.9 MHz, respectively, considerably larger than those for the $\Sigma 0_0$ / $\Sigma 0_{00}$ states of the deuterated complexes. However, this does not indicate a large inversion splittings of $\Pi 1_1^{lower}$ energy levels because the different possible perturbers of the $\Sigma 0_0$ and $\Pi 1_1$ states make a comparison of the tunneling splittings not straightforward. The inversion motion in the $\Pi 1_1$ state is parallel to the van der Waals axis and effectively quenched. The remaining small splitting is mainly induced by the Coriolis interaction with the $\Sigma 1_1$ states. A difference of 138.6 MHz in B constants for Ar-NH_3 corresponds to a tunneling splitting of 376 MHz in the $J = 1$ energy levels.[15]

For the Xe-NH_3 complex, the difference between the corresponding B constants is smaller, which suggests an even smaller energy splitting. This is also supported by roughly the same transition intensities found in the two inversion states and the similar internal dynamics as suggested by the nuclear quadrupole coupling constants.

6.4.4 $\Sigma 1_1$ and $\Pi 1_1^{lower}$ states

The observation of the $\Pi 1_1^{lower}$, but not the $\Sigma 1_1$ state, leads the conclusion that the $\Pi 1_1^{lower}$ state lies lower in energy than the $\Sigma 1_1$ state. This is based on the transition intensity in the $\Pi 1_1^{lower}$ state, which is approximately half of that in the $\Sigma 0_0$ state and follows the prediction of transition intensities from spin statistics of *ortho* and *para* states. Since the $\Sigma 1_1$ and $\Pi 1_1$ states have the same symmetry, the $\Pi 1_1^{lower}$ state must be the lowest *para* state to be more populated. Although a definite conclusion can not be drawn because of the lack of information about the $\Sigma 1_1$ state, this energy level arrangement could explain the shift to negative values of the centrifugal distortion constants D_J for the $\Pi 1_1^{lower}$ state due to the Coriolis interaction with the unobserved $\Sigma 1_1$ state. In addition, the shift of D_J is relatively small which indicates only a small Coriolis perturbation and a relatively large energy gap between the $\Sigma 1_1$ and $\Pi 1_1^{lower}$ states. Therefore, the population of the higher $\Sigma 1_1$ state will be significantly lower than the $\Pi 1_1^{lower}$ state and could be responsible for the unsuccessful search for the $\Sigma 1_1$ state.

Although a similar energy level arrangement has been found in the N_2-NH_3 (Ref. 32) and CO-NH_3 (Ref. 33) complexes, this behavior is distinct from the case of Ar-NH_3, in which the $\Sigma 1_1$ state lies lower in energy.[15] This contrast arising from the

substitution of Ar with Xe is very surprising. A comparison of the Ar- and Xe-NH_3 PESs shows that the Xe-NH_3 potential has a lower barrier (Ar-NH_3: 38.0 cm^{-1},[10] Xe-NH_3: 31.6 cm^{-1}) to NH_3 internal rotation at θ = 180°, which corresponds to a symmetric Rg-NH_3 (Rg = Ar, Xe) configuration with the rare gas atom approaching the N end. Also, at φ = 0°, where one H atom is coplanar with and lies between the rare gas and N atoms, the minimum is at θ = 180° in the Xe-NH_3 system, instead of a roughly T-shaped structure in the Ar-NH_3 case. According to previous experimental and theoretical studies of the Ar-NH_3 complex,[9,15] the $\Pi 1_1^{lower}$ state is localized at θ = 180°, the notion that Xe-NH_3 favors the orientation at θ = 180° could lower its $\Pi 1_1^{lower}$ state. However, the $\Sigma 1_1$ state is localized around the global minimum, and is expected to have lower energy than the localization of $\Pi 1_1^{lower}$ state. Therefore, the energy reordering of the $\Sigma 1_1$ and $\Pi 1_1^{lower}$ state when going from the Ar-NH_3 to the Xe-NH_3 system can not be fully explained. A detailed physical explanation would require wavefunction calculation and bound states determination for each tunneling state. It is hoped that future progress in this direction will provide further insight into the understanding of such a dynamically complicated system.

6.5 Discussion of the Ne-Xe-NH_3 spectroscopic results

6.5.1 Structural parameters and force constants

A comparison of rotational constants reveals that the A rotational constant of the Ne-Xe-NH_3 trimer is rather close to the B constant of the Ne-NH_3 dimer and insensitive to Xe isotopic substitution. This supports the initially predicted triangular

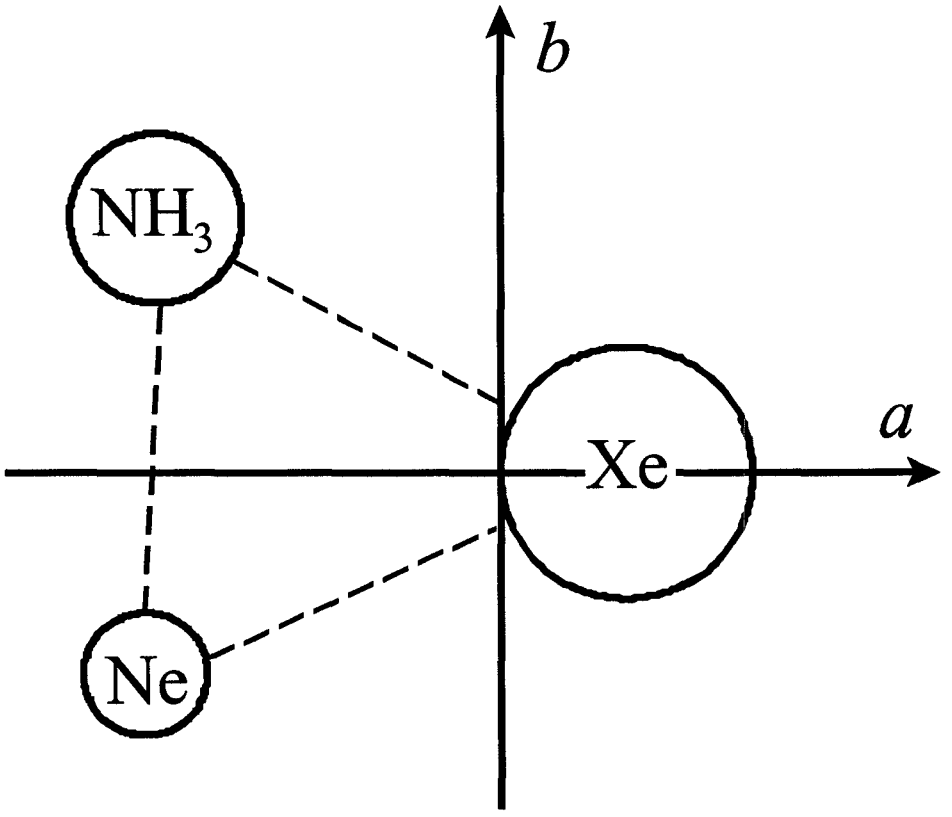

Figure 6-8: Geometry of the Ne-Xe-NH_3 complex in the inertial axis system. The NH_3 molecule is treated as a sphere.

structure of the trimer with the Ne-NH_3 axis almost parallel to the *b*-axis and the Xe atom located close to the *a*- axis (see Figure 6-8). With this picture, the *A* constant has only a small contribution from the Xe atom. The trimer is non-rigid and the large amplitude zero-point vibrational motions are reflected in the size of inertial defect, $\Delta = I_C - I_B - I_A$, which is zero for a planar rigid molecule. For the ^{20}Ne-^{132}Xe-$^{14}NH_3$ isotopomer, Δ is 4.78 amu Å, as a result of the out-of-plane H atoms and vibrational motions of the complex. The contribution from the H atoms can be estimated by considering the mass of H atoms being delocalized over the surface of a sphere with a

radius of the N-H bond length; a value of -2.05 amu Å resulted.[18] This leaves an inertial defect of 6.83 amu Å contributed by the vibrational motions. This value is comparable to that of the Ne_2-NH_3 complex (8 amu Å),[18] and considerably larger than that of planar more rigid molecules, for example, H_2O (0.0486 amu Å).[35] The non-rigidity of the trimer makes it difficult to extract accurate structural parameters because the determined spectroscopic constants are highly averaged values over the large amplitude zero-point vibrational motions. To a first approximation, the Xe-Ne distance ($R_{Ne\text{-}Xe}$), Xe-c.m.(NH_3) distance ($R_{Xe\text{-}NH3}$), and Ne-c.m.(NH_3) ($R_{Ne\text{-}NH3}$) distance, were estimated by treating the NH_3 molecule as a sphere and using the planar moments P_a and P_b (see Table 6-19) of the observed isotopomers, except ^{20}Ne-^{131}Xe-$^{15}NH_3$. The planar moment P_c was not used here because it describes the mass distribution outside the plane of symmetry, which is neglected in this approximation. The STRFIT program[43] was used to perform the structural fit. In the initial fit, the isotopic effects on the van der Waals bond distances were neglected, and values of 3.99(1) Å, 4.09(1) Å and 55.25(3)° were determined for $R_{Ne\text{-}Xe}$, $R_{Xe\text{-}NH3}$, and ∠[Ne-Xe-c.m.(NH_3)], respectively. From these parameters, the $R_{Ne\text{-}NH3}$ value was calculated to be 3.75 Å. The standard deviation of the fit is 0.25 amu Å. In the second fit, the variation of van der Waals bond distances upon isotopic substitution was considered. Based on the isotopic data of the corresponding dimers, the $R_{Ne\text{-}Xe}$ and $R_{Ne\text{-}NH3}$ distances were assumed to shrink by 0.004 Å when substituting ^{20}Ne with ^{22}Ne, and the $R_{Xe\text{-}NH3}$ and $R_{Ne\text{-}NH3}$ values decrease by 0.003 Å upon substitution of ^{14}N with ^{15}N. The effect of the Xe isotope substitution was estimated to be at least one order of magnitude smaller and therefore was neglected here. The deviation of this fit is

substantially reduced to 0.03 amu Å, and the uncertainties of the determined structural parameters are smaller by one order of magnitude. The determined values for $R_{Ne\text{-}Xe}$, $R_{Xe\text{-}NH3}$, and ∠[Ne-Xe-c.m.(NH_3)] are 3.997(1) Å, 4.080(2) Å and 55.303(5)°, respectively. This gives a value of 3.749 Å for $R_{Ne\text{-}NH3}$. The $R_{Ne\text{-}Xe}$, $R_{Xe\text{-}NH3}$, and $R_{Ne\text{-}NH3}$ values increase by 0.003 Å, 0.01 Å, and 0.03 Å, respectively, in the trimer relative to the corresponding dimers.[8,39]

The centrifugal distortion constants of the Ne-Xe-NH_3 complex were used in a harmonic force field analysis to obtain information about van der Waals stretching frequencies and corresponding force constants. The NH_3 molecule was treated as a pseudo atom and the rotational and vibrational degrees of freedom of the NH_3 monomer were disregarded. Therefore, the complex has C_s point group symmetry. There are three vibrational modes in the complex, i.e. the Ne-NH_3 stretch (ν_1), the Ne-Xe stretch (ν_2), and the Xe-NH_3 stretch (ν_3). This results in a 3×3 force constant matrix $\boldsymbol{F}$ with diagonal terms corresponding to the three stretching modes respectively. The harmonic force field analysis was performed using the ASYM20PC program of Hedberg and Mills.[44] The quartic centrifugal distortion constants of seven isotopomers listed in Table 6-19 were used to refine the diagonal force constants. All off-diagonal terms were fixed at zero during the fit. The corresponding harmonic frequencies were then calculated from the obtained force constants using Wilson's GF matrix method.[45] The calculated centrifugal distortion constants are compared with the experimental ones in Table 6-22. In this analysis, the experimental D_J and d_1 centrifugal distortion constants were well reproduced, within 5%. Relatively large differences were found in the D_{JK} and d_2 constants. However, the variation in the calculated D_{JK} constants with

different isotopomers is consistent with the experimental observation. It is noted that the experimental D_{JK} and d_2 constants have relatively large uncertainties. Transitions within higher K stacks, which would improve the accuracy of these two constants, could not be detected in the spectroscopic searches. The determined three force constants are 0.211(4) N m^{-1}, 0.39(1) N m^{-1}, and 0.86(8) N m^{-1} for the Ne-NH_3, Ne-Xe, Xe-NH_3 stretches, respectively, which correspond to vibrational frequencies of 15.9, 20.9, and 32.2 cm^{-1}, respectively. Compared with the corresponding force constants of the dimers (Ne-NH_3: 0.291 N m^{-1},[8] Ne-Xe: 0.97 N m^{-1},[39] and Xe-NH_3: 1.18 N m^{-1}), the values in the trimer are smaller by 27-60%. It is necessary to include non-additive three-body effects to explain the smaller force constants in the trimer. For example, a repulsive triple-dipole dispersion term[46] could contribute to a shallower potential, and therefore smaller force constants. However, the dramatic decrease in the Ne-Xe stretching force constant by 60% only corresponds to 0.003 Å bond lengthening, while the increase of Ne-NH_3 and Xe-NH_3 bond lengths is an order of magnitude larger but the stretching force constants only decrease by 27%. The inconsistency between the variations in van der Waals bond lengths and stretching force constants makes it difficult to draw definite conclusions about the nature of the three-body effects. The situation could be improved by employing a more accurate model for the structural and force field analyses, for example, by taking into account the NH_3 internal degrees of freedom, the isotopic effects on the force constants, and the force field anharmonicity.

6.5.2 Hyperfine structure and angular information

Dynamical information about the Ne-Xe-NH_3 trimer can be extracted from the determined ^{14}N and ^{131}Xe nuclear quadrupole coupling constants. As described in Section 6.4.2, the ^{14}N nuclear quadrupole coupling constants can be interpreted as highly averaged values over the large amplitude NH_3 internal motions using equation (6-2). The Legendre polynomial factors, $\langle P_2(\cos\theta_a)\rangle$ and $\langle P_2(\cos\theta_b)\rangle$, were calculated to be 0.025 and -0.046 for the $^{20}Ne^{132}Xe^{14}NH_3$ isotopomer. These are on the same magnitude as those for the Ne-NH_3 (-0.066)[8] and Xe-NH_3 (-0.018) dimers, indicating that the NH_3 subunit continues to undergo nearly free internal motions within the trimer. The $\langle P_2(\cos\theta_b)\rangle$ value is relatively close to the $\langle P_2(\cos\theta_a)\rangle$ value for the Ne-NH_3 dimer because the Ne-NH_3 axis in the trimer lies nearly parallel to the *b*- axis.

The ^{131}Xe nuclear quadrupole coupling constants provide additional information about the effect of an additional Ne atom on the Xe-NH_3 interaction. As the χ_{cc} value of the trimer is relatively insensitive to the van der Waals vibrational motions, it is expected to be equal to the sum of the corresponding values of the Ne-^{131}Xe and ^{131}Xe-NH_3 dimers if pairwise additivity of this property and unchanged NH_3 internal dynamics from the Xe-NH_3 dimer to the Ne-Xe-NH_3 trimer are assumed. The χ_{cc} value of the ^{131}Xe-NH_3 dimer in the ground state has not been experimentally determined, however, we can estimate it as $-1/2\chi_{aa}$ since NH_3 undergoes nearly free internal motion in the dimer. This is a reasonable assumption because the asymmetry parameters, $\eta = |\chi_{bb}-\chi_{cc}|/\chi_{aa}$, of the ^{131}Xe nuclear quadrupole coupling constants about

the *a*- axis are relatively low even for the $\Pi 1_1^{lower}$ states (~0.08) in which the NH_3 internal motion is more hindered. The summation of χ_{cc} values for ^{22}Ne-^{131}Xe (-0.194 MHz) and ^{131}Xe-$^{15}NH_3$ (-1.207 MHz) gives a value of -1.401 MHz, very close to the value of -1.454 MHz in the ^{22}Ne-^{131}Xe-$^{15}NH_3$ trimer. This suggests that the effective orientation of NH_3 with respect to the Xe atom in the trimer stays similar as in the dimer and the additional Ne atom does not have a dramatic effect.

6.6 Summary

An *ab initio* PES of the Xe-NH_3 complex was constructed at the CCSD(T) level of theory. The global minimum is at a roughly T-shaped structure with the Xe atom located in the direction between two H atoms. The energy barrier at the N end was found to be lower than that approaching the three H face center. Rotational transitions within the $\Sigma 0_0$ and $\Pi 1_1^{lower}$ states for the Xe-$^{14}NH_3$ and Xe-$^{15}NH_3$ isotopomers and the $\Sigma 0_0$ state for the deuterated isotopomers were measured and assigned. Two inversion components were observed for each state except for the 's' component of the $\Sigma 0_0$ state of the isotopomers containing $^{14}NH_3$ and $^{15}NH_3$ containing due to its spin statistical weight of 0. Nuclear quadrupole hyperfine structures arising from the ^{14}N and ^{131}Xe nuclei were detected and analyzed. The observed spectra indicate nearly free internal rotation of NH_3 unit within the complex. They also suggest that the $\Pi 1_1^{lower}$ state has lower energy than the unobserved $\Sigma 1_1$ state, in contrast to the case of Ar-NH_3. A detailed physical explanation for this behavior requires further wavefunction calculations and bound state determination. Rotational spectra of the Xe-$(NH_3)_2$ complex could not be observed, possibly due to the low yield

in the molecular expansion. Instead, several *a*- type and *b*- type transitions of the ground state were measured for the Ne-Xe-NH_3 complex. The structural and harmonic force field analyses performed using the determined spectroscopic constants indicate that non-additive three-body effects are present in this system. Analyses of the ^{14}N and ^{131}Xe nuclear quadrupole coupling constants suggest that the NH_3 unit continues to undergo nearly free internal rotation motion and that the presence of Ne has little effect on the orientation of NH_3 with respect to the Xe atom.

Table 6-1: *Ab initio* interaction energies (in cm^{-1}) of $Xe\text{-}NH_3$.

R / Å	$\varphi = 0°$						
	$\theta = 0°$	15°	30°	45°	60°	75°	90°
3.6	88.39	108.1	177.0	283.0	368.1	357.9	244.1
3.7	-5.6	6.7	50.0	115.7	165.7	153.3	75.7
3.8	-66.3	-59.0	-33.3	5.2	32.2	19.6	-32.2
3.9	-103.4	-99.6	-85.5	-65.2	-52.8	-64.4	-97.9
4.0	-124.0	-122.3	-116.0	-107.3	-104.0	-114.2	-134.8
4.1	-133.2	-132.9	-131.4	-130.1	-132.2	-140.6	-152.4
4.2	-134.7	-135.3	-136.9	-139.8	-139.9	-151.6	-157.3
4.3	-131.3	-132.3	-135.6	-140.9	-147.3	-152.6	-154.2
4.4	-124.8	-126.1	-130.1	-136.5	-143.3	-147.3	-146.4
4.5	-116.5	-117.9	-122.2	-128.9	-135.5	-138.4	-135.9
	$\theta = 105°$	120°	135°	150°	165°	180°	
3.6	105.3	14.2	-16.1	-8.1	10.7	19.8	
3.7	-14.6	-71.7	-89.1	-82.5	-69.9	-63.9	
3.8	-88.9	-123.0	-132.3	-127.6	-119.8	-116.1	
3.9	-131.7	-150.6	-155.1	-152.2	-148.0	-146.0	
4.0	-153.3	-162.3	-164.0	-162.8	-161.2	-160.5	
4.1	-160.7	-163.6	-163.8	-163.9	-164.3	-164.4	
4.2	-159.1	-158.3	-158.0	-159.1	-160.8	-161.5	
4.3	-152.1	-149.2	-148.7	-150.6	-153.2	-154.3	
4.4	-141.9	-138.1	-137.7	-140.1	-143.2	-144.5	
4.5	-130.3	-126.2	-125.9	-128.7	-132.1	-133.5	

R / Å	$\varphi = 15°$						
	$\theta = 0°$	15°	30°	45°	60°	75°	90°
3.6		106.7	166.4	252.2	312.8	290.3	185.9
3.7		5.8	42.8	94.8	128.6	108.1	36.8
3.8		-59.7	-38.0	-8.6	7.9	-9.9	-56.1
3.9		-99.9	-88.5	-73.9	-68.2	-83.1	-113.8
4.0		-122.6	-117.8	-112.6	-113.4	-125.3	-144.2
4.1		-133.1	-132.5	-133.0	-137.4	-146.8	-157.4
4.2		-135.4	-137.4	-141.1	-147.2	-154.4	-159.5
4.3		-132.4	-135.7	-141.2	-147.9	-153.2	-154.5
4.4		-126.1	-130.0	-136.3	-142.8	-146.5	-145.5
4.5		-117.9	-122.0	-128.2	-134.3	-136.9	-134.5
	$\theta = 105°$	120°	135°	150°	165°	180°	
3.6	67.5	-5.4	-21.1	-10.4	10.4		
3.7	-39.9	-84.8	-94.5	-84.1	-70.1		
3.8	-105.3	-131.6	-135.9	-128.7	-119.9		
3.9	-142.0	-156.1	-157.4	-152.9	-148.0		
4.0	-159.4	-165.6	-165.5	-163.2	-161.2		

Table 6-1: (continued).

R / Å	$\varphi = 15°$					
	$\theta = 105°$	120°	135°	150°	165°	180°
4.1	-164.0	-165.4	-164.7	-164.2	-164.3	
4.2	-160.5	-159.1	-158.4	-159.2	-160.8	
4.3	-152.2	-149.4	-148.8	-150.7	-153.2	
4.4	-141.4	-137.9	-137.6	-140.1	-143.2	
4.5	-129.3	-125.7	-125.7	-128.7	-132.0	

R / Å	$\varphi = 30°$						
	$\theta = 0°$	15°	30°	45°	60°	75°	90°
3.6		103.2	141.0	180.1	187.0	139.3	54.9
3.7		3.4	25.6	46.3	44.2	7.2	-50.6
3.8		-61.3	-49.5	-40.5	-47.4	-75.6	-114.2
3.9		-100.9	-95.8	-94.2	-103.2	-124.3	-149.3
4.0		-123.2	-122.3	-124.9	-134.3	-149.8	-165.1
4.1		-133.4	-135.1	-139.8	-148.8	-159.9	-168.5
4.2		-135.5	-138.6	-144.3	-152.3	-160.0	-164.0
4.3		-132.4	-136.0	-142.0	-148.9	-154.0	-155.0
4.4		-126.0	-129.8	-135.5	-141.3	-144.5	-143.4
4.5		-117.8	-121.4	-126.6	-131.4	-133.1	-130.9
	$\theta = 105°$	120°	135°	150°	165°	180°	
3.6	-19.1	-51.2	-43.5	-16.1	9.7		
3.7	-97.8	-115.6	-107.6	-88.0	-70.6		
3.8	-143.1	-151.8	-144.5	-131.2	-120.2		
3.9	-165.7	-168.8	-162.9	-154.6	-148.2		
4.0	-173.3	-173.2	-168.8	-164.2	-161.4		
4.1	-171.4	-169.5	-166.6	-164.8	-164.4		
4.2	-163.6	-161.0	-159.3	-159.6	-160.9		
4.3	-152.6	-149.7	-149.1	-150.8	-153.2		
4.4	-140.0	-137.3	-137.5	-140.1	-143.2		
4.5	-127.0	-124.6	-125.4	-128.6	-132.0		

R / Å	$\varphi = 45°$						
	$\theta = 0°$	15°	30°	45°	60°	75°	90°
3.6		99.7	116.0	111.4	70.9	3.0	-63.6
3.7		1.0	8.6	-0.1	-33.7	-84.0	-129.7
3.8		-62.8	-60.7	-71.1	-98.3	-134.9	-165.6
3.9		-102.0	-103.1	-113.7	-135.2	-161.4	-181.3
4.0		-123.8	-126.7	-136.6	-153.4	-171.7	-183.9
4.1		-133.8	-139.4	-146.3	-159.2	-171.5	-178.3
4.2		-135.7	-139.7	-147.3	-156.9	-164.8	-168.0
4.3		-132.5	-136.3	-142.7	-149.6	-154.4	-155.1

Table 6-1: (continued).

R / Å	$\varphi = 45°$						
	$\theta = 0°$	15°	30°	45°	60°	75°	90°
4.4		-126.0	-129.6	-134.7	-139.7	-142.2	-141.3
4.5		-117.7	-120.9	-125.0	-128.4	-129.3	-127.4
	$\theta = 105°$	120°	135°	150°	165°	180°	
3.6	-99.4	-95.1	-62.3	-21.7	9.0		
3.7	-151.5	-145.0	-120.3	-91.8	-71.1		
3.8	-177.9	-171.0	-153.0	-133.8	-120.5		
3.9	-187.4	-180.9	-168.3	-156.2	-148.5		
4.0	-186.1	-180.4	-172.1	-165.2	-161.5		
4.1	-178.1	-173.4	-168.4	-165.4	-164.5		
4.2	-166.3	-162.6	-160.2	-159.9	-160.9		
4.3	-152.7	-150.0	-149.4	-150.9	-153.2		
4.4	-138.5	-136.6	-137.3	-140.1	-143.2		
4.5	-124.6	-123.4	-125.0	-128.5	-132.0		

R / Å	$\varphi = 60°$						
	$\theta = 0°$	15°	30°	45°	60°	75°	90°
3.6		98.3	105.8	83.8	25.5	-49.6	-109.3
3.7		0.1	1.7	-18.7	-64.1	-119.1	-160.2
3.8		-63.5	-65.3	-83.4	-118.2	-157.7	-185.4
3.9		-102.4	-106.0	-121.5	-147.8	-175.7	-193.6
4.0		-124.1	-128.5	-141.3	-160.9	-180.1	-191.1
4.1		-133.9	-138.5	-148.9	-163.1	-175.9	-182.1
4.2		-135.8	-140.2	-148.4	-158.5	-166.6	-169.4
4.3		-132.5	-136.4	-142.9	-149.8	-154.5	-155.1
4.4		-126.0	-129.5	-134.4	-139.0	-141.2	-140.4
4.5		-117.7	-120.7	-124.3	-127.2	-127.7	-126.0
	$\theta = 105°$	120°	135°	150°	165°	180°	
3.6	-130.9	-112.7	-70.1	-24.1	8.7		
3.7	-172.5	-156.8	-125.5	-93.4	-71.3		
3.8	-191.6	-178.7	-156.4	-134.8	-120.7		
3.9	-196.0	-185.7	-170.5	-156.9	-148.5		
4.0	-191.1	-183.2	-173.4	-165.7	-161.6		
4.1	-180.7	-174.9	-169.1	-165.7	-164.5		
4.2	-167.3	-163.3	-160.5	-160.0	-160.9		
4.3	-152.7	-150.0	-149.4	-151.0	-153.2		
4.4	-137.9	-136.3	-137.2	-140.1	-143.2		
4.5	-123.7	-122.9	-124.8	-128.5	-132.0		

Table 6-2: Measured transition frequencies and determined spectroscopic constants of the $\Sigma 0_{0a}$ state of Xe-NH_3 isotopomers.

		^{136}Xe-NH_3		^{134}Xe-NH_3		^{132}Xe-NH_3		^{129}Xe-NH_3	
J'-J''	F'-F''	ν_{obs} (MHz)	$\Delta\nu$ [a] (kHz)	ν_{obs} (MHz)	$\Delta\nu$ (kHz)	ν_{obs} (MHz)	$\Delta\nu$ (kHz)	ν_{obs} (MHz)	$\Delta\nu$ (kHz)
1-0	0-1	4039.4476	0.01	4046.0626	0.2	4052.8783	0.1	4063.4890	-0.1
	2-1	4039.4822	2.5	4046.0983	2.2	4052.9134	1.7	4063.5242	2.2
	1-1	4039.5015	0.4	4046.1192	0.6	4052.9344	0.4	4063.5442	0.3
2-1	3-2	8078.3017	-2.2	8091.5312	-2.2	8105.1609	-1.4	8126.3755	-1.6
	2-1	8078.3017	-3.7	8091.5312	-3.8	8105.1609	-3.0	8126.3755	-3.2
3-2	4-3	12115.8099	1.7	12135.6474	1.7	12156.0842	1.4	12187.8955	1.5
	3-2	12115.8099	0.8	12135.6474	0.8	12156.0842	0.5	12187.8955	0.6
4-3	5-4	16151.3435	0.1	16177.7873	0.1	16205.0237	0.1	16247.4264	0.1
	4-3	16151.3435	-0.5	16177.7873	-0.5	16205.0237	-0.4	16247.4264	-0.5
B /MHz		2019.7968(3)		2023.1054(3)		2026.5134(3)		2031.8190(3)	
D_J /kHz		27.59(4)		27.76(4)		27.85(4)		28.12(4)	
H_J /kHz		0.005(1)		0.008(1)		0.007(1)		0.012(1)	
χ_{aa}(^{14}N) /MHz		0.071(2)		0.075(2)		0.074(2)		0.073(2)	
σ /kHz [b]		1.7		1.6		1.2		1.4	

[a] $\Delta\nu = \nu_{obs} - \nu_{cal}$.

[b] Standard deviation of the fit.

Table 6-3: Measured transition frequencies and determined spectroscopic constants of the $\Sigma 0_{0a}$ state of ^{131}Xe-NH_3 and ^{131}Xe-$^{15}NH_3$ isotopomers.

	^{131}Xe-NH_3			^{131}Xe-$^{15}NH_3$		
J'-J''	F_1', F' - F_1'', F''	ν_{obs} (MHz)	$\Delta\nu$[a] (kHz)	F' - F''	ν_{obs} (MHz)	$\Delta\nu$ (kHz)
1-0	0.5, 1.5 – 1.5, 2.5	4055.7902	-3.2	0.5 – 1.5	3863.0119	-0.2
	2.5, 3.5 – 1.5, 2.5	4056.2722	4.8	2.5 – 1.5	3863.4938	-1.1
	1.5, 2.5 – 1.5, 2.5	4056.8690	-1.6	1.5 – 1.5	3864.0975	-1.0
2-1	0.5, 1.5 – 1.5, 2.5	8111.0425	-0.7	0.5 – 1.5	7725.5419	0.02
	1.5, 2.5 – 1.5, 2.5	8111.6419	2.2	1.5 – 1.5	7726.1450	-0.5
	3.5, 4.5 – 2.5, 3.5	8112.0667	-0.3	3.5 – 2.5	7726.5765	-0.1
	0.5, 1.5 – 0.5, 1.5	8112.1200	-0.4	0.5 – 0.5	7726.6316	3.3
	2.5, 3.5 – 2.5, 3.5	8112.6650	-1.8	2.5 – 2.5	7727.1786	-1.5
	1.5, 2.5 – 0.5, 1.5	8112.7178	0.9	1.5 – 0.5	7727.2331	1.2
3-2	4.5, 5.5 – 3.5, 4.5	12166.4915	-3.1	4.5 – 3.5	11588.4055	-0.7
	3.5, 4.5 – 2.5, 3.5	12166.4915	-1.7	3.5 – 2.5	11588.4055	-0.7
	2.5, 3.5 – 1.5, 2.5	12166.6425	2.6	2.5 – 1.5	11588.5551	-0.5
	1.5, 2.5 – 0.5, 1.5	12166.6425	2.3	1.5 – 0.5	11588.5551	-0.5
4-3	5.5, 6.5 – 4.5, 5.5	16218.9164	2.5	5.5 – 4.5	15448.4121	-2.2
	4.5, 5.5 – 3.5, 4.5	16218.9164	3.2	4.5 – 3.5	15448.4121	-2.2
	3.5, 4.5 – 2.5, 3.5	16218.9790	-2.9	3.5 – 2.5	15448.4867	2.4
	2.5, 3.5 – 1.5, 2.5	16218.9790	-2.9	2.5 – 1.5	15448.4867	2.4
	B /MHz	2028.2502(2)			1931.8581(1)	
	D_J /kHz	27.51(3)			25.125(5)	
	H_J /kHz	-0.004(1)				
	χ_{aa}(^{131}Xe) /MHz	2.385(1)			2.414(1)	
	χ_{aa}(^{14}N) /MHz	0.074(-)[b]				
	σ/kHz [c]	2.4			1.5	

[a] $\Delta\nu = \nu_{obs} - \nu_{cal}$.
[b] Fixed to the value of ^{132}Xe-NH_3 during the fit.
[c] Standard deviation of the fit.

Table 6-4: Measured transition frequencies and determined spectroscopic constants of the $\Pi 1_{1s}$ states of Xe-NH_3 isotopomers.

		^{136}Xe-NH_3		^{134}Xe-NH_3		^{132}Xe-NH_3		^{129}Xe-NH_3	
J'-J''	F'-F''	ν_{obs} (MHz)	$\Delta\nu$ [a] (kHz)	ν_{obs} (MHz)	$\Delta\nu$ (kHz)	ν_{obs} (MHz)	$\Delta\nu$ (kHz)	ν_{obs} (MHz)	$\Delta\nu$ (kHz)
2-1	2-1	7833.9836	-1.7	7846.3250	-1.6	7859.0327	-1.4	7878.8134	-1.8
	3-2	7834.0925	1.8	7846.4312	1.7	7859.1416	1.5	7878.9222	1.9
	1-0	7834.2449	-0.1	7846.5841	-0.1	7859.2928	-1.0	7879.0741	-0.1
3-2	3-2	11752.0548	5.5	11770.5777	5.4	11789.6490	4.6	11819.3442	5.9
	4-3	11752.0731	-5.5	11770.5954	-5.4	11789.6739	-4.6	11819.3617	-5.9
4-3	4-3			15695.7958	-0.7				
	5-4	15671.0931	0.1	15695.8098	1.0	15721.2660	-0.03	15760.8863	1.0
	3-2	15671.0931	-0.1	15695.8098	0.4	15721.2660	0.03	15760.8863	-1.0
B /MHz		1958.3828(5)		1961.4655(5)		1964.6425(5)		1969.5838(5)	
D_J /kHz		-17.37(5)		-17.64(5)		-17.66(5)		-18.19(5)	
H_J /kHz		-0.067(2)		-0.070(2)		-0.064(2)		-0.071(2)	
$\chi_{aa}(^{14}N)$ /MHz		-0.350(4)		-0.343(4)		-0.352(4)		-0.349(4)	
$\lvert\chi_{bb}(^{14}N) - \chi_{cc}(^{14}N)\rvert$ /MHz		0.326(16)		0.346(16)		0.311(16)		0.325(16)	
$\eta(^{14}N)$ [b]		-0.931		-1.009		-0.884		-0.931	
σ /kHz [c]		3.3		3.1		2.8		3.6	

[a] $\Delta\nu = \nu_{obs} - \nu_{cal}$.

[b] Asymmetry parameter $\eta = |\chi_{bb}-\chi_{cc}|/\chi_{aa}$.

[c] Standard deviation of the fit.

Table 6-5: Measured transition frequencies and determined spectroscopic constants of the $\Pi 1_{1a}$ states of Xe-NH_3 isotopomers.

		^{136}Xe-NH_3		^{134}Xe-NH_3		^{132}Xe-NH_3		^{129}Xe-NH_3	
J'-J''	F'-F''	ν_{obs} (MHz)	$\Delta\nu$ [a] (kHz)	ν_{obs} (MHz)	$\Delta\nu$ (kHz)	ν_{obs} (MHz)	$\Delta\nu$ (kHz)	ν_{obs} (MHz)	$\Delta\nu$ (kHz)
2-1	2-1	7916.0852	-0.8	7928.6928	-0.3	7941.6752	0.4	7961.8853	-0.7
	3-2	7916.2008	0.1	7928.8078	-0.5	7941.7889	-1.3	7962.0014	0.5
	1-0	7916.3175	0.7	7928.9255	0.8	7941.9079	1.0	7962.1172	0.2
3-2	3-3	11873.5307	1.6	11892.4395	1.3	11911.9137	0.8	11942.2308	1.1
	2-1	11873.6194	-1.3	11892.5292	-1.0	11912.0047	-0.4	11942.3206	-0.8
	4-3	11873.6194	-2.0	11892.5292	-1.7	11912.0047	-1.1	11942.3206	-1.5
4-3	4-3	15830.2155	1.5			15881.3972	0.1		
	5-4	15830.2272	-1.5	15855.4429	0.0	15881.4117	-0.1	15921.8353	0.0
B /MHz		1979.1302(4)		1982.2826(4)		1985.5277(4)		1990.5804(4)	
D_J /kHz		10.59(5)		10.67(5)		10.62(5)		10.63(5)	
H_J /kHz		-0.017(2)		-0.015(2)		-0.015(1)		-0.015(2)	
$\chi_{aa}(^{14}N)$ /MHz		-0.369(2)		-0.371(2)		-0.371(2)		-0.370(2)	
σ /kHz [b]		1.3		0.8		0.8		0.8	

[a] $\Delta\nu = \nu_{obs} - \nu_{cal}$.

[b] Standard deviation of the fit.

Table 6-6: Measured transition frequencies of the $\Pi 1_1$ states of $^{131}Xe\text{-}NH_3$.

	$\Pi 1_{1s}$			$\Pi 1_{1a}$		
J'-J''	$F_1', F' - F_1'', F''$	ν_{obs} (MHz)	$\Delta\nu$[a] (kHz)	$F_1', F' - F_1'', F''$	ν_{obs} (MHz)	$\Delta\nu$ (kHz)
2-1	0.5, 1.5 – 0.5, 1.5	7864.7435	-5.6	0.5, 1.5 – 0.5, 0.5	7947.5529	1.7
	0.5, 0.5 – 0.5, 1.5	7864.7435	-5.5	1.5, 2.5 – 0.5, 1.5	7948.0020	-0.7
	1.5, 0.5 – 0.5, 1.5	7865.1983	-2.9	1.5, 1.5 – 0.5, 0.5	7948.0020	-1.3
	1.5, 1.5 – 0.5, 1.5	7865.1983	-2.9	3.5, 3.5 – 2.5, 2.5	7948.1204	-4.1
	1.5, 2.5 – 0.5, 1.5	7865.1983	-2.9	3.5, 4.5 – 2.5, 3.5	7948.2127	3.5
	3.5, 3.5 – 2.5, 2.5	7865.3397	-1.2	3.5, 2.5 – 2.5, 1.5	7948.2317	-2.8
	3.5, 4.5 – 2.5, 3.5	7865.4228	2.3	2.5, 2.5 – 2.5, 2.5	7948.6035	0.3
	3.5, 2.5 – 2.5, 1.5	7865.4565	3.4	1.5, 2.5 – 1.5, 2.5	7948.7051	1.2
	2.5, 2.5 – 2.5, 2.5	7865.7992	4.5	2.5, 3.5 – 1.5, 2.5	7949.0327	1.1
	2.5, 3.5 – 2.5, 3.5	7865.8766	4.4			
	1.5, 2.5 – 1.5, 2.5	7865.9122	1.1			
	1.5, 1.5 – 1.5, 1.5	7865.9923	-1.2			
	1.5, 2.5 – 1.5, 1.5	7865.9923	-1.2			
	1.5, 0.5 – 1.5, 1.5	7865.9923	-1.3			
	2.5, 1.5 – 1.5, 0.5	7866.1734	-4.6			
	2.5, 3.5 – 1.5, 2.5	7866.2381	3.7			
	2.5, 2.5 – 1.5, 1.5	7866.3116	-3.9			
3-2	1.5, 1.5 – 1.5, 1.5	11798.8604	1.0	1.5, 1.5 – 1.5, 1.5	11921.3656	-0.2
	1.5, 1.5 – 1.5, 0.5	11798.8604	1.1	1.5, 2.5 – 1.5, 2.5	11921.4172	3.3
	1.5, 1.5 – 1.5, 2.5	11798.8604	1.0	1.5, 2.5 – 1.5, 1.5	11921.4172	-1.2
	1.5, 2.5 – 1.5, 2.5	11798.8804	0.7	2.5, 3.5 – 2.5, 3.5	11921.7452	-4.9
	4.5, 4.5 – 3.5, 3.5	11799.3001	5.9	4.5, 4.5 – 3.5, 3.5	11921.8312	6.7
	4.5, 5.5 – 3.5, 4.5	11799.3190	-2.6	4.5, 5.5 – 3.5, 4.5	11921.8547	-1.0
	2.5, 2.5 – 1.5, 1.5	11799.5242	-0.6	3.5, 3.5 – 2.5, 2.5	11922.0336	1.5
	2.5, 2.5 – 1.5, 2.5	11799.5242	-0.6	3.5, 4.5 – 2.5, 3.5	11922.0632	-4.0

Table 6-6: (continued).

	$\Pi 1_{1s}$			$\Pi 1_{1a}$		
J'-J''	$F_1', F' - F_1'', F''$	ν_{obs} (MHz)	$\Delta\nu$ (kHz)	$F_1', F' - F_1'', F''$	ν_{obs} (MHz)	$\Delta\nu$ (kHz)
3-2	3.5, 4.5 – 2.5, 3.5	11799.5242	-5.2	3.5, 2.5 – 2.5, 1.5	11922.0777	1.4
	2.5, 3.5 – 1.5, 2.5	11799.5429	1.2	2.5, 3.5 – 1.5, 2.5	11922.0777	-0.1
	3.5, 3.5 – 3.5, 2.5	11799.9597	0.6	3.5, 3.5 – 3.5, 3.5	11922.5127	2.0
	3.5, 3.5 – 3.5, 4.5	11799.9597	-0.4	3.5, 4.5 – 3.5, 4.5	11922.5127	-1.5
	3.5, 3.5 – 3.5, 3.5	11799.9597	-3.8			
	3.5, 4.5 – 3.5, 4.5	11799.9782	-2.9			
4-3	5.5, 5.5 – 4.5, 4.5	15734.1980	-0.7	3.5, 4.5 – 3.5, 4.5	15894.4373	0.6
	5.5, 6.5 – 4.5, 5.5	15734.2155	3.8	5.5, 6.5 – 4.5, 5.5	15894.6252	4.9
	5.5, 4.5 – 4.5, 3.5	15734.2155	2.7	5.5, 4.5 – 4.5, 3.5	15894.6252	4.5
	4.5, 5.5 – 3.5, 4.5	15734.2951	-0.9	4.5, 5.5 – 3.5, 4.5	15894.7026	-3.6
	4.5, 3.5 – 3.5, 2.5	15734.2951	-2.8	4.5, 3.5 – 3.5, 2.5	15894.7026	-4.3
	3.5, 3.5 – 2.5, 3.5	15734.3123	1.6	3.5, 4.5 – 2.5, 3.5	15894.7537	-0.1
	3.5, 4.5 – 2.5, 3.5	15734.3423	-0.9	3.5, 2.5 – 2.5, 1.5	15894.7537	-2.7
	3.5, 2.5 – 2.5, 1.5	15734.3423	-3.7			

[a] $\Delta\nu = \nu_{obs} - \nu_{cal}$.

Table 6-7: Spectroscopic constants of the $\Pi 1_1$ states of ^{131}Xe-NH_3.

	$\Pi 1_{1s}$	$\Pi 1_{1a}$
B /MHz	1966.2630(2)	1987.1850(2)
D_J /kHz	-17.85(2)	10.65(3)
H_J /kHz	-0.0661(7)	-0.0138(8)
$\chi_{aa}(^{131}Xe)$ /MHz	3.360(2)	3.374(3)
$\lvert \chi_{bb}(^{131}Xe) - \chi_{cc}(^{131}Xe) \rvert$ /MHz	0.258(3)	0.258(4)
$\eta(^{131}Xe)$[a]	0.0768	0.0765
$\chi_{aa}(^{14}N)$ /MHz	-0.347(3)	-0.340(3)
$\lvert \chi_{bb}(^{14}N) - \chi_{cc}(^{14}N) \rvert$ /MHz	0.327(3)	
$\eta(^{14}N)$	-0.942	
σ/kHz [b]	3.0	2.9

[a] Asymmetry parameter $\eta = |\chi_{bb}-\chi_{cc}|/\chi_{aa}$.
[b] Standard deviation of the fit.

Table 6-8: Measured transition frequencies and determined spectroscopic constants of Xe-$^{15}NH_3$ isotopomers.

	^{136}Xe-$^{15}NH_3$		^{134}Xe-$^{15}NH_3$		^{132}Xe-$^{15}NH_3$		^{129}Xe-$^{15}NH_3$	
J'-J''	ν_{obs} (MHz)	$\Delta\nu$ [a] (kHz)	ν_{obs} (MHz)	$\Delta\nu$ (kHz)	ν_{obs} (MHz)	$\Delta\nu$ (kHz)	ν_{obs} (MHz)	$\Delta\nu$ (kHz)
				$\Sigma 0_{0a}$				
1-0	3846.6714	0.2	3853.3008	0.3	3860.1285	-0.7	3870.7586	-0.4
2-1	7692.7441	-0.4	7706.0021	0.9	7719.6567	0.5	7740.9128	0.4
3-2	11537.6225	0.3	11557.5009	-1.3	11577.9785	-0.1	11609.8545	-0.2
4-3	15380.7064	-0.1	15407.2040	0.4	15434.4943	-0.01	15476.9803	0.03
B /MHz	1923.3854(2)		1926.7002(2)		1930.1148(2)		1935.4300(2)	
D_J /kHz	24.909(9)		24.994(9)		25.094(9)		25.232(9)	
σ /kHz [b]	0.3		0.8		0.4		0.3	
				$\Pi 1_{1s}$				
2-1	7479.0950	0.0	7491.5170	0.0	7504.3119	0.0	7524.2253	0.0
3-2	11219.1466	0.0	11237.7921	0.0	11256.9919	0.0	11286.8767	0.0
B /MHz	1869.7065(5)		1872.8104(5)		1876.0081(5)		1880.9845(5)	
D_J /kHz	-8.40(3)		-8.61(3)		-8.73(3)		-8.98(3)	
σ /kHz	0.0		0.0		0.0		0.0	
				$\Pi 1_{1a}$				
2-1	7549.5656	0.0	7562.2296	0.0	7575.2733	-2.3	7595.5765	-1.8
3-2	11323.6398	0.0	11342.6359	0.0	11362.2024	2.6	11392.6567	2.0
4-3					15148.2671	-0.8	15188.8752	-0.6
B /MHz	1887.4859(5)		1890.6519(5)		1893.9140(3)		1898.9896(3)	
D_J /kHz	11.81(3)		11.81(3)		11.89(1)		11.88(1)	
σ /kHz	0.0		0.0		2.0		1.6	

[a] $\Delta\nu = \nu_{obs} - \nu_{cal}$.
[b] Standard deviation of the fit.

Table 6-9: Measured transition frequencies and determined spectroscopic constants of the $\Pi 1_1$ states of ^{131}Xe-$^{15}NH_3$ isotopomers.

		$\Pi 1_{1s}$		$\Pi 1_{1a}$	
J'-J''	F'-F''	ν_{obs} (MHz)	$\Delta\nu$ [a] (kHz)	ν_{obs} (MHz)	$\Delta\nu$ (kHz)
2-1	0.5-0.5	7510.0043	4.0	7581.0884	2.6
	1.5-0.5	7510.4448	-6.2	7581.5353	-4.8
	3.5-2.5	7510.6357	0.5	7581.7224	-0.6
	2.5-2.5	7511.0882	2.2	7582.1804	3.0
	1.5-1.5	7511.1552	-0.2	7582.2447	0.8
	2.5-1.5	7511.4771	-0.2	7582.5676	-0.9
3-2	1.5-1.5	11266.2659	-1.0	11371.6606	-0.4
	2.5-2.5	11266.6042	-2.0	11372.0007	-1.4
	4.5-3.5	11266.7041	-0.1	11372.0996	-1.8
	1.5-0.5	11266.7220	4.5	11372.1213	6.1
	3.5-2.5	11266.9103	-4.4	11372.3087	-4.0
	2.5-1.5	11266.9306	2.5	11372.3285	1.9
	3.5-3.5	11267.3660	0.6	11372.7668	-0.3
B /MHz		1877.6396(2)		1895.5765(2)	
D_J /kHz		-8.87(1)		11.72(1)	
$\chi_{aa}(^{131}Xe)$ /MHz		3.368(3)		3.381(3)	
$\lvert\chi_{bb}(^{131}Xe) - \chi_{cc}(^{131}Xe)\rvert$ /MHz		0.237(4)		0.253(4)	
$\eta(^{131}Xe)$ [b]		0.0704		0.0748	
σ/kHz [c]		2.9		2.8	

[a] $\Delta\nu = \nu_{obs} - \nu_{cal}$.
[b] Asymmetry parameter $\eta = |\chi_{bb}-\chi_{cc}|/\chi_{aa}$.
[c] Standard deviation of the fit.

Table 6-10: Measured transition frequencies and determined spectroscopic constants of Xe-ND_3 isotopomers.

J'-J''	^{136}Xe-ND_3		^{134}Xe-ND_3		^{132}Xe-ND_3		^{129}Xe-ND_3	
	ν_{obs} (MHz)	$\Delta\nu$ [a] (kHz)	ν_{obs} (MHz)	$\Delta\nu$ (kHz)	ν_{obs} (MHz)	$\Delta\nu$ (kHz)	ν_{obs} (MHz)	$\Delta\nu$ (kHz)
				$\Sigma 0_{0s}$				
2-1	7004.4910	-0.3	7017.7063	-0.5	7031.3191	-0.7	7052.5108	-1.0
3-2	10505.5422	0.3	10525.3614	0.6	10545.7758	0.8	10577.5567	1.1
4-3	14005.1582	-0.1	14031.5754	-0.2	14058.7844	-0.3	14101.1447	-0.3
B /MHz	1751.2822(3)		1754.5866(3)		1757.9906(3)		1763.2895(3)	
D_J /kHz	19.92(1)		19.99(1)		20.08(1)		20.20(1)	
σ /kHz [b]	0.3		0.5		0.6		0.9	
				$\Sigma 0_{0a}$				
2-1	7004.2406	-0.3	7017.4552	-0.2	7031.0656	-0.9	7052.2580	-0.6
3-2	10505.1668	0.3	10524.9845	0.3	10545.3969	1.0	10577.1756	0.6
4-3	14004.6383	-0.1	14031.0742	-0.1	14058.2803	-0.3	14100.6358	-0.2
B /MHz	1751.2195(3)		1754.5237(3)		1757.9271(3)		1763.2263(3)	
D_J /kHz	19.91(1)		19.98(1)		20.06(1)		20.21(1)	
σ /kHz	0.2		0.2		0.8		0.5	

[a] $\Delta\nu = \nu_{obs} - \nu_{cal}$.
[b] Standard deviation of the fit.

Table 6-11: Measured transition frequencies and determined spectroscopic constants of ^{131}Xe-ND_3.

		$\Sigma 0_{0s}$		$\Sigma 0_{0a}$	
J'-J''	F'-F''	ν_{obs} (MHz)	$\Delta\nu$ [a] (kHz)	ν_{obs} (MHz)	$\Delta\nu$ (kHz)
2-1	1.5-1.5	7037.7625	2.6	7037.5063	1.0
	3.5-2.5	7038.2161	-0.1	7037.9609	-2.7
	0.5-0.5	7038.2680	-3.0		
	2.5-2.5	7038.8627	7.6	7038.6096	4.3
	1.5-0.5	7038.9061	-3.8	7038.6571	-3.2
3-2	4.5-3.5	10556.1696	0.8	10555.7910	0.7
	3.5-2.5	10556.1696	0.8	10555.7910	0.7
	2.5-1.5	10556.3225	-4.5		
	1.5-0.5	10556.3225	-4.6		
4-3	5.5-4.5	14072.6609	1.4	14072.1559	0.7
	4.5-3.5	14072.6609	1.4	14072.1559	0.7
	3.5-2.5	14072.7335	-0.2	14072.2288	-0.9
	2.5-1.5	14072.7335	-0.2	14072.2288	-0.9
B /MHz		1759.7287(1)		1759.6656(2)	
D_J /kHz		20.120(6)		20.117(6)	
$\chi_{aa}(^{131}Xe)$ /MHz		2.556(3)		2.567(3)	
σ /kHz [b]		3.5		2.4	

[a] $\Delta\nu = \nu_{obs} - \nu_{cal}$.
[b] Standard deviation of the fit.

Table 6-12: Measured transition frequencies and determined spectroscopic constants of Xe-ND_2H isotopomers.

	^{136}Xe-ND_2H		^{134}Xe-ND_2H		^{132}Xe-ND_2H		^{129}Xe-ND_2H	
J'-J''	ν_{obs} (MHz)	$\Delta\nu$[a] (kHz)	ν_{obs} (MHz)	$\Delta\nu$ (kHz)	ν_{obs} (MHz)	$\Delta\nu$ (kHz)	ν_{obs} (MHz)	$\Delta\nu$ (kHz)
				$\Sigma 0_{00s}$				
2-1	7319.0548	-0.6	7332.2734	-0.7	7345.8873	-1.1	7367.0819	-0.7
3-2	10977.1742	0.7	10996.9966	0.8	11017.4129	1.3	11049.1958	0.8
4-3	14633.6001	-0.2	14660.0188	-0.3	14687.2293	-0.4	14729.5924	-0.3
B /MHz	1829.9518(3)		1833.2572(3)		1836.6616(3)		1841.9612(3)	
D_J /kHz	23.49(1)		23.59(1)		23.68(1)		23.82(1)	
σ /kHz[b]	0.5		0.6		1.0		0.6	
				$\Sigma 0_{00a}$				
2-1	7319.2596	-1.2	7332.4771	-1.1	7346.0896	-1.0	7367.2835	-0.8
3-2	10977.4850	1.4	10997.3049	1.3	11017.7187	1.2	11049.5003	1.0
4-3	14634.0167	-0.4	14660.4322	-0.4	14687.6421	-0.4	14730.0015	-0.3
B /MHz	1830.0029(3)		1833.3080(3)		1836.7118(3)		1842.0114(3)	
D_J /kHz	23.46(1)		23.56(1)		23.64(1)		23.79(1)	
σ /kHz	1.1		1.0		0.9		0.7	

[a] $\Delta\nu = \nu_{obs} - \nu_{cal}$.
[b] Standard deviation of the fit.

Table 6-13: Measured transition frequencies and determined spectroscopic constants of Xe-NDH_2 isotopomers.

J'-J''	^{136}Xe-NDH_2		^{134}Xe-NDH_2		^{132}Xe-NDH_2		^{129}Xe-NDH_2	
	ν_{obs} (MHz)	$\Delta\nu$[a] (kHz)	ν_{obs} (MHz)	$\Delta\nu$ (kHz)	ν_{obs} (MHz)	$\Delta\nu$ (kHz)	ν_{obs} (MHz)	$\Delta\nu$ (kHz)
				$\Sigma 0_{00s}$				
2-1	7668.9335	0.7	7682.1473	-1.2	7695.7595	0.4	7716.9472	-0.4
3-2	11501.7696	-0.8	11521.5893	1.5	11541.9973	-0.4	11573.7722	0.5
4-3	15332.6534	0.2	15359.0646	-0.5	15386.2674	0.1	15428.6159	-0.2
B /MHz	1917.4504(3)		1920.7551(3)		1924.1586(3)		1929.4569(3)	
D_J /kHz	27.15(1)		27.25(1)		27.35(1)		27.50(1)	
σ /kHz[b]	0.6		1.2		0.3		0.4	
				$\Sigma 0_{00a}$				
2-1	7670.7760	-0.8	7683.9915	-0.04	7697.6026	-0.2	7718.7935	-0.6
3-2	11504.5433	0.9	11524.3588	0.04	11544.7701	0.3	11576.5481	0.7
4-3	15336.3605	-0.3	15362.7717	-0.01	15389.9754	-0.1	15432.3282	-0.2
B /MHz	1917.9106(3)		1921.2150(3)		1924.6186(3)		1929.9177(3)	
D_J /kHz	27.05(1)		27.14(1)		27.24(1)		27.39(1)	
σ /kHz	0.7		0.03		0.2		0.5	

[a] $\Delta\nu = \nu_{obs} - \nu_{cal}$.
[b] Standard deviation of the fit.

Table 6-14: Measured transition frequencies and determined spectroscopic constants of $^{131}Xe\text{-}ND_2H$.

		$\Sigma 0_{00s}$		$\Sigma 0_{00a}$	
J'-J"	*F'-F"*	ν_{obs} (MHz)	$\Delta\nu$ [a] (kHz)	ν_{obs} (MHz)	$\Delta\nu$ (kHz)
2-1	1.5-1.5	7352.3364	-2.3	7352.5358	-2.5
	3.5-2.5	7352.7860	-1.0	7352.9892	-0.7
	0.5-0.5	7352.8446	3.9	7353.0475	3.4
	2.5-2.5	7353.4172	2.7	7353.6259	3.7
	1.5-0.5	7353.4641	-4.2	7353.6713	-5.1
3-2	4.5-3.5	11027.8084	0.9	11028.1149	1.5
	3.5-2.5	11027.8084	0.9	11028.1149	1.5
	2.5-1.5	11027.9631	0.2	11028.2698	-0.2
	1.5-0.5	11027.9631	0.2	11028.2698	-0.2
4-3	5.5-4.5	14701.1077	1.2	14701.5182	1.6
	4.5-3.5	14701.1077	1.2	14701.5182	1.6
	3.5-2.5	14701.1777	-1.6	14701.5880	-2.0
	2.5-1.5	14701.1777	-1.6	14701.5880	-2.0
B /MHz		1838.4000(1)		1838.4507(1)	
D_J /kHz		23.729(6)		23.710(6)	
$\chi_{aa}(^{131}Xe)$ /MHz		2.510(3)		2.529(3)	
σ /kHz [b]		2.4		2.7	

[a] $\Delta\nu = \nu_{obs} - \nu_{cal}$.
[b] Standard deviation of the fit.

Table 6-15: Measured transition frequencies and determined spectroscopic constants of ^{131}Xe-NDH_2.

		$\Sigma 0_{00s}$		$\Sigma 0_{00a}$	
J'-J''	F'-F''	ν_{obs} (MHz)	$\Delta\nu$ [a] (kHz)	ν_{obs} (MHz)	$\Delta\nu$ (kHz)
2-1	1.5-1.5	7702.2258	-0.9	7704.0615	-0.6
	3.5-2.5	7702.6563	-1.9	7704.5013	-0.3
	0.5-0.5	7702.7139	3.9	7704.5566	2.2
	2.5-2.5	7703.2609	-1.4	7705.1156	-1.4
	1.5-0.5	7703.3147	0.5	7705.1705	0.7
3-2	4.5-3.5	11552.3919	0.3	11555.1640	-0.5
	3.5-2.5	11552.3919	0.3	11555.1640	-0.5
	2.5-1.5	11552.5407	-0.5	11555.3166	-0.2
	1.5-0.5	11552.5407	-0.5	11555.3166	-0.2
4-3	5.5-4.5	15400.1391	0.1	15403.8489	-0.3
	4.5-3.5	15400.1391	0.1	15403.8489	-0.3
	3.5-2.5	15400.2091	0.0	15403.9211	0.5
	2.5-1.5	15400.2091	-0.01	15403.9211	0.5
B /MHz		1925.8968(1)		1926.3570(1)	
D_J /kHz		27.410(6)		27.296(6)	
$\chi_{aa}(^{131}Xe)$ /MHz		2.417(3)		2.461(3)	
σ /kHz [b]		1.6		1.0	

[a] $\Delta\nu = \nu_{obs} - \nu_{cal}$.
[b] Standard deviation of the fit.

Table 6-16: Measured transition frequencies of ^{20}Ne-Xe-$^{14}NH_3$ isotopomers.

$J'_{Ka'Kc'}$ - $J''_{Ka''Kc}$	F'-F''	^{20}Ne-^{132}Xe-$^{14}NH_3$		^{20}Ne-^{129}Xe-$^{14}NH_3$	
		ν_{obs} (MHz)	$\Delta\nu$[a] (kHz)	ν_{obs} (MHz)	$\Delta\nu$ (kHz)
2_{02}-1_{01}	1-0	4740.5171	6.6	4761.1563	6.8
	2-2	4740.5171	2.3	4761.1563	2.7
	3-2	4740.5413	0.1	4761.1827	0.9
	2-1	4740.5413	-3.8	4761.1827	-2.9
	1-1	4740.5845	-1.7	4761.2281	-1.5
2_{12}-1_{11}	2-1	4413.1481	-3.7	4431.3079	-4.3
	3-2	4413.1828	2.7	4431.3451	2.7
2_{11}-1_{10}	2-1	5138.3784	-3.1	5162.8619	-3.3
	3-2	5138.4183	2.4	5162.9005	-0.8
	1-1	5138.4757	-0.8	5162.9626	1.1
3_{03}-2_{02}	2-1	7023.9188	-4.5	7053.2525	-4.3
	4-3	7023.9309	-0.7	7053.2647	-0.7
	3-2	7023.9418	2.3	7053.2745	1.1
3_{13}-2_{12}	3-2	6598.0149	-2.4	6624.8533	-1.5
	4-3	6898.0234	0.6	6624.8619	1.0
	2-1	6598.0348	4.2	6624.8717	3.0
3_{12}-2_{11}	2-1	7683.0209	-3.1	7719.2727	-2.4
	3-2	7683.0209	-4.0	7719.2727	-2.9
	4-3	7683.0386	5.1	7719.2905	5.9
4_{04}-3_{03}	3-2	9214.8547	-0.6	9251.3763	0.2
	5-4	9214.8547	-5.0	9251.3763	-4.4
	4-3	9214.8741	3.9	9251.3948	3.6
4_{14}-3_{13}	3-2	8759.7341	-0.3	8794.8504	-0.3
	4-3	8759.7341	2.3	8794.8504	2.4
	5-4	8759.7341	1.9	8794.8504	1.9
4_{13}-3_{12}	3-2	10195.2118	3.1	10242.5637	2.6
	4-3	10195.2118	-1.4	10242.5637	-1.9
	5-4	10195.2118	-3.0	10242.5637	-3.6
5_{15}-4_{14}	6-5	10895.0935	0.3	10938.0860	0.1
	4-3	10895.0935	-0.6	10938.0860	-0.7
	5-4	10895.0935	-1.3	10938.0860	-1.4
1_{11}-0_{00}	0-1	4996.7620	-1.4	5000.5566	0.0
	2-1	4996.8488	-0.2	5000.6432	-0.1
	1-1	4996.9063	0.3	5000.7008	-0.3
2_{12}-1_{01}	1-0	7021.8613	2.3	7033.1506	0.9
	3-2	7021.9217	1.4	7033.2145	1.4
	2-1	7021.9798	0.5	7033.2728	0.01
3_{13}-2_{02}	4-3	8879.4015	-0.4	8896.8930	0.8
	3-2	8879.4483	-3.1	8896.9389	-3.1
3_{03}-2_{12}	4-3	4742.5519	-0.6	4781.2336	-0.5

[a] $\Delta\nu = \nu_{obs} - \nu_{cal}$.

Table 6-17: Measured transition frequencies of Ne-Xe-$^{15}NH_3$ isotopomers.

	^{20}Ne-^{132}Xe-$^{15}NH_3$		^{20}Ne-^{129}Xe-$^{15}NH_3$		^{22}Ne-^{132}Xe-$^{15}NH_3$		^{22}Ne-^{129}Xe-$^{15}NH_3$	
$J'_{Ka'Kc'}$ - $J''_{Ka''Kc}$	ν_{obs} (MHz)	$\Delta\nu$ [a] (kHz)	ν_{obs} (MHz)	$\Delta\nu$ (kHz)	ν_{obs} (MHz)	$\Delta\nu$ (kHz)	ν_{obs} (MHz)	$\Delta\nu$ (kHz)
2_{02}-1_{01}	4642.2352	1.7	4662.8557	1.4	4459.7826	-1.7	4480.3756	-0.8
2_{12}-1_{11}	4319.8333	-1.2	4337.9694	-3.2	4150.1521	-0.2	4168.2652	-1.2
2_{11}-1_{10}	5035.5361	-1.5	5060.0451	-2.7	4837.6497	1.3	4862.1202	0.5
3_{03}-2_{02}	6876.0857	-0.9	6905.3473	0.02	6605.7604	-0.8	6634.9799	-1.1
3_{13}-2_{12}	6457.9438	1.6	6484.7365	4.7	6204.2570	0.3	6231.0144	0.6
3_{12}-2_{11}	7528.6488	0.8	7564.9285	1.4	7232.7677	-1.0	7268.9870	-0.1
4_{04}-3_{03}	9017.4658	-0.5	9053.8311	-1.8	8662.8421	1.8	8699.1614	1.9
4_{14}-3_{13}					8236.1142	0.5	8271.1084	0.5
4_{13}-3_{12}					9596.5171	0.2	9643.8012	-0.1
5_{05}-4_{04}					10630.4409	-1.3	10672.8427	-1.2
1_{11}-0_{00}	4859.9758	1.2	4863.7488	2.6	4665.7750	1.6	4669.5628	0.8
2_{12}-1_{01}	6840.7625	-1.5	6852.0078	-2.5	6568.7902	-1.8	6580.0447	-1.1
3_{13}-2_{02}	8656.4730	0.3	8673.8880	0.1	8313.2649	0.5	8330.6835	0.4
4_{14}-3_{03}					9943.6172	0.3	9966.8102	0.1
4_{04}-3_{13}					6955.3376	0.5	7003.4575	0.2

[a] $\Delta\nu = \nu_{obs} - \nu_{cal}$.

Table 6-18: Measured transition frequencies of Ne-^{131}Xe-$^{15}NH_3$ isotopomers.

$J'_{Ka'Kc'}$- $J''_{Ka''Kc}$	F'-F''	^{20}Ne-^{131}Xe-$^{15}NH_3$ ν_{obs} (MHz)	$\Delta\nu$ [a] (kHz)	^{22}Ne-^{131}Xe-$^{15}NH_3$ ν_{obs} (MHz)	$\Delta\nu$ (kHz)
2_{02}-1_{01}	1.5-1.5			4466.1876	1.8
	3.5-2.5	4648.9584	-0.0	4466.500	1.5
	2.5-2.5			4466.9605	0.3
	1.5-0.5			4466.9840	-3.1
2_{12}-1_{11}	3.5-2.5			4155.9755	-0.7
	2.5-1.5			4156.4239	2.5
2_{11}-1_{10}	0.5-0.5			4845.2320	-0.03
	1.5-0.5			4845.3143	0.9
	3.5-2.5			4845.5819	0.8
	2.5-2.5			4845.6607	-1.8
	1.5-1.5			4845.9684	-0.2
	2.5-1.5			4846.0266	0.3
3_{03}-2_{02}	1.5-1.5	6885.2885	0.7	6614.9650	-0.9
	2.5-2.5	6885.4461	0.1	6615.1208	0.5
	4.5-3.5	6885.6613	-0.7	6615.3267	3.4
	3.5-2.5			6615.3405	-5.5
	1.5-0.5			6615.4302	3.4
	2.5-1.5	6885.7917	-0.9	6615.4485	-1.0
	3.5-3.5	6886.1676	0.8	6615.8075	0.6
3_{13}-2_{12}	4.5-3.5			6212.9860	1.9
	1.5-0.5			6213.0172	-2.9
	3.5-2.5			6213.0999	-0.1
	2.5-1.5			6213.1352	-0.8
3_{12}-2_{11}	1.5-0.5			7244.5747	0.1
	4.5-3.5			7244.6093	0.5
	2.5-1.5			7244.6914	0.2
	3.5-2.5			7244.7247	-0.7
1_{11}-0_{00}	1.5-1.5	4861.1259	0.8	4666.9497	-1.5
	2.5-1.5	4861.2336	-1.7	4667.0335	0.9
	0.5-1.5	4861.3243	0.9	4667.0999	2.3
2_{12}-1_{01}	1.5-1.5			6572.1270	-1.8
	2.5-1.5			6572.3869	-1.7
	3.5-2.5			6572.4704	0.4
	0.5-0.5			6572.5658	-0.5
	2.5-2.5			6572.8320	-1.8
	1.5-0.5			6572.9317	1.7
3_{13}-2_{02}	4.5-3.5			8318.9537	-1.1
	3.5-2.5			8318.9793	5.7
	1.5-0.5			8319.0559	-4.3
	2.5-1.5			8319.0806	1.6

[a] $\Delta\nu = \nu_{obs} - \nu_{cal}$.

Table 6-19: Spectroscopic constants of Ne-Xe-NH_3 isotopomers.

	^{20}Ne-^{132}Xe-$^{14}NH_3$	^{20}Ne-^{129}Xe-$^{14}NH_3$	^{20}Ne-^{132}Xe-$^{15}NH_3$	^{20}Ne-^{131}Xe-$^{15}NH_3$	^{20}Ne-^{129}Xe-$^{15}NH_3$	^{22}Ne-^{132}Xe-$^{15}NH_3$	^{22}Ne-^{131}Xe-$^{15}NH_3$	^{22}Ne-^{129}Xe-$^{15}NH_3$
	Rotational Constants (MHz) and Planar Moments (amu Å^2)							
A	3984.2160(8)	3984.2601(8)	3869.481(1)	3870.362(1)	3869.514(1)	3714.169(1)	3714.1871(8)	3714.224(1)
B	1375.4871(5)	1382.4007(5)	1348.5665(7)	1351.679(2)	1355.4916(7)	1295.5534(4)	1297.8224(3)	1302.4682(4)
C	1012.6873(4)	1016.4379(4)	990.5439(5)	990.851(1)	994.2828(5)	951.6433(3)	952.8687(4)	955.3780(3)
P_a	369.8102	367.9714	377.1749	376.6792	375.2589	392.5394	391.8572	390.4669
P_b	129.2373	129.2346	133.0286	133.3661	133.0260	138.5199	138.5198	138.5164
P_c	-2.3920	-2.3907	-2.4222	-2.7894	-2.4208	-2.4520	-2.4519	-2.4505
	Centrifugal Distortion Constants (kHz)							
D_J	17.681(7)	17.837(7)	16.33(1)		16.47(1)	15.751(7)	15.81(1)	15.908(8)
D_{JK}	-1.1(1)	-1.2(1)	3.1(1)		2.9(1)	-1.6(2)	-1.3(2)	-1.2(2)
d_1	-5.78(2)	-5.82(2)	-5.35(2)		-5.35(2)	-5.062(6)	-5.10(1)	-5.112(6)
d_2	-0.54(7)	-0.43(7)						
H_{JK}	0.139(7)	0.126(7)				0.14(1)	0.16(1)	0.16(1)
	^{14}N Nuclear Quadrupole Coupling Constants (MHz)							
χ_{aa}	-0.101(1)	-0.107(1)						
χ_{bb}	0.190(2)	0.193(2)						
χ_{cc}	-0.089(2)	-0.086(2)						
	^{131}Xe Nuclear Quadrupole Coupling Constants (MHz)							
χ_{aa}				1.887(3)			1.781(1)	
χ_{bb}				-0.442(5)			-0.327(2)	
χ_{cc}				-1.445(5)			-1.454(2)	
	Standard Deviation (kHz)							
σ	2.6	2.4	1.2	0.9	2.4	1.1	2.1	0.9

Table 6-20: Van der Waals bond lengths, stretching frequencies, and force constants for the $\Sigma 0_0/\Sigma 0_{00}$ states of Xe-NH_3 isotopomers.

$\Sigma 0_{0a}$ state	^{136}Xe-NH_3	^{134}Xe-NH_3	^{132}Xe-NH_3	^{131}Xe-NH_3	^{129}Xe-NH_3
R (Å)	4.067	4.067	4.067	4.067	4.067
ν_s (cm^{-1})	36.5	36.4	36.5	36.7	36.4
k_s (N m^{-1})	1.19	1.18	1.18	1.20	1.18
$\Sigma 0_{0a}$ state	^{136}Xe-$^{15}NH_3$	^{134}Xe-$^{15}NH_3$	^{132}Xe-$^{15}NH_3$	^{131}Xe-$^{15}NH_3$	^{129}Xe-$^{15}NH_3$
R (Å)	4.064	4.064	4.064	4.064	4.064
ν_s (cm^{-1})	35.7	35.7	35.7	35.7	35.8
k_s (N m^{-1})	1.19	1.19	1.19	1.19	1.19
$\Sigma 0_{0s}$ state	^{136}Xe-ND_3	^{134}Xe-ND_3	^{132}Xe-ND_3	^{131}Xe-ND_3	^{129}Xe-ND_3
R (Å)	4.064	4.065	4.065	4.065	4.065
ν_s (cm^{-1})	34.6	34.7	34.7	34.7	34.8
k_s (N m^{-1})	1.24	1.24	1.23	1.23	1.23
$\Sigma 0_{0a}$ state	^{136}Xe-ND_3	^{134}Xe-ND_3	^{132}Xe-ND_3	^{131}Xe-ND_3	^{129}Xe-ND_3
R (Å)	4.065	4.065	4.065	4.065	4.065
ν_s (cm^{-1})	34.6	34.7	34.7	34.7	34.7
k_s (N m^{-1})	1.24	1.24	1.24	1.23	1.23
$\Sigma 0_{00s}$ state	^{136}Xe-ND_2H	^{134}Xe-ND_2H	^{132}Xe-ND_2H	^{131}Xe-ND_2H	^{129}Xe-ND_2H
R (Å)	4.067	4.067	4.067	4.067	4.067
ν_s (cm^{-1})	34.1	34.1	34.1	34.1	34.2
k_s (N m^{-1})	1.14	1.14	1.14	1.14	1.14
$\Sigma 0_{00a}$ state	^{136}Xe-ND_2H	^{134}Xe-ND_2H	^{132}Xe-ND_2H	^{131}Xe-ND_2H	^{129}Xe-ND_2H
R (Å)	4.067	4.067	4.067	4.067	4.067
ν_s (cm^{-1})	34.1	34.1	34.2	34.2	34.2
k_s (N m^{-1})	1.14	1.14	1.14	1.14	1.14
$\Sigma 0_{00s}$ state	^{136}Xe-NDH_2	^{134}Xe-NDH_2	^{132}Xe-NDH_2	^{131}Xe-NDH_2	^{129}Xe-NDH_2
R (Å)	4.069	4.069	4.069	4.069	4.069
ν_s (cm^{-1})	34.0	34.0	34.0	34.1	34.1
k_s (N m^{-1})	1.08	1.08	1.08	1.08	1.08
$\Sigma 0_{00a}$ state	^{136}Xe-NDH_2	^{134}Xe-NDH_2	^{132}Xe-NDH_2	^{131}Xe-NDH_2	^{129}Xe-NDH_2
R (Å)	4.068	4.068	4.069	4.069	4.069
ν_s (cm^{-1})	34.1	34.1	34.1	34.1	34.2
k_s (N m^{-1})	1.09	1.09	1.09	1.09	1.09

Table 6-21: Comparison of *ab initio* and experimental values of derived parameters for $^{132}Xe\text{-}NH_3$.

		R (Å)	ν_s (cm^{-1})	k_s($N\ m^{-1}$)
experimental values	$\Sigma 0_{0a}$ state	4.067	36.5	1.18
ab initio values	Global minimum ($\theta = 105°$, $\varphi = 60°$)	3.941	42.7	1.63
	Symmetric Xe-H_3N geometry ($\theta = 0°$, $\varphi = 0°$)	4.234	32.5	0.95
	Symmetric Xe-NH_3 geometry ($\theta = 180°$, $\varphi = 0°$)	4.155	35.9	1.15

Table 6-22: Comparison of calculated quartic centrifugal distortion constants of Ne-Xe-NH_3 from harmonic force field analysis with experimental values.[a]

	^{20}Ne-^{132}Xe-$^{14}NH_3$		^{20}Ne-^{129}Xe-$^{14}NH_3$		^{20}Ne-^{132}Xe-$^{15}NH_3$		^{20}Ne-^{129}Xe-$^{15}NH_3$	
	Exp.	calc.	exp.	calc.	exp.	calc.	exp.	calc.
D_J	17.681(7)	17.548	17.837(7)	17.703	16.33(1)	16.36	16.47(1)	16.51
D_{JK}	-1.1(1)	-0.9	-1.2(1)	-0.6	3.1(1)	2.9	2.9(1)	3.2
d_1	-5.78(2)	-5.87	-5.82(2)	-5.94	-5.35(2)	-5.51	-5.35(2)	-5.58
d_2	-0.54(7)	-0.87	-0.43(7)	-0.88		-0.84		-0.86

	^{22}Ne-^{132}Xe-$^{15}NH_3$		^{22}Ne-^{131}Xe-$^{15}NH_3$		^{22}Ne-^{129}Xe-$^{15}NH_3$	
	exp.	calc.	exp.	calc.	exp.	calc.
D_J	15.751(7)	15.747	15.81(1)	15.80	15.908(8)	15.896
D_{JK}	-1.6(2)	-1.7	-1.3(2)	-1.6	-1.2(2)	-1.4
d_1	-5.062(6)	-5.302	-5.10(1)	-5.324	-5.112(6)	-5.368
d_2		-0.78		-0.78		-0.79

[a] All constants are in kHz.

References

[1] C. Landon, P. Berthault, F. Vovelle, and H. Desvaux, *Protein Sci.* **10**, 762 (2001).

[2] M. M. Spence, S. M. Rubin, I. E. Dimitrov, E. J. Ruiz, D. E. Wemmer, A. Pines, S. Q. Yao, F. Tian, and P. G. Schultz, *Proc. Natl Acad. Sci. USA* **98**, 10654 (2001).

[3] R. F. Tilton and I. D. Kuntz, *Biochemistry* **21**, 6850 (1982).

[4] P. Herbine, T. A. Hu, G. Johnson, and T. R. Dyke, J. Chem. Phys. **93**, 5485 (1990).

[5] G. T. Fraser, D. D. Nelson, Jr., K.I. Peterson and W. Klemperer, J. Chem. Phys. **84**, 2472 (1986).

[6] D. D. Nelson, Jr., G. T. Fraser, and W. Klemperer, J. Chem. Phys. **83**, 6201 (1985).

[7] E. H. T. Olthof, A. van der Avoird, and P. E. S. Wormer, J. Chem. Phys. **101**, 8430 (1994).

[8] J. van Wijngaarden and W. Jäger, J. Chem. Phys. **115**, 6504 (2001).

[9] C. A. Schmuttenmaer, R. C. Cohen, and R. J. Saykally, J. Chem. Phys. **101**, 146 (1994).

[10] F.-M. Tao and W. Klemperer, J. Chem. Phys. **101**, 1129 (1994).

[11] G. Chałasiński, S. M. Cybulski, M. M. Szczęśniak, and S. Scheiner, J. Chem. Phys. **91**, 7809 (1989).

[12] M. Bulski, P. E. S. Wormer, and A. van der Avoird, J. Chem. Phys. **94**, 491 (1991).

[13] G. Chałasiński, M. M. Szczęśniak, and S. Scheiner, J. Chem. Phys. **97**, 8181 (1992).

[14] D. D. Nelson, Jr., G. T. Fraser, K. I. Peterson, K. Zhao, W. Klemperer, F. J. Lovas, and R. D. Suenram, J. Chem. Phys. **85**, 5512 (1986).

[15] E. Zwart, H. Linnartz, W. Leo Meerts, G. T. Fraser, D. D. Nelson, Jr., and W. Klemperer, J. Chem. Phys. **95**, 793 (1991).

[16] J. van Wijngaarden and W. Jäger, J. Chem. Phys. **114**, 3968 (2001).

[17] J. van Wijngaarden and W. Jäger, Mol. Phys. **99**, 1215 (2001).

[18] J. van Wijngaarden and W. Jäger, Chem. Phys. **283**, 29 (2002).

[19] J. van Wijngaarden and W. Jäger, Phys. Chem. Chem. Phys. **4**, 4883 (2002).

[20] J. van Wijngaarden and W. Jäger, J. Am. Chem. Soc. **125**, 14631 (2003).

[21] J. van Wijngaarden and W. Jäger, J. Chem. Phys. **116**, 2379 (2002).

[22] C. Hampel, K. Peterson, and H.-J. Werner, Chem. Phys. Lett. **190**, 1 (1992).

[23] M. J. O. Deegan and P. J. Knowles, Chem. Phys. Lett. **227**, 321 (1994).

[24] MOLPRO, a package of *ab initio* programs designed by H.-J. Werner and P. J. Knowles, version 2002.6, R. D. Amos, A. Bernhardsson, A. Berning, P. Celani, D. L. Cooper, M. J. O. Deegan, A. J. Dobbyn, F. Eckert, C. Hampel, G. Hetzer, P. J. Knowles, T. Korona, R. Lindh, A. W. Lloyd, S. J. McNicholas, F. R. Manby, W. Meyer, M. E. Mura, A. Nicklass, P. Palmieri, R. Pitzer, G. Rauhut, M. Schütz, U. Schumann, H. Stoll, A. J. Stone, R. Tarroni, T. Thorsteinsson, and H.-J. Werner.

[25] K. A. Peterson, D. Figgen, E. Goll, H. Stoll, and M. Dolg, J. Chem. Phys., **119**, 11113 (2003).

[26] T. H. Dunning, Jr., J. Chem. Phys. **90**, 1007 (1989).

[27] S. M. Cybulski and R. R. Toczylowski, J. Chem. Phys. **111**, 10520 (1999).

[28] S. F. Boys and F. Bernardi, Mol. Phys. **19**, 553 (1970).

[29] *CRC Handbook of Chemistry and Physics* 84th Ed. (CRC Press, Boca Raton, 2003).

[30] J. van Wijngaarden and W. Jäger, Mol. Phys. **98**, 1575 (2000).

[31] H. M. Pickett, J. Mol. Spectrosc. **148**, 371 (1991).

[32] K. A. Walker and A. R. W. Mckellar, Mol. Phys. **99**, 1391 (2001).

[33] C. Xia, K. A. Walker, and A. R. W. Mckellar, Mol. Phys. **99**, 643 (2001).

[34] G. T. Fraser, D. D. Nelson, Jr., A. Charo and W. Klemperer, J. Chem. Phys. **82**, 2535 (1986).

[35] W. Gordy and R. L. Cook, *Microwave Molecular Spectra,* 3rd ed. (Wiley, London, 1984).

[36] Y. Liu and W. Jäger, J. Chem. Phys. **120**, 9047 (2004).

[37] Y. Liu and W. Jäger, J. Chem. Phys. **121**, 6240 (2004).

[38] R. J. LeRoy, "LEVEL7.5, A Computer Program for Solving the Radial Schrödinger Equation for Bound and Quasibound Levels," University of Waterloo, Chemical Physics Research Report No. CP-655 2002 (unpublished).

[39] W. Jäger, Y. Xu, and M. C. L. Gerry, J. Chem. Phys. **99,** 919 (1993).

[40] E. J. Campbell, L. W. Buxton, M. R. Keenan, and W. H. Flygare, Phys. Rev. A **24,** 812 (1981).

[41] C. G. Gray and K. E. Gubbins, *Theory of Molecular Fluids, Vol. 1: Fundamentals* (Clarendon, Oxford, 1984).

[42] W. L. Faust and M. N. McDermott, Phys. Rev. **123,** 198 (1961).

[43] Z. Kisiel, J. Mol. Spectrosc. **218,** 58 (2003).

[44] L. Hedberg, I. M. Mills, J. Mol. Spectrosc. **160,** 117 (1993).

[45] D. Kivelson, E. B. Wilson, Jr., J. Chem. Phys. **21,** 1229 (1953).

[46] B. M. Axilrod, and E. Teller, J. Chem. Phys. **11,** 299 (1943).

CHAPTER 7 Microwave Spectra of the Open-Shell Xe-O_2 van der Waals Complex: A Direct Measure of the Magnetic Coupling of the Xe Nucleus with the O_2 Electron Spin

7.1 Introduction

Interactions of Xe with paramagnetic centres are believed to be one of the mechanisms which cause rapid spin relaxation of hyperpolarized ^{129}Xe (nuclear spin $I = 1/2$) in nuclear magnetic resonance (NMR) and magnetic resonance imaging (MRI) experiments. Such a relaxation process happens, for example, when Xe binds to paramagnetic Fe ions in some proteins. The main contributor to spin relaxation in the lung space is the interaction of Xe with oxygen (O_2) molecules.[1,2] A consequence of the spin relaxation is a reduction of the ^{129}Xe nuclear spin polarization and, therefore, a decrease of the NMR signal. Paramagnetic centres also cause large and sensitive responses in the ^{129}Xe chemical shifts. Much larger chemical shifts were observed in paramagnetic than in diamagnetic systems.[3,4,5] Utilizing this property, ^{129}Xe can be used to detect the presence and distribution of paramagnetic centres in the material or system under investigation.

In order to understand the shielding response of Xe to paramagnetic centres, several NMR studies were carried out in a test system consisting of Xe atoms in

oxygen gas (O_2 electron spin $S = 1$).[6,7,8] Fermi contact interaction, due to the presence of unpaired electron spin density at the Xe nucleus, was found to be the major contribution to the large paramagnetic ^{129}Xe shift. This spin density is mainly caused by the overlap between the 5s orbital of the Xe atom and one singly-occupied π_g^* orbital of the O_2 molecule.[6] The magnetic dipole-dipole coupling of the Xe nucleus with the unpaired electron distribution on O_2 is responsible for the relaxation of ^{129}Xe nuclear spin in O_2 gas.[7] Vukovic *et al.* performed a calculation of the intermolecular hyperfine tensors including both Fermi contact and magnetic dipolar parts.[8]

Microwave spectra of the Xe-O_2 complex could provide a more detailed insight into the intermolecular interactions, especially the magnetic coupling of the Xe nucleus with the electron spin of O_2. Fermi contact and dipole-dipole coupling constants have been determined for a system, Xe-NO_2, and were used to probe the unpaired electron delocalization within the complex.[9] Despite the simplicity of the O_2 structure, there are very few spectroscopic studies of O_2-containing van der Waals complexes, mainly because of the presence of the two unpaired electrons in the O_2 molecule which complicates the spectra. Only the $(O_2)_2$ (Ref. 10, 11, and 12) and Ar-O_2 (Ref. 13) spectra were observed in the infrared or visible regions at low resolution, and O_2-N_2O spectra were observed using high resolution infrared spectroscopy.[14] There has not been a report of high resolution microwave study of an O_2-containing complex yet. There are several challenges for microwave studies. First of all, interactions of the magnetic moment of the O_2 molecule with Earth's magnetic field will give rise to complicated Zeeman structures in the rotational spectra. Secondly, due to the presence of the electron spin of O_2, the interpretation of rotational spectra demands an

appropriate angular momentum coupling scheme to account for the coupling of electronic and rotational motion. An appropriate effective Hamiltonian used to determine rotational energy levels has therefore to be established. Two effective Hamiltonians were developed for O_2-containing complexes. Hund's case (a) coupling[15] was used in a rigid system, the O_2-N_2O complex. The electron spin angular momentum $\boldsymbol{S}$ is quantized along the O_2 molecular axis with projection quantum number Σ. The total rotational angular momentum $\boldsymbol{J}$ of the complex and its projection $\boldsymbol{K}$ onto the intermolecular axis, similar as those for a closed-shell symmetric rigid rotor, stay uncoupled with the electronic spin wavefunction [see Figure 7-1(a)]. The effective Hamiltonian[16] based on this coupling scheme was successfully used to explain the observed infrared spectra of O_2-N_2O.[14] For a more floppy rare gas-O_2 complex, a coupling scheme similar to Hund's case (c) was used.[15] The rotational angular momentum $\boldsymbol{N}$ of the O_2 monomer [instead of the electronic orbital angular momentum in Hund's case (c)] is first coupled to the electron spin angular momentum $\boldsymbol{S}$. The projection $\boldsymbol{K}$ of the resultant angular momentum $\boldsymbol{J_a}$ onto the intermolecular axis is then added to the end-over-end rotational angular momentum $\boldsymbol{L}$ of the complex, resulting in the total angular momentum of the complex, $\boldsymbol{J}$ [see Figure 7-1(b)]. Assuming a T-shaped structure of a rare gas-O_2 complex, a model describing its rotation-vibration-electronic spin states was proposed in the 1980's based on this coupling scheme,[17,18] however, so far it has not been tested against experimental rotational spectra.

In this chapter, the microwave study of the Xe-O_2 complex is presented. Rotational spectra of Xe-O_2 within the ground $^3\Sigma^-$ electronic state were recorded. An *ab initio* potential energy surface (PES) of Xe-O_2 was constructed to find the

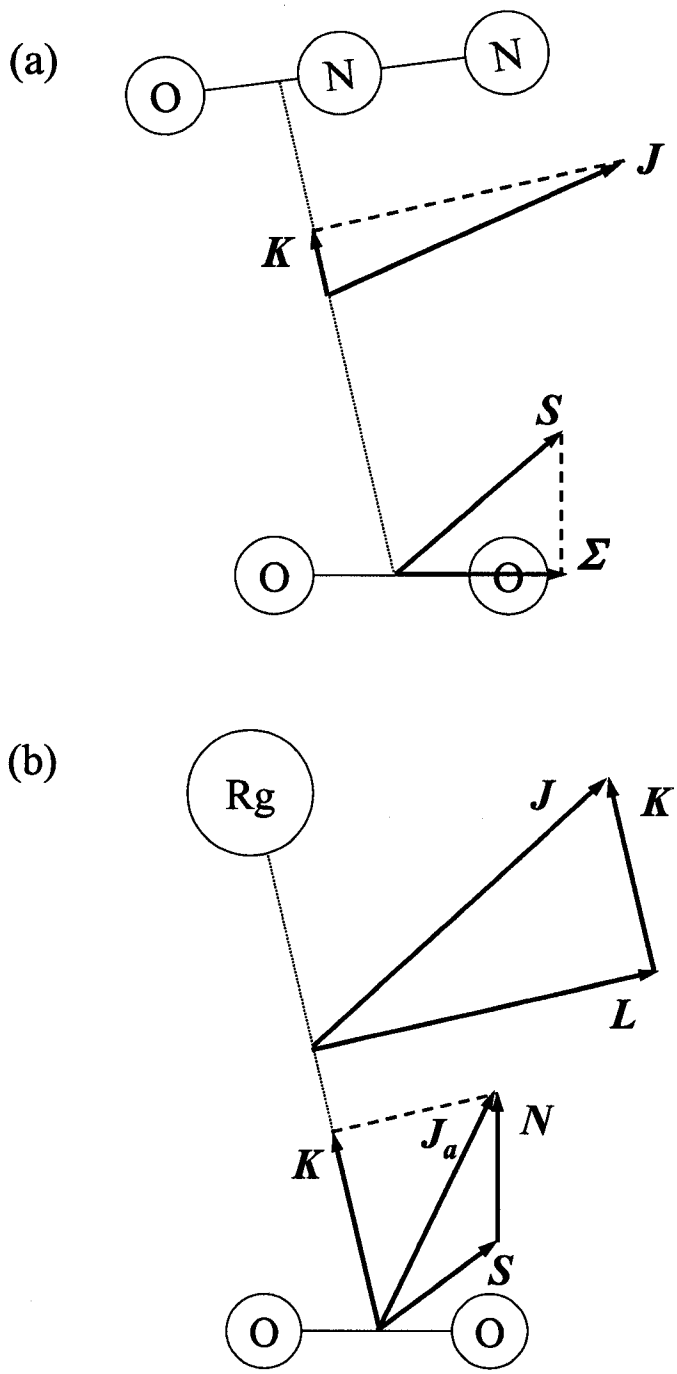

Figure 7-1: Angular momentum vector coupling diagram used for (a) O_2-N_2O, Ref. 16 and (b) rare gas-O_2, Ref. 17.

equilibrium structure of the complex. A resulting T-shaped structure at the global minimum validates the use of the proposed model from Refs. 17 and 18 to assign and analyze the spectra of Xe-O_2. The spectroscopic results were used to extract information about the geometric and electronic structure of the complex. In particular, the determined nuclear quadrupole and magnetic hyperfine constants provide detailed insight into the interactions of the Xe nucleus with the electron spin of O_2.

7.2 *Ab initio* potential energy calculation

7.2.1 Computational details

Potential energies of the Xe-O_2 complex were calculated at the spin unrestricted coupled cluster level of theory [UCCSD(T)][19,20,21] using the MOLPRO 2002.6 package of *ab initio* programs.[22] The restricted open-shell Hartree-Fock (ROHF) function was used as reference wavefunction. The aug-cc-pVQZ-PP basis set[23] was chosen for the Xe atom and the aug-cc-pVTZ basis set[24] for O atoms. The basis sets were supplemented with (3s3p2d2f1g) midbond functions, with the exponents α_s, α_p = 0.94, 0.34, 0.12; α_d, α_f = 0.64, 0.23; α_g = 0.35.[25] The interaction energies were calculated using supermolecule approach. The full counterpoise correction was applied to eliminate basis-set superposition error.[26] The O_2 monomer was fixed at its experimental equilibrium structure, with an O-O distance of 1.2074 Å.[27] The position of the Xe atom was defined in a polar coordinate system (R, θ), with the origin of the system at the center-of-mass (c.m.) of the O_2 unit; $\theta = 0°$ corresponds to a Xe-OO linear configuration and $\theta = 90°$ corresponds to a T-shaped configuration. The Xe-O_2 PES was calculated on a grid of 315 points. The radial grid includes 45

points from 3 to 10 Å, and the angular grid has 7 points with θ from 0° to 90° in steps of 15°. The calculated interaction energies are given in Table 7-1.

7.2.2 Discussion of the calculation results

The calculated PES has the global minimum at a T-shaped structure (R = 3.9 Å, θ = 90°) with a well depth of 138.2 cm^{-1}. A shallow local minimum with energy of -115.0 cm^{-1} was found at a linear configuration (R = 4.4 Å, θ = 0°). These two minima are connected by a transition state at R = 4.4 Å, θ = 30°, with an energy of -113.3 cm^{-1}. The small energy difference (1.7 cm^{-1}) between the transition state and local minimum indicates a very flat potential around the region from θ = 0° to 30°. A contour plot of the potential is shown in Figure 7-2. The resulting T-shaped structure at the global minimum is in accord with the semi-empirical potential constructed by Aquilanti *et al.*[28] The minimum obtained in this work has a 4% shallower well depth and 1% longer van der Waals distance compared with that of the potential by Aquilanti *et al.* (R = 3.87 Å, E_{min} = -144.1 cm^{-1}).[28]

7.3 Spectral search, assignments, and analyses

The angular momentum coupling scheme used here for the Xe-O_2 complex follows that used in Refs. 17 and 18, and is illustrated in a vector diagram shown in Figure 7-1(b). The $^{16}O_2$ monomer follows the Bose-Einstein statistics, which requires the total wavefunction to be symmetric under an interchange of the two equivalent ^{16}O nuclei. ^{16}O has nuclear spin of zero, and therefore only a symmetric spin function of $^{16}O_2$ molecule results. In the ground $^3\Sigma^-$ electronic state, the electronic and vibrational

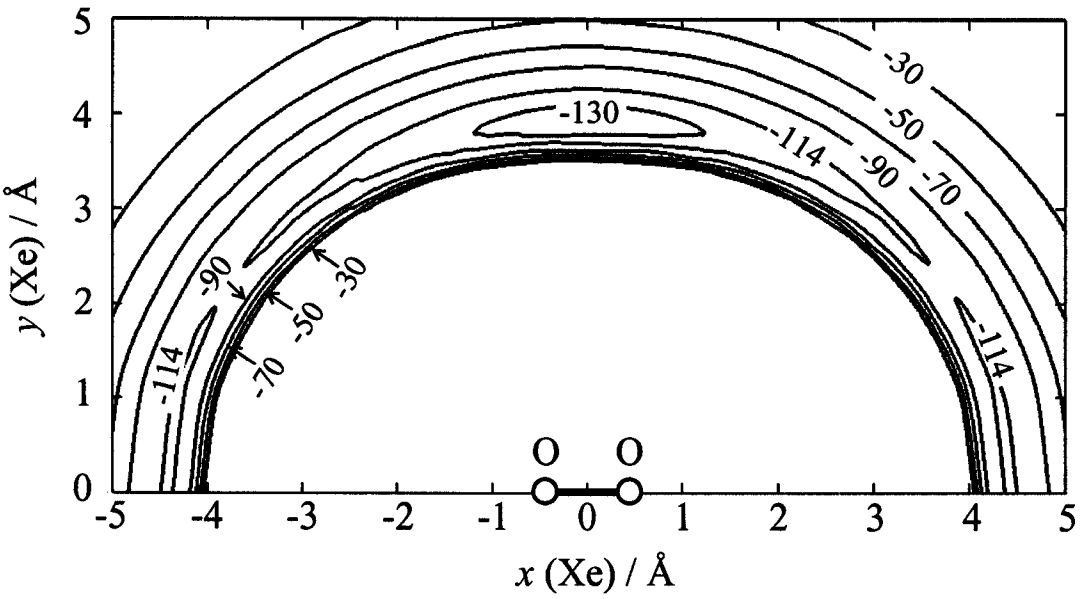

Figure 7-2: Contour diagram of the *ab intio* potential energy surface of Xe-O_2. Potential energies are given in cm^{-1}.

wavefunctions are antisymmetric and symmetric, respectively. As a consequence, only antisymmetric rotational wavefunctions are allowed, i.e., the rotational quantum number N of the $^{16}O_2$ monomer should be odd. Following the above coupling scheme and spin statistics, van der Avoird developed a model to predict the energy level pattern for a rare gas-O_2 complex.[17] This model is based on a T-shaped rare gas-O_2 structure, in accord with the structure of *ab initio* global minimum of Xe-O_2 obtained in section 7.2. Eigenstates of the energy levels associated with $N = 1$ were determined using this model.[17] Excited states with $N > 1$, i.e., states with excited O_2 internal rotation, are not expected to be populated in a supersonic beam experiment because of the low temperature (1-2 K) of the molecular expansion. A schematic diagram of the predicted energy level pattern is redrawn from reference 17 in Figure 7-3. Each level is

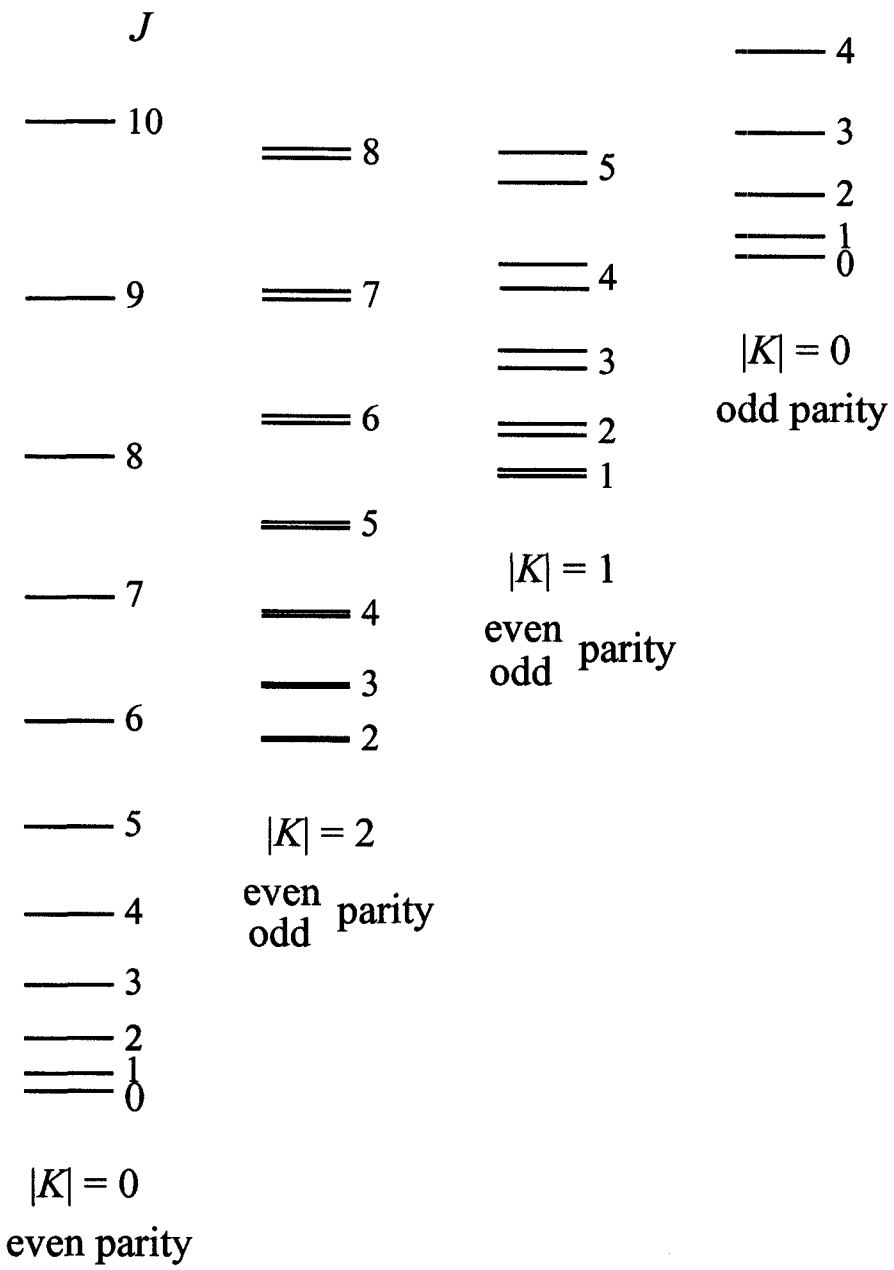

Figure 7-3: A schematic diagram of the predicted energy level pattern for rare gas – O_2, redrawn from Ref. 17.

labeled by J, $|K|$, and parity. Even/odd parity corresponds to symmetric/antisymmetric combinations of different wavefunctions with the same $|K|$ value. With the electron spin quantum number $S = 1$, J_a and K can have three possible values, 0, 1, and 2 ($\boldsymbol{J_a} = \boldsymbol{N} + \boldsymbol{S}$). Therefore, a total of six K stacks results, with each $|K|$ quantum number having two stacks of even and odd parities, respectively. The two stacks with different parities are well separated for $|K| = 0$, while near degenerate for $|K| = 1$ and 2. The small splittings of $|K| = 1$ or 2 stacks are a result of a Coriolis perturbation.

The sample mixtures used for generating the Xe-O_2 complex consisted of 1% Xe and 1% O_2 in Ne backing gas at about 5 atm. Initial transition frequencies were predicted based on a pseudodiatomic approximation. The Xe-c.m.(O_2) distance was estimated to be 4.14 Å, the same as the bond length of Ar-Xe.[29] The rotational constant B and the $J = 2$-1 transition frequency of the ^{132}Xe-O_2 complex were thus predicted to be 1144.8 MHz and 4579.2 MHz, respectively. The spectral search began with the $J =$ 2-1 transition. A set of transitions at 4.7 GHz with spacings characteristic for different Xe isotopes were first located. These transitions were assigned to the $|K| = 0$ stack with even parity. A method to confirm the assignment to the $|K| = 0$ stack is to locate the $J =$ 1-0 transition, however, this transition for Xe-O_2 is out of the frequency range of the spectrometer. Instead, the corresponding transitions for the Ar- and Ne-O_2 complexes were searched and the $J =$ 1-0 transitions were found.[30] This supports the assignment of the observed transitions of Xe-O_2 to the $|K| = 0$ stack by assuming that the energy level patterns for Ar-O_2 and Ne-O_2 are similar as that for Xe-O_2. Extensive searches for other K stacks were conducted but without success, probably due to the low population within these stacks. Higher J transitions for the ground $|K| = 0$ stack (even

parity) were located straightforwardly. The observed transitions show Zeeman structures arising from interactions of the magnetic moment of O_2 with Earth's magnetic field. An example spectrum of the $J = 2\text{-}1$ transition of $^{132}Xe\text{-}O_2$ is given in Figure 7-4 (a). These Zeeman structures, each spreading over 100 kHz, were reduced by the use of Helmholtz coils. Three mutually perpendicular pairs of Helmholtz coils were positioned outside the chamber to generate a nearly homogeneous magnetic field in the area where the microwave radiation and the molecular expansion interact. Each pair consists of two parallel and identical circular magnetic coils that carry equal electrical current flowing in the same direction and are placed symmetrically along a common axis. The electrical current in each pair of coils can be adjusted individually so that the generated magnetic field can cancel out Earth's magnetic field. The use of Helmholtz coils has effectively removed Zeeman structures or at least reduced the splittings to a magnitude below the instrumental spectral resolution (full-width at half-height ~7 kHz). The $J = 2\text{-}1$ transition of $^{132}Xe\text{-}O_2$ observed with the use of Helmholtz coils is shown in Figure 7-4 (b) and has only two components which are due to the Doppler effect.

The transition frequencies were taken as the average of the Doppler components measured with the use of Helmholtz coils, and are given in Tables 7-2 and 7-3. These frequencies were input in Pickett's SPFIT suite of programs[31] to determine the rotational constant B and the centrifugal distortion constants D_J and H_J (see Table 7-2) using a pseudodiatomic approach. The spectra of the $^{129}Xe\text{-}O_2$ and $^{131}Xe\text{-}O_2$ isotopomers are complicated by the hyperfine structures due to the Fermi contact and the dipole-dipole couplings between the electron spin of O_2 ($S = 1$) and the nuclear

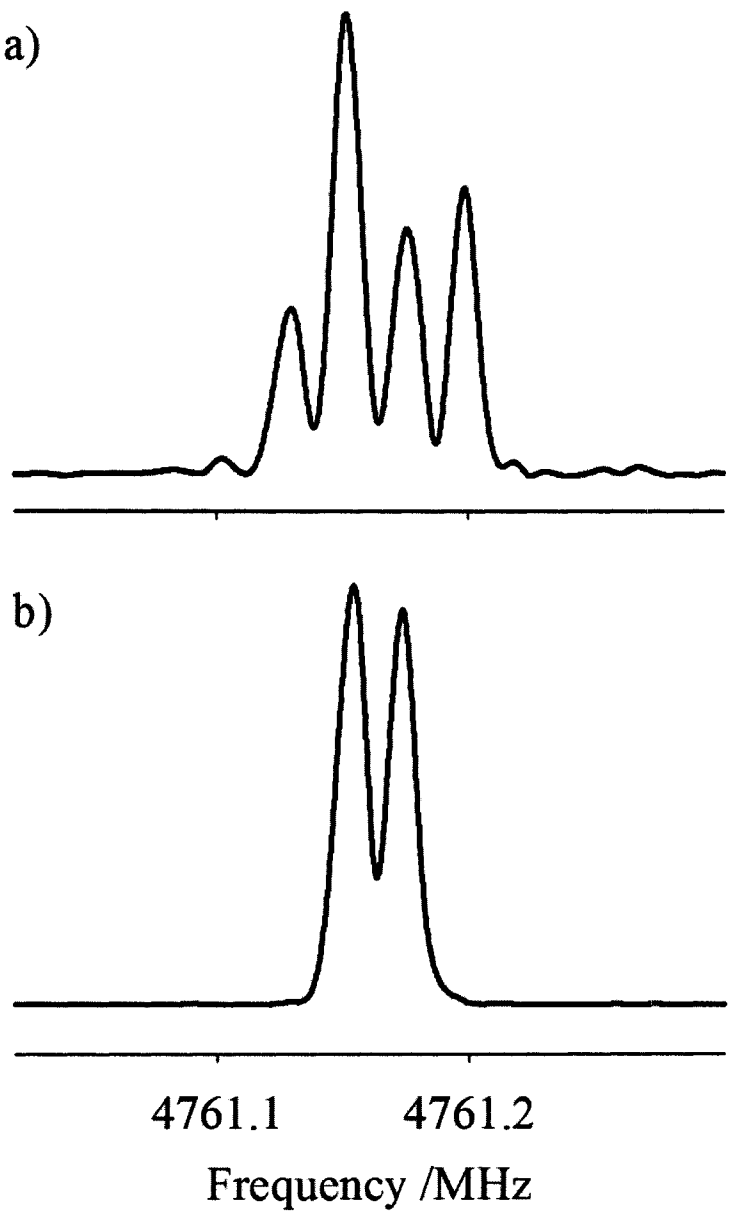

Figure 7-4: Spectra of J = 2-1 transition of $^{132}Xe\text{-}O_2$ recorded using 20 averaging cycles. Spectrum a) shows Zeeman structures and spectrum b) is recorded with the use of Helmholtz coils leaving only two Doppler components.

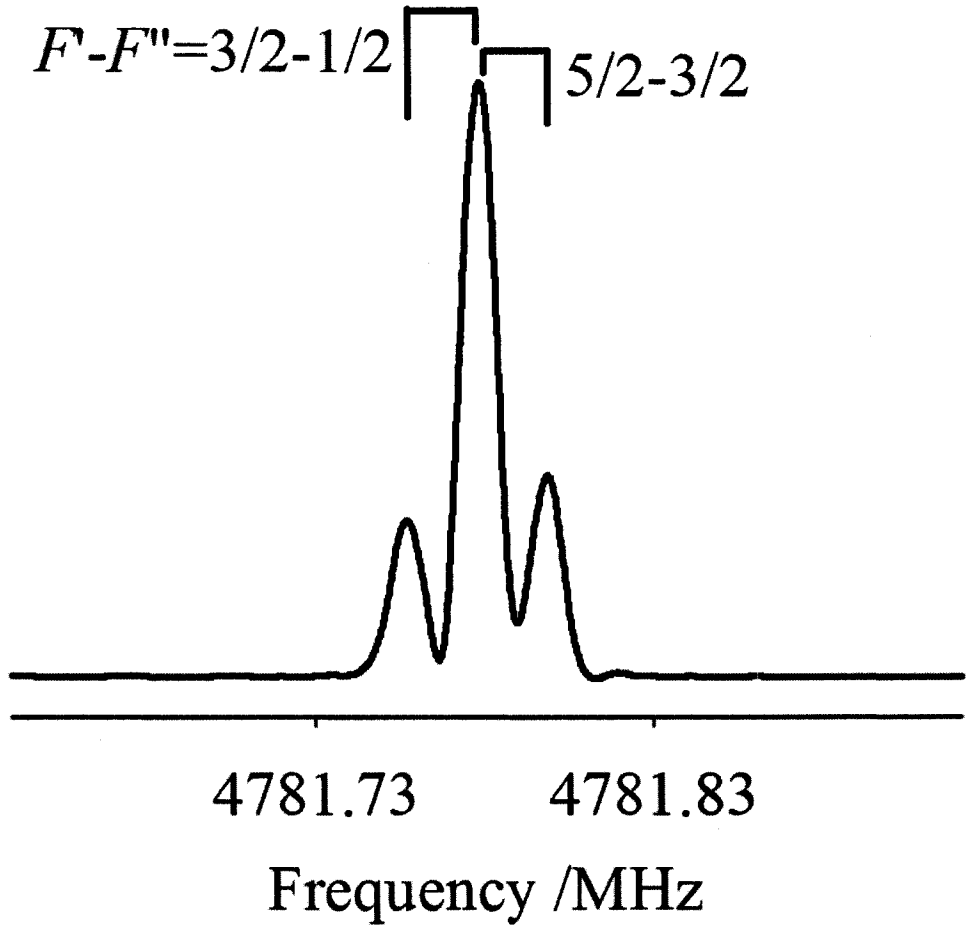

Figure 7-5: A spectrum of $J = 2$-1 transition of ^{129}Xe-O_2 showing magnetic hyperfine structure. This spectrum was recorded using 100 averaging cycles.

spins of ^{129}Xe (I = ½) and ^{131}Xe (I = 3/2). An example spectrum of the J = 2-1 transition of ^{129}Xe-O_2 is shown in Figure 7-5. The electric quadrupole interaction of the ^{131}Xe nucleus is a further contributor to the hyperfine structure of ^{131}Xe-O_2. For these two complexes, the most intense component for each J transition was used to determine B, D_J, and H_J constants. In the above fitting procedure, the electron spin-spin (λ) and spin-rotation constants (γ) were not included because the rotational levels

within the $|K| = 0$ stack (even parity) do not contain information about these two constants according to the calculated eigenstate energies by van der Avoid.[17]

The hyperfine constants of the ^{129}Xe-O_2 and ^{131}Xe-O_2 isotopomers were determined in separate fits from those for the rotational and distortion constants determinations. The Hamiltonian representing the hyperfine interaction between electron and nuclear spins is expressed as follows:[32]

$$\boldsymbol{H}_{hfs} = b_F \boldsymbol{I} \cdot \boldsymbol{S} + c/3(I_z S_z - \boldsymbol{I} \cdot \boldsymbol{S}) \qquad (7\text{-}1)$$

Here, b_F and c are the Fermi contact and the dipole-dipole coupling constants, respectively. The observed spectra of ^{129}Xe-O_2 and ^{131}Xe-O_2 do not have sufficient information to determine b_F and c constants independently. A parameter, $b = b_F - c/3$, was determined instead. For ^{131}Xe-O_2, the ^{131}Xe nuclear quadrupole coupling constant χ_{aa} was also obtained. The fitting procedure utilized the coupling scheme of $\boldsymbol{I} + \boldsymbol{J} = \boldsymbol{F}$. The electron spin-spin (λ) and spin-rotation (γ) constants were fixed at the experimental values of the O_2 monomer.[33] The hyperfine frequencies of ^{129}Xe- and ^{131}Xe-O_2 and the determined b and χ_{aa} values are listed in Table 7-3.

7.4 Discussion of the experimental results

The rotational and centrifugal distortion constants were determined for five Xe-O_2 isotopomers. The van der Waals bond length R between Xe and c.m.(O_2) can be calculated using $R = \left(\frac{h}{8\pi^2 \mu B}\right)$.[33] A value of 4.06 Å was obtained. The isotope effects upon Xe substitution are negligible. Compared with the Xe-N_2 complex (R = 4.21 Å, see Chapter 3), which also has a T-shaped structure, the R value of Xe-O_2 is 0.15 Å

smaller. This is consistent with the shorter equilibrium distance of Xe-O_2 (R_e = 3.90 Å) compared to Xe-N_2 (R_e = 4.10 Å, see Chapter 3) obtained from *ab initio* PESs. The distortion constants D_J (45-47 kHz) of Xe-O_2 are three times larger than those of Xe-N_2 (14 kHz). This is somewhat unexpected since the similar depths of the Xe-N_2 and Xe-O_2 global minima suggest similar rigidity of these two systems. The possible reason is that the observed $|K|$ = 0 stack of Xe-O_2 is mixed with the nearby $|K|$ = 1 stack of the same parity by a Coriolis interaction. As a result, the energy levels within the $|K|$ = 0 stack are compressed and deviate from the typical semi-rigid rotor pattern. This phenomenon was found to be more pronounced in the Ar- and Ne-O_2 systems.[30]

A free ^{131}Xe atom does not have a nuclear quadrupole interaction because of its spherically symmetric electronic charge distribution. The observed quadrupole hyperfine structures in the ^{131}Xe-O_2 complex arise from the distortion of Xe electron distribution by the presence of O_2. Like closed-shell Xe complexes discussed in previous chapters, the electric multipole moments of O_2 and the dispersion interaction between Xe and O_2 both contribute to the electric field gradient at the Xe nucleus. An additional contribution, unique for the open-shell systems, comes from the unpaired electron distribution around the Xe nucleus, due to the overlap between the 5p orbitals of Xe with one singly-occupied π_g^* orbital of O_2.[9] In order to estimate the contributions from all three effects, I first calculated the χ_{aa} constant arising from the electric multipole moments of O_2 using equation (7-2):[34]

$$q_0 = -6Q\left\langle \frac{3\cos^2\theta - 1}{R^5} \right\rangle - \cdots$$

$$\chi_{aa} = -eq_0(1-\gamma)Q_{Xe}/h \qquad (7\text{-}2)$$

Here, q_0 is the electric field gradient component along the intermolecular axis generated by the multipole moments of the O_2 at the site of Xe nucleus. Only the electric quadrupole moment Q = -0.4 D Å (Ref. 35) of O_2 was considered, and higher order electric moments were neglected. The brackets indicate averaging over the large amplitude angular motions. With R = 4.06 Å, a Sternheimer shielding factor γ = -152 (Ref. 34), and the ^{131}Xe nuclear quadrupole moment Q_{Xe} = -0.12 b,[36] a χ_{aa} value of -0.290 MHz was obtained for a T-shaped configuration (θ = 90°). The difference between the experimental value [0.624(2) MHz] and this calculated χ_{aa} value is 0.914 MHz, contributed by the dispersion interactions, the unpaired electron density in the Xe 5p orbitals, and zero-point vibrational effects. The value of 0.914 MHz has the same magnitude as the χ_{aa} value of the ^{131}Xe-^{20}Ne [0.3878(9) MHz], ^{131}Xe-Ar [0.7228(36) MHz], and ^{131}Xe-Kr [0.7079(86) MHz] complexes, in which the dispersion contribution to χ_{aa} dominates.[29] The 0.914 MHz difference is also in accord with the estimated contribution from the dispersion effect (0.828 MHz, see Chapter 3) to χ_{aa} of ^{131}Xe-$^{15}N_2$. Therefore, I expect only a small contribution from the unpaired electron density in the Xe 5p orbitals to the χ_{aa} value of ^{131}Xe-O_2, in the order of 0.1 MHz or even smaller. The corresponding constant is 252 MHz for the metastable $^3P_2$ $5p^5 6s$ state of the Xe atom, in which the unpaired electron is in a pure 5p orbital. A constant of 0.1 MHz corresponds to a spin population of 0.04% in the 5p orbital.

The magnetic hyperfine parameters, $b = b_F - c/3$, were determined for both ^{129}Xe-O_2 [0.42(2) MHz] and ^{131}Xe-O_2 isotopomers [0.095(4) MHz]. The ^{129}Xe / ^{131}Xe ratio of b is -4.4, which agrees reasonably well with the ^{129}Xe / ^{131}Xe magnetic g factor

ratio (-3.4).[37] The difference between these two ratios could be a consequence of the large uncertainties of the determined parameters or zero-point motion effects. The magnetic hyperfine parameters were used to estimate the unpaired electron spin population in the Xe atomic orbitals due to the overlap with one singly-occupied π_g^* orbital of O_2. The main contributor to the isotropic Fermi contact term is the spin population in the Xe 5s orbital, and the spin population in the 5p orbitals gives rise to the anisotropic dipole-dipole term.[38] As the Fermi contact and the dipole-dipole constants can not be determined independently, the interpretation of the magnetic hyperfine parameters can not achieve its fullest potential. According to the ratio of the corresponding constants in the Xe-NO_2 complex[9] and the XeF radical,[38,39] I assume that the two constants in the Xe-O_2 system are on the same order of magnitude. Based on the magnitude of the determined *b* constant, the Fermi contact and dipole-dipole constants were approximated to be in the order of 0.1 - 1 MHz for ^{129}Xe. The atomic ^{129}Xe Fermi contact parameter is 67,790 MHz when the unpaired electron is in a pure 5s orbital and the dipole-dipole parameter is 1,340 MHz when the unpaired electron in a pure 5p orbital.[40] Therefore, I estimate a spin population of 0.00015-0.0015% in the Xe 5s orbital and 0.007-0.07% in the Xe 5p orbital for the Xe-O_2 system. The estimated spin population for the 5p orbital is in accord with the value obtained from the ^{131}Xe nuclear quadrupole coupling constant.

This spin population estimation can only be considered as a fairly crude approximation for a number of reasons: 1. the Fermi-contact and dipole-dipole constants can not be determined independently; 2. a more accurate determination of the *b* constants requires a more accurate electron spin-spin constant λ due to the

relatively high correlation of these two constants; 3. contributions to the magnetic hyperfine structures from other effects, for example, charge transfer of the unpaired electron into the Xe 6s orbital and overlap of other Xe atomic orbitals with the O_2 molecular orbitals, can not be ruled out. More information about the magnetic interactions requires further spectroscopic studies to determine highly accurate constants and quantum chemistry calculations to provide detailed insight into the nature of the interactions.

7.5 Summary

An *ab initio* potential energy surface of the Xe-O_2 complex was constructed at the UCCSD(T) level of theory. The global minimum was found at the T-shaped structure. Rotational transitions of the Xe-O_2 complex within the ground $^3\Sigma^-$ electronic states were measured and assigned. The obtained rotational constant was used to determine the van der Waals bond length. The nuclear quadrupole coupling constant and magnetic hyperfine constants were used to estimate the unpaired electron spin population in the Xe 5s and 5p orbitals. The determined magnetic hyperfine constants can shed light on the Fermi contact and the dipole-dipole interactions, and therefore constitutes a step towards the understanding of large paramagnetic NMR shift and spin relaxation in the Xe-O_2 system.

Table 7-1: *Ab initio* interaction energies (in cm^{-1}) of $Xe\text{-}O_2$.

R / Å	0°	15°	30°	45°	60°	75°	90°
3.00	8951.26	8168.29	6297.10	4308.74	2664.39	1681.19	1352.87
3.10	6272.16	5723.49	4449.97	3001.10	1772.64	1096.20	839.09
3.20	4334.98	3953.57	3056.63	1991.35	1178.48	683.39	484.75
3.30	2946.82	2683.60	2063.71	1316.34	736.63	397.02	244.55
3.40	1961.47	1782.03	1370.55	833.61	445.85	207.28	85.38
3.50	1269.25	1147.42	845.99	496.97	211.08	38.77	-16.88
3.60	788.55	707.25	504.25	267.73	74.05	-41.78	-79.58
3.70	459.20	405.86	272.06	114.15	-14.30	-90.81	-115.23
3.80	237.17	202.76	116.02	14.61	-68.37	-117.25	-132.69
3.85	156.16	128.85	59.96	-21.27	-86.78	-124.61	-136.65
3.90	90.85	69.36	15.15	-48.77	-99.94	-129.00	-138.24
3.95	38.59	21.90	-20.24	-69.90	-109.24	-131.35	-137.97
4.00	-2.81	-15.60	-48.23	-86.13	-115.36	-131.56	-136.25
4.10	-60.21	-67.29	-85.27	-105.65	-120.84	-127.89	-129.73
4.20	-93.00	-96.34	-104.84	-113.73	-119.31	-120.71	-120.72
4.25	-102.83	-105.02	-109.83	-114.94	-116.98	-116.36	-115.73
4.30	-109.37	-110.45	-112.84	-114.58	-113.97	-111.75	-110.58
4.40	-115.02	-114.66	-113.34	-110.59	-106.32	-101.96	-100.15
4.50	-113.93	-112.74	-109.27	-103.95	-97.61	-92.11	-89.98
4.60	-108.79	-107.17	-102.58	-95.94	-88.62	-82.62	-80.39
4.70	-101.41	-99.61	-94.57	-87.44	-79.80	-73.75	-71.54
4.80	-92.99	-91.18	-86.11	-78.97	-71.45	-65.58	-63.50
4.90	-84.32	-82.58	-77.68	-70.86	-63.72	-58.31	-56.26
5.00	-75.85	-74.20	-69.67	-63.31	-56.66	-51.70	-49.81
5.20	-60.51	-59.15	-55.44	-50.17	-44.66	-40.59	-39.06
5.40	-47.82	-46.77	-43.80	-39.61	-35.16	-31.95	-30.73
5.60	-37.73	-36.90	-34.59	-31.30	-27.77	-25.27	-24.32
5.80	-29.82	-29.21	-27.43	-24.86	-22.05	-20.13	-19.39
6.00	-23.67	-23.22	-21.72	-19.74	-17.79	-16.16	-15.56
6.25	-17.92	-17.55	-16.51	-15.04	-13.51	-12.36	-11.94
6.50	-13.70	-13.45	-12.68	-11.56	-10.42	-9.56	-9.24
6.75	-10.59	-10.40	-9.82	-8.99	-8.11	-7.46	-7.23
7.00	-8.28	-8.13	-7.68	-7.04	-6.38	-5.88	-5.71
7.25	-6.54	-6.42	-6.08	-5.58	-5.09	-4.68	-4.55
7.50	-5.24	-5.13	-4.85	-4.50	-4.09	-3.78	-3.67
7.75	-4.22	-4.14	-3.93	-3.63	-3.31	-3.06	-2.97
8.00	-3.43	-3.36	-3.19	-2.95	-2.70	-2.50	-2.43
8.25	-2.80	-2.75	-2.61	-2.42	-2.22	-2.07	-2.00
8.50	-2.31	-2.27	-2.15	-1.99	-1.83	-1.71	-1.66
8.75	-1.92	-1.88	-1.78	-1.66	-1.52	-1.41	-1.38
9.00	-1.60	-1.56	-1.49	-1.38	-1.27	-1.20	-1.15
9.25	-1.34	-1.32	-1.25	-1.16	-1.07	-1.01	-0.96
9.50	-1.13	-1.10	-1.07	-0.98	-0.91	-0.84	-0.81
9.75	-0.96	-0.93	-0.91	-0.83	-0.77	-0.71	-0.68
10.00	-0.82	-0.78	-0.76	-0.70	-0.66	-0.61	-0.58

Table 7-2: Measured transition frequencies and determined spectroscopic constants of Xe-O_2 isotopomers.

	^{136}Xe-O_2		^{134}Xe-O_2		^{132}Xe-O_2		^{131}Xe-O_2		^{129}Xe-O_2	
J'-J''	ν_{obs} (MHz)	$\Delta\nu$[a] (kHz)	ν_{obs} (MHz)	$\Delta\nu$ (kHz)	ν_{obs} (MHz)	$\Delta\nu$ (kHz)	ν_{obs} (MHz)	$\Delta\nu$ (kHz)	ν_{obs} (MHz)	$\Delta\nu$ (kHz)
2-1	4735.0504	4.0	4747.9132	4.1	4761.1584	-3.4	4767.8988	-2.5	4781.7813	0.7
3-2	7099.8695	-4.6	7119.1364	-4.6	7138.9761	-0.4	7149.0875	3.8	7169.8615	-0.8
4-3	9461.4686	1.4	9487.1072	1.5	9513.5077	3.4	9526.9660	-2.1	9554.6058	0.3
5-4					11883.7058	1.5	11900.4955	0.4	11934.9507	0.06
6-5					14248.5784	-3.6			14309.8836	-0.04
7-6					16607.2025	1.2				
B /MHz	1184.1210(3)		1187.3403(3)		1190.6610(2)		1192.3457(4)		1195.8214(3)	
D_J /kHz	44.93(1)		45.38(1)		46.428(8)		46.38(3)		47.13(1)	
H_J /kHz					0.01622(8)		0.0119(5)		0.0158(2)	
σ /kHz[b]	3.6		3.7		2.6		2.5		0.5	

[a] $\Delta\nu = \nu_{obs} - \nu_{cal}$.
[b] Standard deviation of the fit.

Table 7-3: Measured hyperfine frequencies and corresponding hyperfine constants of $^{129}Xe\text{-}O_2$ and $^{131}Xe\text{-}O_2$.

		$^{129}Xe\text{-}O_2$		$^{131}Xe\text{-}O_2$		
$J'\text{-}J''$	$F'\text{-}F''$	ν_{obs} (MHz)	$\Delta\nu$[a] (kHz)	$F'\text{-}F''$	ν_{obs} (MHz)	$\Delta\nu$ (kHz)
2-1	1.5-0.5	4781.7639	3.1	0.5-1.5	4767.6539	-1.0
	2.5-1.5	4781.7813	0.6	1.5-1.5	4767.8031	-0.7
				3.5-2.5	4767.8988	-0.4
				2.5-1.5	4767.8988	-4.9
				2.5-2.5	4768.0752	4.3
				1.5-0.5	4768.0752	-2.1
3-2	2.5-1.5	7169.8471	2.1	1.5-2.5	7148.8886	0.7
	3.5-2.5	7169.8615	-3.1	2.5-2.5	7149.0366	4.2
				4.5-3.5	7149.0875	2.7
				3.5-2.5	7149.0875	-1.7
				2.5-1.5	7149.1340	1.8
				1.5-0.5	7149.1340	-2.7
4-3	3.5-2.5	9554.5848	-3.4	5.5-4.5	9526.9660	5.2
	4.5-3.5	9554.6058	-1.5	4.5-3.5	9526.9660	0.9
				3.5-2.5	9526.9839	-3.6
				2.5-1.5	9526.9839	-7.9
5-4	4.5-3.5	11934.9249	-1.5	4.5-4.5	11900.4755	-0.8
	5.5-4.5	11934.9507	5.9	6.5-5.5	11900.4955	3.8
				5.5-4.5	11900.4955	-0.4
				4.5-3.5	11900.5125	1.8
				3.5-2.5	11900.5125	-2.5
6-5	6.5-5.5	14309.8836	-1.1			
λ /MHz			59501.33[b]			
γ/MHz			-252.59[b]			
χ_{aa}/MHz					0.624(2)	
b /MHz		0.42(2)			-0.095(4)	
σ/kHz[c]		2.9			2.4	

[a] $\Delta\nu = \nu_{obs} - \nu_{cal}$.
[b] Fixed at the experimental values of the O_2 monomer, Ref. 33.
[c] Standard deviation of the fit.

References

[1] A. Cherubini, and A. Bifone, Prog. Nucl. Magn. Reson. Spectrosc. **42**, 1 (2003).

[2] B. M. Goodson, J. Magn. Reson. **155**, 157 (2002).

[3] C. J. Jameson and A. K. Jameson, Mol. Phys. **20**, 957 (1971).

[4] R. Grosse, B. Burmeister, B. Boddenberg, A. Gedeon, and J. Fraissard, J. Phys. Chem. **95**, 2443 (1991).

[5] A. K. Jameson, C. J. Jameson, and H. S. Gutowsky, J. Chem. Phys. **53**, 2310 (1970).

[6] A. D. Buckingham and P. A. Kollman, Mol. Phys. **23**, 65 (1972).

[7] C. J. Jameson, A. K. Jameson, and J. K. Hwang, J. Chem. Phys. **89**, 4074 (1988).

[8] L. Vukovic, C. J. Jameson, and D. N. Sears, Mol. Phys. **104**, 1217 (2006).

[9] C. J. Whitham, R. J. Low, and B. J. Howard, Chem. Phys. Lett. **286**, 408 (1998).

[10] C. A. Long and G. E. Ewing, J. Chem. Phys. **58**, 4824 (1973).

[11] J. Goodman and L. E. Brus, J. Chem. Phys. **67**, 4398 (1977).

[12] J. Goodman and L. E. Brus, J. Chem. Phys. **67**, 4408 (1977).

[13] G. Henderson and G. E. Ewing, J. Chem. Phys. **59**, 2280 (1973).

[14] H.-B. Qian, D. Seccombe, and B. J. Howard, J. Chem. Phys. **107**, 7658 (1997).

[15] F. Hund, Handbuch der Physik, **24**, 561 (1933).

[16] H.-B. Qian, S. J. Low, D. Seccombe, and B. J. Howard, J. Chem. Phys. **107**, 7651 (1997).

[17] A. van der Avoird, J. Chem. Phys. **79**, 1170 (1983).

[18] J. Tennyson and J. Mettes, Chem. Phys. **76**, 195 (1983).

[19] C. Hampel, K. Peterson, and H.-J. Werner, Chem. Phys. Lett. **190**, 1 (1992).

[20] P. J. Knowles, C. Hampel, and H.-J. Werner J. Chem. Phys. **99**, 5219 (1993).

[21] P. J. Knowles, C. Hampel, and H.-J. Werner J. Chem. Phys. **112**, 3106 (2000).

[22] MOLPRO, a package of *ab initio* programs designed by H.-J. Werner and P. J. Knowles, version 2002.6, R. D. Amos, A. Bernhardsson, A. Berning, P. Celani, D. L. Cooper, M. J. O. Deegan, A. J. Dobbyn, F. Eckert, C. Hampel, G. Hetzer, P. J. Knowles, T. Korona, R. Lindh, A. W. Lloyd, S. J. McNicholas, F. R. Manby, W. Meyer, M. E. Mura, A. Nicklass, P. Palmieri, R. Pitzer, G. Rauhut, M. Schütz, U. Schumann, H. Stoll, A. J. Stone, R. Tarroni, T. Thorsteinsson, and H.-J. Werner.

[23] K. A. Peterson, D. Figgen, E. Goll, H. Stoll, and M. Dolg, J. Chem. Phys. **119**, 11113 (2003).

[24] T. H. Dunning, Jr., J. Chem. Phys. **90**, 1007 (1989).

[25] S. M. Cybulski and R. R. Toczylowski. J. Chem. Phys. **111**, 10520 (1999).

[26] S. F. Boys and F. Bernardi, Mol. Phys. **19**, 553 (1970).

[27] *CRC Handbook of Chemistry and Physics* (84th Edition, 2003-2004).

[28] V. Aquilanti, D. Ascenzi, D. Cappelletti, M. de Castro, and F. Pirani, J. Chem. Phys. **109**, 3898 (1998).

[29] W. Jäger, Y. Xu, and M. C. L. Gerry, J. Chem. Phys. **99**, 919 (1993).

[30] Q. Wen and W. Jäger, manuscripts in preparation.

[31] H. M. Pickett, J. Mol. Spectrosc. **148**, 371 (1991).

[32] E. Hirota, *High-Resolution Spectroscopy of Transient Molecules* (Springer, Berlin, 1985), Chap. 2.

[33] W. Gordy and R. L. Cook, *Microwave Molecular Spectra*, 3rd ed. (Wiley, London, 1984).

[34] E. J. Campbell, L. W. Buxton, M. R. Keenan, and W. H. Flygare, Phys. Rev. A **24**, 812 (1981).

[35] C. G. Gray and K. E. Gubbins, *Theory of Molecular Fluid* (Clarendon, Oxford, 1984), Vol. 1.

[36] W. L. Faust and M. N. McDermott, Phys. Rev. **123**, 198 (1961).

[37] R. K. Harris, E. D. Becker, S. A. Cabral de Menezes, R. Goodfellow, and P. Granger, Pure Appl. Chem. **73**, 1795 (2001).

[38] J. R. Morton and W. E. Falconer, J. Chem. Phys. **39**, 427 (1963).

[39] E. Y. Misochko, A. V. Akimov, I. U. Goldschleger, D. A. Tyurin, and D. N. Laikov, J. Chem. Phys. **122**, 034503 (2005).

[40] W. Weltner, Jr., *Magnetic Atom and Molecules* (Van Nostrand Reinhold, New York, 1983), Vol. 2.

CHAPTER 8 Conclusions

Motivated by achieving molecular level interpretations of *in vivo* ^{129}Xe NMR/MRI results, I completed my thesis work which provides fundamental details for our understanding of Xe-molecule interactions. In this work, I report high resolution microwave and *ab initio* studies of seven Xe containing van der Waals complexes, namely Xe-N_2, Xe-CH_4, Xe-H_2O, Xe-$(H_2O)_2$, Xe-NH_3, Ne-Xe-NH_3, and Xe-O_2. The selected binding partners of Xe are main constituents of air and the human body, or closely related to important functional groups of proteins in living tissues. Both experimental and theoretical results have been discussed in detail in Chapters 3 to 7. In the following, I summarize some significant results achieved in this work:

1. From the pure rotational studies, I obtained structural information about the investigated complexes. For all seven complexes, van der Waals distances were estimated from the obtained rotational constants. The observed rotational spectra of the Xe-N_2 complex indicate that the two N nuclei are equivalent and thus a T-shaped structure of the complex was concluded. The Xe-O_2 complex is another system that contains a homonuclear diatomic. Although a definite structure of this complex could not be determined from the experimental results, the observed spectra are in accord with the energy level diagram calculated from a model assuming a T-shaped structure of the complex.[1] For two investigated van der Waals trimers, Xe-$(H_2O)_2$ and Ne-Xe-

NH_3, triangular structures of the complexes were concluded based on the experimental rotational constants by considering the H_2O and NH_3 moieties as spheres.

2. In addition to the structural information, the recorded rotational spectra provide details about the features of the interaction potential energy surfaces and internal dynamics of the complexes. For the Xe-CH_4, Xe-H_2O, and Xe-NH_3 complexes, different tunneling states were observed, indicating nearly free internal rotation of the CH_4, H_2O, and NH_3 units and the inversion motion of NH_3 within the corresponding complexes. Comparisons of spectroscopic parameters of these complexes with those of CH_4, H_2O, and NH_3 binding to other Rg atoms has established a connection between the size and polarizability of the Rg atom and the features of the interaction potentials. For example, less pronounced Coriolis perturbation was found in the $j = 1$, $K = 0$ state of Xe-CH_4 compared to Kr-CH_4 (Ref. 2), indicating an increased angular anisotropy of the potentials in going from Kr-CH_4 to Xe-CH_4. In the case of Xe-NH_3, transitions within the $\Pi 1_1^{lower}$ state were observed while those within the $\Sigma 1_1$ state could not be detected. This suggests that in Xe-NH_3 the $\Pi 1_1^{lower}$ state has a lower energy than the $\Sigma 1_1$ state, in contrast to the Ar-NH_3 case.[3] The puzzle about $\Sigma 1_1/\Pi 1_1^{lower}$ energy level reordering upon the substitution of Ar with Xe still remains. This stimulates further theoretical studies of the interaction potentials and corresponding wavefunctions for each tunneling state.

3. The microwave studies of the Xe-$(H_2O)_2$ and Ne-Xe-NH_3 trimers provide experimental evidence for non-additive three-body effects. In the case of the Xe-$(H_2O)_2$ trimer, it was found that the Xe-H_2O van der Waals bonds are shorter and stronger compared to the Xe-H_2O dimer, suggesting a crucial contribution from an

attractive electrostatic interaction. In contrast, the van der Waals bonds in the Ne-Xe-NH_3 trimer are longer and weaker than the corresponding dimers. This indicates that the repulsive triple-dipole dispersion term is dominant in this case. The detailed characterization of the variations of the structure and vibrational dynamics in going from the dimers to the corresponding trimers constitutes a first step towards the understanding of the interactions between Xe and its bulk phase surroundings.

4. The experimentally determined nuclear quadrupole coupling constants arising from the ^{131}Xe (nuclear spin $I = 3/2$) nucleus and magnetic hyperfine constants due to the ^{129}Xe ($I = 1/2$) and ^{131}Xe nuclei are exquisite probes of the electrostatic environment of the Xe atom. The ^{131}Xe nuclear quadrupole coupling constant provides a measure of the distortion of the spherically symmetric electronic charge distribution of a free Xe atom by the presence of the surrounding molecules. The main contributions to these coupling constants come from the electric multipole moments of the binding partners and dispersion interactions. From these constants, information about the distribution and orientations of the surrounding molecules can be obtained. Large amplitude internal motions of the CH_4, H_2O, and NH_3 subunits in the Xe-CH_4, Xe-H_2O, Xe-NH_3, and Ne-Xe-NH_3 complexes are evident from the relatively small ^{131}Xe coupling constants. Compared with Xe-H_2O dimer, the coupling constants along Xe-H_2O bonds in the Xe-$(H_2O)_2$ trimer are an order of magnitude larger, suggesting that the H_2O internal motions are largely hindered in the trimer by interaction with the second water molecule. The large value of the off-diagonal coupling constant χ_{ab} in the Xe-$(H_2O)_2$ trimer provides evidence for the different orientation of the two H_2O molecules with respect to the Xe atom. The information about the electronic

environment of the Xe atom with one and two surrounding H_2O molecules can be extrapolated to generate a picture of the electronic structure of the Xe atom as a function of the number of surrounding water molecules. In addition to the ^{131}Xe nuclear quadrupole coupling constant, the ^{129}Xe and ^{131}Xe magnetic hyperfine constants were also determined for the open-shell Xe-O_2 system. These constants are a direct probe of the interactions between the nuclear spin of Xe and the electron spin of O_2. These interactions are the major contributors to the large paramagnetic ^{129}Xe NMR shift and the ^{129}Xe spin relaxation in the human lungs in MRI experiments.

5. The spectroscopic studies of Xe containing complexes were complemented by *ab initio* calculations. This combined experimental and theoretical approach allows to gain further insights into the nature of the Xe-molecule interactions. In the Xe-N_2 study, the rotational spectra derived from *ab initio* potential energy surfaces were directly compared with the recorded spectra. This enabled me to construct a scaled *ab initio* Xe-N_2 potential of "microwave accuracy". For the other investigated Xe containing complexes, although no quantitative comparison was attempted between experimental and calculated rotational spectra, the *ab initio* results still provided an in-depth understanding of the systems and afford qualitative explanations for some experimental observations. For example, in the Xe-H_2O study, a comparison of structural parameters and force constants obtained from experiment and an *ab initio* potential indicate the non-negligible contributions of anti-hydrogen bonded and non-planar configurations to the wavefunctions; The dipole moment calculations for Xe-CH_4 can explain the pronounced intensity enhancement observed for the $j = 2$, $K = 1$ transitions; The optimized geometries for Xe-$(H_2O)_2$ support the effective structure

that resulted from reproducing the experimental ^{131}Xe nuclear quadrupole coupling constants.

In general, the present work has furthered our understanding of Xe-molecule interactions. A further step towards the goal of achieving an interpretation of ^{129}Xe NMR/MRI results on the microscopic level would be the study of interactions of Xe with more complex biomolecules. A systematic study of Xe in larger clusters by gradually increasing the number of surrounding molecules would also be necessary to understand the non-additive many-body effects, which are important in the simulation of Xe in *in vivo* environments. The Xe-host site interaction potentials have to be generated based on the above studies. These interaction potentials are ingredients for the construction of the corresponding magnetic shielding surfaces that are required for an interpretation of the NMR/MRI data.

References

[1] A. van der Avoird, J. Chem. Phys. **79**, 1170 (1983).

[2] Y. Liu and W. Jäger, J. Chem. Phys. **120**, 9047 (2004).

[3] D. D. Nelson, Jr., G. T. Fraser, K. I. Peterson, K. Zhao, W. Klemperer, F. J. Lovas, and R. D. Suenram, J. Chem. Phys. **85**, 5512 (1986).